Fluidelastic Instability of Tube Arrays Subjected to Axisymmetric Jet Flow

FLUIDELASTIC INSTABILITY OF TUBE ARRAYS SUBJECTED TO AXISYMMETRIC JET FLOW

By
BUDDY J. LEDGER, B.ENG., P.ENG.

A Thesis
Submitted to the School of Graduate Studies
in Partial Fulfilment of the Requirements
for the Degree
Master of Applied Science

McMaster University

Master of Applied Science (2015) McMaster University
(Department of Mechanical Engineering) Hamilton, Ontario

TITLE: Fluidelastic Instability of Tube Arrays Subjected to Axisymmetric Jet Flow
AUTHOR: Buddy J. Ledger, B.Eng., P.Eng.
SUPERVISOR: Dr. David S. Weaver, Ph.D., P.Eng.
NUMBER OF PAGES: xiii, 190

Abstract

An experimental scale model study was conducted to investigate the onset of fluidelastic instability in a tube array subjected to axisymmetric jet flow. A tube array was constructed using aluminum tubes with 44.45 mm outer diameter, D, which were arranged in a square pattern with 88 mm pitch, P. The pitch to diameter ratio, P/D, was approximately 2.0. The tubes were flexibly mounted using threaded rod and tuned to a first mode natural frequency, f_n, of 9 Hz. Auxiliary damping devices were added to each tube, and tuned, to achieve a damping ratio, ζ, of 1 % of critical. The mass damping parameter, $m(2\pi\zeta)/(\rho D^2)$, of the tube array was 27.9. The tube array was tested under uniform flow conditions in McMaster University's 2 ft wind tunnel to establish the critical reduced velocity, $V_{cr}/(f_n D)$, of 30.0 at the onset of fluidelastic instability. The uniform flow test established a basis for comparing the results with the existing literature and evaluating the validity of the proposed partial admission calculation. The tube array was also tested in open air using an axisymmetric jet, with two different physical arrangements, the first with the jet aimed between tubes and perpendicular to the tube spans and the second with the jet aimed at a tube face and perpendicular to the tube spans. In each case the jet flow velocity was incrementally increased to characterize the onset of fluidelastic instability. To characterize the flow dispersion through the tube array a series of velocity profile measurements were also collected.

The measured velocity profiles were used to estimate the spanwise function of transverse average gap velocity, $\bar{V}(x)$, which was used to predict the equivalent critical uniform gap flow velocity, V_{cr}, using the concept of partial admission. The predicted V_{cr} values showed reasonable agreement with the experimental results. However, the prediction method did indicate instabilities in tube rows where instability was not actually observed.

A simplified prediction approach was developed which was based on using a predicted three dimensional velocity profile, $V(x, y)$, at the z location of the first row tube gap, under the assumption of free field conditions, to calculate an estimate of the spanwise function of transverse average gap velocity, $\bar{V}(x)$. Although the predictions of V_{cr} agreed reasonably well with the experimental results, first row instabilities were not observed in any of axisymmetric jet flow experiments. Therefore, this method can be used to estimate the the critical uniform gap velocity, V_{cr}, but not the spatial location of the instability.

Based on the results of the experiments and calculations, adoption of the modified partial admission formula is recommended and possible avenues for further investigation and verification are suggested.

Acknowledgements

I would like to express my sincere gratitude toward my thesis supervisor Dr. Weaver for his patience, guidance, encouragement and financial support. I would also like to thank him for the profound influence he has had on the form and direction of my professional engineering career in acoustics, noise and vibration consulting.

To my wife, I would like to express my heartfelt appreciation for her patience and support without which the completion of this work would not have been possible.

To my family, Mahsa, Sienna and Liam, you are my inspiration and motivation in all things.

Table of Contents

Abstract iii
Acknowledgements iv
List of Figures viii
List of Tables xi
Nomenclature xiii

1. Introduction 1

2. Background 4
- 2.1 Flow Induced Vibrations . . . 4
  - 2.1.1 Forced Vibrations . . . 4
  - 2.1.2 Self-excited Vibrations . . . 5
  - 2.1.3 Self-controlled Vibrations . . . 5
- 2.2 Fluidelastic Instability . . . 6
  - 2.2.1 Basic Theories . . . 6
  - 2.2.2 Current Design Practice . . . 8
  - 2.2.3 Recommended Design Practice . . . 8
- 2.3 Nonuniform Cross-Flow - Partial Admission . . . 10
- 2.4 Scale Modelling and Distortions . . . 13
- 2.5 Sootblowers . . . 14
- 2.6 Submerged Axisymmetric Turbulent Jets . . . 16
- 2.7 Supersonic Flow and the Effects of Compressibility . . . 17

3. Experimental Apparatus and Methodology 21
- 3.1 Wind Tunnel Facility . . . 21
- 3.2 Air Jet System . . . 22
- 3.3 Model Heat Exchanger Design . . . 22
  - 3.3.1 Tube Geometry and Materials . . . 28
  - 3.3.2 Tube Mode Shape . . . 28
  - 3.3.3 Tube Modal Mass and Mass Ratio . . . 32
  - 3.3.4 Tube Damping . . . 34
- 3.4 Instrumentation and Signal Processing . . . 39
  - 3.4.1 Vibration Measurements . . . 39
  - 3.4.2 Velocity Measurements . . . 43

4. Experimental Results 44
- 4.1 Uniform Flow . . . 44
- 4.2 Jet Flow Centered between Tubes . . . 48

4.2.1 Vibration Measurements 48
4.2.2 Velocity Measurements 48
4.3 Jet Flow Centered on a Tube Face 58
4.3.1 Vibration Measurements 58
4.3.2 Velocity Measurements 58
4.4 Summary 68

5. Discussion 69
5.1 Uniform Flow 69
5.2 Jet Flow 70
5.3 Summary 80

6. Conclusions 91

7. Recommendations 94

References **95**

Appendix A. Tube Mode Shape Calculations **99**
A.1 Rayleigh's Quotient - Approximate Method 99
A.2 Boundary Value Problem - Exact Method 102

Appendix B. Instrument Calibrations and Uncertainty **114**
B.1 Linear Least Squares Regression 114
B.2 Uncertainty Analysis 120
B.3 Strain Gauge Measurements 122
B.4 Pitot Static Tube Measurements 131
B.5 Hot-wire Measurements 135

Appendix C. Experimental Results **146**
C.1 Jet Flow Centered between Tubes 146
C.2 Jet Flow Centered on a Tube Face 146

List of Figures

(2.1) Schematic diagram of fluidelastic amplitude response. 7
(2.2) Fluidelastic stability diagram ASME (2009) 9
(2.3) Recommended design guidelines for fluidelastic instability. 11
(2.4) Retractable lance type sootblower. 15
(2.5) Development of a submerged axisymmetric turbulent jet velocity profile. 18
(2.6) Comparison of incompressible and compressible stagnation pressures. 19
(2.7) Comparison of turbulent mixing of initially compressible and incompressible jets. 20

(3.1) Wind tunnel test facility. 23
(3.2) Air jet system. 25
(3.3) Model tube array. 26
(3.4) Air jet orientation and position. 27
(3.5) Model tube segmented based on physically unique sections. . . . 29
(3.6) Comparison of "approximate" and "exact" mode shape functions. . 33
(3.7) Model tube damper assembly. 37
(3.8) Model tube damping measurement and calculation procedure. . . 41
(3.9) Schroeder plot example. 42

(4.1) Amplitude response of T23 in uniform cross-flow. 45
(4.2) Amplitude response of T43 in uniform cross-flow. 46
(4.3) Amplitude response of T34 in uniform cross-flow. 47
(4.4) Experimental setup: jet flow centred between tubes. 50
(4.5) Amplitude response of T13, jet centred between T13 and T14. . . 51
(4.6) Amplitude response of T23, jet centred between T13 and T14. . . 52
(4.7) Amplitude response of T33, jet centred between T13 and T14. . . 53
(4.8) Amplitude response of T43, jet centred between T13 and T14. . . 54
(4.9) Jet centreline velocity versus nozzle flowrate with jet centred between tubes. 55
(4.10) Horizontal velocity propagation with jet centred between tubes. . 56
(4.11) Vertical velocity propagation with jet centred between tubes. . . . 57
(4.12) Experimental setup: jet flow centred on a tube face. 60
(4.13) Amplitude response of T13, jet centred on face of T13. 61
(4.14) Amplitude response of T23, jet centred on face of T13. 62
(4.15) Amplitude response of T33, jet centred on face of T13. 63

(4.16) Amplitude response of T43, jet centred on face of T13. 64
(4.17) Jet centreline velocity versus nozzle flowrate with jet centred on a tube face. 65
(4.18) Horizontal velocity propagation with jet centreline on a tube face. 66
(4.19) Vertical velocity propagation with jet centered on a tube face. . . 67

(5.1) Normalized velocity profiles with jet centred between T13 and T14. 72
(5.2) Normalized velocity profiles with jet centered on face of T13. . . . 73
(5.3) Illustration of measured velocity profiles around T13. 74
(5.4) Illustration of partial admission calculation as described by Equations (5.12) and (5.16). 84
(5.5) Illustration of partial admission calculation as described by Equations (5.15) and (5.17). 85

(A.1) Model tube segmentation for Rayleigh's quotient calculation. . . . 100
(A.2) Model tube segmentation for boundary value problem. 105
(A.3) Predicted mode shapes and natural frequencies of model tube. . . 113

(B.1) Monitored tube strain gauge sub-assembly. 124
(B.2) Wheatstone bridge circuit with 3-wire gauge connection. 125
(B.3) Tube T13 Strain Gauge Calibrations. 126
(B.4) Tube T23 Strain Gauge Calibrations. 127
(B.5) Tube T33 Strain Gauge Calibrations. 128
(B.6) Tube T43 Strain Gauge Calibrations. 129
(B.7) Tube T34 Strain Gauge Calibrations. 130
(B.8) Ashcroft XL-3-MB8-16-ST-2IW pressure transducer calibration. . 134
(B.9) Hot-wire calibrator nozzle. 140
(B.10) Validyne DP45-30 pressure transducer calibration. 141
(B.11) Hot-wire probe no.1 calibration in transformed coordinates. . . . 142
(B.12) Hot-wire probe no.1 calibration in normal coordinates. 143
(B.13) Hot-wire probe no.2 calibration in transformed coordinates. . . . 144
(B.14) Hot-wire probe no.2 calibration in normal coordinates. 145

(C.1) Horizontal entry profiles with jet centred between tubes. 147
(C.2) Vertical entry profiles with jet centred between tubes. 148
(C.3) Jet centred between tubes, velocity profile along (0,y,318). 149
(C.4) Jet centred between tubes, velocity profile along (0,y,352). 150
(C.5) Jet centred between tubes, velocity profile along (0,y,352). 151
(C.6) Jet centred between tubes, velocity profile along (0,y,352). 152
(C.7) Jet centred between tubes, velocity profile along (0,y,377). 153
(C.8) Jet centred between tubes, velocity profile along (0,y,397). 154
(C.9) Jet centred between tubes, velocity profile along (0,y,441). 155
(C.10) Jet centred between tubes, velocity profile along (0,y,441). 156

(C.11) Jet centred between tubes, velocity profile along (0,y,441). 157
(C.12) Jet centred between tubes, velocity profile along (0,y,486). 158
(C.13) Jet centred between tubes, velocity profile along (0,y,530). 159
(C.14) Jet centred between tubes, velocity profile along (0,y,530). 160
(C.15) Jet centred between tubes, velocity profile along (0,y,530). 161
(C.16) Jet centred between tubes, velocity profile along (0,y,575). 162
(C.17) Jet centred between tubes, velocity profile along (0,y,620). 163
(C.18) Jet centred between tubes, velocity profile along (0,y,620). 164
(C.19) Jet centred between tubes, velocity profile along (0,y,620). 165
(C.20) Jet centred between tubes, velocity profile along (x,0,318). 166
(C.21) Jet centred between tubes, velocity profile along (x,0,352). 167
(C.22) Jet centred between tubes, velocity profile along (x,0,397). 168
(C.23) Jet centred between tubes, velocity profile along (x,0,441). 169
(C.24) Jet centred between tubes, velocity profile along (x,0,486). 170
(C.25) Jet centred between tubes, velocity profile along (x,0,530). 171
(C.26) Jet centred between tubes, velocity profile along (x,0,575). 172
(C.27) Jet centred between tubes, velocity profile along (x,0,620). 173
(C.28) Horizontal entry velocity profiles with jet centred on a tube face. 174
(C.29) Vertical entry velocity profiles with jet centred on a tube face. . . 175
(C.30) Jet centred on a tube face, velocity profile along (0,y,320). 176
(C.31) Jet centred on a tube face, velocity profile along (0,y,354). 177
(C.32) Jet centred on a tube face, velocity profile along (0,y,397). 178
(C.33) Jet centred on a tube face, velocity profile along (0,y,441). 179
(C.34) Jet centred on a tube face, velocity profile along (0,y,441). 180
(C.35) Jet centred on a tube face, velocity profile along (0,y,468). 181
(C.36) Jet centred on a tube face, velocity profile along (0,y,486). 182
(C.37) Jet centred on a tube face, velocity profile along (0,y,496). 183
(C.38) Jet centred on a tube face, velocity profile along (0,y,530). 184
(C.39) Jet centred on a tube face, velocity profile along (0,y,574). 185
(C.40) Jet centred on a tube face, velocity profile along (x,0,320). 186
(C.41) Jet centred on a tube face, velocity profile along (x,0,354). 187
(C.42) Jet centred on a tube face, velocity profile along (x,0,441). 188
(C.43) Jet centred on a tube face, velocity profile along (x,0,486). 189

List of Tables

(2.1) Empirical correlation functions suggested by Weaver and Fitzpatrick (1988) for design against fluidelastic instability. 10
(2.2) Constants recommended by Weaver and Parrondo (1991) for use with Connors' equation. 13

(3.1) Model coordinate transforms. 24
(3.2) Model tube segment physical descriptions. 30
(3.3) Model tube segment material and geometric properties. 31
(3.4) Tube damping and frequency measurement results. 40

(5.1) Linear regression coefficients for Equation (5.8). 77
(5.2) Tube instability predictions using measured velocity profiles for jet centred between T13 and T14. 78
(5.3) Tube instability predictions using measured velocity profiles for jet centred on the face of T13. 79
(5.4) A comparison of the physical model parameters from the current research and those provided by Feenstra et al. (2003, 2004). . . . 88
(5.5) A comparison of the fluidelastic instability results from the current research and those provided by Feenstra et al. (2003, 2004). 89
(5.6) A comparison of the $V(0, 0, Z_m)$ values determined via measurement and prediction for the case where the jet flow was centred between T13 and T14. 90

(A.1) Model tube, simplified beam model, segment properties. 106

(B.1) Linear transforms. 120
(B.2) Voltage Measuring Instrument Accuracy Ratings. 121

Nomenclature

Acronyms

CTA	constant temperature anemometry
DAQ	data acquisition system
HCID	hanging chain impact damper
PSD	power spectral density
RMS	root mean square
TLCD	tuned liquid column damper
TLD	tuned liquid damper
TMD	tuned mass damper

Greek Symbols

γ	ratio of specific heats (-)
ω, ω_n	angular frequency, and angular natural frequency (rad/s)
π	pi (constant)
ρ	density (kg/m^3)
ζ	damping ratio (-)

Roman Symbols

$\hat{Y}$	normalized mode shape function (-)
A	cross-sectional area (m^2)
c	speed of sound in air (m/s)
D	diameter (m)
E	modulus of elastisity (Pa)
e	Eulers' number (constant)

f, f_n	frequency, and natural frequency (Hz)
I	area moment of inertia or second moment of area (m^4)
K	Connors' constant (-)
L	length of tube (m)
M	mass (kg)
m, m_n	effective lineal modal mass (kg/m)
m_s	structural lineal mass (kg/m)
p, p_0	local static pressure, and stagnation pressure (Pa)
P, P_t, P_s	tube pitch, transverse pitch, and streamwise pitch (m)
Q	volumetric flow-rate (cfm or m^3/s)
r	radial coordinate (m)
R_0	nozzle radius (m)
$R_e(z)$	jet expansion radius (m)
V	velocity (m/s)
V_0	nozzle exit velocity (m/s)
x	spanwise coordinate (m)
y	transverse coordinate (m)
z	streamwise coordinate (m)
Z_i	initial jet development length (m)

Non-Dimensional Parameters

$m\left(2\pi\zeta\right)/(\rho D^2)$	mass damping parameter (-)
$m/(\rho D^2)$	mass ratio (-)
$V/(fD)$	reduced velocity (-)
V/c	Mach number (-)

1. Introduction

Many problems in engineering involve fluid flow over flexible structures; the resulting dynamic fluid forces can cause large vibration amplitudes in these structures. The behaviour of these fluid-structure coupled systems depend on both structural and fluid dynamics. The field of engineering devoted to the study of these problems is aptly named fluid-structure interaction or flow-induced vibration. The dynamic interaction between fluids and structures can be very complex. Many flow-induced vibration problems of practical interest are not well understood, despite years of research and publication.

Arrays of circular cylinders, such as those found in large heat exchangers, are known to vibrate when subjected to uniform cross-flow. The severity of these vibrations are dependent on the excitation mechanism and the physical properties of the cylinder array. Many studies have been conducted on this phenomenon, see Weaver and Fitzpatrick (1988) and Paidoussis (1982) for detailed literature reviews. The excitation mechanisms in cylinder array vibrations can be grouped into four categories: (a) turbulent buffeting, (b) Strouhal periodicity, (c) fluidelastic instability and (d) acoustic resonance, each of these excitation mechanisms are described in detail by Blevins (2001a). Turbulent buffeting is characterized by relatively small amplitude random vibrations due to external flow turbulence. Turbulent buffeting is not practically avoidable in heat exchangers and can cause fretting wear at tube supports over long periods of time. Strouhal periodicity or vortex shedding is characterized by the shedding of vortices from alternate sides of a tube when exposed to cross-flow. As each vortex detaches a lateral (transverse) force is induced on the tube. The frequency of this periodic excitation is proportional to the cross-flow velocity. When the vortex shedding frequency approaches the structural natural frequency of the tube a phenomenon called "lock-in" occurs. During "lock-in" the vortex shedding becomes correlated along the tube span and the tube will experience resonant vibrations. However, the amplitude of these vibrations is self limiting as excessive vibration will tend to breakdown the spanwise correlation of vorticity. Increasing the flow velocity will also decrease the vibration amplitude as this increases the vortex shedding frequency and separates it from the structural natural frequency. Fluidelastic instability is characterized by the onset of large amplitude vibrations, at the structural natural frequency of the tubes, after a critical flow velocity is reached. Once the critical velocity is exceeded the rate of change of vibration amplitude with respect to velocity will increase sharply. The resulting vibrations can cause tube failures in a relatively short period of time. The critical velocity is typically determined by plotting vibration amplitude versus uniform gap flow velocity and observing the point at which the slope increases dramatically. Acoustic resonance is characterized by the establishment of an acoustic standing wave within the heat exchanger. This typically occurs when the vortex shedding frequency approaches or becomes coincident with a transverse acoustic natural frequency of the heat exchanger shell (transverse to both the tube span and the fluid flow). The result can be large amplitude vibrations and very loud sound emissions. The typical remedy involves the installation of a solid baffle which increases the acoustic natural frequency and avoids coincidence.

Feenstra et al. (2003, 2004) reported a flow-induced vibration problem which involved the failure of heat exchanger tubes within a kraft recovery boiler. The failure of these tubes caused water to flow into the fireside of the boiler, coming into contact with molten salts, resulting in an explosive expansion which caused approximately 40 million dollars in damages[1]. The subsequent investigation revealed that a sootblower caused the tube failure. A sootblower jet became parked issuing steam down a tube lane, perpendicular to the tube spans. Feenstra et al. (2003, 2004) completed a scale model study and found that fluidelastic instability occurred in the 1st, 2nd and 3rd tube rows, in close proximity to the jet, when the jet was aimed between tubes and remained stationary for a period exceeding approximately 6 to 20 seconds. The model study indicated that when the jet was continuously translating, in the transverse direction across the tube span, fluidelastic instability was not observed. The authors used a modified partial admission calculation to relate the critical jet centreline velocity to the equivalent critical uniform gap flow velocity at the onset of fluidelastic instability. The incoming velocity profile was assumed to be well described by the formulas for the velocity profile of a submerged axisymmetric turbulent jet as provided by Appel et al. (1959). Thus only the centreline velocity of the jet was measured. The partial admission calculation was completed using the average velocity in the "jet core" which was defined using a 15° jet diffusing angle. The authors stated that the nozzle setback of approximately 200 mm was chosen such that the jet would expand to a diameter of approximately 46 mm which was equivalent to the transverse tube pitch, P_t. The partial admission formulation used by Feenstra et al. (2003, 2004) was based on this very specific physical arrangement. The partial admission formulation used was derived from the formulation developed by Connors (1978) but was modified for the case of flow on only one side of a tube as described by Lever and Weaver (1986). The partial admission relationship developed by Connors (1978) was formulated to account for spanwise variations in velocity profile, there is no existing generalized relationship to account for transverse variations in velocity profile. Therefore, the limitations inherent in the partial admission relationship developed by Connors (1978)

---

[1] Information concerning the circumstances of the failure, which were not published in the paper, were obtained from discussions with P. Feenstra and D. S. Weaver

prevent its general use for predicting the onset of fluidelastic instability due to flows with velocity profiles which have variations in both the spanwise and transverse directions.

The purpose of this research is to further investigate the phenomenon of fluidelastic instability due to axisymmetric jet flow and to develop a generalized partial admission formulation which accounts for velocity variations in both the spanwise and transverse directions. The specific motivating example was provided by Feenstra et al. (2003, 2004). However, the intent is to attempt to expand the partial admission theory such that it is not limited to two dimensional flows and can characterize generalized three dimensional flows. This effort has value beyond the application to sootblower systems since three dimensional partial admission flows are also common and unavoidable in shell and tube heat exchanger designs due to inlet geometry. To accomplish this research a model heat exchanger tube array was designed and constructed, then tested under both uniform flow and axisymmetric jet flow conditions. The uniform flow testing was completed in McMaster University's 2 ft wind tunnel and was used to establish the critical reduced velocity of the tube array at the onset of fluidelastic instability. The uniform flow test established a basis for comparing the results with the existing literature and evaluating the validity of the proposed partial admission calculation. The tube array was also tested in open air using an axisymmetric jet, with two different physical arrangements, the first with the jet aimed between tubes and perpendicular to the tube spans and the second with the jet aimed at a tube face and perpendicular to the tube spans. The jet velocities for each physical arrangement were recorded using measurements of the nozzle exit flowrate. The actual incoming/entrance velocity profile, entering the first tube row, was determined via measurement and correlated to the nozzle exit flowrate. Velocity measurements were also completed inside the tube array within the inter-tube spaces to determine how the jet diffused through the array. The measurement data collected was used to validate a modified partial admission relationship which was formulated to account for velocity profiles which vary in both the spanwise and the transverse directions.

Chapter 2 of this thesis provides relevant background theory and information which are pertinent to the research presented. This is followed by Chapter 3 which outlines the experimental apparatus and scale model design. Chapter 4 presents the vibration and velocity measurement results and pertinent observations. This is followed by Chapter 5 which discusses the relationship between the uniform flow and jet flow experimental results. Chapter 6 provides the conclusion of the thesis and the suggested form of the modified partial admission relationship. Finally, Chapter 7 provides a discussion of the limitations of this research and provides recommendations for future study.

2. Background

The sections that follow provide relevant background information on topics pertinent to the current research such as: flow-induced vibration, fluidelastic instability, partial admission flows, scale modelling and distortions, sootblowers, submerged axisymmetric jets, and supersonic flow and the effects of compressibility.

2.1 Flow Induced Vibrations

All flow-induced vibration problems involve the interaction between a structure and a fluid flow. However, they do not all behave in the same manner. In order to properly study flow-induced vibration problems they must be separated into categories, which are based on the underlying physics involved. Weaver (2005) separates flow-induced vibration problems into three mathematically distinct categories: forced vibrations, self-excited vibrations, and self-controlled vibrations. All of these problems can be expressed generally by the mathematical form of Equation (2.1).

$$I(q) + E(q) = F(q,t) \tag{2.1}$$

Weaver (2005) states that, I, E and F, in Equation (2.1), represent general differential operators which govern, inertial, elastic, and fluid forces, respectively. The general differential operators I and E depend on the generalized displacement, q. Whereas the general differential operator F depends on both q and time, t. The categories presented here are physically and mathematically meaningful. However, due to the relative immaturity of this field of engineering, they have not been generally accepted. Each researcher has essentially used their own categorizations and no one set has been deemed definitive. As this field develops, the concepts and theories will be refined and hopefully continuity will emerge in the open literature.

2.1.1 Forced Vibrations

Forced vibrations are defined by Weaver (2005) as problems where the fluid force operator depends on time, t, and has no dependence on the generalized displacement, q. Therefore, the fluid forces are not dependent on structural motion. Also the fluid forces are not periodic in nature because this could lead to resonance: resonant response could produce amplitudes large enough to affect the fluid forces. Therefore the general mathematical expression for this class of problems, which represents a special case of Equation (2.1), reduces to the form of Equation (2.2). An example of a forced vibration is turbulent buffeting where turbulence in the flow field exerts random time dependent forces on the structure.

$$I(q) + E(q) = F(t) \tag{2.2}$$

2.1.2 Self-excited Vibrations

According to Weaver (2005), self-excited vibrations have fluid forces which are dependent on the structural motion. These are in general stability problems, where the movement of the structure can actually increase the fluid forces with each cycle. These instabilities can be dynamic or static, they are caused by either negative fluid damping or negative fluid stiffness respectively. If instability occurs, amplitudes will increase rapidly until non-linearities become significant. The system will experience large limit cycle oscillations which in most cases will lead to structural failures. It is important to note that without structural motion self-excited vibrations can not exist. The general mathematical expression for this class of problems as presented by Weaver (2005) takes the form of Equation (2.1). An example of self-excited vibration is fluid elastic instability in tube arrays which is characterized by a sudden amplitude increase, after a critical flow velocity is reached and exceeded, due to the formation of negative fluid added damping and/or negative fluid added stiffness.

2.1.3 Self-controlled Vibrations

Finally self-controlled vibrations, as described by Weaver (2005), are characterized by the fact that periodic fluid forces exist without structural motion. If the periodic fluid forcing frequency is far removed from the structural natural frequencies, then the fluid forces are independent of structural motion. Therefore the system can be expressed mathematically in the form of Equation (2.2).

If however the fluid forcing frequency coincides with a structural natural frequency, resonance will occur. If the resonant response is sufficiently large, the fluid forces will become dependent on structural motion. Consequently the mathematical description of the system changes to the form of Equation (2.1).

The fluid forcing function initially increases with structural vibration amplitude, then due to fluid and/or structural non-linearities asymptotes to a constant amplitude at which the energy input from the fluid is balanced by the energy dissipated by damping producing a stable limit cycle. The resulting behaviour is a steady self controlled oscillation. An example of a self-controlled vibration is vortex shedding from a flexible right circular cylinder.

Blevins (2001a), shows that initially the periodic lift force, produced by vortex shedding, increases with vibration amplitude. However, after the vibration amplitude exceeds some critical value the periodic lift force begins to decrease. This illustrates the self limiting nature of self-controlled vibrations.

2.2 Fluidelastic Instability

Arrays of circular cylinders are known to vibrate when subjected to uniform cross-flow. The severity of these vibrations are dependent on the excitation mechanism and the physical properties of the cylinder array. Many studies have been conducted on this phenomenon, see Weaver and Fitzpatrick (1988) and Paidoussis (1982) for detailed literature reviews. According to Weaver and Fitzpatrick (1988) the excitation mechanisms in cylinder array vibrations can be grouped into four categories. These categories are (a) turbulent buffeting, (b) Strouhal periodicity, (c) fluidelastic instability and (d) acoustic resonance.

Fluidelastic instability is the most destructive of the excitation mechanisms and has therefore received a great deal of attention in the open literature. Fluidelastic instability is characterized by the onset of large amplitude vibrations, at the structural natural frequency of the tubes, after a critical flow velocity is reached. Once the critical velocity is exceeded the rate of change of vibration amplitude with respect to velocity increases sharply. The resulting vibrations can cause tube failures in a relatively short period of time as discussed by Weaver and Fitzpatrick (1988). Figure 2.1 shows a schematic of the typical amplitude response of a tube array with increasing flow velocity. Fluidelastic instability is an example of a self-excited flow-induced vibration.

2.2.1 Basic Theories

Among the first to study the phenomenon now known as fluidelastic instability, were Roberts (1966) and Connors (1970). Both of these researchers studied instabilities in a row of circular cylinders subjected to perpendicular flow. Although the approaches taken by Roberts and Connors were fundamentally different, they came to essentially the same conclusion; that the critical flow velocity could be expressed using a non-dimensional expression taking the general form of Equation (2.3) which describes the relationship between critical reduced velocity at the onset of fluidelastic instability and the mass damping parameter of the physical system. The critical reduced velocity is the dimensionless ratio of the critical gap flow velocity, V_{cr}, over the product of the structural natural frequency, f_n, and the tube diameter, D. The mass damping parameter is the dimensionless ratio of the product of the tube lineal mass, m, the constant, 2π, and the damping ratio, ζ, over the product of the fluid density, ρ, and the square of the tube diameter, D. The constants, a and

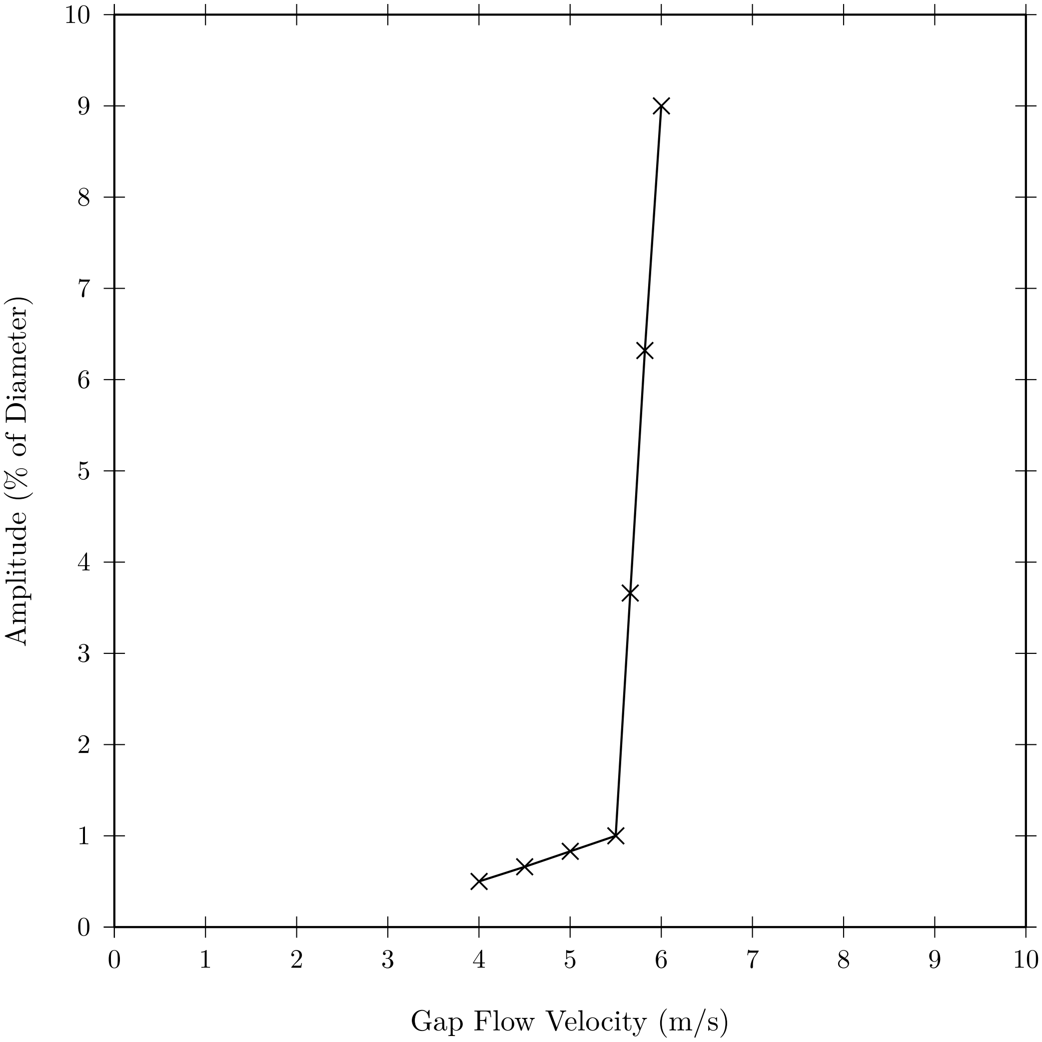

Figure 2.1: Schematic diagram of fluidelastic amplitude response. In this example the instability point is marked by a drastic change in slope at approximately 5.5 m/s.

b, can be determined using existing experimental data and linear least squares regression. Note that the mass damping parameter represents the product of the mass ratio, $m/(\rho D^2)$, and the damping parameter, $2\pi\zeta$. The physical phenomenon of fluidelastic instability is also dependent, to a lesser degree, on other non-dimensional ratios which are not represented in Equation (2.3). Blevins (2001a) provides a brief literature review of research work focused on the dependence of fluidelastic instability on other dimensionless groups.

$$\frac{V_{cr}}{f_n D} = a \left(\frac{m\,(2\pi\zeta)}{\rho D^2} \right)^b \tag{2.3}$$

Connors (1970) developed a simple relationship which describes the stability boundary of a tube row, in the form of Equation (2.4), which agrees well with the available experimental data for tube rows.

$$\frac{V_{cr}}{f_n D} = 9.9 \left(\frac{m\,(2\pi\zeta)}{\rho D^2} \right)^{1/2} \tag{2.4}$$

However, Equation (2.4) does not agree well with the available experimental data for tube arrays. Designers have since adapted Equation (2.4) by changing the constant 9.9 to a value which fits the experimental data for tube arrays consisting of multiple rows. Equation (2.5) is the adapted form, commonly referred to as Connors' equation, which is most often used for tube arrays. Pettigrew and Taylor (1991) and ASME (2009) discuss additional details regarding the use of Equation (2.5) to characterize fluidelastic instability in tube arrays.

$$\frac{V_{cr}}{f_n D} = K \left(\frac{m\,(2\pi\zeta)}{\rho D^2} \right)^{1/2} \tag{2.5}$$

2.2.2 Current Design Practice

Pettigrew and Taylor (1991) suggest a value of $K = 3.0$ in Equation (2.5) for all four standard tube array geometries (square, rotated square, triangle and rotated triangle), while ASME (2009) suggests a value of $K = 2.4$. Figure 2.2 shows a collection of experimental data for all four standard array geometries, reproduced from the Boiler & Pressure Vessel Code ASME (2009). The current design approach involves fitting Equation (2.5) to this experimental data to produce one equation which predicts the minimum critical velocity for all four standard array geometries in a conservative manner. Though this method is practical, from a design standpoint, it neglects the underlying physics of the problem. The data presented in Figure 2.2 contains a great deal of scatter which is obscured by the fact that it is plotted on a log-log scale. Chen (1984), as well as Weaver and Fitzpatrick (1988), have shown that the four standard array geometries do not behave in similar ways, and therefore should be treated separately. Despite this the use of Equation (2.5) using one K value to represent the stability boundary of all standard array geometries remains the industry standard.

2.2.3 Recommended Design Practice

Weaver and Fitzpatrick (1988) presented the available experimental data on four separate graphs each corresponding to one of the standard array geometries. Separating the data considerably reduced the scatter and clear trends became visible. These graphs are reproduced in Figure 2.3. Careful examination of these plots reveals that each geometry behaves in a different manner.

Array Geometry	$\frac{m(2\pi\zeta)}{\rho D^2} < 0.3$	$\frac{m(2\pi\zeta)}{\rho D^2} > 0.3$
Square	$\frac{V_{cr}}{f_n D} = 1.4$	$\frac{V_{cr}}{f_n D} = 2.5\left(\frac{m(2\pi\zeta)}{\rho D^2}\right)^{0.48}$
Rotated square	$\frac{V_{cr}}{f_n D} = 2.2$	$\frac{V_{cr}}{f_n D} = 4.0\left(\frac{m(2\pi\zeta)}{\rho D^2}\right)^{0.48}$
Normal triangle	$\frac{V_{cr}}{f_n D} = 2.0$	$\frac{V_{cr}}{f_n D} = 3.2\left(\frac{m(2\pi\zeta)}{\rho D^2}\right)^{0.40}$
Parallel triangle	$\frac{V_{cr}}{f_n D} = 1.0$	$\frac{V_{cr}}{f_n D} = 4.8\left(\frac{m(2\pi\zeta)}{\rho D^2}\right)^{0.30}$

Table 2.1: Empirical correlation functions suggested by Weaver and Fitzpatrick (1988) for design against fluidelastic instability.

The empirical correlations, suggested by Weaver and Fitzpatrick (1988), for each standard array geometry shown in Table 2.1 are typical of the state of the art in design against fluidelastic instability. The underlying physics of fluidelastic instability are still not fully understood; therefore the only practical design guides are empirical in nature. A number of theoretical models have been developed for the prediction of fluidelastic instability, see Price (1993) for details. However, no theoretical model has yet been able to determine, with certainty, the underlying physics of fluidelastic instability. Additionally all of these models are quite complex in nature. Due to the abundance of available experimental data (see Figures 2.2 and 2.3) there is little incentive for designers to utilize complex theoretical models. Therefore, empirical correlations such as those provided in Table 2.1, are currently the best tools for design purposes.

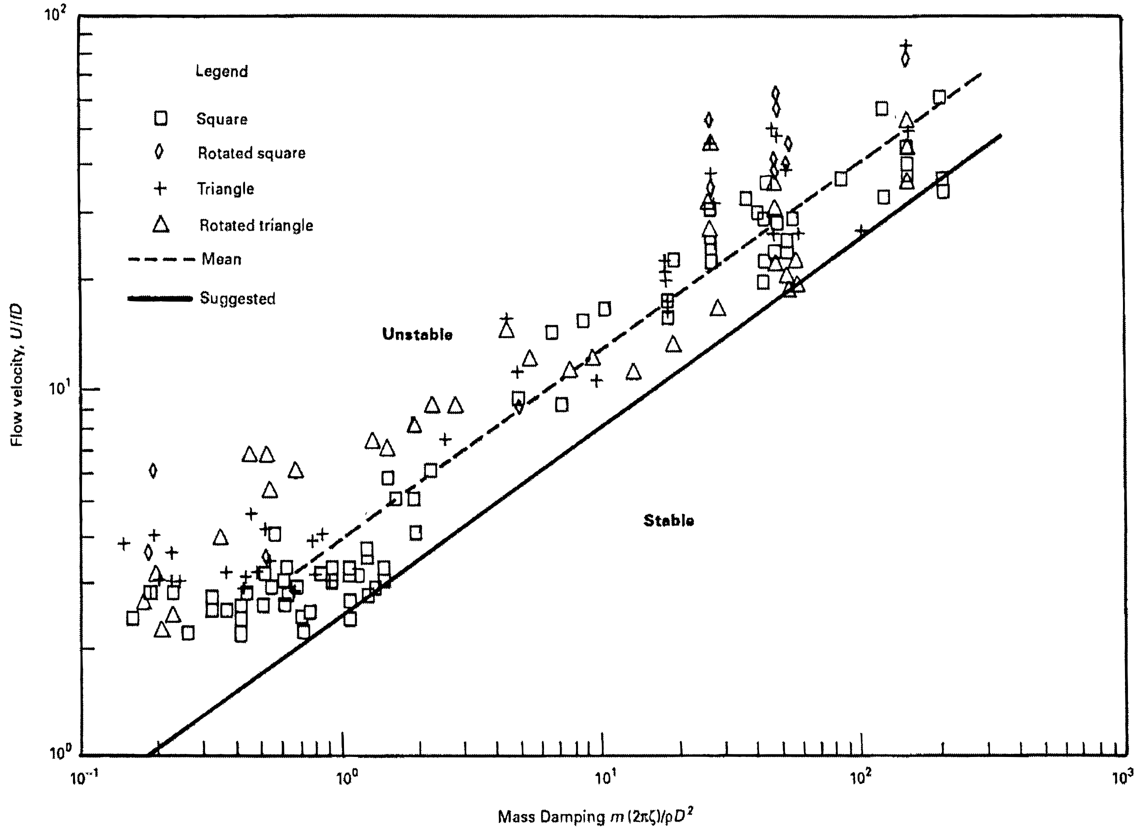

Figure 2.2: Fluidelastic stability diagram, Boiler & Pressure Vessel Code ASME (2009). This diagram shows a great volume of experimental data plotted on a log-log scale. The suggested stability threshold (solid line) corresponds to Equation (2.5) with $K = 2.4$ and the mean value (dashed line) corresponds to $K = 4.0$.

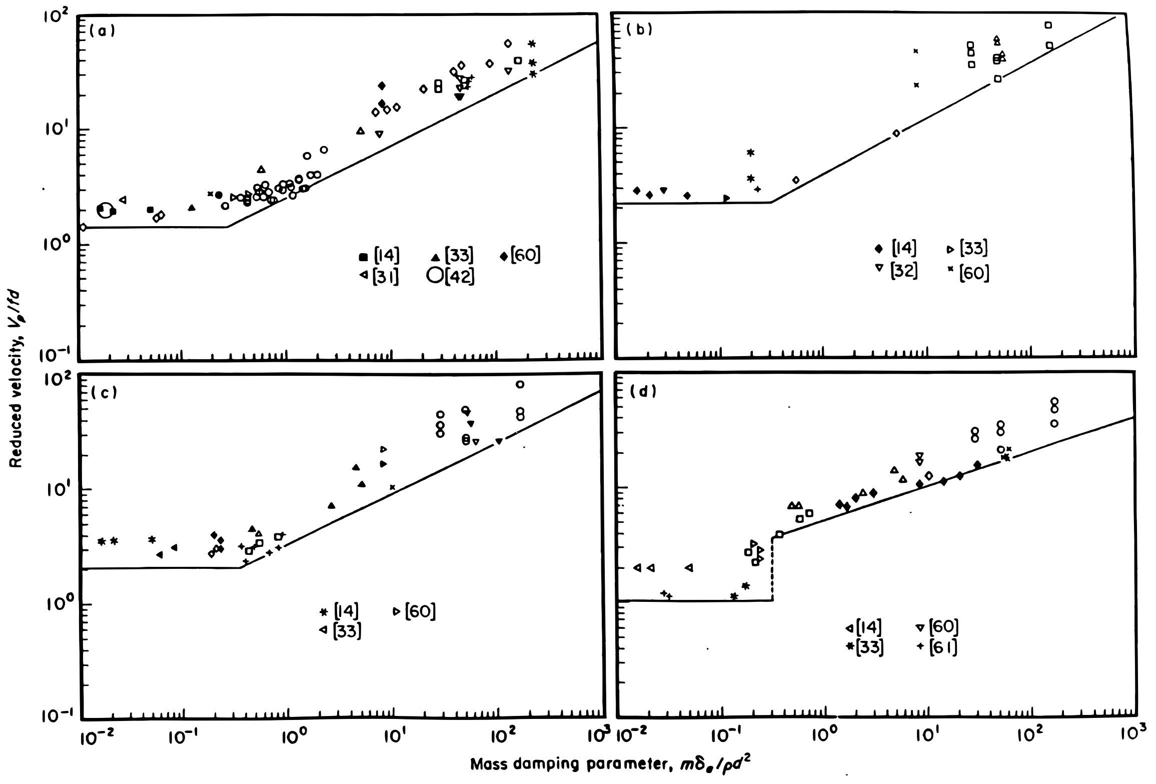

Figure 2.3: Recommended design guidelines for fluidelastic instability as suggested by Weaver and Fitzpatrick (1988). Each graph corresponds to a standard array geometry: (a) square, (b) parallel triangular, (c) rotated square, and (d) normal triangular.

2.3 Nonuniform Cross-Flow - Partial Admission

Section 2.2 discussed fluidelastic instability in tube arrays under uniform cross-flow conditions. However, in many cases the flows over heat exchanger tube arrays are non-uniform. An example of a typical non-uniform flow in a shell and tube heat exchanger occurs at the inlet where the inlet flow can expose a relatively small fraction of the overall tube array to cross-flow. Therefore, Connors (1978) modified his original expression describing fluidelastic instability to account for spanwise variations in flow velocity. The method described by Connors (1978) allows a non-uniform gap flow velocity, $V(x)$, to be expressed as a equivalent uniform gap flow velocity, V_{eq}, using Equation (2.6), where $\hat{Y}(x)$ represents the normalized mode shape function, x represents the spanwise spatial coordinate and L is the tube length.

$$V_{eq} = \left(\frac{\displaystyle\int_0^L V^2(x)\hat{Y}^2(x)dx}{\displaystyle\int_0^L \hat{Y}^2(x)dx} \right)^{1/2} \tag{2.6}$$

Equation (2.6) accounts for variations in spanwise velocity distribution only. Many of the flows encountered within actual heat exchanger systems are three dimensional and undoubtedly have velocity variations in the transverse direction as well, this is particularly true for sootblowing systems. Feenstra et al. (2003, 2004) avoided this problem by calculating the average velocity of the jet core, and using this value as a stepwise uniform flow over one side of the tube within Equation (2.6). The validity of Equation (2.6) has been studied by many researchers such as, Waring and Weaver (1988), Weaver and Goyder (1990), Chen and Chandra (1991), Weaver and Parrondo (1991) and Parrondo et al. (1997). Waring and Weaver (1988), in particular, found that agreement between experiment and Equation (2.6) was poor for parallel triangular arrays. Parallel triangular arrays in cross-flow deviate from the typical behaviour described by the Connors' equation, see Figure 2.3 and Table 2.1. It was suggested by Waring and Weaver (1988), that this was the reason for the relatively poor agreement between Equation (2.6) and the experimental data. Changing the exponent, α, from 1/2 in Equation (2.6) to a value which more closely represents a parallel triangular array, see Table 2.1, significantly improved the agreement with the experimental data. Weaver and Goyder (1990), and Weaver and Parrondo (1991), confirmed that agreement between experiment and Equation (2.6) was improved by using an exponent, α, smaller than 1/2 for parallel triangular arrays. Weaver and Parrondo (1991) further suggested using a characteristic exponent for each array geometry, as seen in

Table 2.2. Equations (2.7) and (2.8) would be used in the place of Equations (2.5) and (2.6) for the prediction of the critical flow velocity.

$$V_{eq} = \left(\frac{\int_0^L V^2(x)\hat{Y}^2(x)dx}{\int_0^L \hat{Y}^2(x)dx} \right)^{\alpha} \tag{2.7}$$

$$\frac{V_{eq}}{f_n D} = K \left(\frac{m\,(2\pi\zeta)}{\rho D^2} \right)^{\alpha} \tag{2.8}$$

Array Geometry	K	α
Square	2.5	0.48
Rotated square	4.0	0.48
Normal triangle	3.2	0.40
Parallel triangle	4.8	0.30

Table 2.2: Constants recommended by Weaver and Parrondo (1991) for use with Connors' equation, for predicting the stability threshold in air flow, for arrays with mass damping parameter greater than 0.3.

Chen and Chandra (1991) reported that the simple equivalent velocity concept is only valid for large reduced velocities. This is due to the fact that the equivalent velocity concept was derived from Connors' equation. Figure 2.3 and Table 2.1 show that regardless of array geometry the Connors-type equation does not accurately predict the stability boundary in the region of small mass damping factor (less than 0.3), which corresponds to low reduced velocity.

2.4 Scale Modelling and Distortions

Problems involving fluid-structure interaction are often encountered in engineering. Unfortunately many of these problems are far too complex for purely analytical solutions. In many cases the only way to approach these problems, is to conduct experiments on scale models. Considerable insight can be achieved from such experiments if all pertinent parameters are properly controlled. Using dimensional analysis and similitude, the results from a relatively small set of experiments can be used to predict the behaviour of many real world systems. By determining and controlling non-dimensional parameters in this manner, a practical problem can be characterized without the need for an analytical solution. However, complete similarity between the model and prototype is often impossible, particularly for very complex problems. As a result some error is introduced when the model data is used to predict prototype response. So called distorted models can be used if necessary, provided that the errors introduced by these distortions are relatively small. It can be difficult to determine the effects of modelling distortions *a priori*. In order to determine these effects, it may be necessary to perform experiments focusing on the distortion. It may also be possible to justify neglecting the effects of distortions using theoretical or qualitative arguments. Baker et al. (1973) is an excellent reference on similarity analysis and scale modelling. The aforementioned text contains an entire chapter on modelling distortions and accuracy analysis.

2.5 Sootblowers

Many heat exchanger applications require that one side of the exchanger be exposed to hot products of combustion. Often as a result of incomplete combustion or impurities in the fuel, solid byproducts are formed. Barsin and Kychakoff (1992) refer to these byproducts as ash or soot; they state that this material can adhere to the heat exchange surfaces and seriously impede heat transfer. Kraft recovery boilers are particularly susceptible to the buildup of soot, because of the fuel they consume (black liquor). Black liquor is a byproduct of the kraft pulping process, which is subsequently used as fuel for steam generation. The black liquor is a very low grade fuel which produces a relatively large volume of soot, see Barsin and Kychakoff (1992) for details. In order to maintain operation these deposits must be periodically removed via sootblowing. Sootblowing is accomplished by spraying the heat exchanger tubes with a fluid jet. The blowing medium used for sootblowing is typically steam which must be superheated to prevent water droplets from forming. Water droplets in the sootblower jet can quickly lead to tube erosion problems, see Moskal et al. (1993). Modern sootblowers perform cleaning online without interrupting boiler operation. However, occasionally it may still become necessary to shut down operation and wash the tubes with water, see Uloth et al. (1996). Figure 2.4 shows a schematic diagram of a retractable type sootblower. The sootblower jets trace out a double helix cleaning pattern through the tube array. During normal operation the jets are in continuous translational and rotational motion. Feenstra et al. (2003, 2004) determined that in order for a fluid jet to induce local fluidelastic instability, the jet must be stationary to allow sufficient time for the fluidelastic mechanism to become dominant. Therefore normal sootblower operation should not cause fluidelastic instability.

Heat exchanger tubes are often quite long and slender, as a result they can be very flexible and susceptible to vibration. A study to determine the effect of a fluid jet on a tube array was conducted by Feenstra et al. (2003, 2004). The aforementioned study was motivated by the failure of an industrial heat exchanger due to sootblower jet excitation. To this author's knowledge, Feenstra et al. (2003, 2004) are the only publications in the open literature to specifically study fluidelastic instability due to flows with significant transverse velocity variations. More research is required in order to gain a fundamental understanding of this very complex problem. As discussed in Section 2.2 the fluid-structure interaction of a tube array subjected to uniform cross-flow is not fully understood even after many years of study. A sootblower issuing into a tube array represents an even more complex problem. The flow field in this problem is nonuniform with very high velocities. Considering the current state of knowledge, the most practical way to study this problem is through scale modelling and experimentation.

2.6 Submerged Axisymmetric Turbulent Jets

The properties of submerged axisymmetric turbulent jets are described in Blevins (1984), relations which describe the velocity profile, temperature profile and species concentration of a submerged axisymmetric turbulent jet are provided. An air jet issuing into quiescent air is an example of a submerged jet. Jets characterized by Reynolds numbers greater than 3000 are considered turbulent. When modelling a steam sootblower jet which issues into flue gas (a two fluid jet) with an air jet which issues into still air (a submerged jet), consideration for the differences in the behaviour of each is very important. Jameel et al. (1994) studied the hydrodynamics of a sootblower jet, and developed a theoretical model describing a fully expanded jet. It was determined that since the density ratio of superheated steam to flue gas is nearly unity, a sootblower jet should behave roughly like a submerged single fluid jet. The experimental data presented in Jameel et al. (1994) supported this conclusion. The velocity field of a submerged axisymmetric jet is characterized by Equations (2.9) to (2.13) which are derived from experimental data. Figure

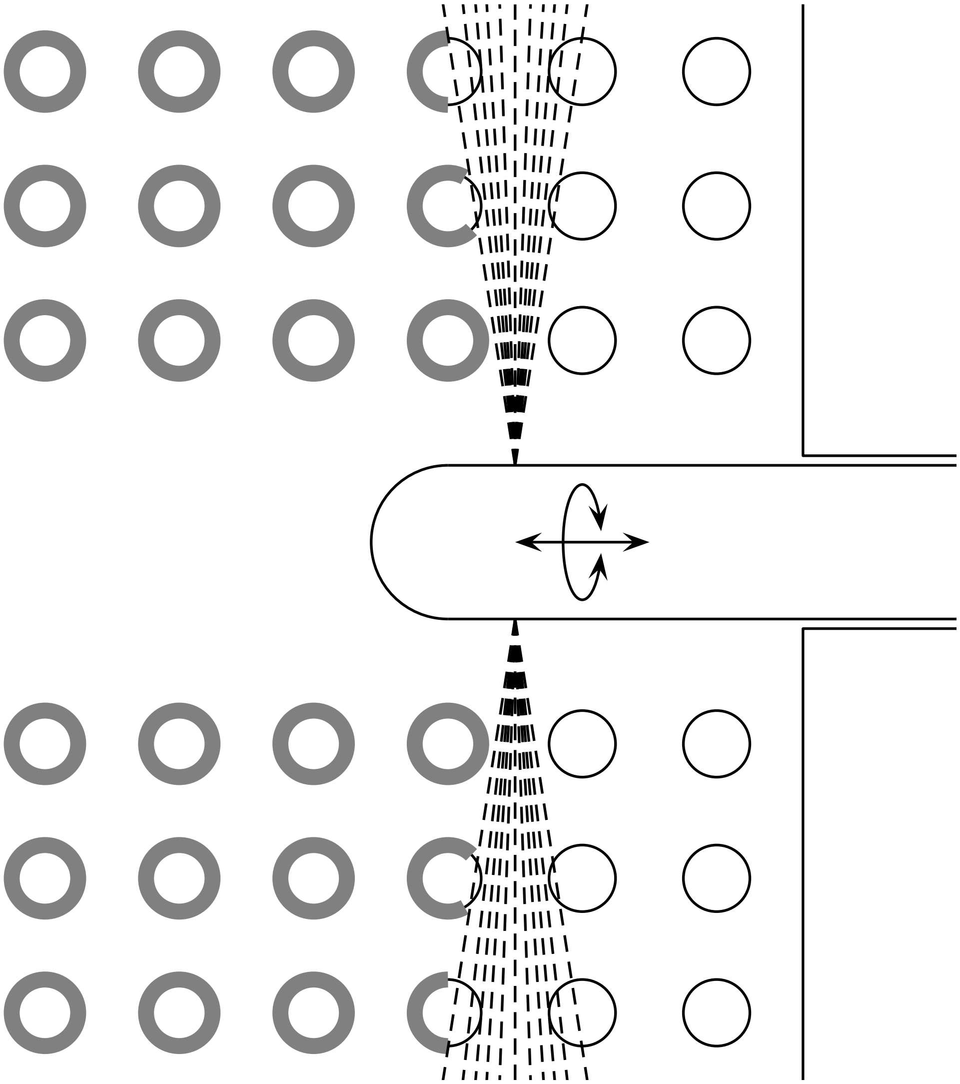

Figure 2.4: Retractable lance type sootblower. This diagram shows the configuration and operation of a typical lance sootblower. The soot blower lance is extended into the tube array whilst simultaneously spinning. This provides a helical spray pattern from the two opposing nozzles at the end of the lance.

2.5 shows a schematic diagram of the expansion of a submerged axisymmetric turbulent jet.

$$Z_i = 10R_0 \tag{2.9}$$

$$V(0,z) = a\left(\frac{R_0}{z}\right)V(0,0) = 12\left(\frac{R_0}{z}\right)V_0 \tag{2.10}$$

$$\frac{V(r,z)}{V(0,z)} = e^{-B(r/z)^2} = e^{-94(r/z)^2} \tag{2.11}$$

$$R_e(z) = z\sqrt{\frac{\ln(\hat{V}_e)}{-94}} \tag{2.12}$$

$$Q(z) = 0.16\left(\frac{z}{R_0}\right)Q(0) \tag{2.13}$$

Equation (2.9) describes the initial jet development length, Z_i, in terms of the jet nozzle radius, R_0. Equation (2.10) describes the jet centerline velocity, $V(0,z)$, in terms of the jet nozzle radius, R_0, nozzle exit velocity, $V(0,0) = V_0$, the distance from the nozzle, z, and the constant, $a = 12$. Equation (2.11) describes the normalized Gaussian velocity profile of the jet. Equation (2.12) is based on Equation (2.11) and defines the expansion radius of the jet, R_e, at a distance, z, from the nozzle exit. The jet expansion radius, R_e, is defined as the point at which the normalized velocity profile equals, $\hat{V}_e$. Finally, Equation (2.13) describes the volumetric flowrate, $Q(z)$, at a distance, z, from the nozzle exit in terms of the nozzle exit radius, R_0, and the nozzle exit flow rate, $Q(0) = Q_0$. The volumetric flowrate increases with distance due to fluid entrainment. See Blevins (1984) for more details regarding the relationships discussed as well as other properties of submerged axisymmetric turbulent jets.

2.7 Supersonic Flow and the Effects of Compressibility

Steam sootblowers typically operate with supersonic nozzle exit velocities, V_0, in order to maximize the energy delivered to the soot deposits, Jameel et al. (1994). Figure 2.6 shows the change in stagnation pressure, for an isentropic flow of ideal gas, with increasing Mach number, $Ma = V/c$. Fox and McDonald (1998) report that at $Ma = 0.45$ neglecting compressibility produces an error in the reported stagnation pressure of approximately 5%. Typically flows are considered incompressible when $Ma \leq 0.3$ because the error introduced is minimal. However, as the Mach number is increased beyond 0.3, the errors introduced from neglecting compressibility become significant. Equations (2.14) and (2.15), represent the incompressible and compressible stagnation pressures respectively, see Fox and McDonald (1998). In each case the equations define

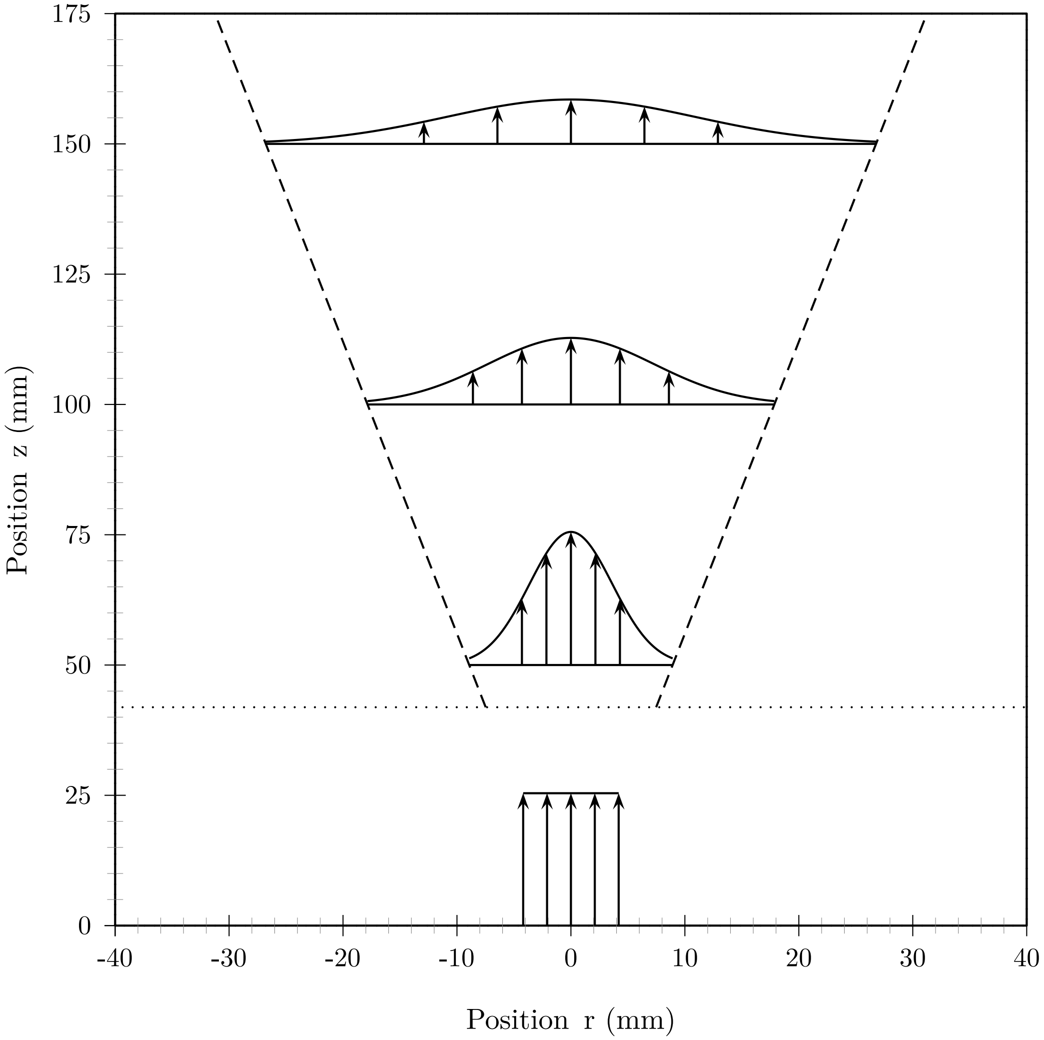

Figure 2.5: Development of a submerged axisymmetric turbulent jet velocity profile as described by Equations (2.9) to (2.12). The figure is plotted assuming that the nozzle exit radius is $R_0 = 4.19mm$ and the velocity scale is arbitrary. The horizontal dotted line represents the initial development length Z_i according to Equation (2.9). The diagonal dashed lines represent the points at which the jet velocity falls below 5% of the centreline velocity according to Equation (2.12).

the ratio of the stagnation pressure, p_0, and the local static pressure, p, in terms of the Mach number, Ma and the ratio of specific heats, γ. When a bluff body is placed in a supersonic flow, shock waves will form upstream, see Shapiro 1953. The appearance of shock waves indicates the presence of irreversibilities, and discontinuities within the flow field. However, Figure 2.5 shows that subsonic submerged axisymmetric turbulent jet velocities decrease rapidly with distance due to spreading and entrainment. Therefore initially supersonic jets would quickly slow to subsonic speeds after exiting the nozzle. However, Zaman (1998) showed that the spread angle of an axisymmetric turbulent jet decreases with increasing exit Mach number, even after the jet has slowed to subsonic speeds. This concept is illustrated in Figure 2.7 where the spread angle decreases slightly for $Ma = 1$ versus $Ma < 1$, but decreases more dramatically for $Ma > 1.0$ and above.

$$\frac{p_0}{p} = 1 + \frac{\gamma}{2}(Ma)^2 \tag{2.14}$$

$$\frac{p_0}{p} = \left[1 + \frac{\gamma - 1}{2}(Ma)^2\right]^{\gamma/(\gamma-1)} \tag{2.15}$$

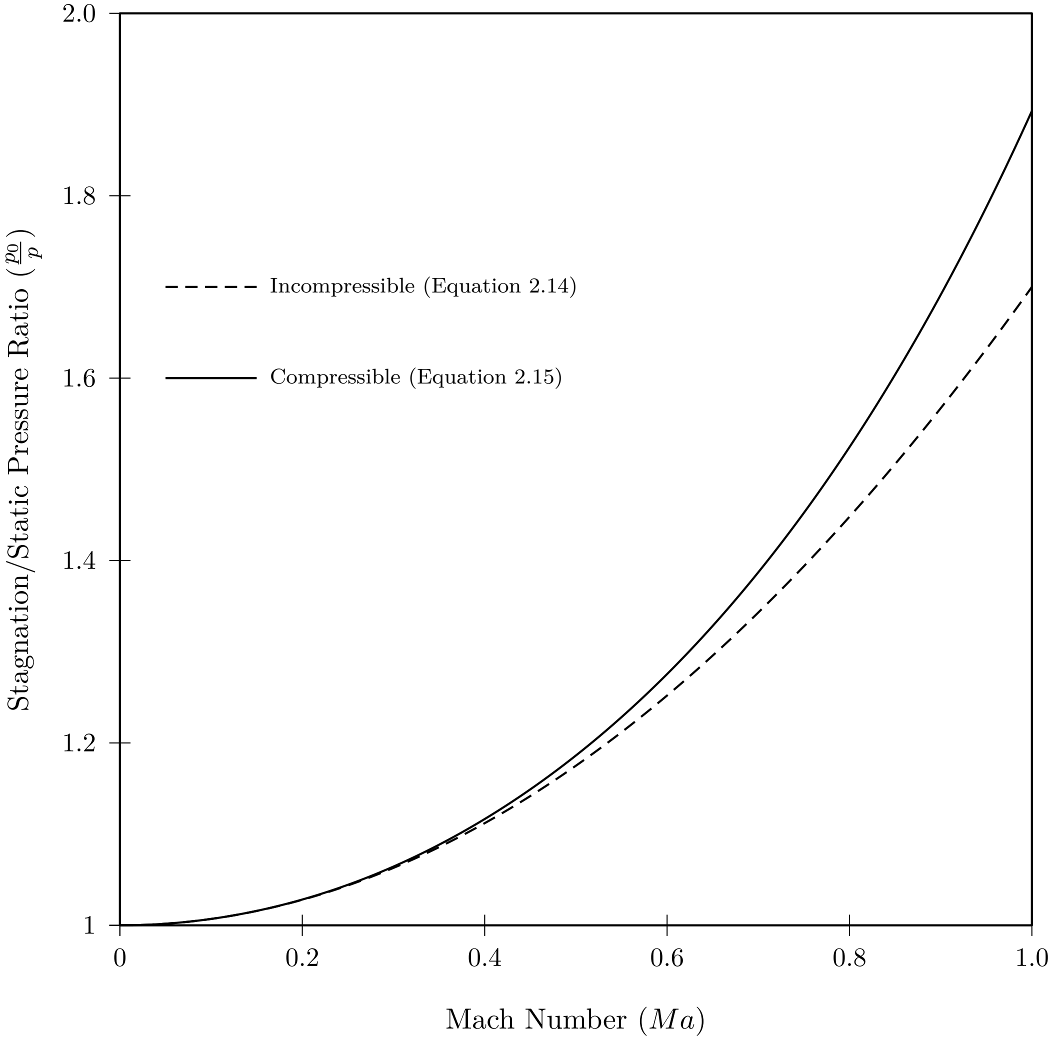

Figure 2.6: Comparison of incompressible, Equation (2.14), and compressible, Equation (2.15), stagnation pressures with increasing Mach number, Ma, for an isentropic flow of ideal gas where the ratio of specific heats is $\gamma = 1.4$. Fox and McDonald (1998) report that at $Ma = 0.45$ neglecting compressibility produces an error in the reported stagnation pressure of approximately 5 %. Typically flows are considered incompressible when $Ma \leq 0.3$ because the error introduced is minimal. However, as the Mach number is increased beyond 0.3, the errors introduced from neglecting compressibility become significant.

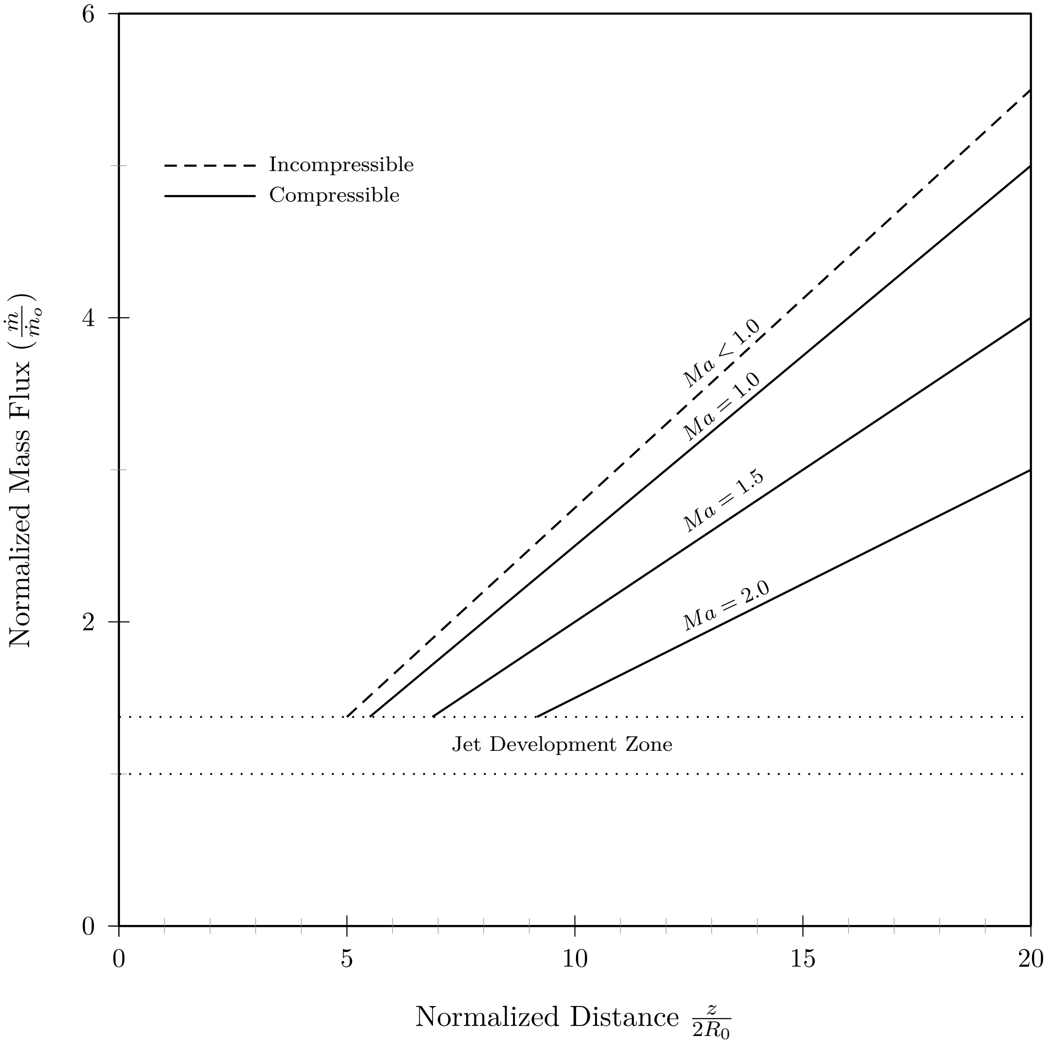

Figure 2.7: Comparison of turbulent mixing of initially compressible and incompressible jets. The normalized mass flux is the ratio of the downstream mass flux, $\dot{m}$, over the nozzle exit mass flux, $\dot{m}_o$. The normalized distance is the ratio of the downstream position, z, over two times the nozzle exit radius, R_0. The plot shows that the spread angle decreases slightly for $Ma = 1$ versus $Ma < 1$, but decreases more dramatically for $Ma > 1.0$ and above. See Zaman (1998) for a detailed description of this phenomenon.

3. Experimental Apparatus and Methodology

An experimental test program was designed, constructed and executed to study the vibration amplitude response of a scale model of a tube array heat exchanger to both uniform and non-uniform flow. The geometric scaling of the tube array was designed to reflect parameters common in kraft recovery boilers. This contrasts much of the previous work in the literature where the tube scaling (pitch to diameter ratio) is representative of heat exchangers found within nuclear steam generators. The non-uniform flow conditions were simulated using an axisymmetric air jet which is similar in characteristics to steam soot blowers commonly utilized in kraft recovery boilers. The non-uniform velocity therefore varies along the tube span (spanwise direction) as well as across the tube span (transverse direction). Again this contrasts much of the previous experimental work regarding non-uniform flow conditions as typically only spanwise velocity variations have been considered, with few exceptions. This chapter provides detailed descriptions of the wind tunnel test facility, tube array model, air jet system, instrumentation and signal processing methods used to complete this research.

3.1 Wind Tunnel Facility

The experiments were conducted in an open circuit wind tunnel facility. The wind tunnel has a octagonal inlet section with a span of 1219 mm and transitions smoothly to an octagonal section with a span of 610 mm approximately 600 mm upstream of the test section. The sectional area from inlet to just upstream of the test section contracts by a ratio of four to one (4:1), this accelerates the flow to four times the average entrance velocity. The wind tunnel inlet has a bank of 305 mm deep inlet screens to break up large scale vorticity. The standard test section for this wind tunnel has an octagonal section and could not accommodate the model tube array. To accommodate the model tube array a new 686 mm long test section with 610 mm by 610 mm square cross section was constructed. The square test section cross sectional area is 20 % larger than the upstream and downstream octagonal sections. As a result some flow irregularities were expected under uniform flow conditions, in the form of stagnant areas in the corners of the square test section. However, these flow irregularities were not expected to effect the results of the study since they are well outside the regions of observation. These flow effects were tolerated so that all tubes within the tube array could be mounted on flexible supports whereas an octagonal section would have required 66 % rigid tubes (outer 2 tube columns on each side). Figure 3.1 shows a diagram of the wind tunnel facility and associated instrumentation.

3.2 Air Jet System

For the current research the effects of a sootblower jet were modelled using an air jet. Jameel et al. (1994) presents comparative measurements and discusses the appropriateness of modelling superheated steam sootblower jets which normally issue into hot flue gas using air jets issuing into an air environment. Jameel et al. (1994) concludes that dimensional similarity is maintained since the the density ratios for steam-to-flue gas and air-to-air are approximately unity. The measurements presented supported this conclusion. Jameel et al. (1994) does concede that the ratio of specific heats, γ, is not similar in these two cases and attributes the expected higher peak impact pressure of steam jets to this difference.

A high velocity air jet was required to sufficiently excite the tube array, the available air supply was a 100 psi (nominal pressure) air line. To reduce flow losses through the jet supply piping, large diameter (25 mm) tubes and fittings were used. The flowrate was controlled by a gate valve and measured using a precision rotameter (OMEGA FL4411). A low pressure loss filter was placed inline with the supply air to remove any fine particulate matter. The jet nozzle was mounted on a 900 mm long stainless steel tube to facilitate the placement of the jet in the test section. The stainless support/supply tube was mounted to the wind tunnel using a mounting plate which allowed for spatial adjustments in all three axis directions. The jet nozzle exit diameter was designed such that the flowrate would be at a maximum measurable value (40 scfm) with a fully open valve. The nozzle exit diameter was 8.4 mm and at a flowrate of 40 scfm this produced a nozzle exit velocity of 342 m/s. Therefore the nozzle exit velocity approached a Mach number of $Ma = 1.0$ which is the critical/limiting value for a converging nozzle. A schematic of the jet system is shown in Figure 3.2.

The nozzle was positioned such that the nozzle exit was 330 mm upstream of the first row tube faces and 100 mm from the free end of the model tubes. Figure 3.4 shows the position of the nozzle. During experiments with jet flow the wind tunnel test section was not enclosed and remained open to outside air. Further the upstream section windows were removed. This was done to reduce confinement effects on the air jet entrainment, see Blevins (1984).

3.3 Model Heat Exchanger Design

The model heat exchanger was designed to fit within the new wind tunnel test section. The model tubes were constructed of aluminum alloy (6061-T6)

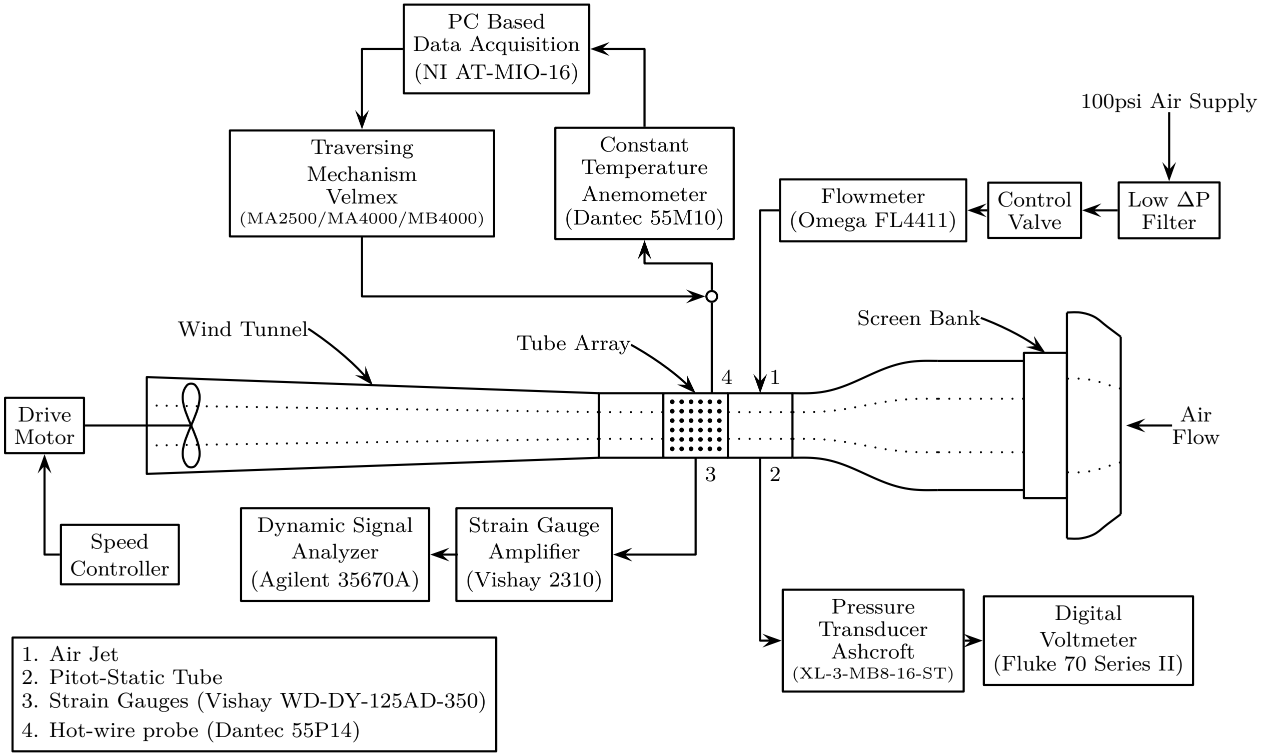

Figure 3.1: Wind tunnel test facility - plan view.

tubing with an outer diameter of 44.45 mm and a wall thickness of 1.59 mm. A machined aluminum plate was used to support the tubes with length, width and height dimensions of 495 mm, 495 mm and 25 mm, respectively. Each tube was attached to the plate in a cantilevered configuration using UNF 3/8-24 B7 alloy threaded rod. Plastic caps were machined to plug the open end of each tube. The caps were also used as a mechanism for attaching tuning masses. The whole assembly was bolted rigidly to a structural steel (A36) support structure. Finally a set of clear acrylic walls were manufactured to seal the test section, while still allowing visual observation. The final assembly consisted of 36 tubes, 6 tubes in the streamwise direction and 6 tubes in the transverse direction, mounted with a tube pitch of 88 mm producing a pitch to diameter ratio of 1.98. Figure 3.3 shows a diagram of the tube array geometry. Figure 3.4 shows the relative positions of the jet and the tube array. Figure 3.4 also establishes several convenient coordinate systems. These will aid in subsequent physical descriptions and in the development of mathematical relationships. The first is the global (g) system which is the only system with a fixed origin. The global system will serve as a fixed reference for all other systems. The jet (j) system has an origin which corresponds to the jet nozzle position. The tube (t) system is defined for each tube in the array and in each case the origin corresponds to the base of the tube support. Finally the hybrid (h) system is also defined for each tube and combines elements of the jet (j) and tube (t) systems. The hybrid system is formally defined as (x_j, y_t, z_t). Table 3.1 shows the coordinate transforms between the jet system and the global system for the two jet positions shown in Figure 3.4. Table 3.1 also shows the coordinate transforms for the hybrid and tube systems for tube T13. Equation (3.1) illustrates an example calculation to transform between hybrid(h13) and global(g) coordinates.

$$\begin{aligned}(x, y, z)_g &= (x, y, z)_{h13} + (T_x, T_y, T_z)_{h13g} \\ &= (x, y, z)_{h13} + (0, -44, 352)_{h13g}\end{aligned} \tag{3.1}$$

Coordinate	$jdl \to g$	$jot \to g$	$h13 \to g$	$t13 \to g$
T_x	0	0	0	-651
T_y	0	-44	-44	-44
T_z	0	0	352	352

Table 3.1: Model coordinate transforms between jet down lane(jdl), jet on tube(jot), hybrid(h13), tube(t13) to global(g).

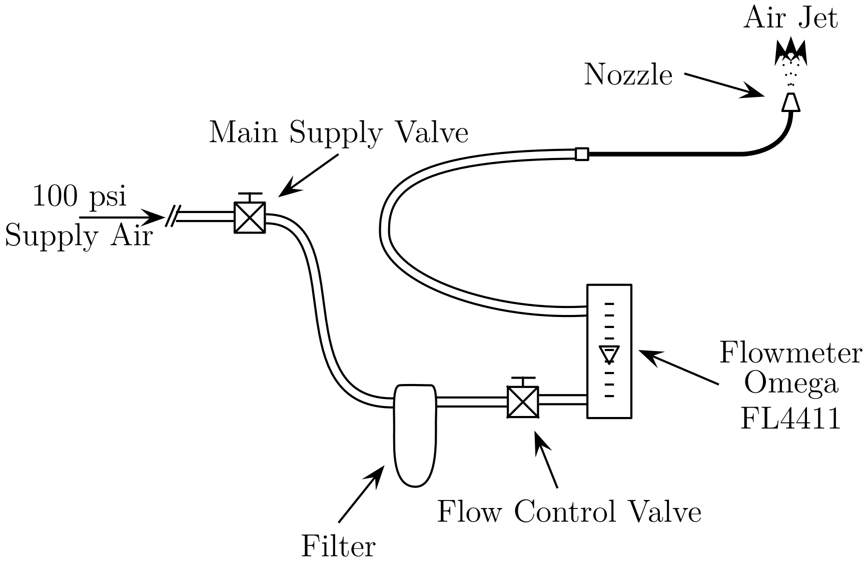

Figure 3.2: Air jet system.

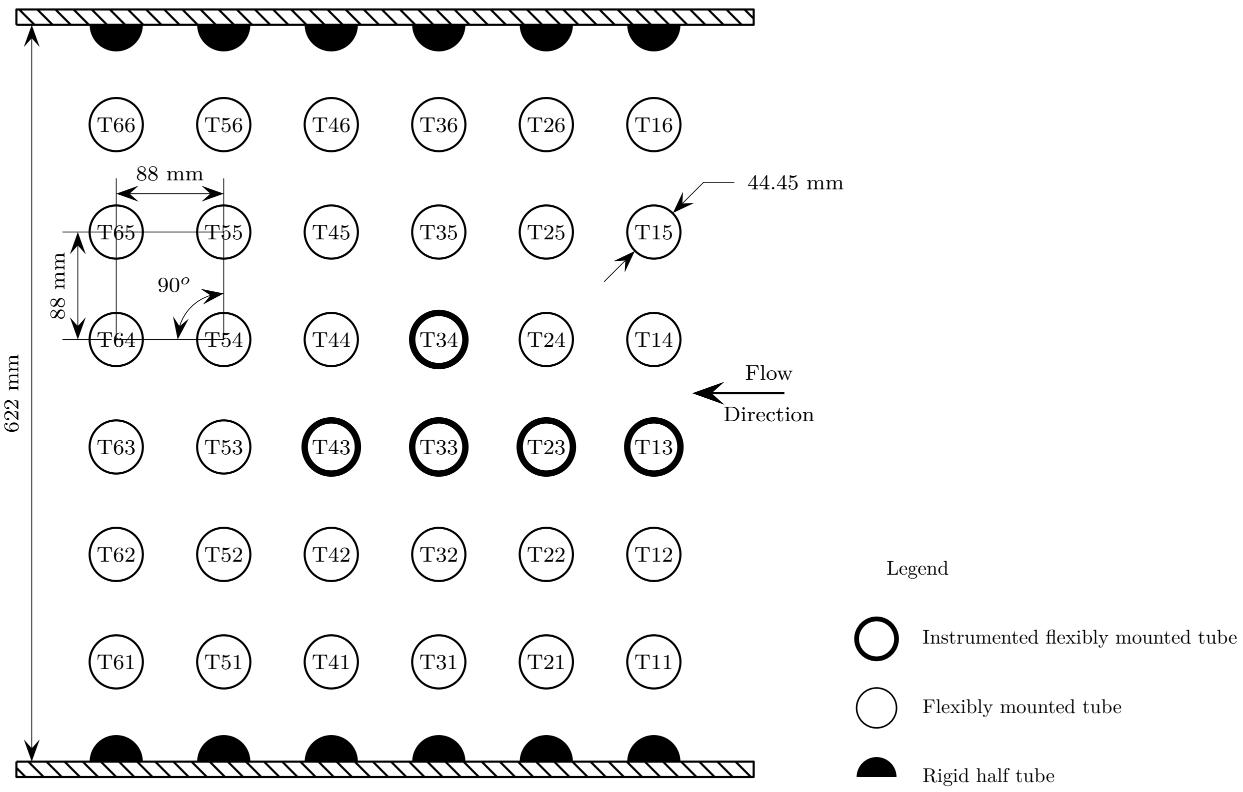

Figure 3.3: Model tube array - plan view.

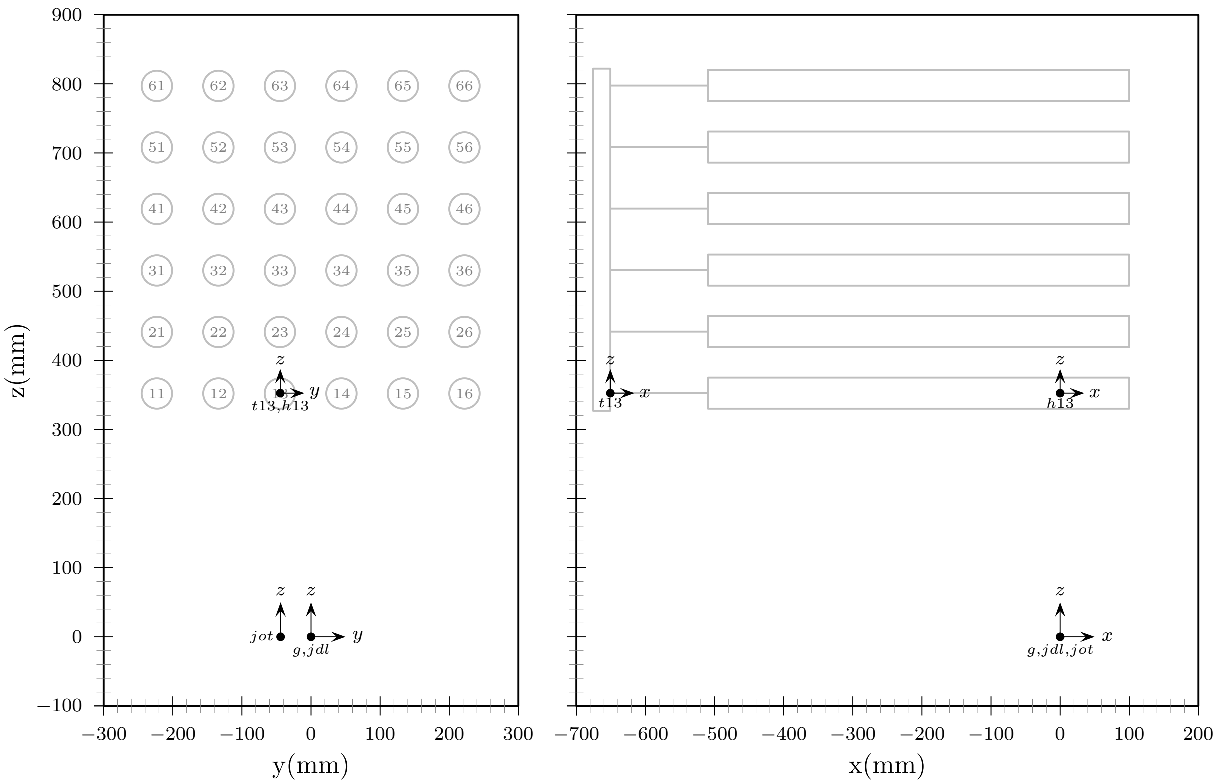

(a) Plan view.

(b) Side view.

Figure 3.4: Air jet orientation and position. This diagram shows the orientation and relative positions of the model components. Descriptive coordinate systems are introduced which will be used for subsequent mathematical derivations. The configuration shown is generic as multiple jet locations are illustrated.

3.3.1 Tube Geometry and Materials

The model tubes were constructed of aluminum tubes attached to threaded steel rod supports. Only the aluminum portion of the model was subjected to fluid flow and the steel rod acted as the primary stiffness element. The upper aluminum section was designed such that the flexural rigidity (EI) was much greater than that of the steel support and therefore the steel rod bends while the aluminum tube remains primarily straight under static loading. The structural mass per unit length of the aluminum tube (ρA) was chosen to be significantly greater than that of the steel rod such that the primary mass element is the aluminum tube. Figure 3.5 shows a diagram of a model tube and shows the division into ten unique segments each with its own sectional material and geometric properties. Table 3.2 outlines the specific composition of each segment and Table 3.3 provides relevant sectional properties for each segment.

3.3.2 Tube Mode Shape

The critical gap flow velocity, V_{cr}, which defines the onset of fluidelastic instability is typically determined by plotting vibration amplitude versus gap flow velocity and observing the point at which the slope increases dramatically. Once the critical velocity has been determined the results can be related to the existing experimental data using Equation (2.5) which describes the relationship between the critical reduced velocity and the mass damping parameter. To calculate the critical reduced velocity requires the critical velocity, V_{cr}, tube natural frequency, f_n, and tube outer diameter, D. To calculate the mass damping parameter requires the tube effective lineal modal mass, m, tube damping ratio, ζ, tube outer diameter, D, and the fluid density, ρ. The values of V_{cr}, f_n, D, ζ and ρ can be measured directly. However, the effective lineal modal mass, m, for tubes, or models, with non-uniformly distributed mass depends on the mode shape function, $\hat{Y}(x)$, for the corresponding natural frequency, f_n. Also in the case of partial admission flow, Equation (2.6), the mode shape function is required to calculate the equivalent uniform velocity, V_{eq}, regardless of whether the mass distribution is uniform or not.

In Appendix A the first mode natural frequency and mode shape were determined in two very different ways. Section A.1 utilized the static deflection curve as an estimated first mode shape and Rayleigh's Quotient to determine the natural frequency of 9 Hz (the "approximate" solution). Section A.2 utilized the solution of the differential eigenvalue/boundary-value problem to find both the mode shape and frequency of 9 Hz (the "exact" solution). The exact solution required considerably more effort than the approximate solution. Also the functional form of the mode shape provided by the exact solution is much more complicated than the approximate solution. The mode shape is

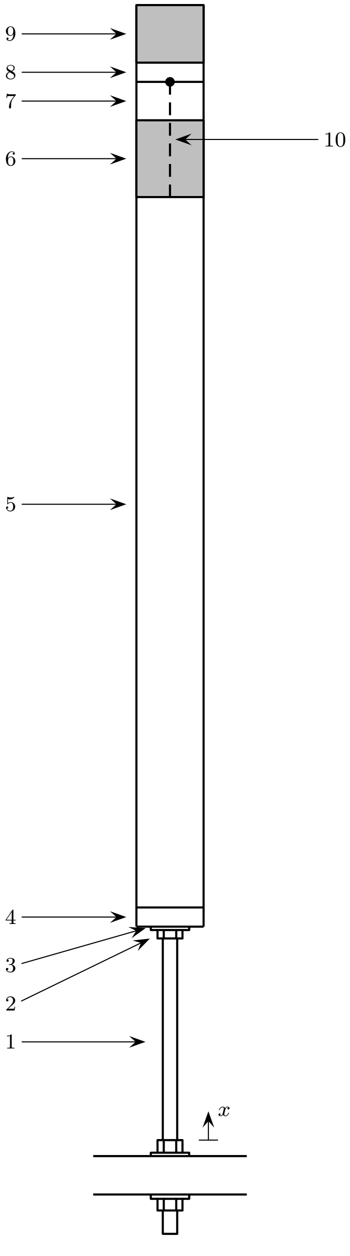

Figure 3.5: Model tube segmented based on physically unique sections.

Segment 1:	133.35 mm long solid steel threaded rod (3/8-24 UNF) with effective bending diameter of 8.28 mm.
Segment 2:	5.59 mm long solid steel hexagonal section (3/8-24 UNF jam nut) with distance across flats of 14.28 mm.
Segment 3:	2.24 mm long solid steel circular section (washer) with a diameter of 25.40 mm.
Segment 4:	12.70 mm long composite tube/support joint with solid steel threaded rod core with effective bending diameter of 8.28 mm, surrounded by a solid aluminum annulus with outer diameter of 44.45 mm.
Segment 5:	469.90 mm long tubular aluminum section with inner diameter 41.28 mm and outer diameter of 44.45 mm.
Segment 6:	50.80 mm long tubular aluminum section (same as Segment 5) with non-structural mass (damper fluid) of 1181.10 g/m.
Segment 7:	25.40 mm long tubular aluminum section (same as Segment 5).
Segment 8:	12.70 mm long tubular aluminum section (same as Segment 5).
Segment 9:	38.10 mm long tubular aluminum section (same as Segment 5) with non-structural mass (end plug) of 1312.34 g/m.
Segment 10:	76.20 mm damper chain (double jack chain) with lineal mass 44.73 g/m. The chain is mounted from the point between Segment 7 and Segment 8 and hangs downward to the starting point of Segment 6.

Table 3.2: Model tube segment physical descriptions.

Segment	l(mm)	A_s(mm^2)	A_a(mm^2)	m_{ns}(g/m)	m(g/m)	I_s(mm^4)	I_a(mm^4)	EI(N $\cdot$ m^2)
1	133.35	53.85	-	-	423.27	230.77	-	46.15
2	5.59	160.33	-	-	1260.16	2045.48	-	409.10
3	2.24	506.71	-	-	3982.72	20431.71	-	4086.34
4	12.70	53.85	1497.94	-	4467.71	230.77	191396.35	13443.90
5	469.90	-	213.77	-	577.17	-	49158.82	3441.12
6	50.80	-	213.77	1181.10	577.17	-	49158.82	3441.12
7	25.40	-	213.77	-	577.17	-	49158.82	3441.12
8	12.70	-	213.77	-	577.17	-	49158.82	3441.12
9	38.10	-	213.77	1312.34	577.17	-	49158.82	3441.12
10	76.20	-	-	-	44.73	-	-	-

Table 3.3: Model tube segment material and geometric properties. l(mm) - segment length, A_s(mm^2) - steel cross-sectional area, A_a(mm^2) - aluminum cross-sectional area, m_{ns}(g/m) - non-structural lineal mass, m(g/m) - structural lineal mass, I_s(mm^4) - steel section area moment of inertia, I_a(mm^4) - aluminum section area moment of inertia. The following material properties for steel and aluminum were used: $\rho_s = 7860\,\mathrm{kg/m^3}$ - density of steel, $E_s = 200\,\mathrm{GPa}$ - modulus of elasticity for steel, $\rho_a = 2700\,\mathrm{kg/m^3}$ = density of aluminum, $E_a = 70\,\mathrm{GPa}$ - modulus of elasticity for aluminum.

required to calculate the partial admission factor and it would be beneficial to determine if the extra effort required to solve for the exact solution was indeed warranted. If not the remaining calculations could then utilize the simpler functional form of the mode shape obtained by approximate methods.

Figure 3.6 shows a plot of both the approximate and exact mode shapes which appear to be practically identical. For the present research only the first mode shape is required. Therefore, the static deflection curve may be used for the remainder of the calculations. Figure 3.6 also includes two dashed lines which represent the limits to which any cantilevered tube model should be constrained. The upper curve is simply x/L and represents a rigid beam attached to a rotational spring (zero length spring). The lower curve is from Blevins (2001b) and represents the first mode shape of a uniform cantilevered beam (full length flexural element).

3.3.3 Tube Modal Mass and Mass Ratio

For a beam with uniformly distributed mass the mass ratio, $m/\rho D^2$, can be calculated directly from the structural lineal mass, $m_s = \rho A$. However, for a beam with non-uniformly distributed mass the effective lineal modal mass, m, must be used to calculate the mass ratio. For fluidelastic instability in air the vibrations typically occur at the first natural frequency and mode and therefore the effective lineal modal mass must reflect that condition ($m = m_1 = m_n$). The expression for the effective lineal modal mass can be derived by equating the kinetic energy of the real non-uniformly distributed system to that of the effective uniformly distributed system as in Equation (3.2).

$$\begin{gathered}\left(\frac{1}{2}\right) m_n \int_0^L (\omega_n \hat{Y}_n(x))^2 dx = \left(\frac{1}{2}\right) \int_0^L m_s(x)(\omega_n \hat{Y}_n(x))^2 dx \\ m_n = \frac{\int_0^L m(x)\hat{Y}_n^2(x)dx}{\int_0^L \hat{Y}_n^2(x)dx}\end{gathered} \tag{3.2}$$

Using the "exact" first mode shape, calculated in Appendix A: Section A.2 and the associated sectional mass properties from Table A.1, the first mode effective lineal modal mass (m_1) is approximately 1004 g/m which is 28% greater than the average structural lineal mass of approximately 782 g/m. The effective mass ratio of 423.5 can be calculated using the effective lineal modal mass and Equation (3.3).

$$\frac{m_n}{\rho D^2} = \frac{(1.004\,\mathrm{kg/m})}{(1.2\,\mathrm{kg/m^3})(0.044\,45\,\mathrm{m})^2} = 423.5 \tag{3.3}$$

It is worth noting that using the "approximate" mode shape from Appendix A: Section A.1 and the sectional mass properties from Table 3.3 results in a

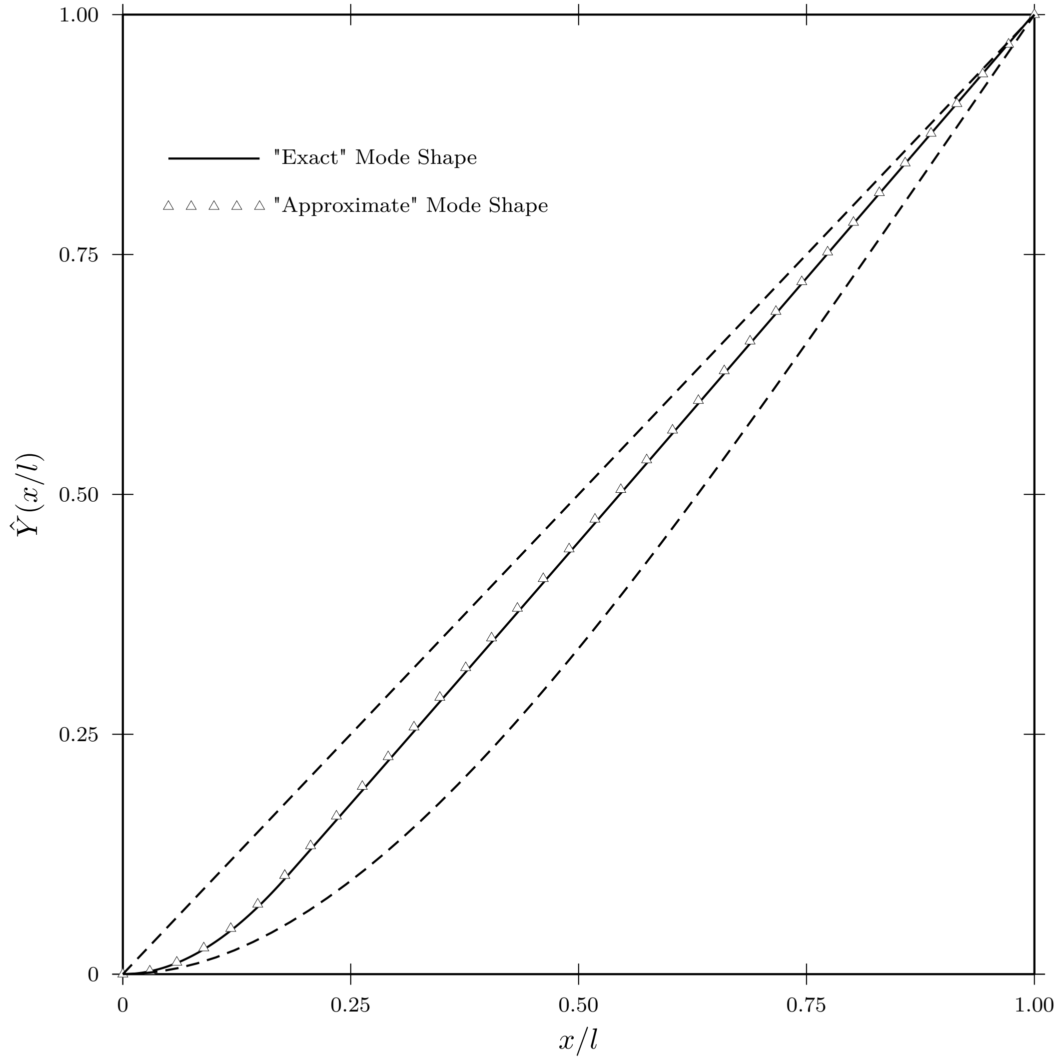

Figure 3.6: Comparison of mode shape functions derived in Appendix A: Sections A.1 ("Approximate" Mode Shape) and A.2 ("Exact" Mode Shape). From the plot the approximate and exact mode shapes appear to be practically identical. Note that the upper dashed curve is x/L and the lower dashed curve is the first mode shape of a uniform cantilever beam (Blevins 2001b).

difference in the calculated effective lineal modal mass of approximately 3 %. Since the "exact" and "approximate" mope shape functions have practically identical shapes, see Figure 3.6, this difference can be attributed to the the differences in tube segmentation and associated mass distributions between Table 3.3 and Table A.1. Perhaps more significant is that using a mode shape estimate of $\hat{Y}(x) = x/L$ results in a difference in the calculated effective lineal modal mass of only 5 %.

3.3.4 Tube Damping

Each of the the model tubes was fitted with a damper assembly as illustrated in Figure 3.7. The damper assemblies were used to achieve a first mode damping ratio of 1.0 % of critical for each tube. The tube damping without these assemblies was on the order of 0.1 % of critical. The additional damping was required to increase the uniform flow critical gap flow velocity, V_{cr}, to a value which could be measured reliably using a pitot static tube.

The design objectives for the damper were to provide damping which was independent of vibration amplitude (linear damping force) and direction. Kulkarni et al. (2012) divided passive damping devices into direct energy dissipation and indirect energy dissipation devices. Direct energy dissipation can be achieved by increasing inherent material damping or by the attachment of a damper attached to a stationary frame of reference (support). Indirect energy dissipation is achieved by the attachment of an auxiliary vibrating absorber system to the main structure. Examples of indirect dissipation systems include: tuned mass dampers, tuned liquid dampers and impact dampers.

The addition of a viscous damper (dashpot) in parallel with the system stiffness element is the simplest way to add damping to a system. A key example of such a situation is an automatic door closer which is typically designed to be critically damped. However, in many dynamic systems there is no stationary support on which to mount such a damper or the forces required to restrain the inertial motion are simply too large for direct attachment systems. It may therefore be advantageous to attach a secondary mass element connected to the main structure via a stiffness and damping element. When there is relative motion between the main structure and the auxiliary system energy will be dissipated within the damping element, the magnitude of the damping and it's specific dependencies will depend on the specific damping mechanism employed.

Tuned mass dampers (TMDs) typically consist of a solid mass attached to the main structure by springs and dashpots. Hartog (1985) describes the theoretical background and design of a "Damped Vibration Absorber" which is essentially a TMDs. These auxiliary systems are characterized by fine tuning the mass, damping and stiffness of the auxiliary system in relation to the properties of the main system. The damping within TMDs is typically provided by a dashpot or a series of dashpots. Depending on the dashpot design TMDs can provide linear damping (constant damping ratio) over large ranges of vibration amplitude. In order to implement a traditional TMD inside each of the model tubes thirty six precisely manufactured TMDs would have been required. There would also have been challenges with respect to the dimensional scale in relation to achieving the required stiffness and damping while maintaining directional independence.

Tuned Liquid Dampers (TLDs) typically consist of one or more large tanks filled with fluid. The specific properties and design of TLDs are outlined in Fujino et al. (1988). TLDs are further divided into tuned sloshing dampers (TSDs) and tuned liquid column dampers (TLCDs). However, the current discussion will be constrained to TSDs. TSDs are a special form of TMD, where the solid mass is replaced by fluid mass constrained in a container and the damping mechanism is provided by fluid sloshing. The motion of liquids in moving containers is discussed in detail by Abramson (1966). TSDs effectiveness and design is constrained to very low frequencies (below 2 Hz) and correspondingly large containers. Low frequency systems work quite well for tall buildings where the fundamental natural frequencies are below 2 Hz. The damping provided by TSDs is nonlinear as the system damping ratio is dependent on vibration amplitude.

Impact dampers dissipate energy by promoting the collision of objects, each collision dissipates energy, when the main structure vibrates. Due to the nature of the disipation mechanism there are potentially, and really, many types of impact dampers. However, the current discussion will be constrained to hanging chain impact dampers (HCIDs) the properties and design of which are discussed in detail by Reed (1967) and summarized by Koss and Melbourne (1995). These systems are characterized by a long hanging chain covered in a resilient material and suspended in a relatively narrow gap. The damping mechanism is produced from the impacting of the chain on the walls of the gap. When the vibration amplitude and the forcing frequency fall within the appropriate ranges, as outlined in Reed (1967), the chain will impact the gap walls twice each full cycle of vibration. Due to the dissipation mechanism damping provided by HCIDs is highly nonlinear with respect to vibration amplitude.

The damper design shown in Figure 3.7 was developed using an experimental approach. A variety of container sizes, fluid types, chain lengths and chain geometries were tested. Although the chain in oil damper was not designed using analytical methods, the literature on various damper types was reviewed. The objective was to avoid methods which would lead to amplitude or directionally dependent damping.

Before the final configuration was selected several trial designs were tested. During some of the trials the damper bottles were filled with 50-60 % water only (no chain). This configuration lead to highly non-linear damping. Attempts were also made with light and heavy mineral oil. Although the oil showed less tendency to produce non-linear damping the achieved damping ratios were too small. The hanging chain was added to increase the dissipation within the fluid. However, the chain would occasionally impact the side walls and the damping achieved was inconsistent. It was also found that the chain geometry could introduce directional dependence.

The final damper design consisted of a bottle filled with 60 ml of 10w40 diesel oil with a length of double jack chain (symmetric profile in transverse and streamwise directions) suspended at the centre such that it was just short of touching the bottom of the bottle. The more viscous 10w40 oil did not slosh and did not allow the chain to impact the side walls. The result was a chain in oil damper which provided a constant damping ratio of 1 % of critical, for vibration amplitudes up to approximately 30 mm pk-pk (68 % of tube diameter). Higher amplitudes where not tested. The damping was also found to be symmetric in the transverse and streamwise directions.

Prior to completing experiments the natural frequency and damping ratio of each tube were tuned using the following procedure. The damping of each tube was determined via analysis of the measured time domain response to a step displacement input. The resulting tube motion was measured using a Dytran model 3225F1 mini accelerometer, Kistler 5134A accelerometer power supply and a computer data acquisition system (DAQ). The data acquisition system consisted of a National Instruments AT-MIO-16 and a custom Labview program. The voltage output from the Kistler 5134A was sampled using the DAQ at a rate of 1000 samples per second. Figure 3.8 shows an overview of the post processing steps used to calculate the first mode damping for each tube. The acquired time domain signal in Figure 3.8a shows the amplitude decay of all frequency components within the measurement bandwidth (0-500 Hz). Figure 3.8b shows the power spectrum of Figure 3.8a which was calculated to determine the first mode natural frequency of 9 Hz. Note that the second mode natural frequency is also visible on Figure 3.8b. The measured second mode natural frequency was 165.4 Hz. Whereas the predicted value from Figure A.3 was 183 Hz. The error of 17.6 Hz (approximately 11 % of measured) is relatively small and can be attributed to the basic assumptions invoked in Appendix A: Section A.2. The calculation was based on the Euler-Bernoulli beam equation and neglected the effects of rotary inertia, however for higher modes with greater curvature rotary inertia is not negligible. A digital bandpass filter was designed to filter components of the signal not associated with the first mode natural frequency. The filter response is shown on Figure 3.8c, the passband was 8-10 Hz. The original acquired signal was low-pass filtered,

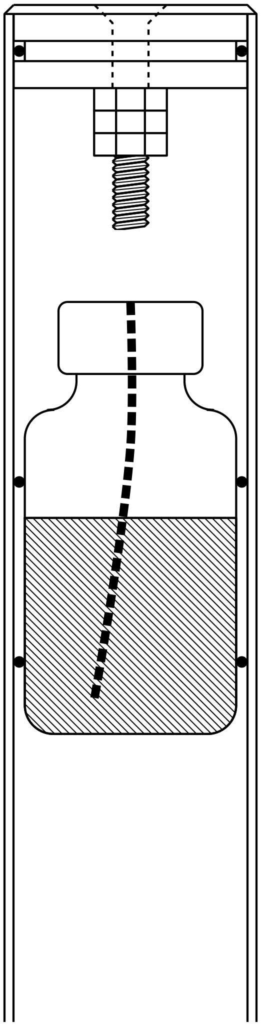

Figure 3.7: Model tube damper assembly.

decimated (to reduce the effective sampling rate), and then band-pass filtered such that the only remaining energy was associated with the first mode natural frequency (Figure 3.8d). The power spectrum of the filtered signal was then calculated (Figure 3.8e). The amplitude decay rate of the filtered signal was calculated using the method described by Schroeder (1965). This method utilizes reverse or backward integration of the squared time domain signal to determine the energy decay rate. This method is most often used to measure reverberant decay of sound pressure within an enclosed space. The plot of the reverse integrated time domain response is often referred to as the Schroeder plot (Figure 3.8f). The Schroeder plot was fit with a linear curve from 70 % (-3dB) of initial amplitude to 30 % (-10dB) of initial amplitude (Figure 3.9). The slope of this fit represents the decay rate in decibels per second of the energy within the pass-band of Figure 3.8c.

$$Y(t) = \left[ae^{-\zeta 2\pi f_n t}\right] cos(\sqrt{1-\zeta^2} 2\pi f_n t - \phi) \tag{3.4}$$

$$\hat{a}(t) = e^{-\zeta 2\pi f_n t} \tag{3.5}$$

Equation (3.4) describes the free vibration of a damped single degree of freedom simple harmonic oscillator, see Rao (1995). Equation (3.5), $\hat{a}(t)$, represents the normalized amplitude exponential decay envelope. Schroeder (1965) describes a method which can be used to determine the damping ratio, ζ, from measurements of amplitude decay. The measured amplitude decay, $Y(t)$, is reversed in time, if the measurement period in seconds is T then after reversal of $Y(t)$, $Y_r(0) = Y(T)$. This reversal can be implementing by introducing the coordinate transform: $t = T - \tau$. The reversed amplitude function, $Y_r(\tau)$, is then squared and integrated with respect to τ. After integration the function $IY_r(\tau)$ is reversed again using $\tau = T - t$. Finally, Equation (3.8) represents the Schroeder curve which is normalized to zero decibels at $t = 0$.

$$IY_r(\tau) = \int_0^{\tau} (Y_r(\tau))^2 d\tau \tag{3.6}$$

$$IY(t) = IY_r(T - t) \tag{3.7}$$

$$S(t) = 10 \log_{10}(IY(t)/IY(0)) \tag{3.8}$$

The slope of $S(t)$ represents the decay rate, η, of the squared amplitude in decibels per second. If the signal of interest is concentrated at the natural frequency, f_n, the damping ratio, ζ, can be calculated directly from the decay rate. Equation (3.9) describes the relationship between the decay rate, η, and the damping ratio, ζ.

$$\eta t = 10\log_{10}(\hat{a}^2(t)) = 20\log_{10}(e^{-\zeta 2\pi f_n t}) = -\zeta 2\pi f_n t 20\log_{10}(e)$$

$$\zeta = \frac{-\eta}{2\pi f_n 20\log_{10}(e)} \tag{3.9}$$

The damping and frequency of each tube in the array was calculated from decay measurements as described above. Table 3.4 shows the average results of three damping measurements for each tube. The error estimate, $\delta\zeta$, represents the root sum of squares of the estimated fit slope 95 % confidence intervals for the three measurements. The average damping ratio for all tubes was 1.05 % of critical with a 95 % confidence interval of ±0.01 % and the measured extreme values were 0.98 % and 1.16 %. The measured first mode natural frequency was 9.0 Hz for all tubes. The frequency measurement was accomplished using the Fourier transform with a resolution of 0.2 Hz. Therefore the estimated error in the frequency values is approximately ±0.1 Hz.

3.4 Instrumentation and Signal Processing

The sections which follow describe the various measurement types, associated instrumentation and data reduction techniques used for the completion of this experimental work. Further technical details including equipment calibrations and uncertainty analysis are included in Appendix B.

3.4.1 Vibration Measurements

The model tube vibrations were measured using Vishay Micro-Measurements model WD-DY-125AD-350 strain gauges mounted to the tube supports. Five tubes (T13, T23, T33, T43 and T34) were instrumented in this way as shown in Figure 3.3. The strain gauges were mounted to the tube supports orthogonally such that the vibration amplitudes could be measured in both the transverse, y, and streamwise, z, directions. Each strain gauge was connected using a quarter wheatstone bridge configuration. Bridge completion, excitation voltage and output signal conditioning were provided by Vishay 2310 strain amplifiers. The amplified outputs were captured and analyzed using an Agilent 35670A dynamic signal analyzer. The Agilent 35670A was setup to acquire the power spectral density (psd) on each channel, with a frequency span of 0-50 Hz and resolution of 0.25 Hz, using 100 root mean square (rms) averages. Due to the nature of the signal a hanning window function was utilized to minimize spectral leakage. The measurement was initiated once a steady state condition was reached and acquisition required approximately 400 seconds $((1/0.25\,\text{Hz})\times$

Tube	ζ_n	$\delta\zeta$	f_n	δf
T_{11}	1.0206	0.0021	9.0	0.1
T_{21}	1.0334	0.0019	9.0	0.1
T_{31}	1.0204	0.0022	9.0	0.1
T_{41}	1.0068	0.0020	9.0	0.1
T_{51}	1.0175	0.0021	9.0	0.1
T_{61}	1.0569	0.0023	9.0	0.1
T_{12}	1.0850	0.0024	9.0	0.1
T_{22}	1.1564	0.0028	9.0	0.1
T_{32}	1.0921	0.0024	9.0	0.1
T_{42}	1.0118	0.0015	9.0	0.1
T_{52}	1.0990	0.0025	9.0	0.1
T_{62}	0.9931	0.0022	9.0	0.1
T_{13}	1.0246	0.0020	9.0	0.1
T_{23}	1.0557	0.0020	9.0	0.1
T_{33}	1.0879	0.0023	9.0	0.1
T_{43}	1.0981	0.0024	9.0	0.1
T_{53}	1.0701	0.0024	9.0	0.1
T_{63}	1.0484	0.0021	9.0	0.1
T_{14}	1.0357	0.0024	9.0	0.1
T_{24}	1.0106	0.0024	9.0	0.1
T_{34}	1.0656	0.0024	9.0	0.1
T_{44}	1.0201	0.0020	9.0	0.1
T_{54}	1.0341	0.0025	9.0	0.1
T_{64}	1.1153	0.0025	9.0	0.1
T_{15}	0.9860	0.0017	9.0	0.1
T_{25}	1.0063	0.0020	9.0	0.1
T_{35}	1.0459	0.0021	9.0	0.1
T_{45}	1.0396	0.0025	9.0	0.1
T_{55}	1.0400	0.0023	9.0	0.1
T_{65}	1.0421	0.0022	9.0	0.1
T_{16}	0.9803	0.0019	9.0	0.1
T_{26}	1.0399	0.0021	9.0	0.1
T_{36}	1.0078	0.0019	9.0	0.1
T_{46}	1.0582	0.0022	9.0	0.1
T_{56}	1.0466	0.0020	9.0	0.1
T_{66}	1.0787	0.0024	9.0	0.1

Table 3.4: Tube damping and frequency measurement results. ζ_n represents the average damping from three individual measurements and $\delta\zeta$ represents the corresponding 95% confidence interval for ζ_n. f_n is the measured first mode natural frequency and δf represents the estimated uncertainty for f_n.

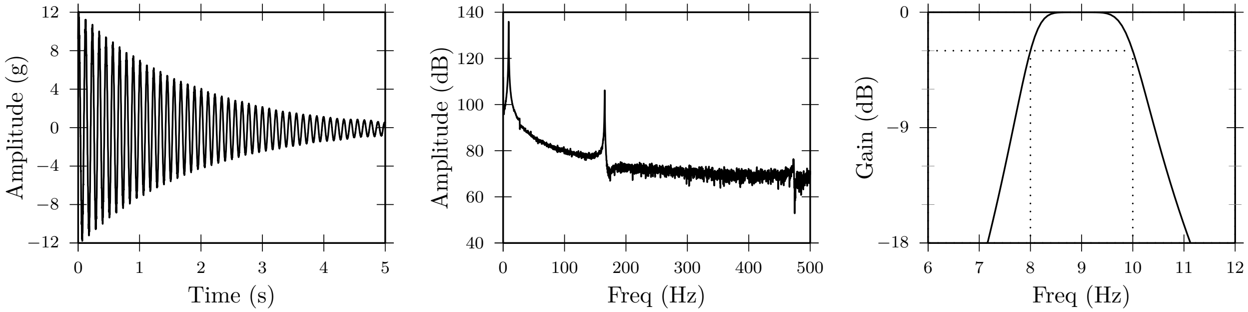

(a) Unfiltered amplitude decay.
(b) Power Spectrum.
(c) Band pass filter.

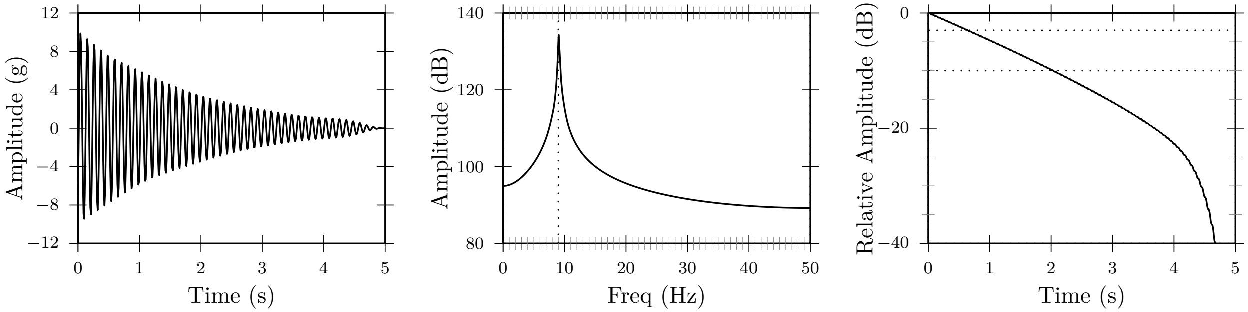

(d) Filtered and decimated.
(e) Power Spectrum.
(f) Schroeder Plot.

Figure 3.8: Model tube damping measurement and calculation procedure. (a) through (f) illustrate the post-processing steps used to determine the first mode structural damping from amplitude decay measurements. (a) and (b) show the unfiltered time history and power spectrum of the decay measurement. (c) shows the band-pass filter tuned to the first mode natural frequency. (d) and (e) show the filtered time history and power spectrum of the decay measurement. (f) shows the Schroeder plot which was calculated from (d) and used to determine the damping value.

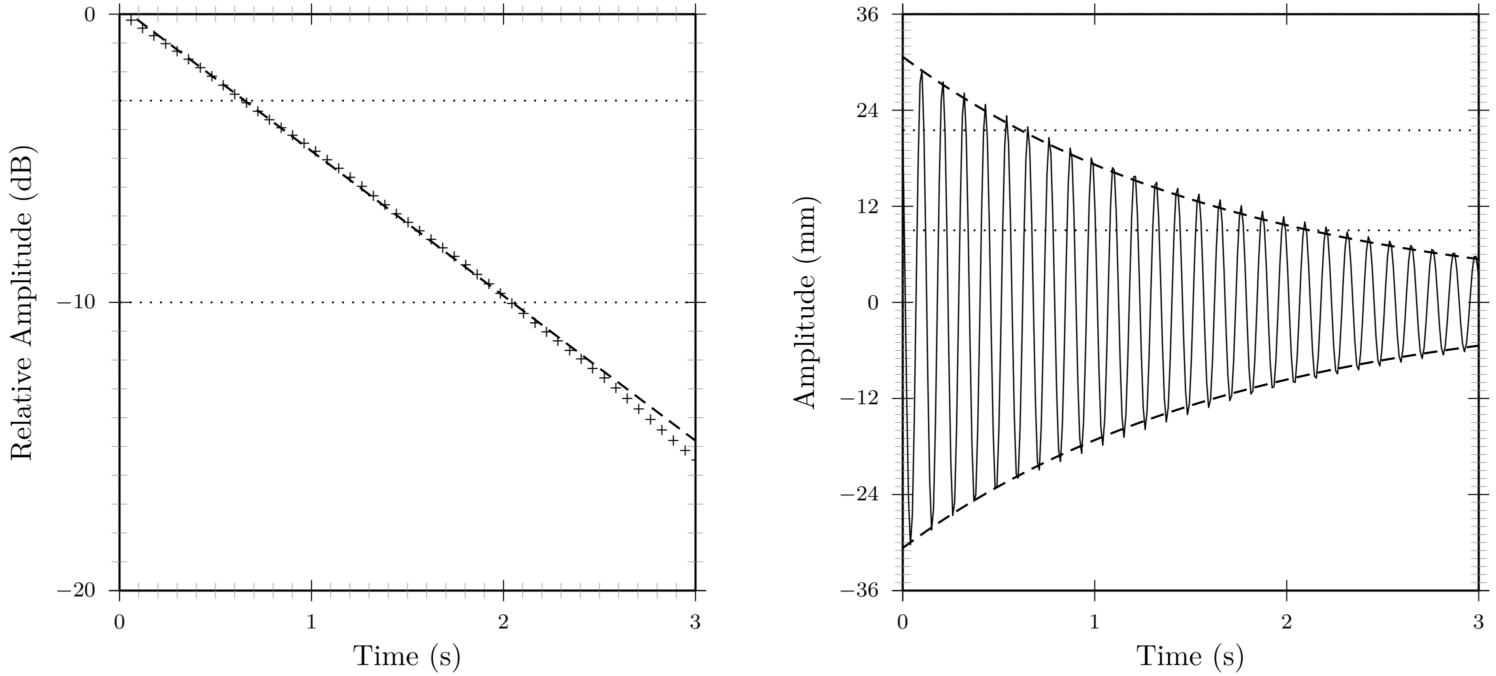

(a) Schroeder Plot.

(b) Filtered and decimated amplitude decay.

Figure 3.9: Schroeder plot example. (a) shows a Schroeder plot with a straight-line (dashed) linear regression fit from between 70% and 30% of initial amplitude (dotted lines). The damping can be calculated from (a) by using the slope, η, of the straight-line fit and Equation (3.9). (b) shows the actual measured amplitude decay and the calculated decay envelope, using Equation (3.9), which corresponds to the straight-line fit of (a).

100 = 400). The vibration amplitude at 9 Hz was determined approximately by summing the psd components from 8.5 - 9.5 Hz, multiplying by the frequency resolution (0.25 Hz) and taking the square root. Further details regarding the vibration measurement setups, calibrations and estimated uncertainties are provided in Appendix B.3.

3.4.2 Velocity Measurements

Fluid velocity measurements were acquired using a pitot static tube and hotwire anemometry. The pitot static tube was utilized to measure the uniform flow velocity in the wind tunnel and was chosen for its simplicity. For velocity measurements inside the tube array a miniature hotwire was utilized due to space constraints.

The wind tunnel uniform flow velocity was measured using a pitot-static tube. The induced pressure across the pitot-static tube was measured using an Ashcroft model XL-3-MB8-16-ST differential pressure transducer. The output voltage from the Ashcroft pressure transducer was measured using a Fluke 70 Series II Multimeter. Details regarding the pitot static tube setup, calibration procedure, and estimated uncertainty are provided in Appendix B.4.

The jet flow nozzle exit flow rate was measured using an Omega FL4411 rotameter. This data along with the known nozzle diameter (8.4 mm) was used to calculate the average nozzle exit velocity.

Hotwire Anemometry was employed to acquire detailed measurements of jet fluid velocities inside and outside the tube array. The hotwire system consisted of a Dantec model 55P14 miniature hotwire probe connected to a Dantec 55M10 constant temperature anemometry (CTA) bridge. The output voltage from the CTA bridge was captured using a National Instruments model AT-MIO-16 data acquisition system (DAQ). Details regarding the hotwire setup, calibration procedure and estimated uncertainties are provided in Appendix B.5.

To facilitate measurements at multiple locations the 55P14 probe was mounted on a positioning system comprised of a series of Velmex (models MB4000, MA4000 and MA2500) traversing mechanisms assembled in a three axis configuration. A National Instruments Labview program was used to move the positioning system to a specified starting location, start acquisition, dwell for a specified acquisition time (5 seconds) and then move to the next measurement location along a specified line. This automated method facilitated the efficient acquisition of detailed velocity profiles.

4. Experimental Results

The sections that follow describe the uniform and jet flow experimental results. The scope of this section is limited to the presentation of results and detailed discussions are deferred to Chapter 5.

4.1 Uniform Flow

The results of the uniform flow experiment are presented in Figures 4.1 to 4.3 which depict the root mean square (rms) vibration amplitudes versus the gap flow velocity for T23, T43 and T34 respectively. The vibration amplitudes in the figures were normalized by the tube diameter (44.45 mm) and presented as percentages. All three figures show the onset of fluidelastic instability at a uniform gap flow velocity of approximately 12 m/s.

From Figure 4.1 it is seen that the vibration amplitude of T23 is very small at the starting velocity of approximately 8.6 m/s and at this velocity the transverse and streamwise components of vibration are similar in magnitude. The vibration amplitude increases slowly between 8.6 m/s and 12 m/s, with the transverse component increasing from approximately 0.1 % to approximately 0.3 %, and in this velocity range the transverse and streamwise components of vibration are similar in magnitude. The response behavior between 8.6 m/s and 12 m/s is characteristic of small amplitude response to random turbulence which is typically called turbulent buffeting. The vibration amplitude increases dramatically between 12 m/s and 12.3 m/s, with the transverse component increasing from approximately 0.3 % to approximately 4.2 %, indicating a dramatic change in the slope of the vibration response curve at about 12 m/s. At 12.3 m/s the transverse component of vibration (4.2 %) is greater than the streamwise component (3.2 %). Thus, 12 m/s is taken as the fluidelastic instability threshold or critical velocity. The results presented in Figures 4.2 and 4.3 show similar behavior.

Although the vibration responses of the remainder of the tubes where not measured, all tubes in the array were visually observed during the experiment. All tubes in the array were observed to reach the onset of fluidelastic instability at about the same time, and under the same flow conditions, as T23, T43 and T34.

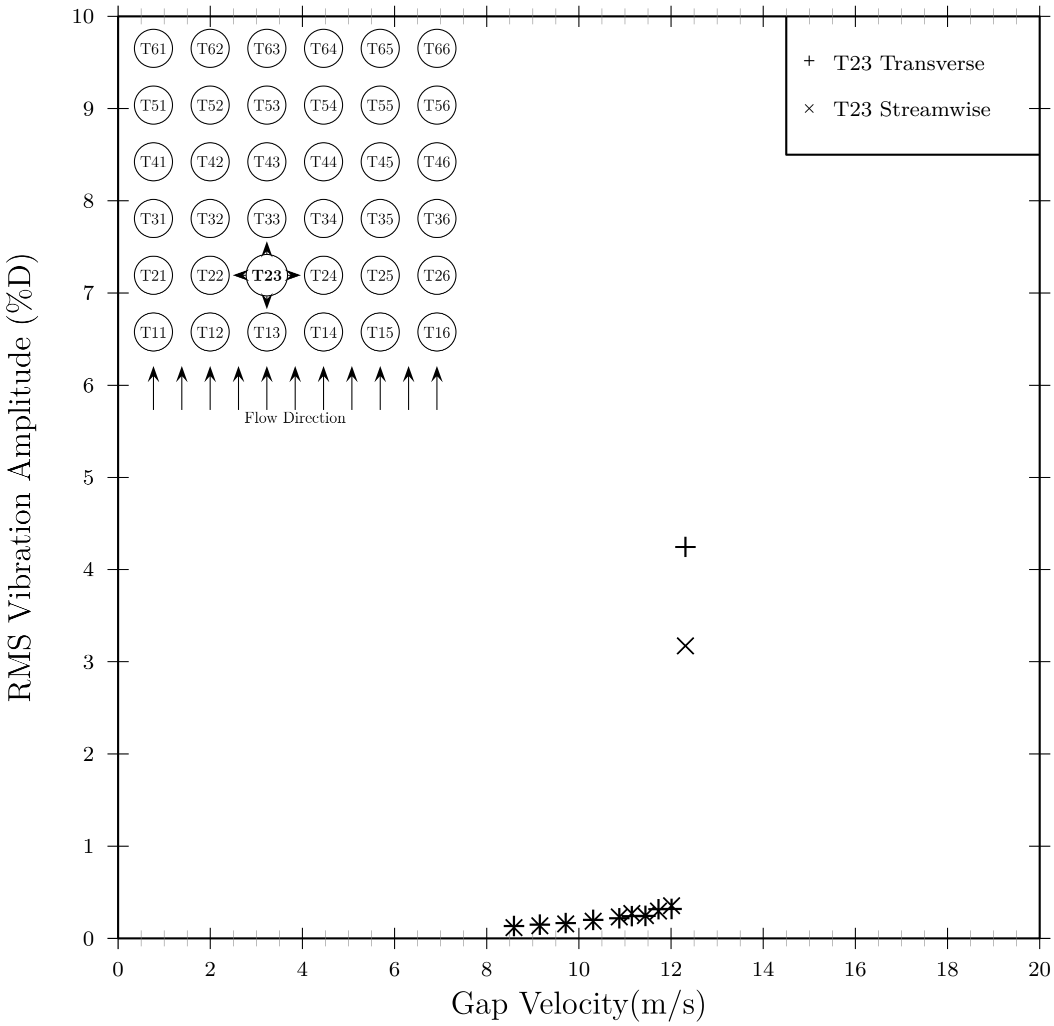

Figure 4.1: Amplitude response of T23 in uniform cross-flow.

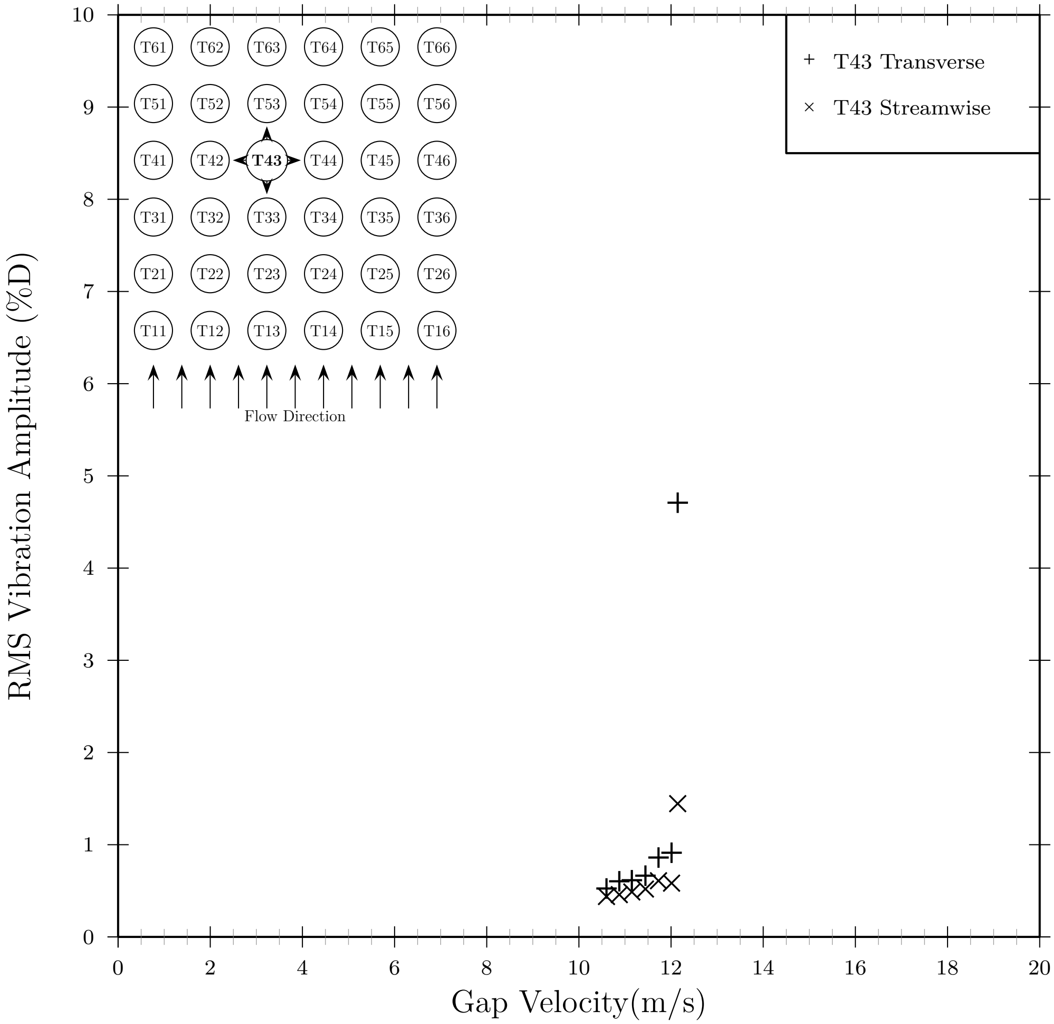

Figure 4.2: Amplitude response of T43 in uniform cross-flow.

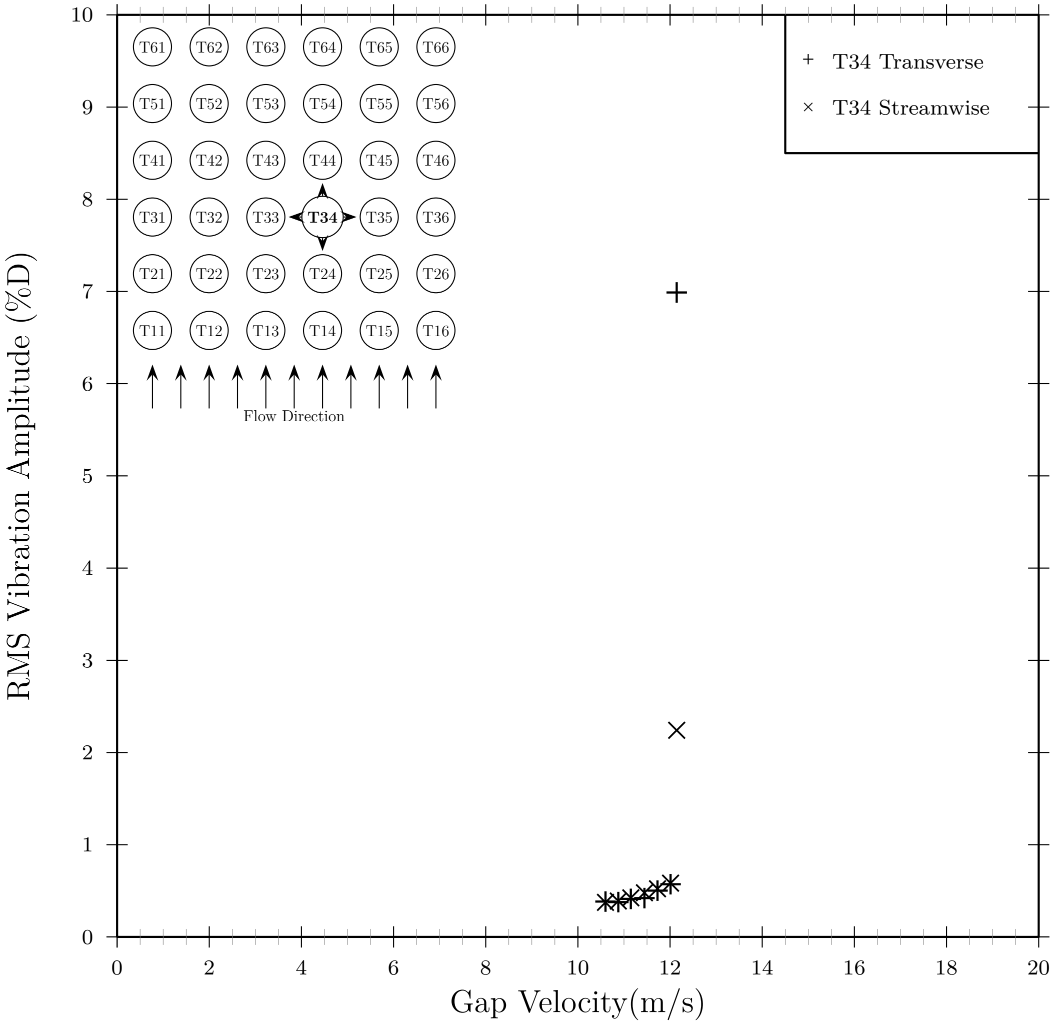

Figure 4.3: Amplitude response of T34 in uniform cross-flow.

4.2 Jet Flow Centered between Tubes

This section describes the results of the vibration and velocity measurements where the jet flow was centred between tubes T13 and T14. Figure 4.4 shows a diagram of the experimental setup. To aid in subsequent descriptions and in the development of mathematical relationships several convenient coordinate systems have been defined in Figure 4.4. These are the global(g), jet(j), hybrid(h) and tube(t) coordinate systems. Figure 4.4 is presented in terms of the global coordinate system.

4.2.1 Vibration Measurements

The results of the vibration measurements are presented in Figures 4.5 to 4.8 which depict the tube root mean square (rms) vibration amplitudes (scaled to percent of a tube diameter) versus nozzle flowrate (cfm) for T13, T23, T33 and T43 respectively. Figures 4.5 and 4.6 show that while the turbulent buffeting amplitudes are much higher than seen with uniform flow, T13 and T23 remained stable at flow rates up to 35 cfm. Whereas Figures 4.7 and 4.8 show that T33 and T43 experienced an increase in their transverse vibration response slope, resulting in significant vibration amplitudes, which indicates that they became unstable. While the change in vibration response slope is not as abrupt, or well defined, as in the case of uniform flow, visual observation indicated a modulated response to large amplitudes in the transverse direction, the direction typically observed as critical for fluidelastic instability. The change in vibration response slope occurs at about 26 cfm, corresponding to a nozzle exit velocity of 222 m/s.

Although the vibration responses of the remainder of the tubes where not measured all tubes in the array were visually observed during the experiment. Tubes T34 and T44, which were not instrumented, became unstable at the same time as their instrumented neighbors T33 and T43. This behavior was expected since these tubes experienced similar flow fields due to flow and model symmetry.

4.2.2 Velocity Measurements

The results of the velocity measurements are presented in Figures 4.9 to 4.11. For the velocity measurements the tube endpoints were locked to each other to "fix" the array and prevent significant tube movement. The array was fixed to allow measurement of the inter-tube velocity profiles under steady state conditions.

Figure 4.9 shows the measured jet centreline velocity just in front of the tube array for different nozzle exit flow rates. In a free field the jet centreline velocity and the nozzle exit velocity can be related using Equation (2.10).

However from Figure 4.9 this behavior is not observed, which is not entirely unexpected, since the tube array is an obstacle in the flow path and the measurements were taken in close proximity to the obstacle. It is worth noting that for uniform flow the upstream and gap flow velocities are related by the factor $P/(P - D)$ which for the configurations tested in this work is approximately 2.0. For the lowest flowrate tested (15 cfm) the observed centreline velocity was close to that predicted by Equation (2.10) and for the highest flowrate (35 cfm) the value was higher than expected. Figure 4.9 shows two dotted lines corresponding to Equation (2.10) and the product of $P/(P - D)$ and Equation (2.10). Both straight line and quadratic least squares regression curves are shown using dashed lines. Over the measurement range the values are reasonably represented by the straight line fit. However, the quadratic fit better represents the trend in the data.

Figures 4.10 and 4.11 show the detailed velocity measurements taken in the inter-tube spaces for a fixed nozzle exit flowrate of 30 cfm. The velocity data represented in Figures 4.10 and 4.11 is also presented in a series of detailed figures provided in Appendix C. Examination of Figure 4.10 reveals that the flow distributions, in the horizontal plane, around T13 and T23 are highly asymmetric with the majority of flow on one side of the tubes. Whereas the flow distributions around T33 and T43, although not exactly symmetric, are more evenly distributed on both sides of the tubes. T13 and T23 remained stable for nozzle exit flow rates of up to 35 cfm, whereas T33 and T43 became unstable at a nozzle exit flow rate of approximately 26 cfm. T33 and T43 became unstable, whereas T13 and T23 did not, despite the fact that they are deeper in the tube array than T13 and T23 and experienced lower overall average velocities due to jet diffusion.

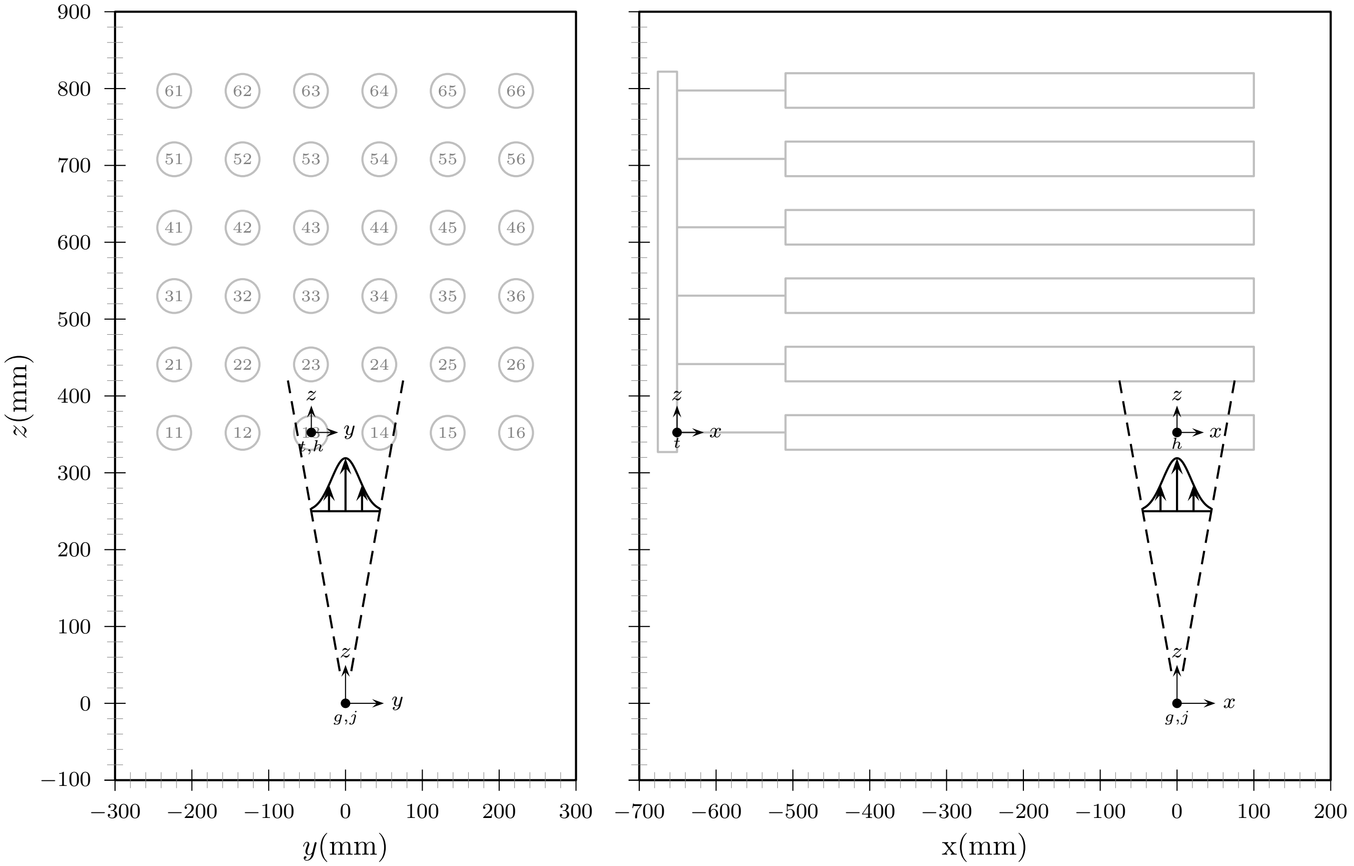

(a) Plan view.

(b) Side view.

Figure 4.4: Experimental setup: jet flow centred between T13 and T14.

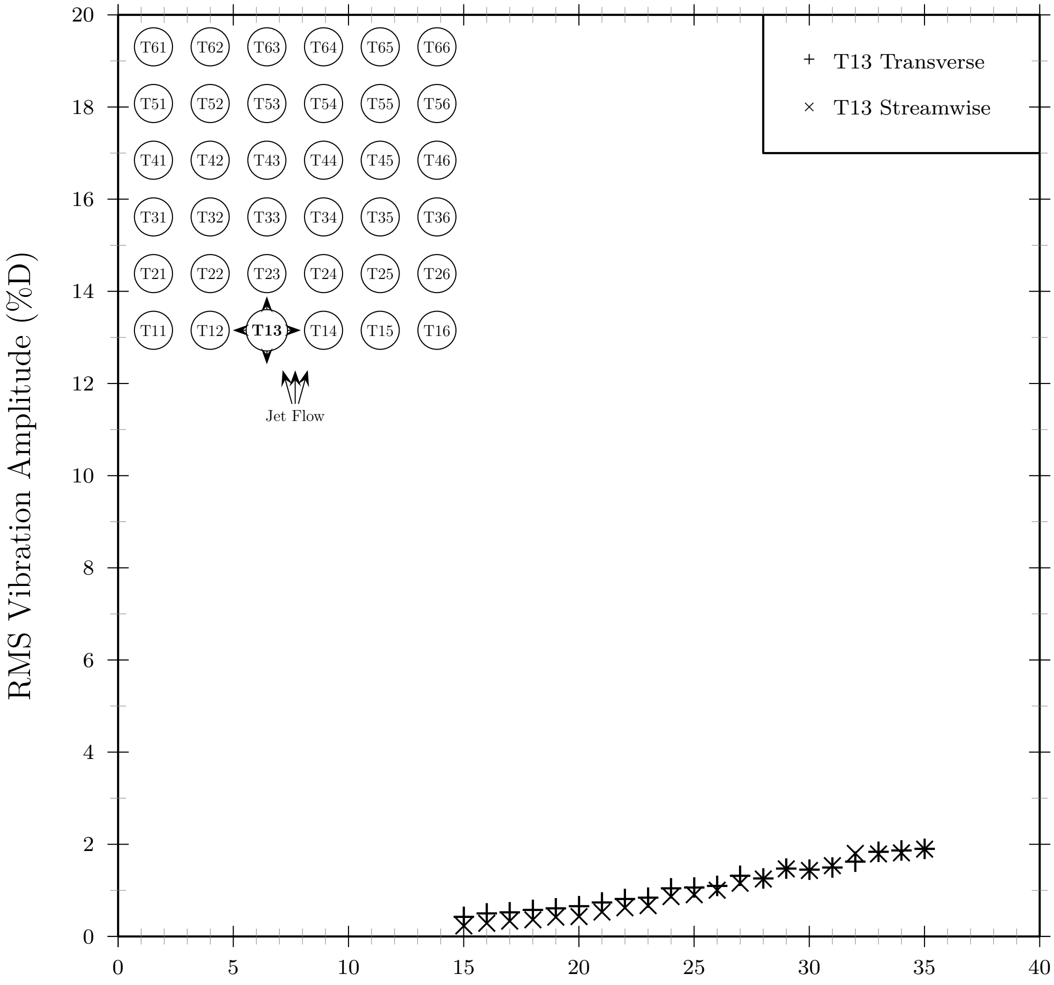

Figure 4.5: Amplitude response of T13, jet centred between T13 and T14.

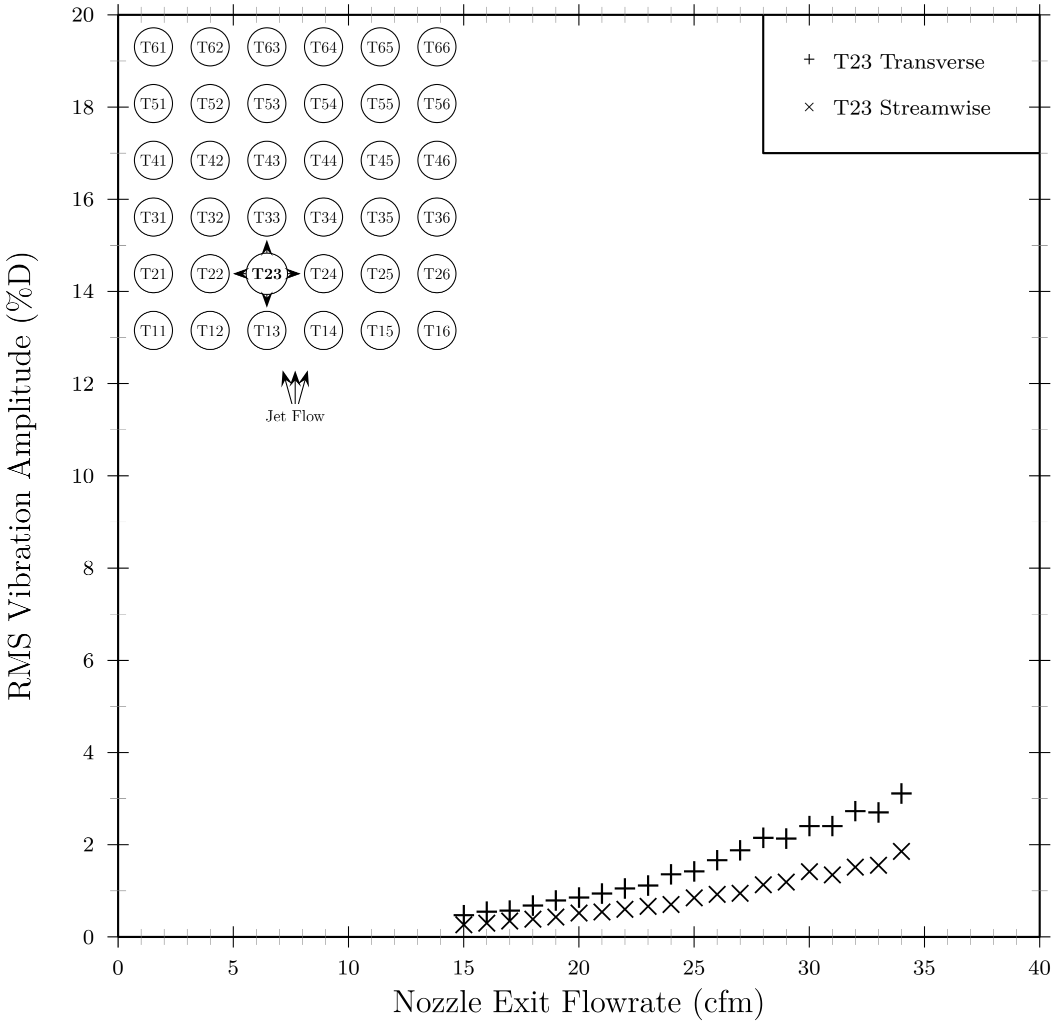

Figure 4.6: Amplitude response of T23, jet centred between T13 and T14.

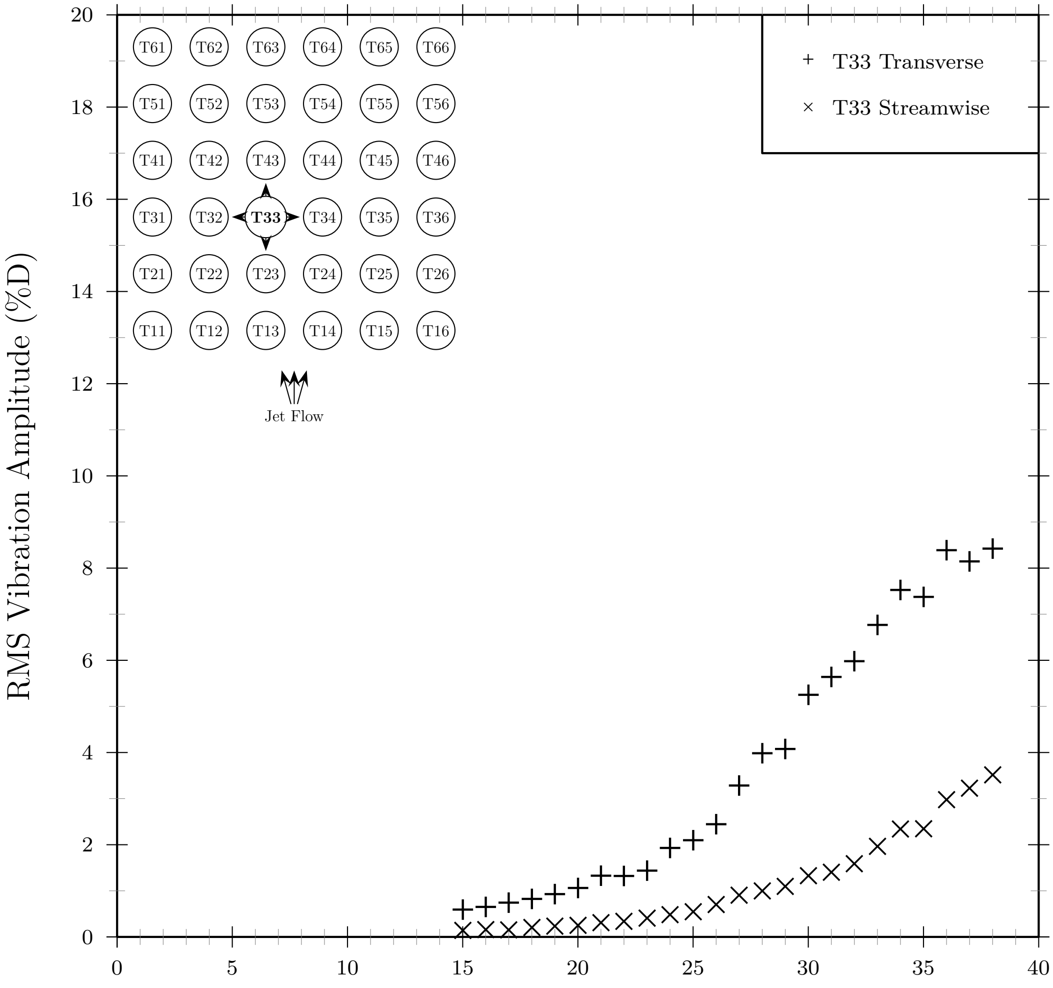

Figure 4.7: Amplitude response of T33, jet centred between T13 and T14.

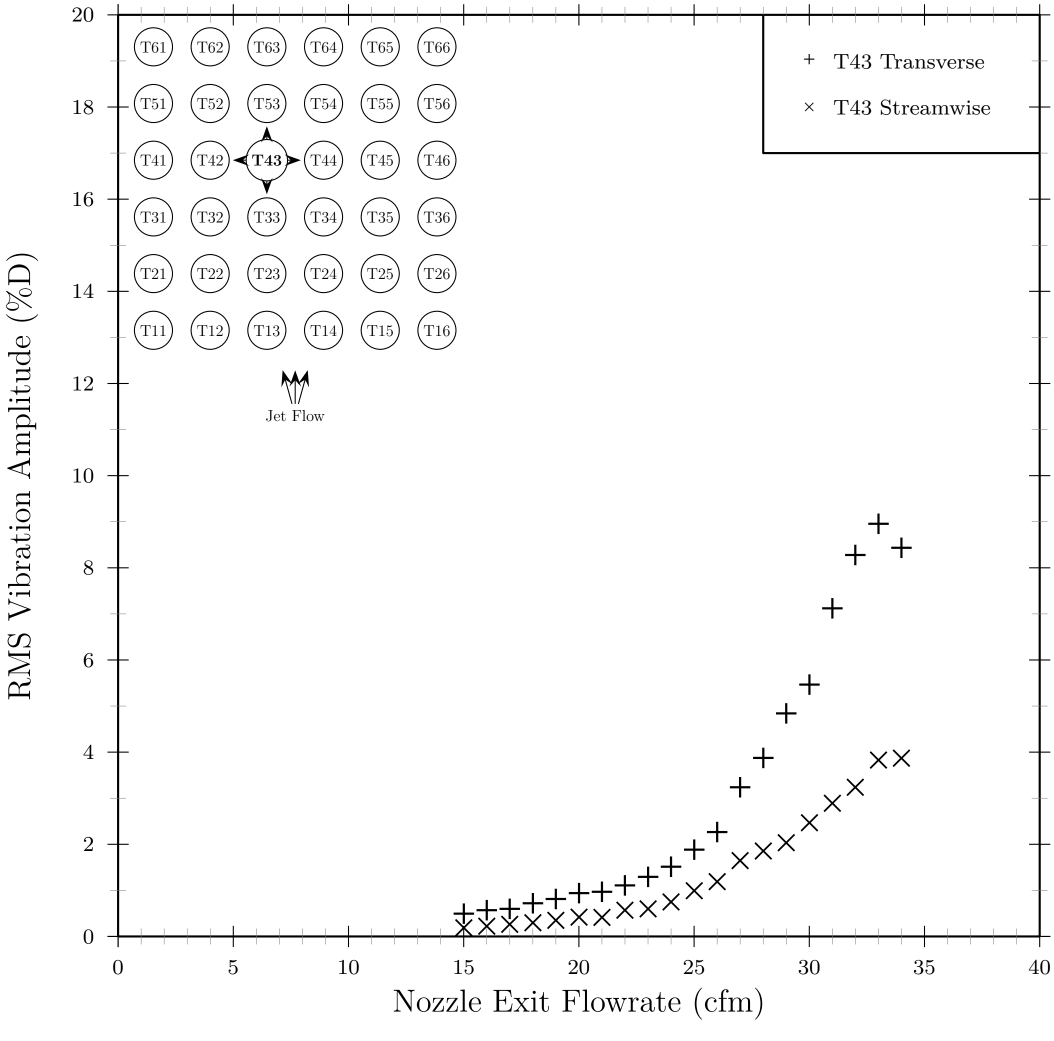

Figure 4.8: Amplitude response of T43, jet centred between T13 and T14.

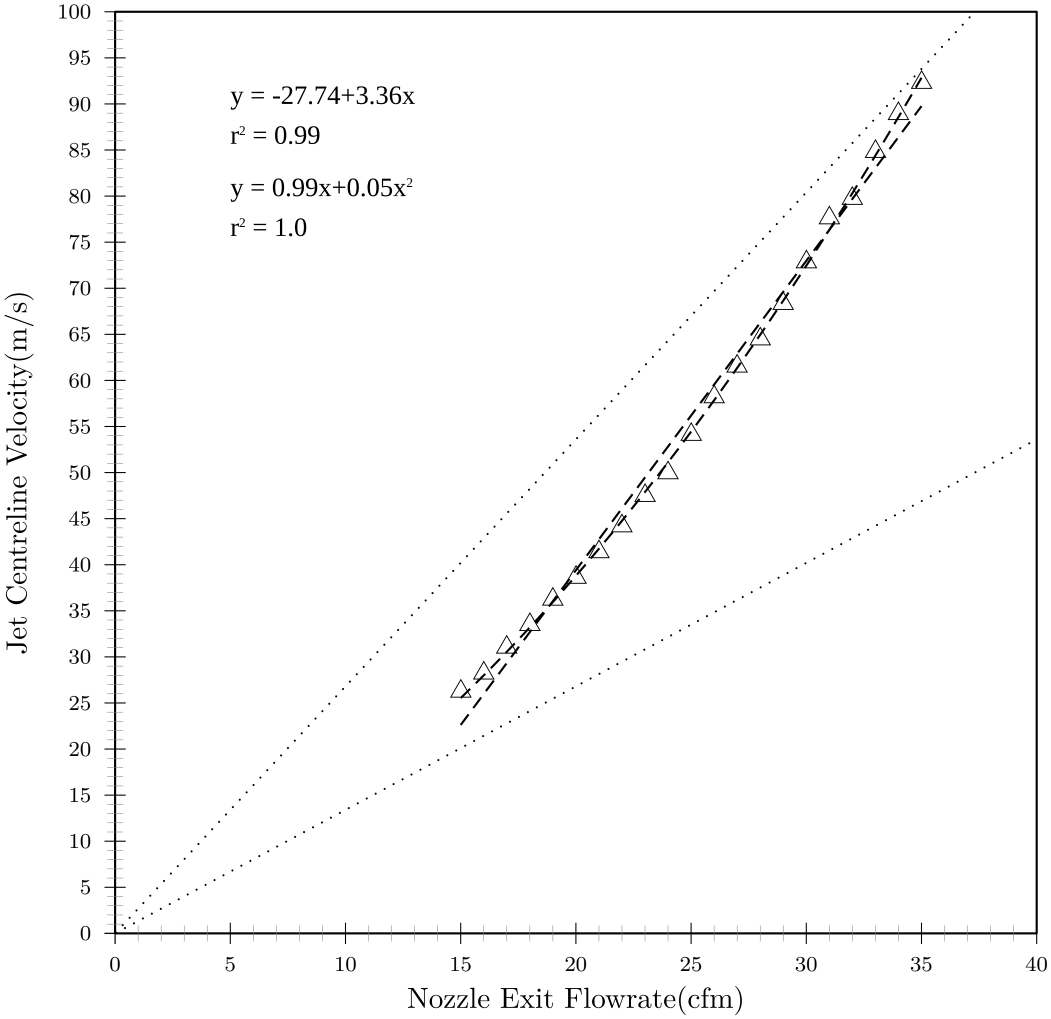

Figure 4.9: Jet centreline velocity at $z = 320\,\text{mm}$ versus nozzle flowrate for jet centred between tubes T13 and T14. The lower dotted line represents the expected centreline velocity of a free submerged axisymmetric turbulent jet as predicted using Equation (2.10). The upper dotted line represents Equation (2.10) multiplied by the gap confinement factor $P/(P-D) = 2.0$. Both straight line and quadratic least squares regression curves are shown using dashed lines. Over the measurement range the values are reasonably represented by the straight line fit. However, the quadratic fit better represents the trend in the data.

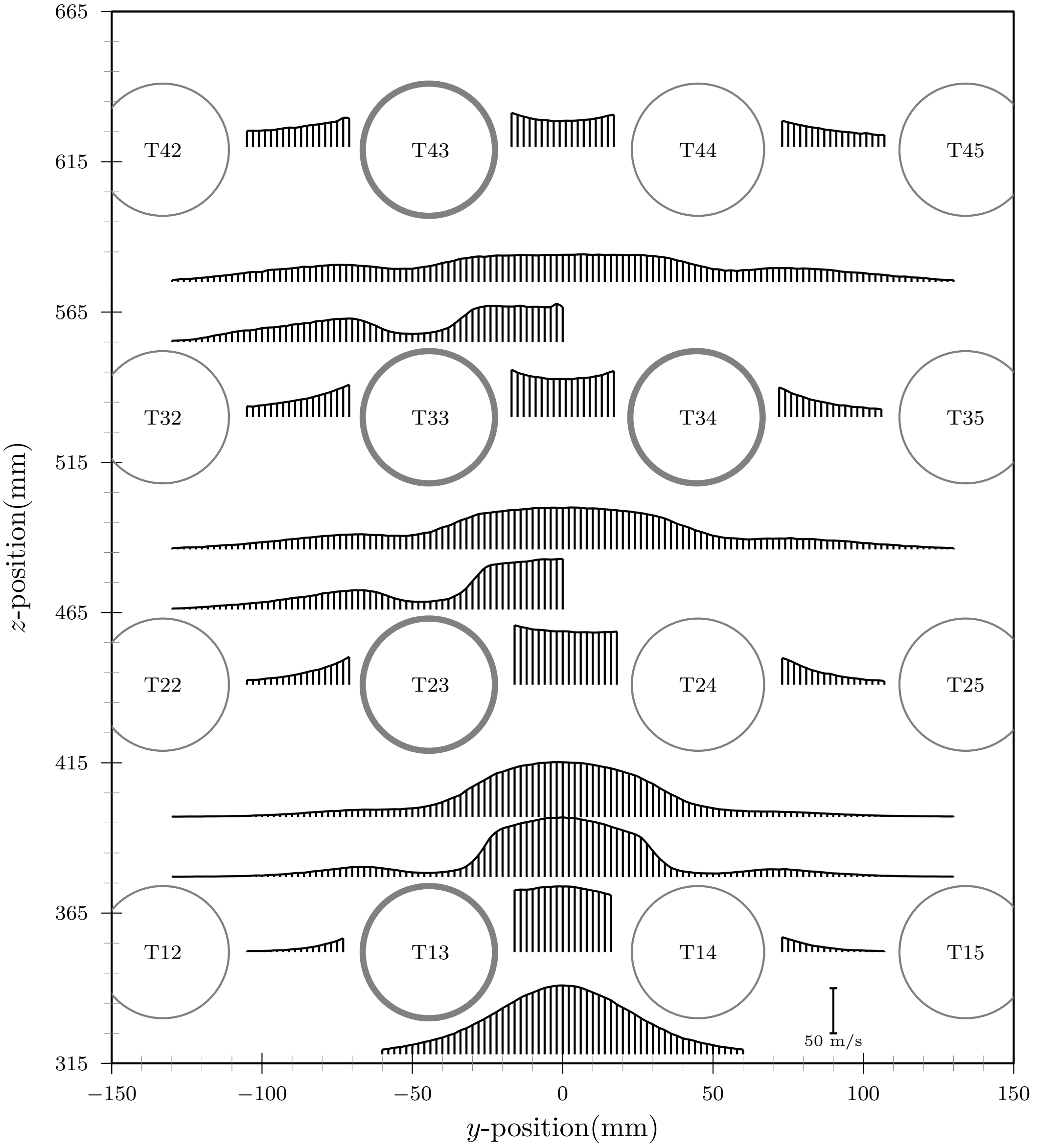

Figure 4.10: Velocity propagation through the tube array with jet centred between T13 and T14 as shown by horizontal velocity profiles. Measurements taken across horizontal axis (y-axis) at various streamwise positions (z-axis) with constant span-wise position (x-axis) centered on jet centerline.

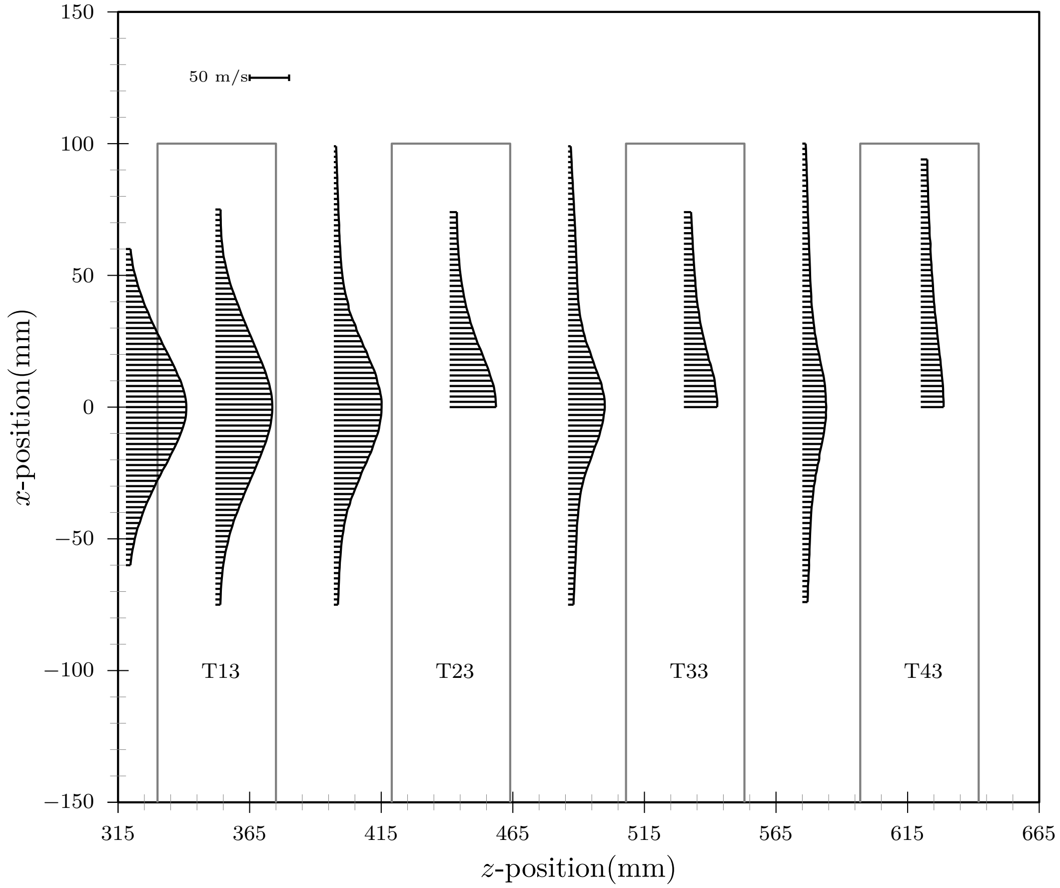

Figure 4.11: Velocity propagation through the tube array with jet centred between T13 and T14 as shown by vertical velocity profiles. Measurements taken across vertical axis (x-axis) at various streamwise positions (z-axis) with constant transverse position (y-axis) centered on jet centerline.

4.3 Jet Flow Centered on a Tube Face

This section describes the results of the vibration and velocity measurements where the jet flow was centred on the face of tube T13. Figure 4.12 shows a diagram of the experimental setup. To aid in subsequent descriptions and in the development of mathematical relationships several convenient coordinate systems have been defined in Figure 4.12. These are the global(g), jet(j), hybrid(h) and tube(t). Figure 4.12 is presented in terms of the global coordinate system.

4.3.1 Vibration Measurements

The results of the vibration measurements are presented in Figures 4.13 to 4.16 which depict the tube root mean square (rms) vibration amplitudes (scaled to percent of a tube diameter) versus nozzle flowrate (cfm) for T13, T23, T33 and T43 respectively. Figures 4.13, 4.15 and 4.16 show that while the turbulent buffeting amplitudes are much higher than seen with uniform flow, particularly in the transverse direction, T13, T33 and T43 remained stable at flow rates up to 40 cfm. Whereas Figure 4.14 shows that T23 experienced an increase in transverse vibration response slope, resulting in significant vibration amplitudes, which indicates that T23 became unstable. While the change in vibration response slope is not as abrupt, or well defined, as in the case of uniform flow, visual observation indicated a modulated response to large amplitudes in the transverse direction, the direction typically observed as critical for fluidelastic instability. The change in vibration response slope occurs at about 30 cfm, corresponding to a nozzle exit velocity of 257 m/s.

Although the vibration responses of the remainder of the tubes where not measured all tubes in the array were visually observed during the experiment. Tube T23 was the only tube in the array to become unstable during the experiment.

4.3.2 Velocity Measurements

The results of the velocity measurements are presented in Figures 4.17 to 4.19. For the velocity measurements the tube endpoints were locked to each other to "fix" the array and prevent significant tube movement. The array was fixed to allow measurement of the inter-tube velocity profiles under steady state conditions.

Figure 4.17 shows the measured velocity just in front of the tube array for different nozzle flow rates. In a free field the jet centreline velocity and the nozzle exit velocity can be related using Equation (2.10). However from Figure 4.17 this behavior is not observed, which is not entirely unexpected, since the tube array is an obstacle in the flow path and the measurements were taken in close proximity to the obstacle. It is worth noting that for uniform flow the upstream and gap flow velocities are related by the factor $P/(P-D)$ which for the configurations tested in this work is approximately 2.0. For the lowest flowrate tested (15 cfm) the observed centreline velocity was close to that predicted by Equation (2.10) and for the highest flowrate (35 cfm) the value was higher than expected. Figure 4.17 shows two dotted lines corresponding to Equation (2.10) and the product of $P/(P-D)$ and Equation (2.10). Both straight line and quadratic least squares regression curves are shown using dashed lines. Over the measurement range the values are reasonably represented by the straight line fit. However, the quadratic fit better represents the trend in the data.

Figures 4.18 and 4.19 show the detailed velocity measurements taken in the inter-tube spaces for a fixed flowrate of 32 cfm. The velocity data represented in Figures 4.18 and 4.19 is also presented in a series of detailed figures provided in Appendix C.

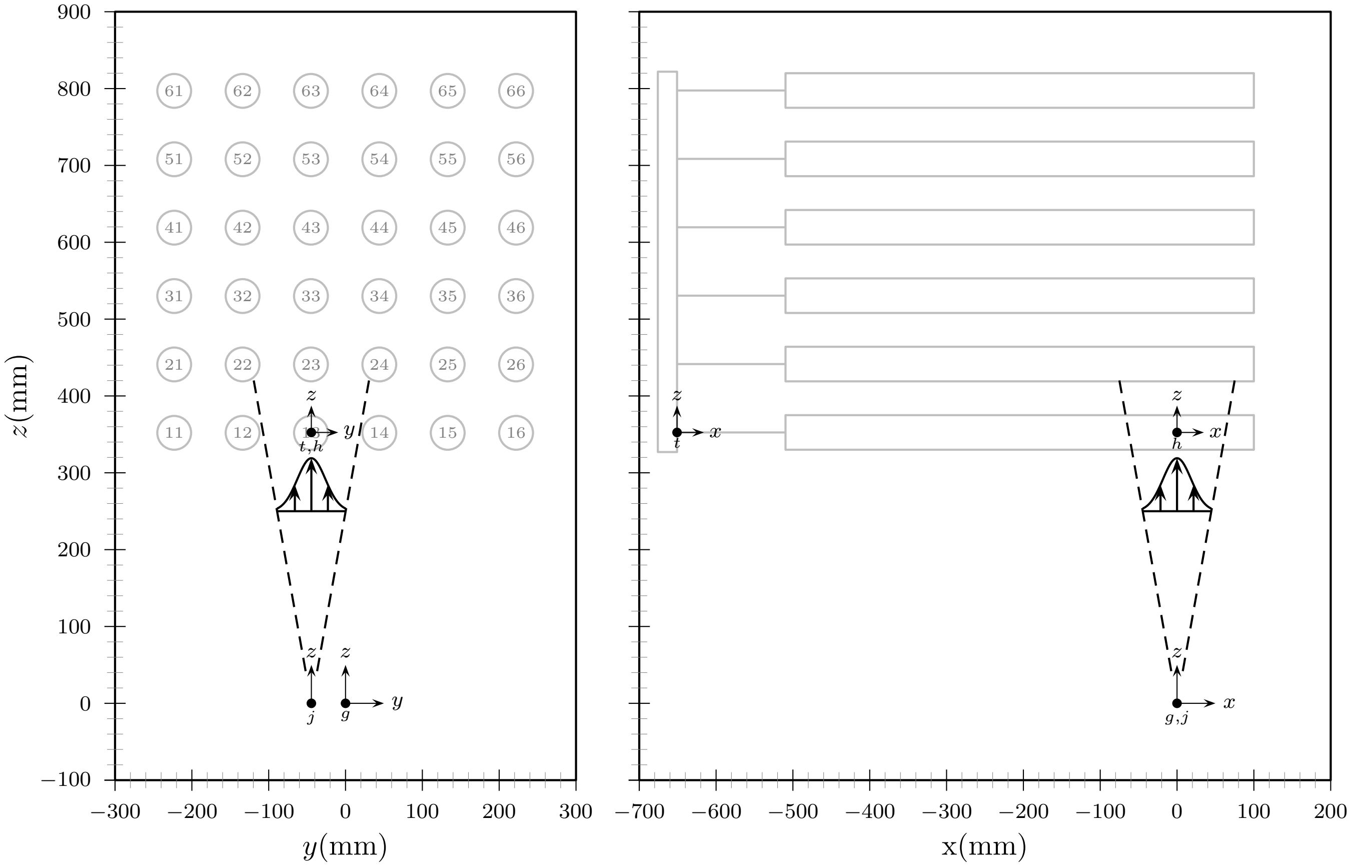

(a) Plan view.

(b) Side view.

Figure 4.12: Experimental setup: jet flow centred on the face of T13.

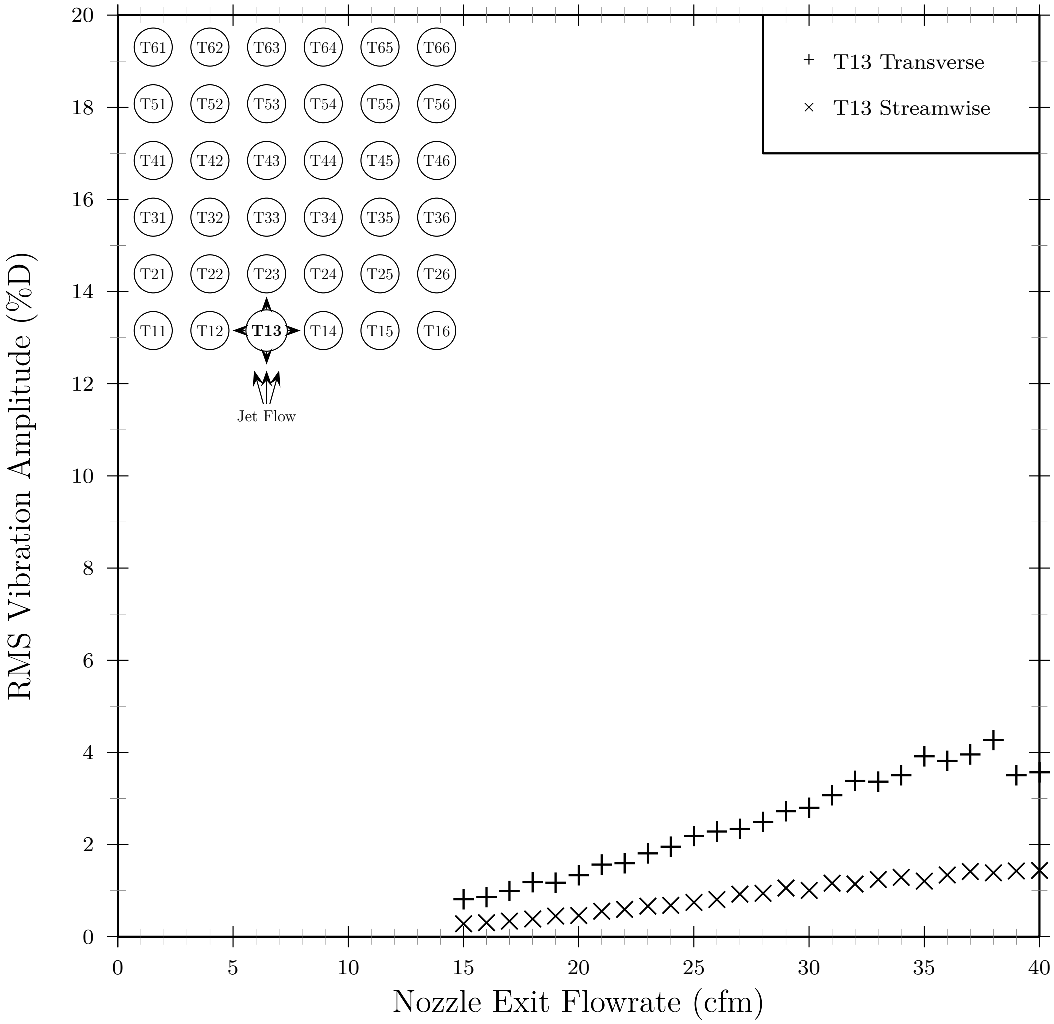

Figure 4.13: Amplitude response of T13, jet centred on face of T13.

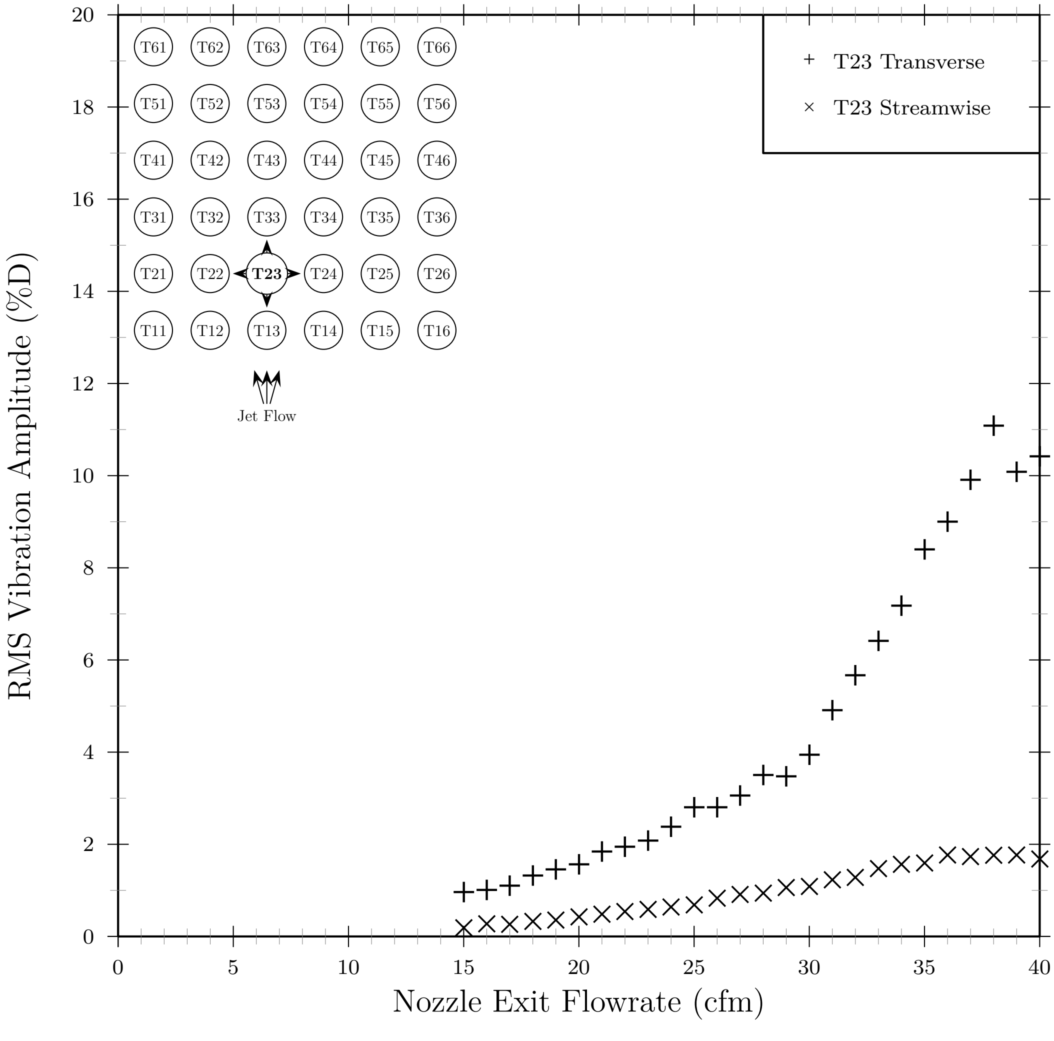

Figure 4.14: Amplitude response of T23, jet centred on face of T13.

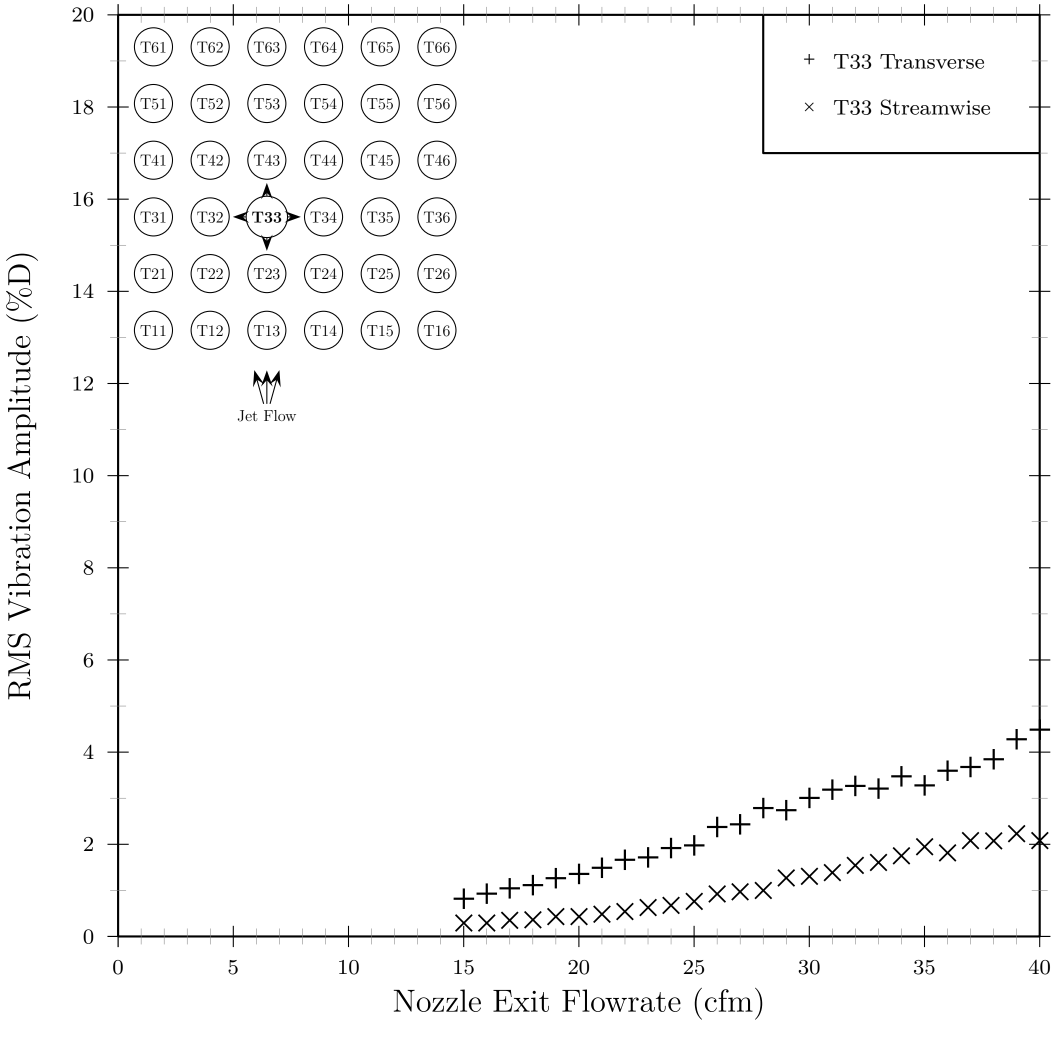

Figure 4.15: Amplitude response of T33, jet centred on face of T13.

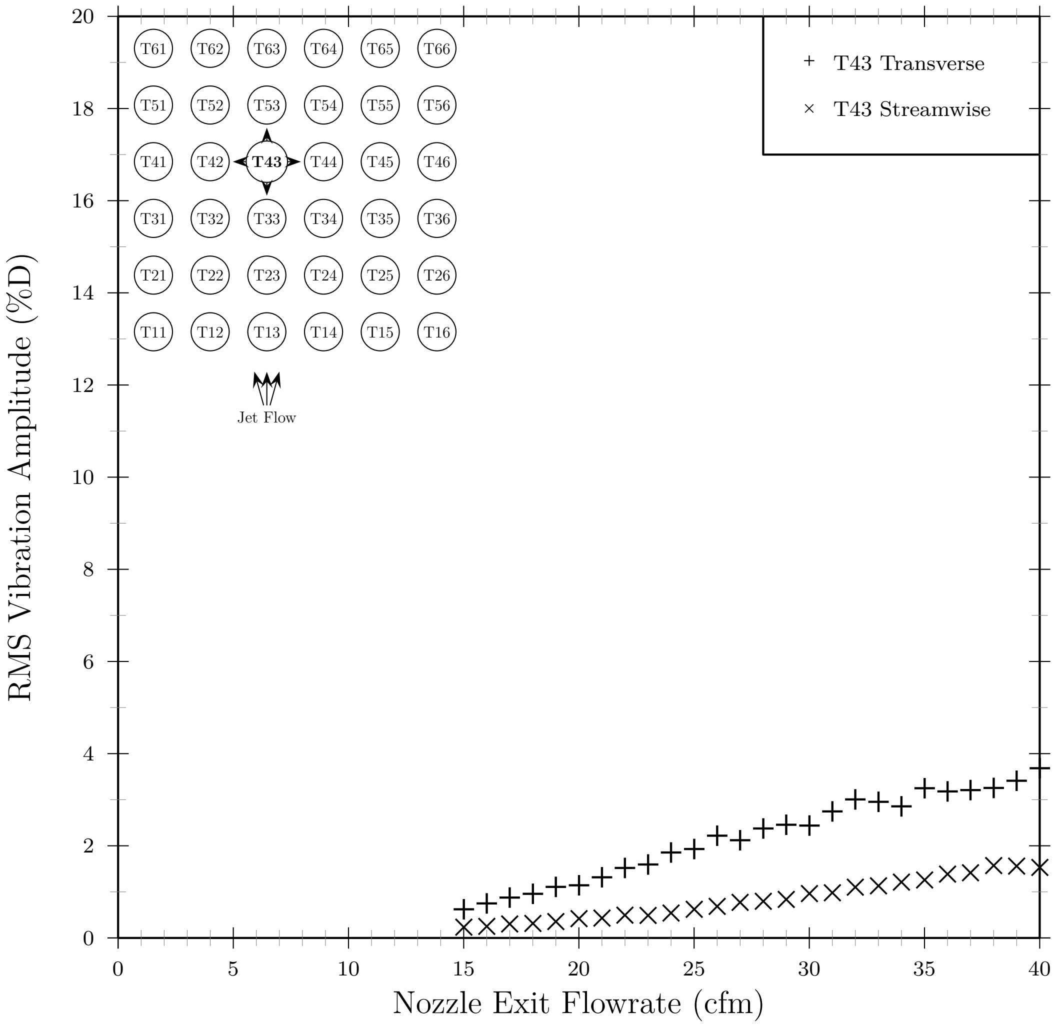

Figure 4.16: Amplitude response of T43, jet centred on face of T13.

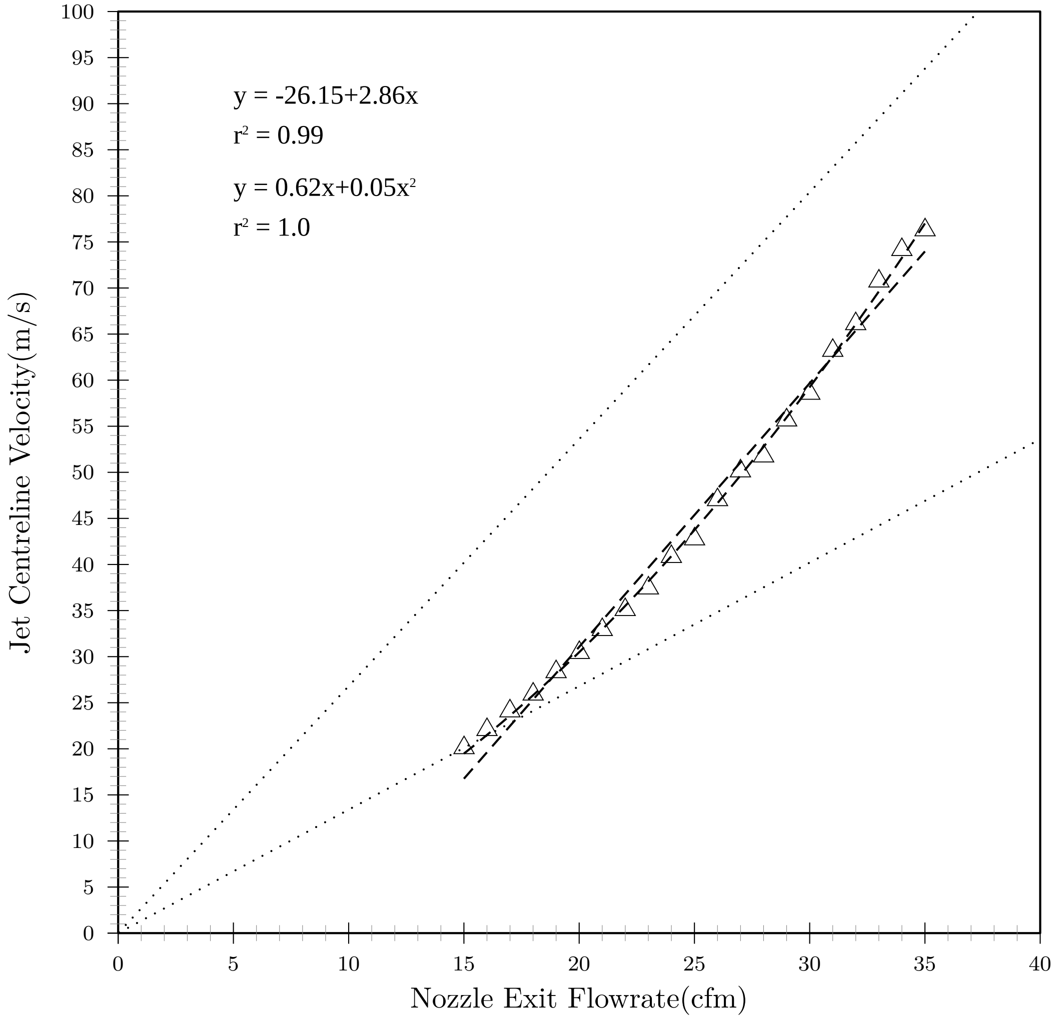

Figure 4.17: Jet centreline velocity at $z = 320\,\mathrm{mm}$ versus nozzle flowrate for jet centred on face of T13. The lower dotted line represents the expected centreline velocity of a free submerged axisymmetric turbulent jet as predicted using Equation (2.10). The upper dotted line represents Equation (2.10) multiplied by the gap confinement factor $P/(P-D) = 2.0$. Both straight line and quadratic least squares regression curves are shown using dashed lines. Over the measurement range the values are reasonably represented by the straight line fit. However, the quadratic fit better represents the trend in the data.

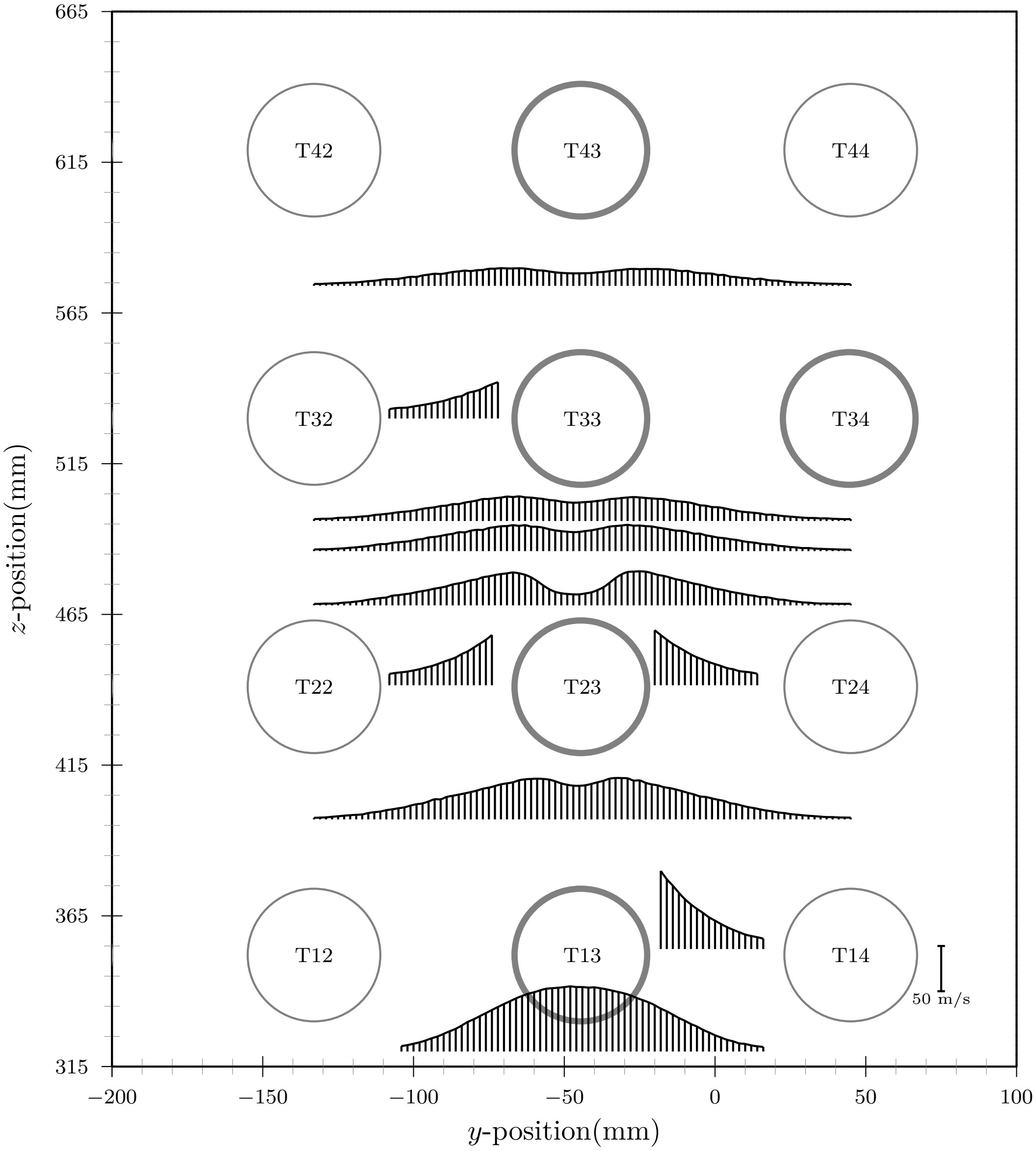

Figure 4.18: Velocity propagation through the tube array with jet centred on face of T13 as shown by horizontal velocity profiles. Measurements taken across horizontal axis (y-axis) at various streamwise positions (z-axis) with constant span-wise position (x-axis) centered on jet centerline.

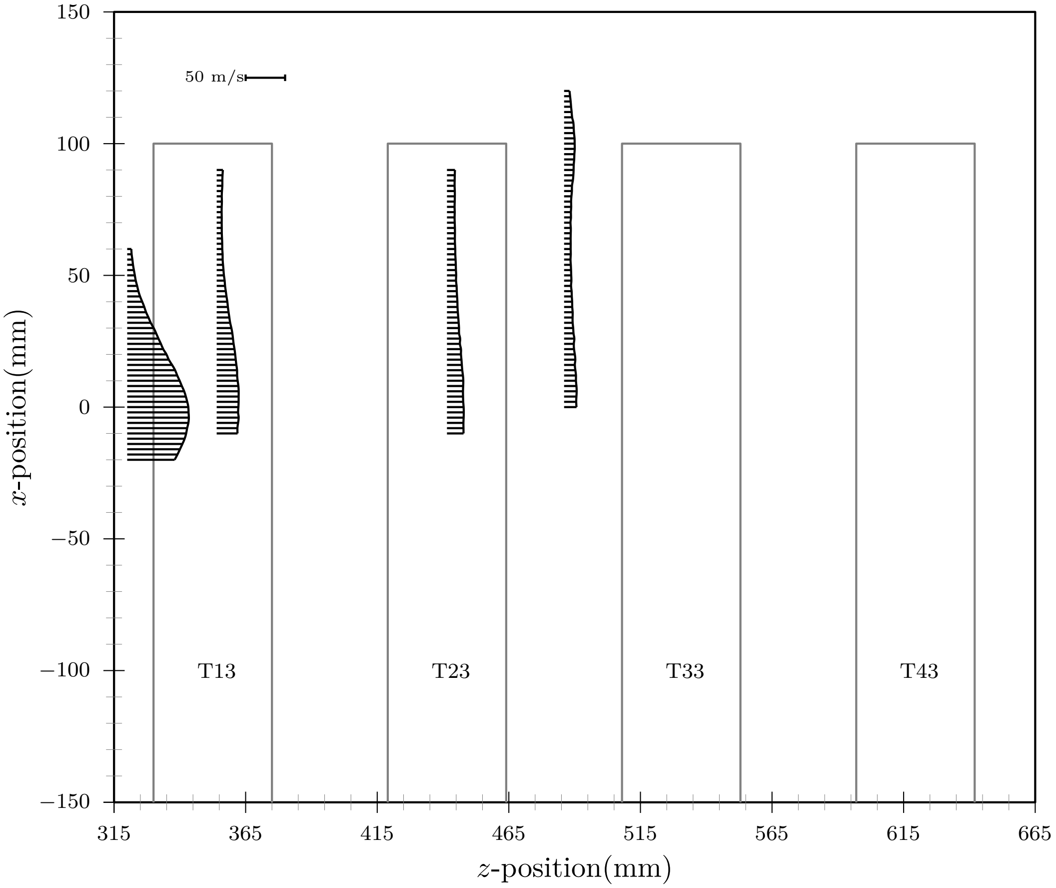

Figure 4.19: Velocity propagation through the tube array with jet centred on face of T13 as shown by vertical velocity profiles. Measurements taken across vertical axis (x-axis) at various streamwise positions (z-axis) with constant transverse position (y-axis) centered on jet centerline.

4.4 Summary

This section provides a brief summary of the vibration results, including the measured instability thresholds and observed spatial locations of instability, for the uniform and jet flow experiments.

The results of the uniform flow experiment indicated a critical uniform gap flow velocity of approximately 12 m/s. Fluidelastic instability was observed to occur for all tubes in the array at about the same time, and under the same flow conditions.

The results of the vibration measurements for jet flow between tubes indicated that the 3rd row tubes, T33 and T34, and 4th row tubes, T43 and T44, which were adjacent to the jet flow, became unstable at a nozzle exit flowrate of 26 cfm, corresponding to a nozzle exit velocity of 222 m/s. Referring to Figure 4.9 a nozzle exit flowrate of 26 cfm corresponds to a measured jet centerline velocity, $V(0, 0, 320\,\text{mm})$, of approximately 60 m/s.

The results of the vibration measurements for jet flow centred on a tube face indicated that the 2nd row tube, inline with the jet centreline, became unstable at a nozzle exit flowrate of 30 cfm, corresponding to a nozzle exit velocity of 257 m/s. Referring to Figure 4.17 a nozzle exit flowrate of 30 cfm corresponds to a measured jet centerline velocity, $V(0, 0, 320\,\text{mm})$, of approximately 64 m/s.

5. Discussion

The purpose of this research was to develop a partial admission formulation which can account for velocity variations in both the spanwise and transverse directions. Equations (2.6) and (2.7) address cases where the fluid velocity varies in the spanwise, x, direction only. However, a submerged axisymmetric jet has a velocity profile which varies in both the spanwise and transverse directions, x and y respectively. Throughout the next few sections the experimental results will be discussed in detail to establish if transverse velocity variations can be incorporated into the partial admission calculation. Note that Equations (2.6) and (2.7), below, are both expressed in terms of the tube coordinate system ($x = x_t$).

$$V_{eq} = \left(\frac{\int_0^L V^2(x)\hat{Y}^2(x)dx}{\int_0^L \hat{Y}^2(x)dx} \right)^{0.5} \tag{2.6 revisited}$$

$$V_{eq} = \left(\frac{\int_0^L V^2(x)\hat{Y}^2(x)dx}{\int_0^L \hat{Y}^2(x)dx} \right)^{\alpha} \tag{2.7 revisited}$$

5.1 Uniform Flow

The uniform cross-flow results presented in Section 4.1 show that the critical gap flow velocity at the onset of fluidelastic instability was approximately 12 m/s. The tube vibrations were observed to occur at the first mode natural frequency of 9 Hz. Using the models' physical parameters as described in Chapter 3, the critical reduced velocity, $V_{cr}/(f_n D)$, mass damping parameter, $m(2\pi\zeta)/(\rho D^2)$, and the corresponding Connors' constant, K, were thus 30.0, 27.9 and 5.7, respectively. The Connor's constant ($K \approx 5.7$) was calculated using Equation (2.5).

$$\frac{V_{cr}}{f_n D} = K\left(\frac{m\,(2\pi\zeta)}{\rho D^2}\right)^{0.5} \qquad \text{(2.5 revisited)}$$

$$\frac{V_{cr}}{f_n D} = \frac{12\,\mathrm{m/s}}{(9\,\mathrm{Hz})(0.044\,45\,\mathrm{m})} \approx 30.0$$

$$\frac{m\,(2\pi\zeta)}{\rho D^2} = \frac{(1.004\,\mathrm{kg/m})(2\pi 0.0105)}{(1.2\,\mathrm{kg/m^3})(0.044\,45\,\mathrm{m})^2} \approx 27.9$$

$$K \approx \frac{30.0}{\sqrt{27.9}} = 5.7$$

As discussed in Section 2.2, the Boiler & Pressure Vessel Code ASME (2009) suggests a design Connors' constant which represents the suggested lower bound on the available experimental data. Figure 2.2, which is plotted in log-log format, shows the suggested lower bound ($K = 2.4$) and the mean value ($K = 4.0$). Examination of the figure shows that there is a great deal of scatter in the available experimental data even when plotted in log-log format.

Note that although Weaver and Fitzpatrick (1988) found that Equation (2.8) agrees better with the available experimental data than Equation (2.5), as discussed in Chapter 2, both Feenstra et al. (2003, 2004) and the Boiler & Pressure Vessel Code ASME (2009) use and reference Equation (2.5). Therefore, this discussion also utilizes Equation (2.5) to allow direct comparison with Feenstra et al. (2003, 2004) and the Boiler & Pressure Vessel Code ASME (2009). Since the array geometry for the current research has a square tube layout, from Table 2.1, the expected impact of using Equation (2.5) versus Equation (2.8) is minimal.

5.2 Jet Flow

Section 4.2 presents the results of the vibration and velocity measurements for the case where the axisymmetric jet flow was centred between T13 and T14. Section 4.3 presents similar results with the jet centred on the face of T13. This section presents a discussion of these results and compares the jet flow results to the uniform flow results by scaling the measured velocity profiles from Sections 4.2 and 4.3 and using these within a modified partial admission formulation.

Equation (2.11) describes the expected velocity profile of a submerged axisymmetric turbulent jet in terms of the coordinates r_j and z_j. Equation (2.11) can also be expressed in terms of the rectilinear coordinates x_j, y_j and z_j as shown below. The resulting velocity profile can be expressed by Equation (5.1), subscripts omitted for clarity, which is comprised of the velocity at the coordinate $(0, 0, z)$, the jet centreline, multiplied by two normalized Gaussian functions.

$$\begin{aligned}
V(r,z) &= V(0,z)e^{-B(r/z)^2} = V(0,z)e^{-94(r/z)^2} && \text{(2.11 revisited)}\\
r^2 &= x^2 + y^2\\
V(x,y,z) &= V(0,0,z)e^{\frac{-B(x^2+y^2)}{z^2}}\\
&= V(0,0,z)e^{\frac{-C(x^2)}{z^2}}e^{\frac{-D(y^2)}{z^2}}\\
&= V(0,0,z)\hat{V}_1(x,0,z)\hat{V}_2(0,y,z) && (5.1)
\end{aligned}$$

Equation (5.1) shows that the velocity profile of an axisymmetric jet at a fixed position z can be described by a relatively simple set of measurements. It is important to note that the constant B in Equations (2.11) and (5.1) was presented in Blevins (1984) as a value determined from experimentation. Therefore, the value of B may vary depending on the specific conditions of the experiment. For example Appel et al. (1959) presents a velocity profile with a slightly different form which is equivalent to setting B to equal to 77 rather than 94 as represented by Blevins (1984).

To experimentally determine the constant B in Equation (2.11) would require a series of velocity measurements at a fixed position z. These measurements would start at $r = 0$ and continue until some practical limit value of r was reached. This set of measurements would establish the shape of one half of the velocity profile. However, since the profile is axisymmetric this represents all the required information. Equation (5.1) is somewhat more complicated if we abandon the basic assumption that the constants C and D should equal B. This allows for the possibility that minor variations may occur in the profile shape along each rectilinear axis. To establish the values of C and D and thus the shape of the velocity profile experimentally at a fixed position z, a series of velocity measurements would be required. The first set of measurements would be made in the x-direction along the y-centreline, these would be divided by the centreline velocity to determine $\hat{V}_1(x, 0, z)$. The same procedure would then be completed in the y-direction along the x-centreline to determine $\hat{V}_2(0, y, z)$. These two profiles, when multiplied, would represent an approximation of the normalized three dimensional velocity profile of the jet at the z-axis location of the measurements. Figures 5.1 and 5.2 show the normalized horizontal and vertical entry velocity profiles measured for various nozzle flowrates. These profiles appear similar to each other once normalized, for comparison the non-normalized data is provided in Appendix C. The profiles also compare favorably to the the theoretical curve represented by Equation (2.11).

The velocity measurements presented in Sections 4.2.2 and 4.3.2 show that once the jet enters the tube array the spanwise (x-axis) velocity profiles between tubes (within the gap space) maintain the characteristic Gaussian shape. However, the transverse (y-axis) velocity profiles within the gap spaces do not retain the Gaussian shape. Assume that for each gap space we can use the measured spanwise velocity profile to construct a normalized profile $\hat{V}(x, P/2, 0)_h$. Let us assume that the transverse velocity variations within the gap spaces at a given spanwise position x can be characterized by the mean value at the jet centerline $\bar{V}(0, 0, 0)_h$ multiplied by $\hat{V}(x, P/2, 0)_h$. The resulting mean velocity function, $\bar{V}(x, 0, 0)_h$, could then be used in Equation (2.6) to calculate partial admission. Figure 5.3 shows the measured transverse velocity profiles for T13. The average transverse gap velocity for T13 at $x = 0$ is calculated by integrating the measured velocity over the inter-tube gaps and dividing by the gap width as shown by Equation (5.2).

$$\begin{aligned}\bar{V}(0,0,0)_{h13} &= \frac{1}{2}\left(\frac{\displaystyle\int_{-D/2}^{-P+D/2} V(0,y,0)_{h13}dy}{(P-D)}\right)\\ &+ \frac{1}{2}\left(\frac{\displaystyle\int_{P-D/2}^{D/2} V(0,y,0)_{h13}dy}{(P-D)}\right)\\ &= \frac{1}{2}\left(\bar{V}_{Left} + \bar{V}_{Right}\right)\end{aligned} \tag{5.2}$$

$$\begin{aligned}\bar{V}(x,0,0)_{h13} = \bar{V}(x)_{h13} &\approx \bar{V}(0,0,0)_{h13}\left(\frac{V(x,P/2,0)_{h13}}{V(0,P/2,0)_{h13}}\right)\\ &\approx \bar{V}(0,0,0)_{h13}\left(\frac{V(x,-P/2,0)_{h13}}{V(0,-P/2,0)_{h13}}\right)\end{aligned} \tag{5.3}$$

Equation (5.3) represents the average velocity function corresponding to the measured velocity field. Figure 5.3 shows the measured velocity profiles in the horizontal plane, around T13, for both jet configurations. For each jet configuration the resulting velocity field was measured with a fixed jet flowrate.

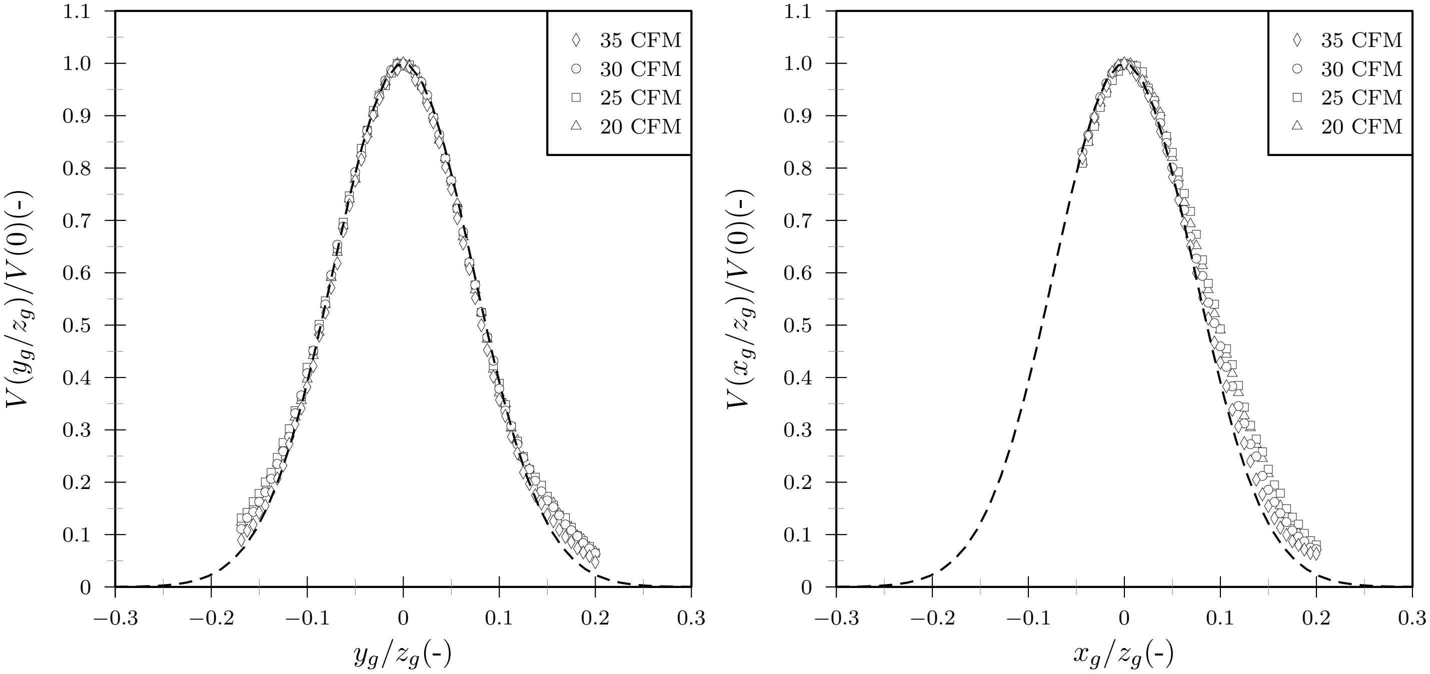

(a) Horizontal Profile.

(b) Vertical Profile.

Figure 5.1: Normalized velocity profiles at z_g=320mm, for jet centred between tube T13 and T14. The dashed lines in (a) and (b) represent Equation (2.11).

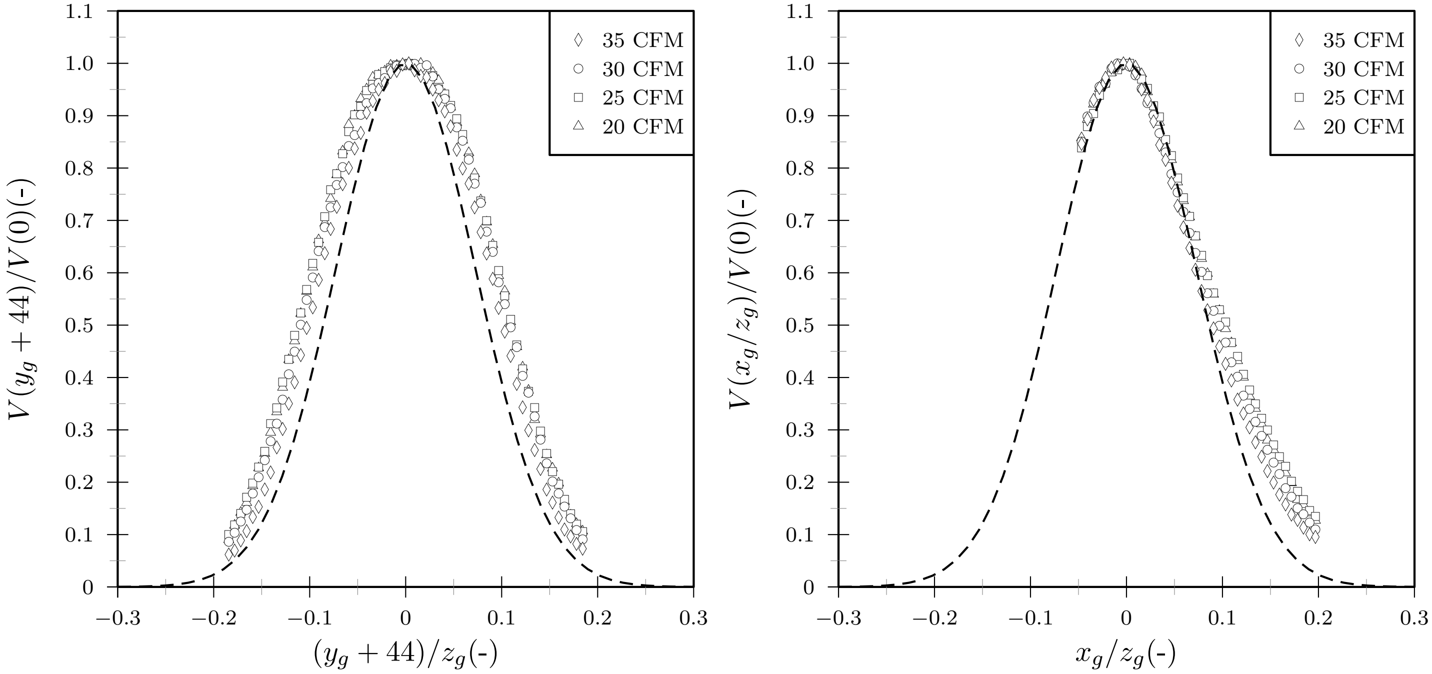

(a) Horizontal Profile.

(b) Vertical Profile.

Figure 5.2: Normalized velocity profiles at z_g=320mm, for jet centred on face of tube T13. The dashed lines in (a) and (b) represent Equation (2.11).

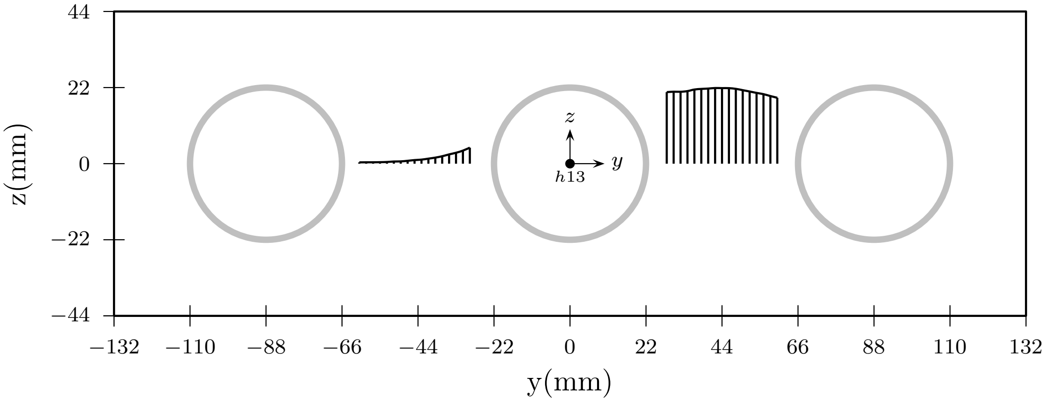

(a) Jet flow centred between tubes.

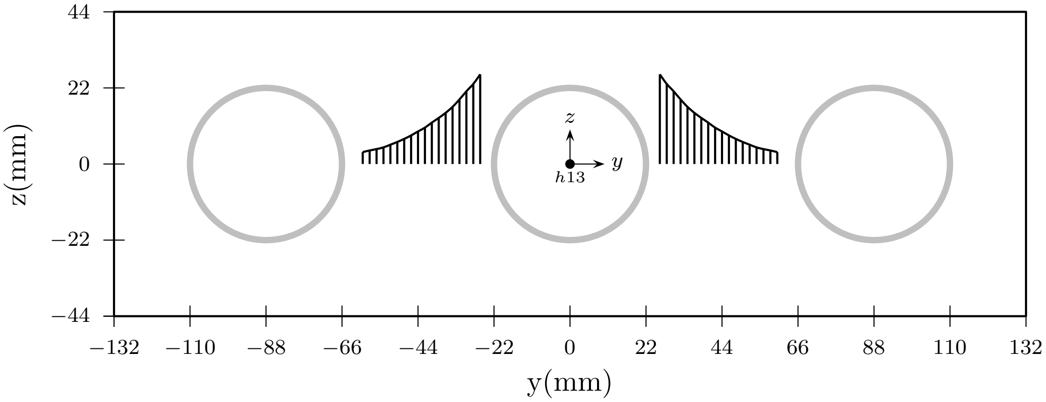

(b) Jet flow centred on a tube face.

Figure 5.3: Illustration of measured velocity profiles on the left and right sides of T13.

Assume that the measured velocity field, V_m, is scalable to estimate/predict the resultant velocity field, V_p, for higher or lower flowrates.

$$\bar{V}_p(x,0,0)_h \approx \bar{V}_m(0,0,0)_h \left(\frac{V_m(x,P/2,0)_h}{V_m(0,P/2,0)_h}\right)\left(\frac{V_p(0,0,320)_j}{V_m(0,0,320)_j}\right) \tag{5.4}$$

$$\hat{V}_m(x,P/2,0)_h = \left(\frac{V_m(x,P/2,0)_h}{V_m(0,P/2,0)_h}\right) \tag{5.5}$$

$$\bar{V}_p(x,0,0)_h = \bar{V}_p(x)_h \approx \bar{V}_m(0,0,0)_h \hat{V}_m(x,P/2,0)_h \left(\frac{V_p(0,0,320)_j}{V_m(0,0,320)_j}\right) \tag{5.6}$$

Equation (5.6) is scaled using the velocity at the centreline of the jet immediately in front of the tube array, $V(0,0,320)_j$. Figures 4.9 and 4.17 each show measurements of the centreline velocity, $V(0,0,320)_j$, versus nozzle flowrate, Q. In a free field the jet centreline velocity and the nozzle outlet velocity can be related using Equation (2.10). The results presented in Figures 4.9 and 4.17 do not reflect agreement with Equation (2.10) and do not agree with each other. Although Figures 4.9 and 4.17 represent non-linear relationships these non-linearities are "weak" and the relationships can be approximated using linear functions over the range of measured values (15-35 cfm).

$$\frac{V_p(0,0,320)_j}{V_m(0,0,320)_j} \approx \frac{a_0 + a_1 Q_p}{a_0 + a_1 Q_m} \tag{5.7}$$

$$\bar{V}_p(x,0,0)_h = \bar{V}_p(x_h) \approx \bar{V}_m(0,0,0)_h \hat{V}_m(x,P/2,0)_h \left(\frac{a_0 + a_1 Q_p}{a_0 + a_1 Q_m}\right) \tag{5.8}$$

Using Equation (5.8) and Table 5.1, Equation (2.6) can be used to express V_{eq} in terms of the velocity measurements presented in Sections 4.2.2 and 4.3.2. After substituting Equation (5.8) into Equation (2.6) the resulting expression can be rearranged to determine the predicted nozzle flowrate, Q_p, for the given equivalent uniform gap velocity, V_{eq}. If the critical uniform gap flow velocity, V_{cr}, is substituted for the equivalent uniform gap flow velocity, V_{eq}, the critical nozzle flowrate, $Q_{p,cr}$, at the onset of fluidelastic instability will be predicted. By comparing the critical nozzle flowrate, $Q_{p,cr}$, predicted by Equation (5.9) and the actual critical nozzle flowrate, $Q_{m,cr}$, measured during the jet flow vibration measurements the validity of the preceding formulation and assumptions can be assessed.

$$V_{eq}^2 = \left(\frac{\displaystyle\int_0^L \bar{V}_p^2(x_h)\hat{Y}^2(x_t)dx_t}{\displaystyle\int_0^L \hat{Y}^2(x_t)dx_t} \right)$$

$$x_h = x_t - 651$$

$$V_{eq}^2 = \left(\frac{\displaystyle\int_0^L \bar{V}_p^2(x_t - 651)\hat{Y}^2(x_t)dx_t}{\displaystyle\int_0^L \hat{Y}^2(x_t)dx_t} \right)$$

$$V_{eq}^2 = \left(\bar{V}_m(0,0,0)_h \frac{a_0 + a_1 Q_p}{a_0 + a_1 Q_m} \right)^2 \left(\frac{\displaystyle\int_0^L \hat{V}_m^2(x_t - 651, P/2, 0)\hat{Y}^2(x_t)dx_t}{\displaystyle\int_0^L \hat{Y}^2(x_t)dx_t} \right)$$

$$Q_p = \left(\frac{1}{a_1}\right) \left(\frac{(a_0 + a_1 Q_m)^2 V_{eq}^2 \displaystyle\int_0^L \hat{Y}^2(x_t)dx_t}{\bar{V}_m^2(0,0,0)_h \displaystyle\int_0^L \hat{V}_m^2(x_t - 651, P/2, 0)\hat{Y}^2(x_t)dx_t} \right)^{1/2} + \frac{a_0}{a_1} \quad (5.9)$$

Experiment	a_0	a_1	Reference
Jet Between Tubes	-27.74	3.36	Figure 4.9
Jet On Tube Face	-26.15	2.86	Figure 4.17

Table 5.1: Linear regression coefficients for Equations (5.7) and (5.9).

Table 5.2 shows the calculated values of $\bar{V}_m(0)_{Left}$,$\bar{V}_m(0)_{Right}$,$\bar{V}_m(0)$ and $Q_{p,cr}$ as well as the measured value $Q_{m,cr}$ for each tube T13, T23, T33 and T43, for the jet flow experiment where the jet was centred between T13 and T14. The velocity measurements presented in Figures 4.10 and 4.11 were made with a constant nozzle exit flow rate of 30 cfm. Therefore the values of $\bar{V}_m(0)_{Left}$, $\bar{V}_m(0)_{Right}$ and $\bar{V}_m(0)$ reflect this flow condition. The final two columns of Table 5.2 provide a comparison of the predicted critical nozzle flowrates, $Q_{p,cr}$, versus the measured critical nozzle flowrates, $Q_{m,cr}$. The comparison shows reasonable agreement between the predicted and measured critical flowrates, $Q_{m,cr}$, for the 3rd and 4th row tubes. The predicted values indicate that fluidelastic instability of the 1st and 2nd row tubes should occur before the 3rd and 4th tube rows (for lower flowrates). However, this behavior was not observed and instead the 1st and 2nd row tubes remained stable for flowrates as high as 35 cfm. It is unclear why the 1st and 2nd row tubes did not experience fluidelastic instability. However, there are some physical differences of note between the 1st/2nd and the 3rd/4th row tubes. The flow distributions on either side of T13 and T23, 1st and 2nd row respectively, are highly uneven with the majority of the flow on the right side. Whereas the flow patterns around T33 and T43 are much more evenly distributed. The 3rd and 4th row tubes would also experience a higher degree of fluid coupling with neighboring tubes since they are deeper within the tube array.

Tube	$\bar{V}_m(0)_{Left}$ (m/s)	$\bar{V}_m(0)_{Right}$ (m/s)	$\bar{V}_m(0)$ (m/s)	$Q_{p,cr}$ (cfm)	$Q_{m,cr}$ (cfm)
T13	4.98	69.95	37.47	25.74	-
T23	14.21	59.79	37.00	26.53	-
T33	20.66	45.29	32.97	27.75	26
T43	23.06	31.27	27.17	27.99	26

Table 5.2: Tube instability predictions using measured velocity profiles for jet centred between T13 and T14.

Table 5.3 shows the calculated values of $\bar{V}_m(0)_{Left}$,$\bar{V}_m(0)_{Right}$,$\bar{V}_m(0)$ and $Q_{p,cr}$ as well as the measured value $Q_{m,cr}$ for each tube T13, T23, T33 and T43, for the jet flow experiment where the jet was centred on the face of T13. The velocity measurements presented in Figures 4.18 and 4.19 were made with a constant nozzle exit flow rate of 32 cfm. Therefore the values of $\bar{V}_m(0)_{Left}$, $\bar{V}_m(0)_{Right}$ and $\bar{V}_m(0)$ reflect this flow condition. The final two columns of Table 5.3 provide a comparison of the predicted critical nozzle flowrates, $Q_{p,cr}$, versus the measured critical nozzle flowrates, $Q_{m,cr}$. The comparison shows fair agreement between the predicted and measured critical flowrates, Q_{cr}, for the 2nd row tube. The predicted values indicate that instability should occur in the 1st row before the 2nd row. However, this behavior was not observed and instead the 1st, 3rd and 4th row tubes remained stable for nozzle flowrates as high as 40 cfm. It is unclear why the 1st and 3rd tube rows did not experience fluid elastic instability. This is particularly true since, from Figure 4.18, the distribution of flow around each of the 1st, 2nd and 3rd row tubes was nearly identical in shape if not magnitude.

Tube	$\bar{V}_m(0)_{Left}$ (m/s)	$\bar{V}_m(0)_{Right}$ (m/s)	$\bar{V}_m(0)$ (m/s)	$Q_{p,cr}$ (cfm)	$Q_{m,cr}$ (cfm)
T13	37.73	37.73	37.73	25.49	-
T23	29.81	29.81	29.81	26.99	30
T33	21.73	21.73	21.73	29.26	-
T43	-	-	-	-	-

Table 5.3: Tube instability predictions using measured velocity profiles for jet centred on the face of T13.

The measured tube vibrations and fluid velocities from Section 4.2 and Section 4.3 have been related to each other using the partial admission theory. The assumption has been made that the spanwise function of transverse average velocity $\bar{V}(x)$ can be used in Equation (2.6) to predict the equivalent uniform flow velocity (V_{eq}). The comparison of predicted and measured instability thresholds indicated reasonable agreement between the predictions and measurements where instability was actually observed. Unfortunately the predictions also indicated instability in spatial locations where the phenomenon was not observed during measurements. Although the theory fails to predict the spatial location of the instability, the predicted stability threshold for the first row was lower than the observed value in both cases. This suggests that the prediction method is conservative. However, to utilize the prediction method detailed velocity measurements were required to calculate average gap velocities and establish normalized spanwise velocity functions. These velocity parameters would change based on tube pitch, tube diameter, tube pattern, jet offset from first tube row and possibly other parameters such as the degree of confinement, etc. For the model presented here to be generally applicable, extensive studies would have to be completed to determine the velocity parameter dependence on these scaling parameters. If the model accurately predicted the spatial location of localized tube instabilities then the development of such a generally applicable model would be a worthwhile undertaking. However, since that is not the case the results of this section serve to verify that $\bar{V}(x)$ can be used in Equation (2.6) if we neglect the fact that instability may not occur in every location predicted, but that it is likely to occur somewhere.

The fundamental starting assumptions of the current research, and that of Feenstra et al. (2003, 2004), were that Connors' equation for stability threshold, Equation (2.5), and equivalent velocity under partial admission, Equation (2.6), accurately describe the underlying physics of fluidelastic instability. The work presented by Weaver and Fitzpatrick (1988), as well as the current research, suggest that fluidelastic instability may involve more complex interactions which are not fully captured by Connors' equations.

Feenstra et al. (2003, 2004) described the failure of a heat exchanger due to axisymmetric jet flow centred between tubes as the motivation for conducting a model study of the phenomenon. The failure in the actual boiler occurred in a 2nd row tube, there was no failure of 1st row tubes, though the model study indicated fluidelastic instability in the 1st, 2nd and 3rd tube rows. This coupled with the results of the current research where, for the comparable scenario with the jet centred between tubes, fluidelastic instability was observed in the 3rd and 4th tube rows but not in the 1st or 2nd tube rows. The disparity in the spatial location of the instability between all three examples suggests that velocity on one side of a tube may not be sufficient to produce fluidelastic instability and other factors may be important. Factors such as the need for coupling with adjacent tubes or for sufficient velocity on both sides of a tube which would require that sufficient jet diffusion has taken place to involve both a tube and its neighbours.

5.3 Summary

The physical model parameters and the fluidelastic instability data are provided in Table 5.4 and Table 5.5, respectively, for the current research and the work of Feenstra et al. (2003, 2004). The model tube arrays are geometrically similar since both the transverse and streamwise pitch ratios, P_t/D and P_s/D respectively, are within ±10 %. Additionally, the gap confinement factor $P_t/(P_t - D)$ was also within ±12.5 %. The geometric scaling of the jet is characterized by the ratios Z_j/R_0, Z_j/P_t and X_j/L which were within ±16 %, ±17 % and ±7 %, respectively.

The model tube array utilized by Feenstra et al. (2003, 2004) had a mass damping parameter of approximately 14.4 whereas the model used for the current research had a mass damping parameter of 27.9. The higher mass damping parameter is due to the material choice for the model tubes, aluminum vs acrylic, and the higher associated lineal modal mass of 1.004 kg/m (aluminum tubes) versus 0.161 kg/m (acrylic tubes). Similarity could have been achieved by reducing the damping ratio, ζ, or increasing the tube diameter, D. However, a slightly higher mass damping parameter was desired to ensure that the uniform upstream flow velocities in the wind tunnel could be measured accurately with a pitot static tube. Using the lower bound Connors' constant ($K = 2.4$) from Figure 2.2 the expected critical uniform gap flow velocity is approximately 5 m/s which corresponds to an upstream velocity of 2.5 m/s. The estimated relative velocity error at 2.5 m/s is ±10 %, the relative velocity error increases further with decreasing velocity. Although, the mass damping parameters were not strictly similar, when viewed on the log-log scale of Figure 2.2 the difference between 14.4 and 27.9 does not appear particularly significant.

Feenstra et al. (2003, 2004) reported a Connors' constant of 6.4, about 12 % higher than the value of 5.7 found in the current research, which is 60 % higher than the mean value of 4.0 reported in ASME (2009). The explanation given for the higher than expected value was due to the relatively large transverse and streamwise pitch ratios as compared to the bulk of the experimental data in the literature. Weaver and Fitzpatrick (1988) state that generally for a given array geometry the critical reduced velocity increases with increasing pitch ratio. The bulk of the experimental data contained in ASME (2009), and used to develop the stability threshold guidelines, are from studies of nuclear steam generators which typically have pitch ratios of approximately 1.5. This may help explain why both Connors' constants were much higher than the expected mean value. However, the deviation from the mean value may, at least in part, be attributed to the high degree of scatter in the existing experimental data.

Feenstra et al. (2003, 2004) determined both the critical uniform gap flow velocity, V_{cr}, of 7.8 m/s and the critical jet centreline velocity, $V(0, 0, 200\,\mathrm{mm})$, of approximately 55 m/s via experiment, see Table 5.5. The authors proposed an analytical relationship which could be used to predict the partial admission factor which was defined as the ratio of the critical uniform gap velocity and the critical jet centreline velocity. The prediction method was based on determining the average velocity in the "jet core" and using this as an equivalent uniform flow over the tube span intersecting the jet core area. The jet core was defined based on a 15° spray angle as stated by the nozzle manufacturer. The nozzle setback to the first row of tubes, $Z_j = 216\,\mathrm{mm}$, was carefully selected such that the jet expansion diameter, $R_e(z)$, would approximately equal the transverse tube pitch at the first row of tubes. The offset, X_j, between the jet centreline and the tube base was 619 mm which placed the jet centreline approximately 50 mm from the tube endpoints. The average jet core velocity was calculated using Equations (5.10) and (5.11), where $\alpha = 77$, and the partial admission factor was calculated using Equation (5.12). Notice that Equation (5.12) is essentially similar to Equation (2.6) except that it includes an additional one half factor which accounts for the jet flow on one side of the tube. Feenstra et al. (2003, 2004) found that the resulting partial admission factor agreed reasonably well with the experimental data. The predicted critical jet centreline velocity for the geometry described by Feenstra et al. (2003, 2004) using Equations (5.10) to (5.12) is 59 m/s which is within 7 % of the measured value of 55 m/s.

$$\hat{V}(r) = e^{-\alpha r^2/z^2} \tag{5.10}$$

$$\bar{V}_N = \frac{1}{\pi R_e^2}\int_0^{2\pi}\int_0^{R_e}\hat{V}(r)rdrd\theta = \frac{2\pi}{\pi R_e^2}\int_0^{R_e}\left(e^{-\alpha r^2/z^2}\right)rdr \tag{5.11}$$

$$\frac{V_{eq}}{V(0,0,Z_m)} = \frac{1}{2}\left(\frac{\displaystyle\int_{Xj-R_e}^{Xj+R_e}\bar{V}_N^2\hat{Y}^2(x)dx}{\displaystyle\int_0^L\hat{Y}^2(x)dx}\right)^{1/2} \tag{5.12}$$

The method outlined above and utilized by Feenstra et al. (2003, 2004) requires the definition of an essentially arbitrary jet core area. The definition of the jet expansion radius, R_e, determines the limits of integration for both Equations (5.11) and (5.12) and thus effects the resulting values. Also the formulation represented by Equations (5.11) and (5.12) applies only to the very specific problem of axisymetric jet flow centred between two tubes.

Alternatively, the incoming velocity profile could be averaged in the transverse direction only, as in Section 5.2, and normalized by the jet centreline velocity, $V(0,0,Z_m)$, this creates a normalized spanwise function of transverse average velocity, $\bar{V}_N(x)$. The normalized spanwise function of transverse average velocity can be calculated using Equations (5.13) and (5.14) and the partial admission factor can be calculated using Equation (5.15). Equation (5.15) produces values similar in magnitude to Equation (5.12) but removes all arbitrary definitions and the limits of integration instead represent real physical boundaries. Also Equations (5.14) and (5.15) can be used in situations where there is significant flow on both sides of the tube. The predicted critical jet centreline velocity for the geometry described by Feenstra et al. (2003, 2004) using Equations (5.14) and (5.15) is 58 m/s which is within 5 % of the measured value of 55 m/s.

$$\hat{V}(x,y) = \left(e^{-\alpha x^2/z^2}\right)\left(e^{-\alpha y^2/z^2}\right) \tag{5.13}$$

$$\bar{V}_N(x) = \frac{e^{(-\alpha x^2/z^2)}}{2P}\int_{-P}^{P}e^{(-\alpha y^2/z^2)}dy \tag{5.14}$$

$$\frac{V_{eq}}{V(0,0,Z_m)} = \left(\frac{\displaystyle\int_0^L\bar{V}_N^2(x-X_j)\hat{Y}^2(x)dx}{\displaystyle\int_0^L\hat{Y}^2(x)dx}\right)^{1/2} \tag{5.15}$$

Thus far the effect of gap confinement has been neglected and although the results from using Equations (5.10) to (5.12) and Equations (5.13) to (5.15) agree reasonably well with each other, and the experimental results of Feenstra et al. (2003, 2004), they do not agree well with the experimental results of the current research. From Table 5.5 the critical uniform gap flow velocity, V_{cr}, was 12 m/s and the critical jet centreline velocity, $V(0, 0, 320\,\mathrm{mm})$, was approximately 60 m/s. Using Equations (5.10) to (5.12) the predicted critical jet centreline velocity is 100 m/s and using Equations (5.13) to (5.15) the predicted critical jet centreline velocity is 106 m/s. Note that for both of the preceding calculations the value of α was set to 94 in Equations (5.10) and (5.13) as this value more closely matched the measured velocity profiles in the current research. The determination of the exponent α is discussed briefly in Section 5.2. Equation (5.16), below, represents an amendment of Equation (5.11) where the jet velocity is averaged over the intersecting gap space. Using Equation (5.16) and Equation (5.12) the predicted critical jet centreline velocity is approximately 64 m/s which is within 7 % of the measured value of 60 m/s. Figure 5.4a shows an illustration of the tube geometry, the integration area, πR_e^2 (dashed circle), and the intersecting gap space, $2R_e(P-D)$ (grey area). Figures 5.4b and 5.4c illustrate the transformation of the incoming three dimensional velocity profile, $V(r,\theta)$, into a step-wise estimate of the average gap flow velocity, $\bar{V}(x)$.

$$\begin{aligned}\bar{V}_N &= \frac{1}{(2R_e)(P-D)}\int_0^{2\pi}\int_0^{R_e}\hat{V}(r)r\,dr\,d\theta \\ &= \frac{2\pi}{(2R_e)(P-D)}\int_0^{R_e}\left(e^{-\alpha r^2/z^2}\right)r\,dr\end{aligned} \tag{5.16}$$

Equation (5.17), below, represents a similar amendment of Equation (5.14) which averages the jet velocity, in the transverse direction, over the intersecting gap space. Using Equation (5.17) and Equation (5.15) the predicted critical jet centreline velocity is approximately 53 m/s which is within approximately 12 % of the measured value of 60 m/s. Figure 5.5a shows an illustration of the tube geometry, the integration area, $2PL_e$ (dashed rectangle), and the intersecting gap spaces, $2(P-D)L_e$ (grey areas). Figures 5.5b and 5.5c illustrate the transformation of the incoming three dimensional velocity profile, $V(x,y)$, into an estimate of the spanwise function of transverse average gap velocity, $\bar{V}(x)$.

$$\begin{aligned}\bar{V}_N(x) &= \frac{1}{2(P-D)}\int_{-P}^{P}\hat{V}(x,y)\,dy \\ &= \frac{e^{(-94x^2/z^2)}}{2(P-D)}\int_{-P}^{P}e^{(-94y^2/z^2)}\,dy\end{aligned} \tag{5.17}$$

Table 5.6 shows a comparison of the measured critical jet centreline velocities and those calculated using Equations (5.12) and (5.15) both with and

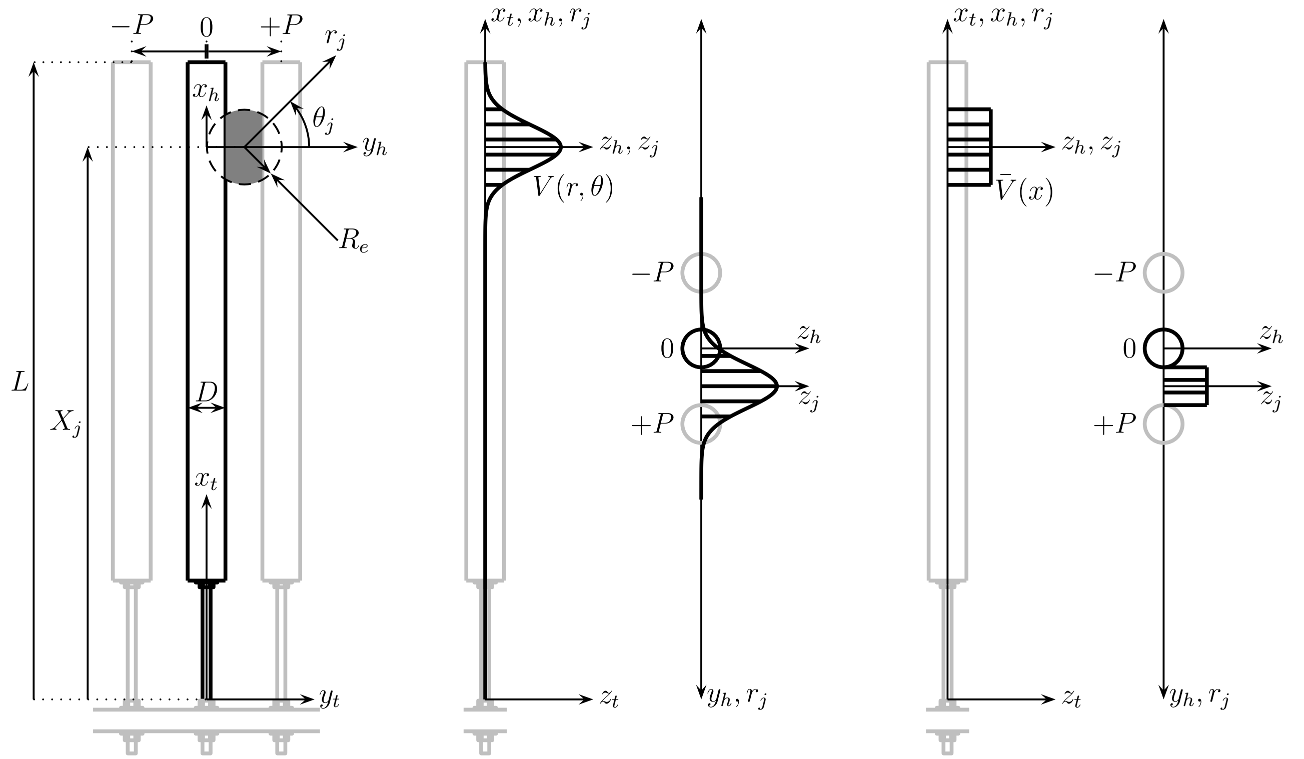

(a) **(b)** **(c)**

Figure 5.4: Illustration of partial admission calculation as proposed by Feenstra et al. (2003, 2004), but modified to account for gap confinement, as described by Equations (5.12) and (5.16). (a) Front view, $x_t - y_t$ plane, of tube geometry, integration area, πR_e^2 (dashed circle), and averaging area, $2R_e(P-D)$ (grey area). (b) Predicted three dimensional free-field velocity profile $V(r,\theta)$ shown in the side view $x_t - z_t$ plane (left) and in the plan view $y_h - z_h$ plane (right). (c) Estimated step-wise average gap velocity $\bar{V}(x)$ shown in the side view $x_t - z_t$ plane (left) and in the plan view $y_h - z_h$ plane (right).

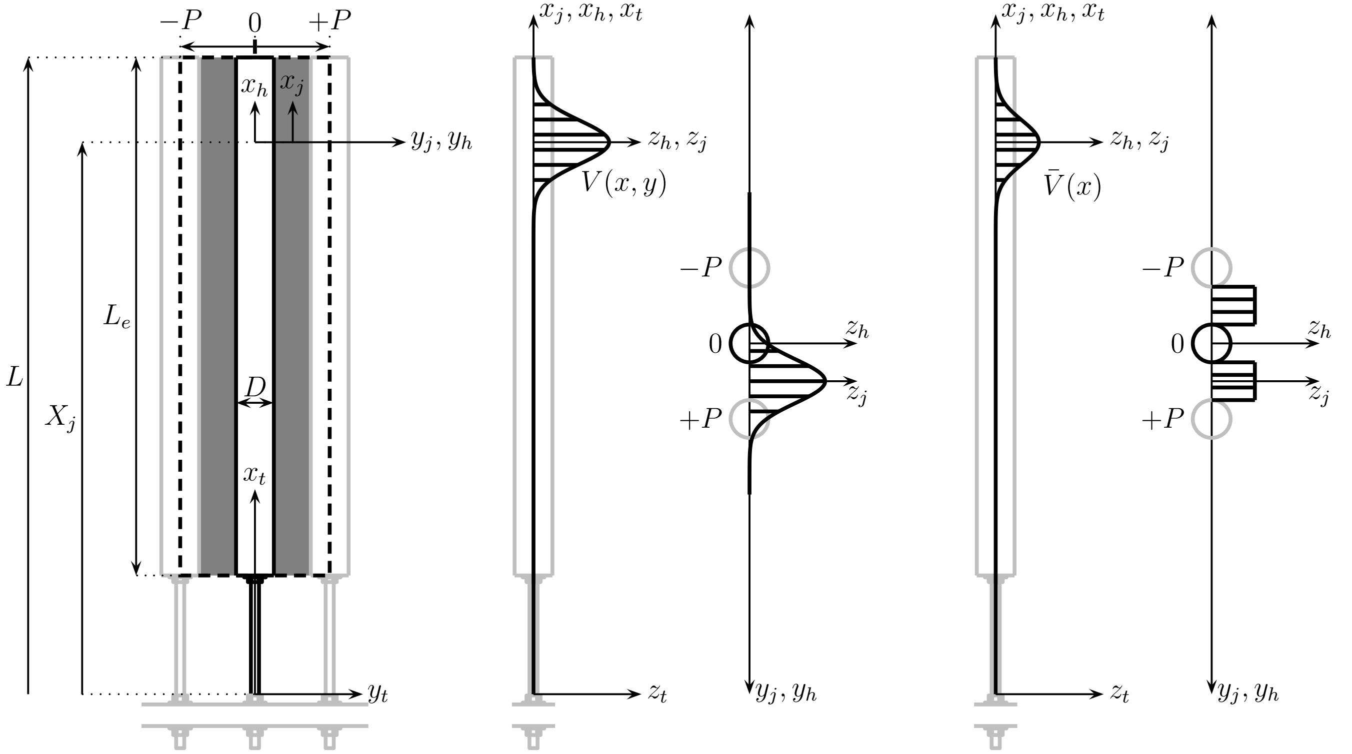

(a) **(b)** **(c)**

Figure 5.5: Illustration of partial admission calculation as described by Equations (5.15) and (5.17). (a) Front view, $x_t - y_t$ plane, of tube geometry, integration area, $2PL_e$ (dashed rectangle), and averaging area, $2(P - D)L_e$ (grey areas). (b) Predicted three dimensional free-field velocity profile $V(x, y)$ shown in the side view $x_t - z_t$ plane (left) and in the plan view $y_j - z_j$ plane (right). (c) Estimated spanwise function of transverse average gap velocity $\bar{V}(x)$ shown in the side view $x_t - z_t$ plane (left) and in the plan view $y_j - z_j$ plane (right).

without considering the effects of gap confinement. From column one of Table 5.6 the measured value of $V(0, 0, 320\,\mathrm{mm})$ agrees reasonably well with the predictions based on the confined average velocity as described by Equation (5.16) and Equation (5.17). Column two indicates that the measured value of $V(0, 0, 200\,\mathrm{mm})$, from Feenstra et al. (2003, 2004), agrees well with the prediction based on the unconfined average velocity as described by Equation (5.11) and Equation (5.14). Although these results seem contradictory they may be reasonably explained by considering that the flow conditions when approaching the tube array will not change abruptly and thus the effects of gap confinement will propagate upstream. Therefore the measured jet velocities just upstream of the tube array will be slightly higher than those measured at the same position for a jet in a free field. This is illustrated in Figures 4.9 and 4.17 which show higher than expected centreline velocities directly upstream of the tube array, this effect also increases for larger nozzle exit flow rates as the effects propagate further upstream. The upstream velocity measurements for the current research were made at a position approximately 12 mm ($Z_m = 320\,\mathrm{mm}$) in front of the first row tube face. Whereas the upstream velocity measurements made by Feenstra et al. (2003, 2004) were made approximately 3 mm in front of the first row tube face. This further supports the argument that the velocity measurements completed by Feenstra et al. (2003, 2004) were representative of the confined state and thus accounting for confinement using Equation (5.16) or Equation (5.17) is inappropriate.

Based on comparison between the results of the uniform flow and axisymmetric jet flow experiments the assumption that the spanwise gap velocity profile $V(x)$, in Equation (2.6), can be replaced with the spanwise function of transverse average gap velocity $\bar{V}(x)$ yields reasonable results. Therefore, in cases where the three dimensional gap velocity, $V(x, y)$, profile is known Equations (5.18) and (5.19) can be used to calculate the equivalent uniform gap velocity V_{eq}.

$$\bar{V}(x) = \frac{1}{2(P-D)}\left(\int_{-(P-D/2)}^{-D/2} V(x,y)dy + \int_{D/2}^{P-D/2} V(x,y)dy\right) \tag{5.18}$$

$$V_{eq} \approx \left(\frac{\int_0^L \bar{V}^2(x)\hat{Y}^2(x)dx}{\int_0^L \hat{Y}^2(x)dx}\right)^{1/2} \tag{5.19}$$

However, Equation (5.18) applies only to situations where the three dimensional gap velocity profile is known. This formulation is useful for the purpose of directly comparing uniform flow and axisymmetric flow measurement results. However, the gap velocity profile is rarely known, when the gap velocity profile is unknown the spanwise function of transverse average gap velocity

$\bar{V}(x)$ may be estimated using the general form of Equation (5.20). Where $V(x, y)$ is the velocity profile at the gap location but under the assumption of free field conditions. Therefore, $V(x, y)$ represents flow as it would be without the presence of the tube array. Equation (5.20) can be used in combination with a predicted free field velocity profile, such as Equation (2.11), and Equation (5.19) to calculate the equivalent uniform gap velocity V_{eq}.

$$\bar{V}(x) \approx \frac{1}{2(P-D)} \int_{-P}^{P} V(x, y) dy \tag{5.20}$$

Parameter	Current Research	Feenstra et al. (2003, 2004)
Tube Array		
tube diameter, D	44.45 mm	25.4 mm
transverse pitch, P_t	88 mm	45.7 mm
transverse pitch ratio, P_t/D	2.0	1.8
streamwise pitch, P_s	88 mm	55.9 mm
streamwise pitch ratio, P_s/D	2.0	2.2
$P_t/(P_t - D)$	2.0	2.25
total tube length, L	751 mm	669 mm
length exposed to uniform flow, L_e	610 mm	619 mm
L_e/L	0.81	0.93
tube natural frequency (1^{st} mode), f	9 Hz	12.6 Hz
effective tube lineal mass, m	1.004 kg/m	0.161 kg/m
tube damping ratio, ζ	1.05 %	1.1 %
$m\,(2\pi\zeta)\,/\,(\rho D^2)$	27.9	14.4
Jet		
nozzle radius, R_0	4.20 mm	2.19 mm
jet offset from 1st row centre, Z_j	354 mm	216 mm
Z_j/R_0	84.29	98.63
Z_j/P_t	4.02	4.73
jet offset from tube base, X_j	651 mm	619 mm
X_j/L	0.87	0.93
jet measurement position, Z_m	320 mm	200 mm
$2(Z_j - Z_m)/D$	1.53	1.23

Table 5.4: A comparison of the physical model parameters from the current research and those provided by Feenstra et al. (2003, 2004).

Parameter	Current Research	Feenstra et al. (2003, 2004)
Uniform Flow		
critical gap flow velocity, V_{cr}	12 m/s	7.8 m/s
$V_{cr}/\left(fD\right)$	30.0	24.3
Connor's constant, K	5.7	6.4
Jet flow centred between T13 and T14		
critical jet nozzle exit flowrate, Q_{cr}	26 cfm	-
critical jet nozzle exit velocity, $V_{0,cr}$	222 m/s	-
critical jet centreline velocity, $V_{j,cr}$	60 m/s	55 m/s
partial admission factor, $V_{cr}/V_{j,cr}$	0.200	0.142
Jet flow centred on face of T13		
critical jet nozzle exit flowrate, Q_{cr}	30 cfm	-
critical jet nozzle exit velocity, $V_{0,cr}$	256 m/s	-
critical jet centreline velocity, $V_{j,cr}$	60 m/s	-
partial admission factor, $V_{cr}/V_{j,cr}$	0.200	-

Table 5.5: A comparison of the fluidelastic instability results from the current research and those provided by Feenstra et al. (2003, 2004).

Description of $V(0, 0, Zm)$ value	Current Research $V(0, 0, 320\,\text{mm})$	Feenstra et al. (2003, 2004) $V(0, 0, 200\,\text{mm})$
Measured	**60**	**55**
No Confinement:		
Eqs. (5.11) and (5.12)	100	**59**
Eqs. (5.14) and (5.15)	106	**58**
With Confinement:		
Eqs. (5.16) and (5.12)	**64**	34
Eqs. (5.17) and (5.15)	**53**	27

Table 5.6: A comparison of the $V(0, 0, Z_m)$ values determined via measurement and prediction for the case where the jet flow was centred between T13 and T14.

6. Conclusions

This research was motivated by the catastrophic failure of a kraft recovery boiler, due to heat exchanger tube failures, caused by a steam sootblower lance which became parked while issuing jet flow down a tube lane perpendicular to the tube spans. The failure was investigated by Feenstra et al. (2003, 2004) however the approach employed neglected the three dimensionality of the jet flow. The result was a predictive approach which, although useful for its intended purpose, was limited in application to other configurations. The primary purpose of this research was to further investigate the phenomenon of fluidelastic instability, in a tube array, due to axisymmetric jet flow and to develop a partial admission formulation which accounts for velocity variations in both the spanwise and transverse directions to improve predictive capability. To accomplish this a model heat exchanger tube array was designed, constructed and then tested under both uniform flow and axisymmetric jet flow conditions. The uniform flow testing was completed in McMaster University's 2 ft wind tunnel and was used to establish the critical reduced velocity of the tube array at the onset of fluidelastic instability. The uniform flow test established a basis for comparing the results with the existing literature and evaluating the validity of the proposed partial admission calculation. The tube array was also tested in open air using an axisymmetric jet, with two different physical arrangements, the first with the jet aimed between tubes and perpendicular to the tube spans and the second with the jet aimed at a tube face and perpendicular to the tube spans. The jet velocities for each physical arrangement were recorded using measurements of the nozzle exit flowrate. Velocity measurements were subsequently completed to relate the nozzle exit flowrate to the actual incoming velocity profile entering the first tube row. Velocity measurements were also completed inside the tube array within the inter-tube spaces to determine how the jet diffused through the array. The measurement data collected from the uniform and axisymmetric jet flow testing was used to validate a modified partial admission formula which accounts for velocity variations in both the spanwise and the transverse directions. The modified partial admission formula was developed by assuming that the spanwise gap velocity profile $V(x)$ can be replaced with the spanwise function of transverse average gap velocity $\bar{V}(x)$.

The axisymmetric jet experimental results, both vibration and velocity measurements, were used to calculate the predicted equivalent critical uniform gap velocity using the modified partial admission formula. Comparison of predicted and measured critical uniform gap velocity, the instability threshold, indicated reasonable agreement where instability was actually observed.

Unfortunately the predictions also indicated instability in spatial locations where the phenomenon was not observed. Although the theory fails to predict the spatial location of the instability, the predicted stability threshold for the first row tubes was lower than the observed value in all cases. This suggests that the prediction method is conservative. The fact that instability was not observed in spatial locations where it was predicted to occur also suggests that velocity on one side of a tube may not be sufficient to produce fluidelastic instability and other factors may be important. Factors such as the need for coupling with adjacent tubes or for sufficient velocity on both sides of a tube which would require that sufficient jet diffusion has taken place to involve both a tube and its neighbours. The inability to predict the spatial location of fluidelastic instability may suggest a gap in the fundamental relationships such as the Connors' equation and the equivalent velocity concept, this is discussed further in Chapter 7.

The modified partial admission formula requires the spanwise function of transverse average gap velocity $\bar{V}(x)$ and can be used directly for the purpose of comparing the uniform flow and axisymmetric flow measurement results. However, in most cases the gap velocity profile is unknown and therefore $\bar{V}(x)$ is also unknown. However, $\bar{V}(x)$ can be estimated using a predicted or measured velocity profile $V(x, y)$, at the gap location z, under the assumption of free field conditions. The velocity profile $V(x, y)$ can be integrated from $-P$ to $+P$ and divided by the available gap area $2(P-D)$ the result is an estimate of $\bar{V}(x)$.

Most of the published literature on fluidelastic instability due to partial admission flow is concentrated on the investigation of fluid velocity profiles with spanwise velocity variations and essentially uniform transverse velocity. However, Feenstra et al. (2003, 2004) did complete a model study to investigate fluidelastic instability due to axisymmetric jet flows. To enable direct comparison with this earlier study the model for the current research was carefully designed to be geometrically similar. Feenstra et al. (2003, 2004) proposed a modified partial admission calculation for the specific case tested, which relied on defining an arbitrary jet expansion diameter and carefully locating the jet nozzle such that this diameter exactly matched the tube array transverse pitch. The methodology described in Chapter 5 and reiterated here does not rely on defining a jet expansion diameter. Instead transverse flow variations are accounted for by generating a velocity function which represents the average value around a tube at all spanwise locations. This can be achieved through analysis of a measured or assumed velocity profile. The only necessary assumption is that a three dimensional velocity profile $V(x, y)$ over a tube and occurring between $-P$ to P, can be represented by a function representing the average value $\bar{V}(x)$ at each spanwise point x and this function can replace $V(x)$ when calculating partial admission. A detailed comparison of the approach proposed herein and that proposed by Feenstra et al. (2003, 2004) was undertaken in Chapter 5 which revealed reasonable agreement between the two approaches. However, the approach described here does not require the arbitrary definition of a jet expansion diameter and the limits of integration instead represent real physical boundaries. The approach described here can also be utilized in situations where there is significant flow on both sides of the tube. This represents a significant generalization over the methodology proposed by Feenstra et al. (2003, 2004) and is therefore more widely applicable.

7. Recommendations

The experimental study conducted for this research was focused on axisymmetric jet flow with the jet centred between tubes or on a tube face. Although, Equation (5.19) very accurately related the axisymmetric jet flows studied to the uniform flow case, and thus the great body of existing experimental data, more investigation would be required to determine if the relationship is generally applicable to all or most situations. It would be useful to conduct a parametric study, or series of studies, to investigating the effects of mass damping parameter, $m(2\pi\zeta)/(\rho D^2)$, tube pitch to diameter ratio, P/D, nozzle z-offset to tube pitch ratio, Z_j/P, and nozzle x-offset to tube length ratio, X_j/L. These parametric studies should be completed for all relevant array geometries such as square, rotated square, etc. Further confidence could be established if it could be demonstrated that Equation (5.19) could accurately represent other non-uniform flows. Although testing all combinations of parameters represents an unreasonable expectation and a perhaps an unjustifiable effort, verification of a few cases with drastically different parameters should demonstrate the applicability of Equation (5.19) for representing the equivalent uniform gap flow velocity, V_{eq}, represented by a non-uniform flow $V(x, y)$ with significant velocity variations in both the spanwise, x, and transverse, y, directions.

The results of this research indicate that an assessment of the adequacy of the underlying theoretical framework, which is currently applied throughout the industry, may be warranted. The current research used Connors' equation and the equivalent velocity concept, which are widely used in industry, to develop a predictive approach for flows with significant transverse velocity variations. The result was a prediction methodology which predicted the minimum critical gap flow velocity reasonably well. However, the method also predicted fluidelastic instability in spatial locations, in tube rows, where the phenomenon was not observed during experiment. This suggests that Connors' equation and the equivalent velocity concept do not completely describe the fundamental physics of fluidelastic instability. The work presented by Weaver and Fitzpatrick (1988), as well as the current research, suggest that fluidelastic instability may involve more complex interactions which are not fully captured by Connors' equations. Therefore, additional research is required to further develop our understanding of the fundamental underlying physics of fluidelastic instability.

References

Abramson, H. N. (1966). The dynamic behavior of liquids in moving containers. Nasa Report NASA SP-106. Southwest Research Institute.

Appel, D. W., P. G. Hubbard, L. Landweber, E. M. Laursen, J. S. McNown, H. Rouse, T. T. Siao, A. Toch, and C. S. Yih (1959). *Advanced Mechanics of Fluids*. New York: John Wiley and Sons.

ASME (2009). 2007 boiler & pressure vessel code.

Baker, W. E., P. S. Westine, and F. T. Dodge (1973). *Similarity Methods in Engineering Dynamics: Theory and Practice of Scale Modelling*. NJ: Hayden Book Company.

Barsin, J. A. and G. Kychakoff (1992, June). Increasing the load carrying capacity of a kraft recovery steam generator. In *International Chemical Recovery Conference*. TAPPI Press.

Beer, F. P. and E. R. Johnston (1992). *Mechanics of Materials 2nd edition* (Second ed.). McGraw-Hill.

Blevins, R. D. (1984). *Applied Fluid Dynamics Handbook*. New York: Van Nostrand Reinhold Company.

Blevins, R. D. (2001a). *Flow-Induced Vibration* (Second ed.). Florida: Krieger Publishing.

Blevins, R. D. (2001b). *Formulas for Natural Frequency and Mode Shape* (Reprint ed.). New York: Krieger Publishing Company.

Chapra, S. C. and R. P. Canale (1998). *Numerical Methods for Engineers: with programming and software applications* (Third ed.). McGraw-Hill.

Chen, S. S. (1984). Guidelines for the instability flow velocity of tube arrays in crossflow. *Journal of Sound and Vibration 93*(3), 439–455.

Chen, S. S. and S. Chandra (1991). Fluidelastic instabilities in tube bundles exposed to nonuniform cross-flow. *Journal of Fluids and Structures 5*, 299–322.

Connors, H. J. (1970). Fluidelastic vibration of tube arrays excited by cross flow. In D. D. Reiff (Ed.), *Flow-Induced Vibration in Heat Exchangers*, New York, pp. 42–56. ASME.

Connors, H. J. (1978). Fluidelastic vibration of heat exchanger tube arrays. *Journal of Mechanical Design 100*, 347–353.

Devore, J. L. (1999). *Probability and Statistics: For Engineering and the Sciences* (Fifth ed.). CA, USA: Druxbury.

Draper, N. R. and H. Smith (1998). *Applied Regression Analysis* (Third ed.). NY, USA: John Wiley & Sons, Inc.

Dunn, P. F. (2010). *Measurement and Data Analysis for Engineering and Science* (2nd ed ed.). Florida: CRC Press.

Feenstra, P., D. S. Weaver, and Z. Abdullah (2003, July 20-24). Fluid-elastic instability in a tube array subjected to uniform and jet flow. In *2003 ASME Pressure Vessels and Piping Conference*.

Feenstra, P., D. S. Weaver, and Z. Abdullah (2004). Fluid-elastic instability in a tube array subjected to uniform and jet flow. *ASME Journal of Pressure Vessel Technology 126*, 269–274.

Figliola, R. S. and D. E. Beasley (2006). *Theory and Design for Mechanical Measurements* (Fourth ed.). John Wiley & Sons, Inc.

Fox, R. W. and A. T. McDonald (1998). *Introduction to Fluid Mechanics* (Fifth ed.). New York: John Wiley and Sons.

Fujino, Y., B. M. Pacheco, P. Chaiseri, and L. M. Sun (1988, October). Parametric studies on tuned liquid dampers (tld) using circular containers by free-oscillation experiments. *Structural Engineering / Earthquake Engineering 5*(2), 381s–391s.

Hartog, J. P. D. (1985). *Mechanical Vibrations. 1956. Reprint.* New York: Dover Publications, Inc.

Jameel, M. I., D. E. Cormack, H. Tran, and T. E. Moskal (1994). Sootblower optimization part 1: Fundamental hydrodynamics of a sootblower nozzle and jet. *TAPPI Journal 77*(5), 135–142.

Koss, L. L. and W. H. Melbourne (1995). Chain dampers for control of wind-induced vibration of tower and mast structures. *Engineering Structures 17*(9), 622–625.

Kulkarni, S., D. Jadhav, and P. Khadke (2012). Passive control for tall structures. *International Journal on Theoretical and Applied Research in Mechanical Engineering (IJTARME) 1*(2), 87 – 91.

Lamb, H. (1920). *Higher Mechanics.* Cambridge.

Lever, J. and D. S. Weaver (1986). On the stability behavior of heat exchanger tube bundles: Part 1 - modified theoretical model. *Journal of Sound and Vibration 107*, 375–392.

Maxima (2014). Maxima, a computer algebra system. version 5.34.1.

Meirovitch, L. (2001). *Fundamentals of Vibrations.* NY: McGraw-Hill, New York, NY.

Moskal, T. E., M. A. Bunton, and C. A. Jordan (1993, October). Results of laboratory testing and field trials of improved sootblower nozzles. In *TAPPI Engineering Conference*.

Paidoussis, M. P. (1982). A review of flow-induced vibrations in reactors and reactor components. *Nuclear Engineering and Design 74*, 31–60.

Parrondo, J., C. Santolaria, and D. S. Weaver (1997). Fluidelastic instability in a tube array subjected to partial admission water cross-flow. *Journal of Fluids and Structures 11*, 159–181.

Pettigrew, M. J. and C. E. Taylor (1991). Fluidelastic instability of heat exchanger tube bundles: Review and design recommendations. *ASME Journal of Pressure Vessel Technology 113*, 242–256.

Price, S. J. (1993). A review of theoretical models for fluidelastic instability of cylinder arrays in cross-flow. *Journal of Fluids and Structures 9*, 463–518.

Rao, S. S. (1995). *Mechanical Vibrations 3rd edition* (Third ed.). Addison-Wesley Publishing.

Reed, W. H. I. (1967, September). Hanging-chain impact dampers: A simple method for damping tall flexible structures. International Research Seminar - Wind Effects on Buildings and Structures, Ottawa, Canada, pp. 283–321.

Roberts, B. W. (1966). Low frequency, aeroelastic vibrations in a cascade of circular cylinders. *Mechanical Engineering Science Monograph No. 4*.

Schroeder, M. R. (1965). New method of measuring reverberation time. *Journal of the Acoustical Society of America 37*, 409–412.

Shapiro, A. H. (1953). *The Dynamics and Thermodynamics of Compressible Fluid Flow*. New York: The Ronald Press Company.

Stanton, S. C. and B. P. Mann (2010). On the dynamic response of beams with multiple geometric or material discontinuities. *Mechanical Systems and Signal Processing 24*, 1409–1419.

Timoshenko, S., D. H. Young, and W. Weaver (1974). *Vibration Problems in Engineering* (4th ed.). New York: John Wiley & Sons. TA 355.T55 1974.

Uloth, V. C., J. T. Markovic, J. T. Wearing, and A. Walsh (1996). Observations on the dynamics and efficiency of sootblowing in kraft recovery furnaces part i: Dynamics. *Pulp and Paper Canada 97*(6), 59–65.

Waring, L. F. and D. S. Weaver (1988). Partial admission effects on the stability of a heat exchanger tube array. *Journal of Pressure Vessel Technology 110*, 194–198.

Weaver, D. S. (2005). *An Introduction to Flow-Induced Vibrations: Course Notes*. McMaster University.

Weaver, D. S. and J. A. Fitzpatrick (1988). A review of cross-flow induced vibrations in heat exchanger tube arrays. *Journal of Fluids and Structures 2*, 73–93.

Weaver, D. S. and H. G. D. Goyder (1990). An experimental study of fluidelastic instability in a three-span tube array. *Journal of Fluids and Structures 4*, 429–442.

Weaver, D. S. and J. Parrondo (1991). Fluidelastic instability in multispan heat exchanger tube arrays. *Journal of Fluids and Structures 5*, 323–338.

Zaman, K. B. M. Q. (1998). Asymptotic spreading rate of initially compressible jets-experiment and analysis. *Physics of Fluids 10*(10), 2652–2660.

Appendix A.

Tube Mode Shape Calculations

This section describes the methods used for predicting the natural frequencies and mode shapes of the model tubes.

A.1 Rayleigh's Quotient - Approximate Method

Figure 3.5 shows a diagram of the model tube structure. This structure is divided into Segments 1 through 10 which differ in terms of material, geometric or mass properties. However, the model segmentation can be simplified if we neglect mass properties and focus on segmentation based on stiffness (material/geometric) properties. The threaded rod support is the flexural element in the model as indicated by the relatively low flexural rigidity (EI) shown in Table 3.3. Segments 2 through 9 can be regarded as rigid by comparison. Segment 10 (the damper chain) will be neglected entirely for this approximate analysis due to it's relatively small mass and negligible stiffness. The lengths of the steel support (l_s) and the rigid segment (l_t) are shown below in terms of the segments defined in Figure 3.5 and Tables 3.2 and 3.3.

$$l_s = l_1 \tag{A.1}$$

$$l_t = \sum_{i=2}^{9} l_i \tag{A.2}$$

The equations for the static deflection of cantilever beams are provided in Appendix D of Beer and Johnston (1992). Let us assume that when vibrating at the first natural mode the inertial force passes through the centre of gravity of the beam (tube). Accordingly the deflection (Y_s) of the steel support rod can be found by combining the force (P) and moment (M) loading as shown

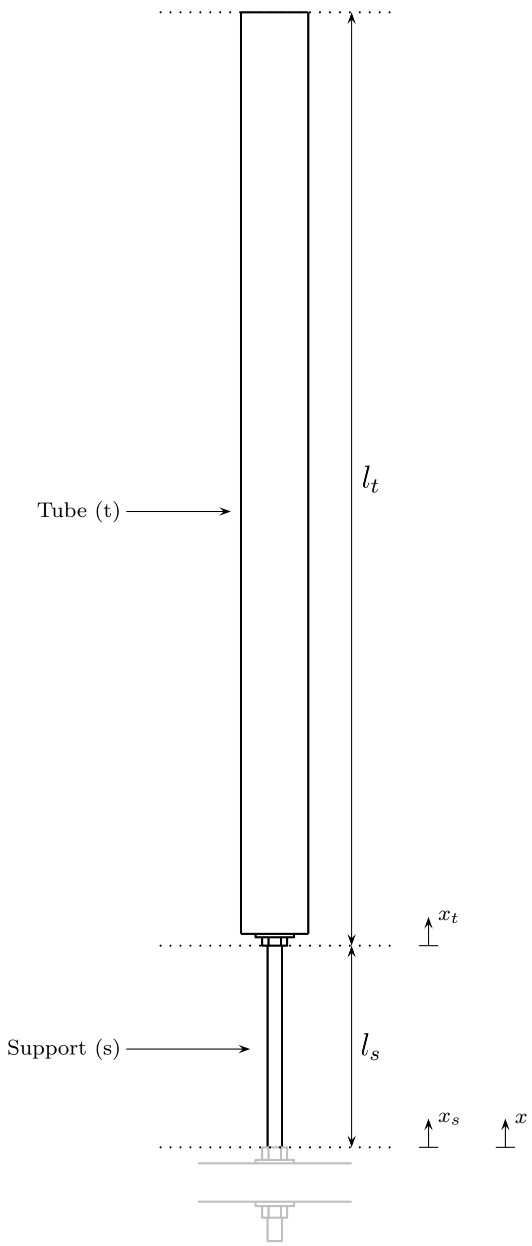

Figure A.1: Model tube simplified segmentation for Rayleigh's quotient calculation.

below in Equation (A.4). The deflection (Y_t) of the rigid tube segment is given by Equation (A.5).

$$x = \begin{cases} x_s : & 0 \le x_s \le l_s \\ x_t + l_s : & 0 \le x_t \le l_t \end{cases} \tag{A.3}$$

$$Y_s(x) = \frac{P(3l_s x^2 - x^3)}{6E_s I_s} + \frac{Mx^2}{2E_s I_s} \text{ for } 0 \le x \le l_s \tag{A.4}$$

$$Y_t(x) = \frac{2Pl_s^3}{6E_s I_s} + \frac{Ml_s^2}{2E_s I_s} + \left(\frac{Pl_s^2}{2E_s I_s} + \frac{Ml_s}{E_s I_s}\right)(x - l_s) \text{ for } l_s \le x \le l_s + l_t \tag{A.5}$$

The location of the centre of gravity can be determined using Equation (A.6). Equation (A.7) represents the inertial force (P) which acts upon the centre of gravity. Equation (A.8) represents the moment (M) induced about the end of the steel support.

$$l_{cg} = \frac{\int \rho(x)A(x)x dx}{\int \rho(x)A(x)dx} = \frac{\int m(x)x dx}{\int m(x)dx} = \frac{\int m(x)x dx}{M} \tag{A.6}$$

$$P = \int \rho(x)A(x)\ddot{y}(x)dx \tag{A.7}$$

$$M = (l_{cg} - l_s)P \tag{A.8}$$

Normalized deflection functions can be produced by substituting for M, dividing each function by P and $Y_t(l_s + l_t)$ and introducing the coordinate transformation $x = \hat{x}(l_s + l_t)$, where $\hat{x} = 0$ to 1.

$$\begin{aligned} \hat{Y}_s(\hat{x}) &= \frac{3l_s(\hat{x}(l_s + l_t))^2 + 3(l_{cg} - l_s)(\hat{x}(l_s + l_t))^2 - (\hat{x}(l_s + l_t))^3}{2l_s^3 + 3(l_{cg} - l_s)l_s^2 + 3l_s^2 l_t + 6(l_{cg} - l_s)l_s l_t} \\ &= 3.646\hat{x}^2 - 2.162\hat{x}^3 \end{aligned} \tag{A.9}$$

$$\begin{aligned} \hat{Y}_t(\hat{x}) &= \frac{2l_s^3 + 3(l_{cg} - l_s)l_s^2 + (3l_s^2 + 6(l_{cg} - l_s)l_s)(\hat{x}(l_s + l_t) - l_s)}{2l_s^3 + 3(l_{cg} - l_s)l_s^2 + 3l_s^2 l_t + 6(l_{cg} - l_s)l_s l_t} \\ &= 1.091\hat{x} - 0.091 \end{aligned} \tag{A.10}$$

$$\hat{Y}(\hat{x}) = \begin{cases} \hat{y}_s(\hat{x}) : & 0 \le \hat{x} \le l_s/(l_s + l_t) \\ \hat{y}_t(\hat{x}) : & l_s/(l_s + l_t) \le x \le 1 \end{cases} \tag{A.11}$$

Assuming that the static deflection curve represents the first mode shape of vibration we can now use Rayleigh's quotient to determine the natural frequency Rao (1995). Rayleigh's quotient is derived by setting the maximum potential energy of the system equal to the maximum kinetic energy of the system. Equations (A.12) and (A.13) represent the approximate potential (E_p) and kinetic energy (E_k) of the system, respectively. The first mode natural frequency can be estimated by equating Equations (A.12) and (A.13) and invoking the simple harmonic motion assumption represented by Equation (A.14). The resulting equality can be rearranged to produce Equation (A.15). The natural frequency can then be calculated using Equations (A.9) and (A.10) in combination with Equation (A.15). For the system defined in Figure A.1 the natural frequency (f_n) predicted using Rayleigh's quotient was 9.08 Hz, as shown below.

$$E_p = \frac{1}{2}\int E(x)I(x)\left(\frac{d^2y(x,t)}{dx^2}\right)^2 dx \tag{A.12}$$

$$E_k = \frac{1}{2}\int \rho(x)A(x)\left(\frac{dy(x,t)}{dt}\right)^2 dx \tag{A.13}$$

$$y(x,t) = Y(x)cos(\omega t + \phi) \tag{A.14}$$

$$\omega_n^2 = \frac{\int E(x)I(x)\left(\frac{d^2Y(x)}{dx^2}\right)^2 dx}{\int \rho(x)A(x)Y^2(x)dx} \tag{A.15}$$

$$f_n = \frac{\omega_n}{2\pi} = 9.08 \text{ Hz} \tag{A.16}$$

A.2 Boundary Value Problem - Exact Method

The free vibration of a continuous beam can be modelled exactly using Timoshenko beam theory Timoshenko et al. (1974). However, in the case of a slender beam the effects of rotary inertia and shear forces may be neglected which simplifies the governing relations significantly. The result is the Euler-Bernoulli beam theory Meirovitch (2001) which is regarded as exact for slender beams and low order mode shapes. Equation (A.17) is the Euler-Bernoulli beam equation.

$$\rho(x)A(x)\frac{\partial^2 y(x,t)}{\partial t^2} + \frac{\partial^2}{\partial x^2}\Big(E(x)I(x)\frac{\partial^2 y(x,t)}{\partial x^2}\Big) = 0 \tag{A.17}$$

Equation (A.17) is the general form and expresses the material and geometric properties of the beam as continuous functions depending on the x coordinate. However, let us assume, as is most often the case, that the material properties are constant.

$$\rho A\frac{\partial^2 y(x,t)}{\partial t^2} + \frac{\partial^2}{\partial x^2}\Big(EI\frac{\partial^2 y(x,t)}{\partial x^2}\Big) = 0 \tag{A.18}$$

Equation (A.18) can be separated into temporal and spatial components if we invoke the assumption of simple harmonic motion.

$$y(x,t) = Y(x)cos(\omega t + \phi) \tag{A.19}$$

Taking the second derivatives with respect to t and x yields:

$$\frac{\partial^2 y(x,t)}{\partial t^2} = -\omega^2 Y(x)cos(\omega t + \phi) \tag{A.20}$$

$$\frac{\partial^2 y(x,t)}{\partial x^2} = \frac{d^2 Y(x)}{dx^2} cos(\omega t + \phi) \tag{A.21}$$

Substituting these into Equation (A.18) and simplifying:

$$-\omega^2 \rho A Y(x) + EI\frac{d^4 Y(x)}{dx^4} = 0 \tag{A.22}$$

$$\frac{d^4 Y(x)}{dx^4} - \beta^4 Y(x) = 0 \tag{A.23}$$

$$\beta^4 = \frac{\omega^2 \rho A}{EI} = \frac{\omega^2 m}{EI} \tag{A.24}$$

The general solution of Equation (A.23) takes the form of Equation (A.25). Equations (A.23) to (A.25) describe a boundary value problem. Solutions are found by applying the appropriate boundary conditions, solving for the eigenvalues (β) which represent the existence of non-trivial solutions and for each eigenvalue determining the eigenfunction represented by Equation (A.25). Meirovitch (2001) provides a more comprehensive description of vibration of continuous beams and Blevins (2001b) provides the equations for the natural frequencies (eigenvalues) and mode shapes (eigenfunctions) for various combinations of boundary conditions.

$$Y(x) = a\sin(\beta x) + b\cos(\beta x) + c\sinh(\beta x) + d\cosh(\beta x) \tag{A.25}$$

Equations (A.23) and (A.25) describe a single span beam with constant material and geometric properties. However, the experimental apparatus for this work was constructed of multiple beams attached at their ends and each with different material and geometric properties. Further at the points of attachment the material and geometric changes are discontinuous (step functions) and therefore the entire assembly cannot be expressed in terms of the general Euler-Bernoulli Equation (A.17) since the material and geometric properties cannot be expressed as continuous functions over the entire assembly. To solve this more complicated problem the discontinuous beam can be subdivided into smaller continuous segments with constant material and geometric properties.

The functions describing each segment are then tied together by enforcing compatibility conditions at each interface. The solution process for beams with multiple material or geometric discontinuities is described in Stanton and Mann (2010). Using this solution method Equation (A.25) can be written for each beam segment (i). The boundary conditions and compatibility conditions are then used to write a system of equations which can be solved for the eigenvalues.

$$Y_i(x_i) = a_i \sin(\beta_i\, x_i) + b_i \cos(\beta_i x_i) + c_i \sinh(\beta_i x_i) + d_i \cosh(\beta_i x_i) \tag{A.26}$$

$$\beta_i^4 = \frac{\omega^2\, m_i}{E_i\, I_i} \tag{A.27}$$

Figure 3.5 illustrates that the model tube is comprised of ten unique segments and would thus require the solution of ten boundary value problems with compatibility conditions. However, by making a few assumptions this effort can be reduced by almost half. First examination of Figure 3.5 shows that the addition of nonstructural mass requires the creation of a new segment as the overall density of the associated segment changes. By assuming that the non-structural masses can be represented as point masses attached at segment interfaces two segments can be eliminated. The mounting plug which attaches the steel support to the aluminum tube is comprised of several elements with relatively short lengths. This composite structure can be modeled as an equivalent homogeneous element and another two segments can be eliminated. Utilizing these additional assumptions the number of unique segments are reduced to six. These minor simplifications should not effect the results for the first mode natural frequency and mode shape. However, calculations for higher modes of vibration may be effected.

Figure A.2 shows a revised schematic of the multi-segment beam used in the experimental investigation. Table A.1 lists the physical properties of each segment. Also illustrated is the chain component of the damper. The motion of a hanging chain is described by Lamb (1920). The details are not presented here, however the mode shapes of a vertical hanging chain are described by Equation (A.28).

$$Y_i(x_i) = a_i J_0\Big(2\omega\sqrt{\frac{x_i}{g}}\Big) \tag{A.28}$$

The five beam segments can be coupled and solved for the natural frequencies and mode shapes of the composite system. Additionally the sixth segment representing the hanging chain can also be coupled and the resulting natural frequencies and modes can be found. The system of equations which represents the motion of the physical system in Figure A.2 is presented below. These equations are written in terms of the segment local coordinate (x_i).

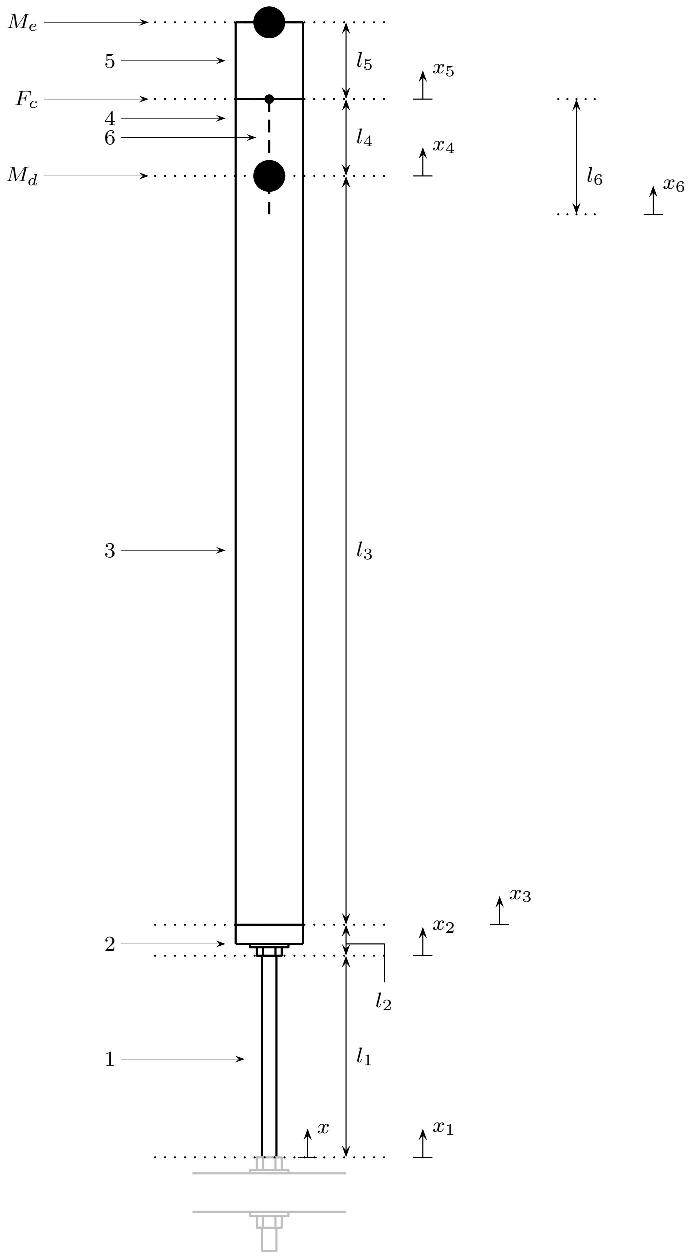

Figure A.2: Model tube segmentation for boundary value problem.

Segment	l(mm)	$EI(\mathrm{N} \cdot \mathrm{m}^2)$	m(g/m)	M(g)
1	133.35	46.15	423.27	0.00
2	20.52	642.52	3541.54	0.00
3	495.30	3441.12	577.17	60.00
4	50.80	3441.12	577.17	20.00
5	50.80	3441.12	577.17	50.00
6	76.20	0.00	44.73	0.00

Table A.1: Model tube, simplified beam model, segment material and geometric properties. l(mm) - segment length, $EI(\mathrm{N} \cdot \mathrm{m}^2)$ - flexural rigidity, m(g/m) - lineal mass, M(g) - segment end mass. The following material properties for steel and aluminum were used: $\rho_s = 7860\,\mathrm{kg/m^3}$(density of steel), $E_s = 200\,\mathrm{GPa}$(modulus of elasticity for steel), $\rho_a = 2700\,\mathrm{kg/m^3}$(density of aluminum), E_a= $70\,\mathrm{GPa}$(modulus of elasticity for aluminum).

The system has 21 unknown constant coefficients and the frequency (ω) is also unknown. By applying the boundary conditions at each end of the composite beam and all the applicable compatibility conditions we could write 21 equations with 22 unknowns and from this construct the frequency equation. However, this approach results in having to deal with very large matrices. Instead we can follow the solution method proposed by Stanton and Mann (2010), with some modifications to account for the hanging chain as well as point masses. This method starts at one side of the structure and progresses through each segment while eliminating constants at each interface throughout the calculation.

$$Y_1(x_1) = a_1 \sin(\beta_1 x_1) + b_1 \cos(\beta_1 x_1) + c_1 \sinh(\beta_1 x_1) + d_1 \cosh(\beta_1 x_1) \tag{A.29}$$

$$Y_2(x_2) = a_2 \sin(\beta_2 x_2) + b_2 \cos(\beta_2 x_2) + c_2 \sinh(\beta_2 x_2) + d_2 \cosh(\beta_2 x_2) \tag{A.30}$$

$$Y_3(x_3) = a_3 \sin(\beta_3 x_3) + b_3 \cos(\beta_3 x_3) + c_3 \sinh(\beta_3 x_3) + d_3 \cosh(\beta_3 x_3) \tag{A.31}$$

$$Y_4(x_4) = a_4 \sin(\beta_4 x_4) + b_4 \cos(\beta_4 x_4) + c_4 \sinh(\beta_4 x_4) + d_4 \cosh(\beta_4 x_4) \tag{A.32}$$

$$Y_5(x_5) = a_5 \sin(\beta_5 x_5) + b_5 \cos(\beta_5 x_5) + c_5 \sinh(\beta_5 x_5) + d_5 \cosh(\beta_5 x_5) \tag{A.33}$$

$$Y_6(x_6) = a_6 J_0\left(2\omega\sqrt{\frac{x_6}{g}}\right) \tag{A.34}$$

Equations (A.29) to (A.33) can also be expressed in matrix form.

$$Y_1(x_1) = \phi_1(x_1)\alpha_1 \tag{A.35}$$

$$\phi_1(x_1) = \begin{bmatrix}\sin(\beta_1 x_1) & \cos(\beta_1 x_1) & \sinh(\beta_1 x_1) & \cosh(\beta_1 x_1)\end{bmatrix} \tag{A.36}$$

$$\alpha_1 = \begin{bmatrix}a_1 & b_1 & c_1 & d_1\end{bmatrix}^T \tag{A.37}$$

The composite beam is fixed at $x_1 = 0$ therefore the applicable boundary condition at that point is:

$$Y_1(0) = 0$$

$$\frac{dY_1(0)}{dx} = 0$$

Therefore, applying these to $Y_1(x_1)$ results in the elimination of c_1 and d_1:

$$Y_1(x_1) = a_1[\sin(\beta_1 x_1) - \sinh(\beta_1 x_1)] + b_1[\cos(\beta_1 x_1) - \cosh(\beta_1 x_1)] \tag{A.38}$$

$$\phi_1(x_1) = \begin{bmatrix}\sin(\beta_1 x_1) - \sinh(\beta_1 x_1) & \cos(\beta_1 x_1) - \cosh(\beta_1 x_1)\end{bmatrix} \tag{A.39}$$

$$\alpha_1 = \begin{bmatrix}a_1 & b_1\end{bmatrix}^T \tag{A.40}$$

The next boundary condition requires that the displacement, slope, moment and shear force at the interface between Segment 1 and Segment 2 be equal:

$$Y_1(l_1) = Y_2(0) \tag{A.41}$$

$$\frac{dY_1(l_1)}{dx} = \frac{dY_2(0)}{dx} \tag{A.42}$$

$$E_1 I_1 \frac{d^2 Y_1(l_1)}{dx^2} = E_2 I_2 \frac{d^2 Y_2(0)}{dx^2} \tag{A.43}$$

$$E_1 I_1 \frac{d^3 Y_1(l_1)}{dx^3} = E_2 I_2 \frac{d^3 Y_2(0)}{dx^3} \tag{A.44}$$

These compatibility conditions can be expressed in matrix form as:

$$\Phi_1(l_1)\alpha_1 = \Phi_2(0)\alpha_2 \tag{A.45}$$

$$\alpha_1 = [a_1 \quad b_1]^T \tag{A.46}$$

$$\alpha_2 = [a_2 \quad b_2 \quad c_2 \quad d_2]^T \tag{A.47}$$

$$\Phi_1(l_1) = \begin{bmatrix} \phi_1(l_1) \\ \frac{d\phi_1(l_1)}{dx} \\ E_1I_1\frac{d^2\phi_1(l_1)}{dx^2} \\ E_1I_1\frac{d^3\phi_1(l_1)}{dx^3} \end{bmatrix} \qquad \Phi_2(0) = \begin{bmatrix} \phi_2(0) \\ \frac{d\phi_2(0)}{dx} \\ E_2I_2\frac{d^2\phi_2(0)}{dx^2} \\ E_2I_2\frac{d^3\phi_2(0)}{dx^3} \end{bmatrix} \tag{A.48}$$

$$\phi_1(x_1) = \begin{bmatrix} \sin(\beta_1 x_1) - \sinh(\beta_1 x_1) & \cos(\beta_1 x_1) - \cosh(\beta_1 x_1) \end{bmatrix} \tag{A.49}$$

$$\phi_2(x_2) = \begin{bmatrix} \sin(\beta_2 x_2) & \cos(\beta_2 x_2) & \sinh(\beta_2 x_2) & \cosh(\beta_2 x_2) \end{bmatrix} \tag{A.50}$$

Although Φ_1 and Φ_2 are written above as four element column vectors, ϕ_1 is a 2 element row vector and ϕ_2 is a 4 element row vector. Therefore Φ_1 is a 4x2 matrix and Φ_2 is a 4x4 matrix. Using these relations α_2 can be re-written in terms of α_1 and the transformation function T_1.

$$\alpha_2 = \Phi_2(0)^{-1}\Phi_1(l_1)\alpha_1 \tag{A.51}$$

$$T_1 = \Phi_2(0)^{-1}\Phi_1(l_1) \tag{A.52}$$

$$\alpha_2 = T_1\alpha_1 \tag{A.53}$$

$$Y_2(x_2) = \phi_2(x_2)\alpha_2 = \phi_2(x_2)T_1\alpha_1 \tag{A.54}$$

Using the same procedure the compatibility equations for Segment 2 and Segment 3 are derived below.

$$Y_2(l_2) = Y_2(0) \tag{A.55}$$

$$\frac{dY_2(l_2)}{dx} = \frac{dY_2(0)}{dx} \tag{A.56}$$

$$E_2I_2\frac{d^2Y_2(l_2)}{dx^2} = E_3I_3\frac{d^2Y_3(0)}{dx^2} \tag{A.57}$$

$$E_2I_2\frac{d^3Y_2(l_2)}{dx^3} = E_3I_3\frac{d^3Y_3(0)}{dx^3} \tag{A.58}$$

This leads to the transformation function (T_2) which relates α_2 and α_3.

$$\alpha_3 = \Phi_3(0)^{-1}\Phi_2(l_2)\alpha_2 \tag{A.59}$$

$$T_2 = \Phi_3(0)^{-1}\Phi_2(l_2) \tag{A.60}$$

$$\alpha_3 = T_2\alpha_2 = T_2T_1\alpha_1 \tag{A.61}$$

$$Y_3(x_3) = \phi_3(x_3)\alpha_3 = \phi_3(x_3)T_2T_1\alpha_1 \tag{A.62}$$

Figure A.2 shows a point mass at the interface between Segment 3 and Segment 4 which represents the mass of the damper fluid. This introduces additional shear force and requires slightly different compatibility conditions:

$$Y_3(l_3) = Y_4(0) \tag{A.63}$$

$$\frac{dY_3(l_3)}{dx} = \frac{dY_4(0)}{dx} \tag{A.64}$$

$$E_3 I_3 \frac{d^2 Y_3(l_3)}{dx^2} = E_4 I_4 \frac{d^2 Y_4(0)}{dx^2} \tag{A.65}$$

$$E_3 I_3 \frac{d^3 Y_3(l_3)}{dx^3} = E_4 I_4 \frac{d^3 Y_4(0)}{dx^3} - \omega^2 M_d Y_4(0) \tag{A.66}$$

Using the same procedure as before:

$$\alpha_4 = \Phi_4(0)^{-1} \Phi_3(l_3) \alpha_3 \tag{A.67}$$

$$T_3 = \Phi_4(0)^{-1} \Phi_3(l_3) \tag{A.68}$$

$$\alpha_4 = T_3 \alpha_3 = T_3 T_2 \alpha_2 = T_3 T_2 T_1 \alpha_1 \tag{A.69}$$

$$Y_4(x_4) = \phi_4(x_4) \alpha_4 = \phi_4(x_4) T_3 T_2 T_1 \alpha_1 \tag{A.70}$$

Figure A.2 also shows a point mass at the interface between Segment 4 and Segment 5 which represents the inertial force from the movement of the swinging chain.

$$Y_4(l_4) = Y_5(0) \tag{A.71}$$

$$\frac{dY_4(l_4)}{dx} = \frac{dY_5(0)}{dx} \tag{A.72}$$

$$E_4 I_4 \frac{d^2 Y_4(l_4)}{dx^2} = E_5 I_5 \frac{d^2 Y_5(0)}{dx^2} \tag{A.73}$$

$$E_4 I_4 \frac{d^3 Y_4(l_4)}{dx^3} = E_5 I_5 \frac{d^3 Y_5(0)}{dx^3} + F_c \tag{A.74}$$

The force exerted by the hanging chain on the tube can be accounted for by considering the y component of the chain tension (P). The following discussion assumes that the angle (θ) is small and therefore utilizes the small angle approximations.

$$P(x_6) = m_6 g x_6 \tag{A.75}$$

$$P_y = P(l_6) sin(\theta) \tag{A.76}$$

$$sin(\theta) \sim \frac{dY_6(l_6)}{dx_6} \tag{A.77}$$

$$F_c = P_y = P(l_6)\frac{dY_6(l_6)}{dx_6} = m_6 g l_6 \frac{dY_6(l_6)}{dx_6} \tag{A.78}$$

The expression above for F_c includes the term a_6. In order to proceed this must be expressed in terms of α_4 or α_5. To achieve this we can utilize the boundary condition at the chain attachment point. At this location the displacements of Segment 4, Segment 5 and Segment 6 are by necessity identical. This requirement for co-location is actually two boundary conditions, we have used the first in the compatibility conditions for Segment 4 and 5 ($Y_4(l_4) = Y_5(0)$). The second condition can be expressed as shown below.

$$Y_6(l_6) = Y_5(0) \tag{A.79}$$

$$a_6 J_0\left(2\omega\sqrt{\frac{l_6}{g}}\right) = \phi_5(0)\alpha_5 \tag{A.80}$$

$$a_6 = \frac{\phi_5(0)\alpha_5}{J_0\left(2\omega\sqrt{\frac{l_6}{g}}\right)} \tag{A.81}$$

$$T_5 = \frac{\phi_5(0)}{J_0\left(2\omega\sqrt{\frac{l_6}{g}}\right)} \tag{A.82}$$

$$\alpha_6 = a_6 = T_5\alpha_5 \tag{A.83}$$

$$Y_6(x_6) = a_6 J_0\left(2\omega\sqrt{\frac{x_6}{g}}\right) = T_5\alpha_5 J_0\left(2\omega\sqrt{\frac{x_6}{g}}\right) \tag{A.84}$$

$$\begin{aligned} F_c &= \frac{-m_6 g l_6 a_6 \omega}{l_6}\sqrt{\frac{l_6}{g}} J_1\left(2\omega\sqrt{\frac{l_6}{g}}\right) \\ &= \frac{-m_6 g l_6 T_5 \alpha_5 \omega}{l_6}\sqrt{\frac{l_6}{g}} J_1\left(2\omega\sqrt{\frac{l_6}{g}}\right) \end{aligned} \tag{A.85}$$

Eliminating a_6 in the expression for $\frac{dY_6(l_6)}{dx_6}$ allows us to express F_c in terms of α_5 and proceed as before:

$$\alpha_5 = \Phi_5(0)^{-1}\Phi_4(l_4)\alpha_4 \tag{A.86}$$

$$T_4 = \Phi_5(0)^{-1}\Phi_4(l_4) \tag{A.87}$$

$$\alpha_5 = T_4\alpha_4 = T_4T_3\alpha_3 = T_4T_3T_2\alpha_2 = T_4T_3T_2T_1\alpha_1 \tag{A.88}$$

$$Y_5(x_5) = \phi_5(x_5)\alpha_5 = \phi_5(x_5)T_4T_3T_2T_1\alpha_1 \tag{A.89}$$

Finally, the boundary conditions at the end point of Segment 5 are represented by Equations (A.90) and (A.91).

$$E_5I_5\frac{d^2Y_5(l_5)}{dx^2} = 0 \tag{A.90}$$

$$E_5I_5\frac{d^3Y_5(l_5)}{dx^3} + \omega^2M_5Y_5(l_5) = 0 \tag{A.91}$$

This system of equations is shown in matrix form below. Note that $\phi_5(l_5)$ is a four element row vector and therefore $\Phi_5(l_5)$ is a 2x4 matrix. The form written below has not been expanded to show all the individual terms in $\Phi_5(l_5)$.

$$\Phi_5(l_5)\alpha_5 = \begin{bmatrix} E_5I_5\frac{d^2\phi_5(l_5)}{dx^2} \\ E_5I_5\frac{d^3\phi_5(l_5)}{dx^3} + \omega^2M_5\phi_5(l_5) \end{bmatrix} \begin{bmatrix} a_5 \\ b_5 \\ c_5 \\ d_5 \end{bmatrix} = 0 \tag{A.92}$$

By using the transformations T_1 through T_4 we can replace the references to α_5 and re-write the system of equations in terms of α_1. Once written in this form we can construct a 2x2 matrix system by grouping $\Phi_5(l_5)$ and the transformation matrices:

$$\Phi_5(l_5)\alpha_5 = \Phi_5(l_5)T_4T_3T_2T_1\alpha_1 = Z\alpha_1 = 0 \tag{A.93}$$

$$Z\alpha_1 = \begin{bmatrix} Z_{11} & Z_{12} \\ Z_{21} & Z_{22} \end{bmatrix} \begin{bmatrix} a_1 \\ b_1 \end{bmatrix} = 0 \tag{A.94}$$

The frequency equation is obtained by taking the determinant of Z the natural frequencies (eigenvalues) are the roots of that equation. Once a natural frequency is found this can be substituted back into Z and the corresponding coefficients a_1 and b_1 can be determined.

$$\begin{vmatrix} Z_{11} & Z_{12} \\ Z_{21} & Z_{22} \end{vmatrix} = 0 \tag{A.95}$$

Using the resulting frequencies the response of both the beam and chain can be determined using Equation (A.94) to solve for b_1 in terms of a_1 for each natural frequency.

$$b_1 = a_1 \left(\frac{-Z_{11}}{Z_{12}} \right) \tag{A.96}$$

The term a_1 is an arbitrary scaling factor which can be determined in a variety of ways. The scaling below is equivalent to what is generally described as mass normalization. The kinetic energy (E_k) of the mode of vibration is set to equal the frequency of vibration squared (ω_n^2). Another scaling technique is to set the maximum value of the mode shape to one such that the amplitude is contained within the envelope between -1 to +1.

$$E_k = \omega_n^2 = a_1^2 \omega_n^2 \left(A + B \right) \tag{A.97}$$

$$A = \sum_i^n \left(\int_0^{l_i} \rho_i A_i \left[\frac{Y_i(x_i)}{a_1} \right]^2 dx \right) \tag{A.98}$$

$$B = \sum_i^n \left(M_i \left[\frac{Y_i(l_i)}{a_1} \right]^2 \right) \tag{A.99}$$

$$a_1 = \sqrt{1/(A+B)} \tag{A.100}$$

Once a_1 is determined the functions $Y_1(x_1)$, $Y_2(x_2)$, $Y_3(x_3)$, $Y_4(x_4)$, $Y_5(x_5)$ and $Y_6(x_6)$ can be established for the applicable angular natural frequency (ω_n). These functions where calculated and plotted, using Maxima (2014), over the composite beam length coordinate (x) using the coordinate transformations indicated in Figure A.2 and Equation (A.101). Figure A.3 shows Y_1 to Y_5 plotted for each of the first three predicted natural frequencies 9 Hz, 183 Hz and 550 Hz. The mode shapes in Figure A.3 were calculated assuming that $F_c = 0$ due to the very small relative mass of the chain when compared to the tube.

The complete solution including chain coupling was also solved and the 1st, 2nd and 3rd beam modes (though they now represent higher order modes of the composite system) where found to be identical to those calculated without coupling. However, the coupled solution has many more natural frequencies most of which correspond roughly to the natural frequencies of the hanging chain without coupling. This very weak coupling is due to the very small ratio of chain mass to tube mass (M_c/M_t) and the poor frequency tuning ratio ($\omega_{n,c}/\omega_{n,t}$).

$$x_j = x - \sum_{i=1}^{j-1} l_i \quad \text{for} \quad \sum_{i=1}^{j-1} l_i \leq x \leq \sum_{i=1}^{j} l_i \tag{A.101}$$

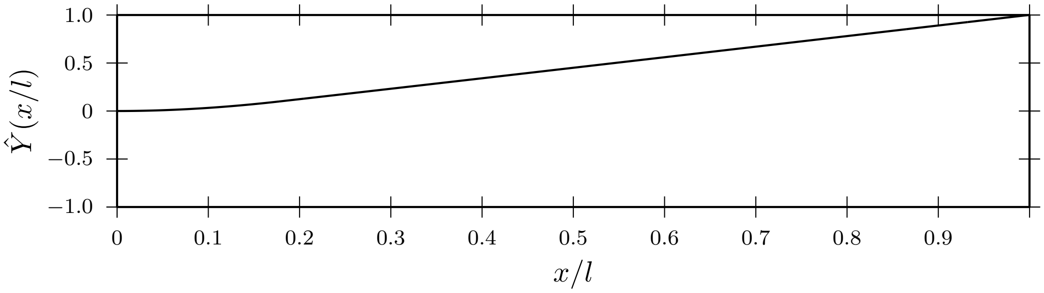

(a) First Mode (9Hz).

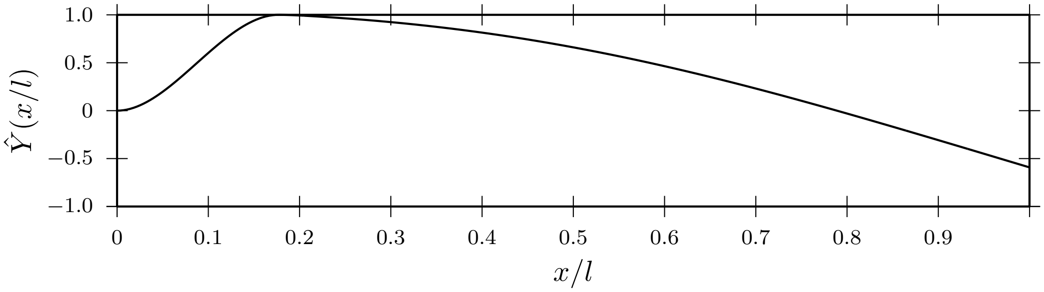

(b) Second Mode (183Hz).

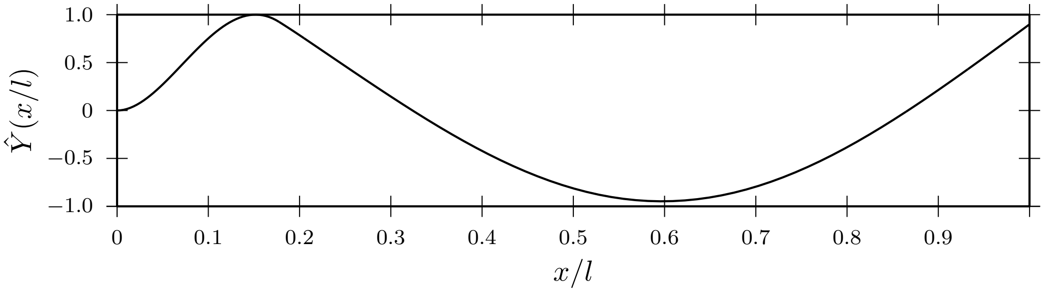

(c) Third Mode (550Hz).

Figure A.3: Predicted mode shapes and natural frequencies of model tube. First three mode shapes shown in terms of $\hat{x} = x/l$ and with the amplitude normalized to the range -1 to +1. Mode shapes and frequencies were calculated, using Maxima (2014), based on the formulation described in Section A.2

Appendix B.

Instrument Calibrations and Uncertainty

This appendix contains descriptions of the calibration methods and uncertainty estimates for the instrumentation used to collect experimental data presented for this thesis.

B.1 Linear Least Squares Regression

Controlled calibrations were carried out on the various transducers used to acquire the experimental data, these include strain gauges, pressure transducers and hot-wire probes. In each case a series of known inputs (the independent or stimulus variable) were used to characterize the system output (the dependent or response variable). The inputs were appropriate to each transducer and in all cases the output was a voltage. This procedure was used to generate calibration plots of voltage versus physical input. In each case a functional relationship for output voltage in terms of the physical input was calculated by means of curve fitting using linear least squares regression (linear regression). The basic theoretical background and implementation of linear regression is described in detail by Chapra and Canale (1998). Linear regression produces a functional relationship in the form represented by Equation (B.1) which defines a polynomial of order m. However, polynomial regression is rarely required for establishing calibration curves. Instead straight line regression is typically adequate and more appropriate as most transducers have a constant voltage sensitivity (slope) with respect to the physical unit being measured. Straight line regression is achieved by setting the order of the polynomial to $m = 1$ as shown by Equation (B.2). From Equations (B.1) and (B.2) x and y represent the independent and dependent variables, respectively. The terms a_k are the polynomial coefficients and e is the residual.

$$y_f = \left(\sum_{k=0}^{m} a_k x^k \right) + e \tag{B.1}$$

$$y_f = \left(\sum_{k=0}^{1} a_k x^k \right) + e = a_0 + a_1 x + e \tag{B.2}$$

The basic aim of linear regression is to find a functional relationship which minimizes the sum of squares of the residuals. The residual is defined, for each of the n measured calibration points (x, y), as the difference between the actual measured value y_i and the value predicted by the linear regression representation. Equation (B.3) shows the expression for the sum of squares of the residuals for a polynomial and Equation (B.4) shows the simplified form for a straight line.

$$S_e = \sum_{i=1}^{n} e_i^2 = \sum_{i=1}^{n} (y_i - y_{fi})^2 = \sum_{i=1}^{n} \left(y_i - \sum_{k=0}^{m} a_k x_i^k \right)^2 \tag{B.3}$$

$$S_e = \sum_{i=1}^{n} (y_i - a_0 - a_1 x_i)^2 \tag{B.4}$$

To find the coefficients a_k which minimize S_e a system of equations can be developed by differentiating S_e with respect to each unknown coefficient and setting the result equal to zero. This results in m simultaneous equations which can be solved using linear algebra methods such as Gaussian elimination.

$$j = 0 \to m, \qquad \frac{\partial S_e}{\partial a_j} = \frac{\partial}{\partial a_j} \left[\sum_{i=1}^{n} \left(y_i - \sum_{k=0}^{m} a_k x_i^k \right)^2 \right] = 0 \tag{B.5}$$

Linear regression assumes that the independent variable x is known exactly and contains no error. This is not practical as there is error present in every measurement and process regardless of efforts to eliminate it. However, it is reasonable to minimize the error in x and to ensure that such error is much less than that present in the dependent variable y. The theoretical limitations, statistical properties and analysis of linear regression results are discussed in Dunn (2010), Devore (1999) and Draper and Smith (1998), these references are listed in order of increasing theoretical and statistical rigor.

For any set of measurement data (x, y) there are a set of statistical parameters which can be calculated directly from the data and which are pertinent to linear regression. These parameters include the mean of x $(\bar{x})$, the mean of y $(\bar{y})$, the sum of squares of x (S_{xx}), the sum of squares of y (S_{yy}) and the sum of the product of x and y (S_{xy}).

$$\bar{x} = \left(\frac{1}{n}\right)\sum_{i=1}^{n} x_i \tag{B.6}$$

$$\bar{y} = \left(\frac{1}{n}\right)\sum_{i=1}^{n} y_i \tag{B.7}$$

$$S_{xx} = \sum_{i=1}^{n} \left(x_i - \bar{x}\right)^2 \tag{B.8}$$

$$S_{yy} = \sum_{i=1}^{n} \left(y_i - \bar{y}\right)^2 \tag{B.9}$$

$$S_{xy} = \sum_{i=1}^{n} \left(x_i - \bar{x}\right)\left(y_i - \bar{y}\right) \tag{B.10}$$

In the special case of straight line regression the coefficients a_0 and a_1 from Equation (B.2) may be calculated directly from these parameters:

$$a_1 = S_{xy}/S_{xx} \tag{B.11}$$

$$a_0 = \bar{y} - a_1\bar{x} \tag{B.12}$$

Once the regression parameters are known the statistical relationship between the fit and the data can be assessed. Typical statistical parameters which are used to assess linear regression results include: the sum of squares of regression (SSR), the sum of squares of the error (SSE), the standard error (S_{yx}) and the statistical degrees of freedom (ν).

$$SSR = \sum_{i=1}^{n} \left(y_{fi} - \bar{y}\right)^2 \tag{B.13}$$

$$SSE = \sum_{i=1}^{n} \left(y_i - y_{fi}\right)^2 \tag{B.14}$$

$$S_{yx} = \sqrt{\frac{SSE}{\nu}} = \sqrt{\frac{\sum_{i=1}^{n} \left(y_i - y_{fi}\right)^2}{n-2}} \tag{B.15}$$

$$\nu = n - m - 1 \tag{B.16}$$

These parameters are not typically interpreted on their own as the absolute values depend on the respective units for each of x and y. Instead these in combination with the statistical values based on only the data can be used to calculate correlation coefficients, confidence intervals, prediction intervals, etc. The coefficient of determination r^2 is the most commonly used parameter for assessing the quality of a curve fit. The value of r^2 is always bounded between 0 and 1, generally values greater than 0.9 represent a significant correlation between the fit and the data.

$$r^2 = 1 - \frac{SSE}{S_{yy}} = \frac{SSR}{S_{yy}} \tag{B.17}$$

The value of y_f represented by a curve fit which is calculated using linear regression is an estimate of the mean value of y at x. However, y is a random variable and it is important to estimate the error in y. Note that at no point during the preceding discussion was the error in y quantified in terms of the actual estimated error in each measurement. Instead the error in y is dependent on the statistics of the measured values and the curve fit, notwithstanding the actual errors in the values of the measured y. This is similar to single value statistical estimation where many measurements are used to establish the standard deviation and the standard deviation squared represents the expected variance in y, without knowledge of the actual measurement errors involved. The parameter Syx represents the standard error of the fit which is analogous to the standard deviation used in single value statistics. Confidence intervals extend the concept of mean value prediction to probable value prediction. A confidence interval sets upper and lower limits which are associated with some probability that either a previously measured value of y or a future prediction of y will lie between the two curves for each value of x. There are many types of confidence intervals each with it's own purpose, the current discussion will be constrained to the three most relevant for the current purpose. Equation (B.18) represents the confidence interval of the mean response. For a large sample of y_i at a corresponding x this interval establishes the probability range of the corresponding $\bar{y}_i$. This interval is a pair of hyperbolic curves above and below the fit line. Equation (B.19) represents the precision interval which establishes the probability range for values of y_i corresponding to a particular x with a large sample population. The precision interval is a set of straight lines parallel to the fit and representing the upper and lower bounds of the interval, it is wider than the preceding interval. Equation (B.20) represents the confidence interval for prediction of x_i from a measured y_i this interval is also hyperbolic and is slightly wider than each of the preceding intervals. This interval is used for inverse regression (determination of x_i from y_i) by drawing a straight horizontal line at the y_i the corresponding mean value $\bar{x}_i$ and the upper and lower estimates x_u, x_l are determined by where this line intersects the fit and the lines describing the interval. Equations (B.18) to (B.20) all include the term $t_{\nu,P}$ which denotes the value of the two sided Student t-distribution for ν statistical degrees of freedom and probability P.

$$\bar{y} = y_{fi} \pm t_{\nu,P} S_{yx} \sqrt{\frac{1}{n} + \frac{(x_i - \bar{x})^2}{S_{xx}}} \tag{B.18}$$

$$y = y_{fi} \pm t_{\nu,P} S_{yx} \tag{B.19}$$

$$y = y_{fi} \pm t_{\nu,P} S_{yx} \sqrt{\frac{1}{q} + \frac{1}{n} + \frac{(x_i - \bar{x})^2}{S_{xx}}} \tag{B.20}$$

At this point we have defined how to calculate a calibration curve using linear regression, how to assess the adequacy of the curve and how to specify the confidence interval. However, the goal of a calibration curve is to define a curve so that a measured y can be used to determine x. This is the exact inverse procedure to calibration itself and is thus called inverse regression. Since the quantity of interest is actually x under measurement conditions, we need confidence intervals on values of x not y. Inverse regression is discussed in considerable detail in Draper and Smith (1998). However that discussion is focused on new observations of y under fixed conditions, such as adding one more data point during calibration. Confidence bands on values of x are derived by manipulating Equation (B.20). However, new measurements of y are rarely taken under fixed conditions (using the same equipment and subject to the same systematic and random errors). Instead the calibration curve is generated and expected to represent the mean response. Therefore it is more appropriate to derive a portable estimation of the confidence bands on x using Equation (B.18) and assess the new measurement errors independently. Whereas measurement errors were inherently accounted in the inverse calibration derived in Draper and Smith (1998) since new measurements were assumed to be acquired under fixed conditions.

The hyperbolic shape of Equation (B.18) is dependent on the term $(x_i - \bar{x})^2/S_{xx}$ for moderate to large datasets this term should be relatively small. If we neglect this term as suggested by Figliola and Beasley (2006) we essentially assume that the uncertainty at $\bar{x}$ is representative of the uncertainty over all x of interest. This removes the dependence on x_i and simplifies the inverse regression problem significantly. Using this simplifying assumption Equation (B.23) represents the upper and lower estimates x_u, x_l of x corresponding to specific values of y. In this relationship the uncertainty $e_{f,y}$ is constant and represents the straight line upper and lower bounds to the fitted line. From

$e_{f,y}$ and the assumption of straight line regression we can derive an estimate of the corresponding $e_{f,x}$ as represented by Equation (B.24).

$$\begin{aligned} e_{f,y} &= \pm t_{\nu,P} S_{yx} \sqrt{\frac{1}{n} + \frac{(x_i - \bar{x})^2}{S_{xx}}} \\ &\approx \pm t_{\nu,P} \frac{S_{yx}}{\sqrt{n}} \end{aligned} \tag{B.21}$$

$$y = a_0 + a_1 x \pm e_{f,y} \tag{B.22}$$

$$\left.\begin{matrix} x_u \\ x_l \end{matrix}\right\} = \left(\frac{y - a_0}{a_1}\right) \pm \left(\frac{e_{f,y}}{a_1}\right) = x \pm e_{f,x} \tag{B.23}$$

$$e_{f,x} \approx \pm t_{\nu,P} \frac{S_{yx}}{a_1 \sqrt{n}} \tag{B.24}$$

So far we have naively assumed that Equation (B.1) represents an appropriate and adequate fit model. However, many physical systems are governed by relationships that are not linear with respect to the unknown coefficients a_k. Table B.1 includes examples of functions which are nonlinear and the corresponding transformations which can be used to produce a linear function with transformed variables. Through manipulation into a linear form in terms of y' and x' these functions can be fitted using linear regression. However, the fitted function and all relative statistical properties would be in terms of y' and x'. Therefore although linear regression will minimize the square root of sum of squares of the residuals of y', the fit may not represent the minimum square root of sum of squares of the residuals of y. Also the error structure of the original variable y may be altered from additive to multiplicative as shown in Equation (B.27) for the example of a Power function. This and other topics relating to errors and uncertainty are discussed in Appendix B.2

$$y' = \log(\alpha) + \beta x' \pm e_y \tag{B.25}$$

$$\log(y) = \log(\alpha) + \beta \log(x) \pm e_y \tag{B.26}$$

$$y = \left(\alpha x^{\beta}\right) 10^{\pm e_y} \tag{B.27}$$

Function	Equation	Transformations	Linear Form
Exponential	$y = \alpha e^{\beta x}$	$y' = \ln(y)$	$y' = \ln(\alpha) + \beta x$
Power	$y = \alpha x^{\beta}$	$y' = \log(y), x' = \log(x)$	$y' = \log(\alpha) + \beta x'$
Logarithmic	$y = \alpha + \beta \log_b(x)$	$x' = log_b(x)$	$y = \alpha + \beta x'$
Reciprocal	$y = \alpha + \beta(1/x)$	$x' = (1/x)$	$y = \alpha + \beta x'$

Table B.1: Linear Transforms.

B.2 Uncertainty Analysis

The concept of uncertainty was discussed in Section B.1 in terms of statistical confidence intervals. When measuring quantities there is always some finite error or uncertainty in the result. Uncertainties are typically classified into two categories systematic and random. Figliola and Beasley (2006) discusses uncertainty analysis including the classification of errors in detail. From Section B.1, Equations (B.21) and (B.24) are related by the constant slope of the regression line a_1. In it's present form this result can only be used for straight lines. It is important to realize that Equations (B.21) and (B.24) represent a specific example of a very general rule as discussed in Figliola and Beasley (2006). For a variable y which is a function of x the resultant uncertainty in y, δy, due to uncertainty in x, δx, is expressed by Equation (B.28).

$$\delta y = \frac{\partial y}{\partial x} \delta x \tag{B.28}$$

The combination of multiple uncertainties which are statistically independent (uncorrelated) can be accomplished using the square root of the sum of squares method (rss method). For a variable y which is a function of x_i the resultant uncertainty in y is expressed by Equation (B.30). The rss method represents the probable uncertainty in the resulting y value. Therefore all of the input errors should represent the same level of statistical confidence. An arbitrary but often used value of statistical confidence is 95%.

$$y = f(x_1, x_2, ...x_N) \tag{B.29}$$

$$\delta y = \sqrt{\sum_{i=1}^{N} \left(\frac{\partial y}{\partial x} \delta x \right)^2} \tag{B.30}$$

The combination of multiple uncertainties which are not statistically independent (correlated) can be accomplished using the sum of absolute value of the errors. Again for a variable y which is a function of x_i the resultant uncertainty in y is expressed by Equation (B.31). This method represents the maximum uncertainty in the resulting y value. Accuracy specifications for measurement equipment are typically generated using Equation (B.31).

$$\delta y = \sum_{i=1}^{N} \left(\left| \frac{\partial y}{\partial x} \right| \delta x \right) \tag{B.31}$$

Table B.2 shows the manufacturer uncertainty/accuracy ratings for the three primary measurement instruments used for acquiring the experimental data. The instruments listed in Table B.2 were used to measure the transducer/signal conditioner output voltages. The Fluke 70 Series II multimeter was used to measure output voltages for all of the calibration curves in this appendix. The Fluke meter is a multi-range device and its accuracy is specified in two components, the first as a percentage of the reading (RD) and the second as a percentage of full scale output (FS). The manufacturer has formatted the total uncertainty specification such that it represents the maximum correlated uncertainty. The Agilent 35670A Dynamic Signal Analyzer (DSA) was used to measure the output voltage from the Vishay 2310 strain gauge amplifiers. The uncertainty/accuracy specification of the Agilent DSA is again provided as two components one dependent on the reading (RD) and one dependent on the full scale (FS) output. Unlike the Fluke specification the Agilent specification does not stipulate how these uncertainties should be combined. The National Instruments AT-MIO-16 data acquisition card was used for measuring the hotwire output voltages during the detailed velocity experiments. The uncertainty/accuracy specification for this device is provided as a one number value which is equal to the resolution. These represent the primary uncertainties in the voltage measurements. Sections B.3 through B.5 will discuss the calibration and operation of each transducer and measurement equipment setup including the related uncertainties in the measured physical quantities due to measurement uncertainties.

Instrument	Range	Resolution	Accuracy
Fluke 70 Series II	DC 0 to 0.32,3.2,32V	0.03125%FS	$\pm(0.5\%RD + 0.03125\%FS)$
Agilent 35670A	AC/DC $(-51$ to $27)dBV_{rms}$ in $2dB$ steps $(3.99m$ to $31.7)V_{pk}$	0.0019%FS	$\pm 2.92\%RD, \pm 0.025\%FS$
NI AT-MIO-16	AC/DC $\pm 10V$	$4.88mV(0.05\%FS)$	$\pm 4.88mV(0.05\%FS)$

Table B.2: Voltage Measuring Instrument Accuracy Ratings.

B.3 Strain Gauge Measurements

As discussed in Section 3.4.1 tube vibration amplitudes were monitored using strain gauges mounted to the tube supports. Vishay Micro-Measurements model WD-DY-125AD-350 strain gauges were utilized for this purpose. The strain gauges were mounted to the tube supports orthogonally such that the vibration amplitudes could be measured in both the transverse (y) and streamwise (z) directions as shown in Figure B.1. Each strain gauge was connected using a quarter wheatstone bridge circuit as shown in Figure B.2. Vishay 2310 signal conditioning amplifiers were used to supply the bridge excitation voltage (E_{ex}) and condition the output voltage (E_{out}) from each bridge circuit. The instrumented tubes were calibrated to determine the relationship between tube tip displacement and voltage output. The calibration plots are provided in Figures B.3 to B.7. Each Vishay 2310 amplifier was operated with the following settings during both calibration and experimental data acquisition: amplifier gain ($G = 1000$), bridge excitation voltage ($E_{ex} = 5\,\mathrm{V}$) and a low pass filter with a cut-off frequency (f_{cl}) of $100\,\mathrm{Hz}$ ($-3\,\mathrm{dB}$).

The calibration plots were generated using a standard height gauge to measure tube tip displacement. The height gauge had a resolution of $0.001\,\mathrm{in}$ and an accuracy rating of $\pm 0.001\,\mathrm{in}$. The height gauge was used to measure both the starting and ending position and therefore the maximum uncertainty in the displacement measurement was $\pm 0.002\,\mathrm{in}$. The resulting direct current (DC) voltage output from the Vishay 2310 amplifier was measured using a Fluke 70 Series II Multimeter. Table B.2 shows the maximum uncertainty (accuracy) ratings for the Fluke meter. Figures B.3 to B.7 are plotted with the measurement uncertainties shown as error bars, though in most of the plots these are not visible as they are so small.

The WD-DY series strain gauges are constructed of an isoelastic alloy, have a high gage factor and a high fatigue life. These gauges are intended for dynamic strain measurements since they are not temperature compensated and thus experience zero drift. Therefore, the only relevant parameter established in Figures B.3 to B.7 is the slope for each gauge as the y intercept is expected to fluctuate. Because of this expected zero drift the Vishay 2310 amplifiers were operated with the high pass, AC coupling, filter enabled, and filter (ac coupling) cut-off frequency (f_{ch}) of $1.7\,\mathrm{Hz}$ ($-3\,\mathrm{dB}$).

During the vibration experiments the output voltages from the strain gauge amplifiers were measured using an Agilent 35670A Dynamic Signal Analyzer. The manufacturers published accuracy specifications are provided in Table B.2. The measured voltages during experiments were effected by both the instrument measurement uncertainty (δE_m) and the calibration fit uncertainty (δE_c). The calibration uncertainty can be estimated using Equation (B.24).

These two sources of uncertainty are statistically independent and can thus be combined using the rss method via Equation (B.30).

The uncertainty in the voltage reading of the Agilent 35670A is dependent on the reading value and the full scale value. Therefore, to develop an estimate of the error we need to establish the maximum reading value and full scale range expected. During the vibration experiments the measured amplitudes were on the order of 5 to 10 % of a tube diameter and in all cases below 20 % of a tube diameter (approx 9 mm). As a conservative estimate we will use 9 mm as the maximum amplitude estimate. The voltage output corresponding to 9 mm can be calculated from the calibration plot and associated linear fit estimates. For the remaineder of this example we will use the values represented in Figure (a). Using the slope of the regression fit from Figure (a) (170.75 mV/mm) the expected reading value at 9 mm is 1536.75 mV. This corresponds to the nearest full scale range of ±1778.28 mV for the Agilent 35670A. From Table B.2 the error in the Agilent voltage reading is ±2.92 % of the reading and ±0.025 % of full scale. Note that Agilent does not stipulate how these errors should be combined. To be conservative we will adopt the maximum correlated error estimate for the combined Agilent voltage error. As shown below the resulting error estimate for the transverse displacement (y) of tube T13 is ±0.27 mm or ±0.6 % of a tube diameter. Note that this error estimate does not consider the error introduced by the Vishay 2310 amplifiers. The Vishay 2310 has it's own set of accuracy ratings provided by the manufacturer. However, much of the error reported by the manufacturer relates to the adjustable gain of the amplifier. The Vishay 2310 amplifiers were part of the calibration setup and the gain settings were not adjusted between calibrations and measurements.

Error estimate:

$$
\begin{aligned}
\delta E_m &= \pm\left(\left|\frac{2.92}{100} y_{max}\frac{\delta E}{\delta y}\right| + \left|\frac{0.025}{100} FS\right|\right) \\
&= \pm\left(\left|\frac{2.92}{100} 9\,\mathrm{mm}\frac{170.75\,\mathrm{mV}}{1\,\mathrm{mm}}\right| + \left|\frac{0.025}{100} 1778.28\,\mathrm{mV}\right|\right) \\
&= \pm\left(|44.87\,\mathrm{mV}| + |0.44\,\mathrm{mV}|\right) = \pm 45.31\,\mathrm{mV}
\end{aligned}
$$

$$
\begin{aligned}
\delta E_c &= \pm 11.47\,\mathrm{mV}(\text{from Figure (a)}) \\
\delta y &= \pm\sqrt{\left(\frac{\partial y}{\partial E}\delta E_m\right)^2 + \left(\frac{\partial y}{\partial E}\delta E_c\right)^2} \\
&= \pm\sqrt{\left(\frac{1\,\mathrm{mm}}{170.75\,\mathrm{mV}}45.31\,\mathrm{mV}\right)^2 + \left(\frac{1\,\mathrm{mm}}{170.75\,\mathrm{mV}}11.47\,\mathrm{mV}\right)^2} \\
&= \pm 0.27\,\mathrm{mm} \\
&= \pm 0.6\%\ \text{of Diameter}
\end{aligned}
$$

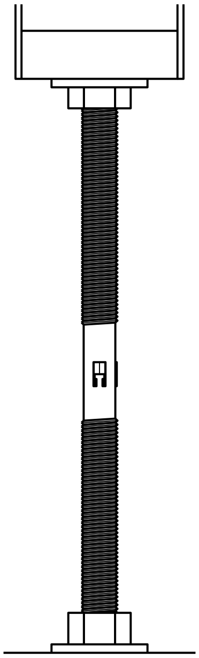

Figure B.1: Monitored tube strain gauge sub-assembly.

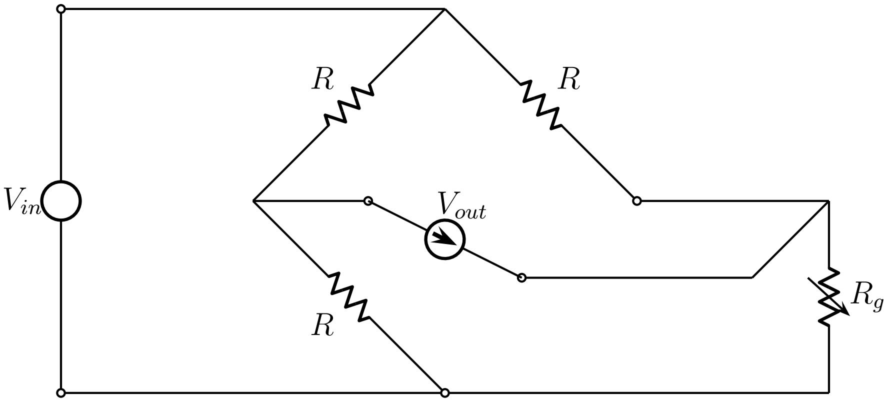

Figure B.2: Wheatstone bridge circuit with 3-wire gauge connection.

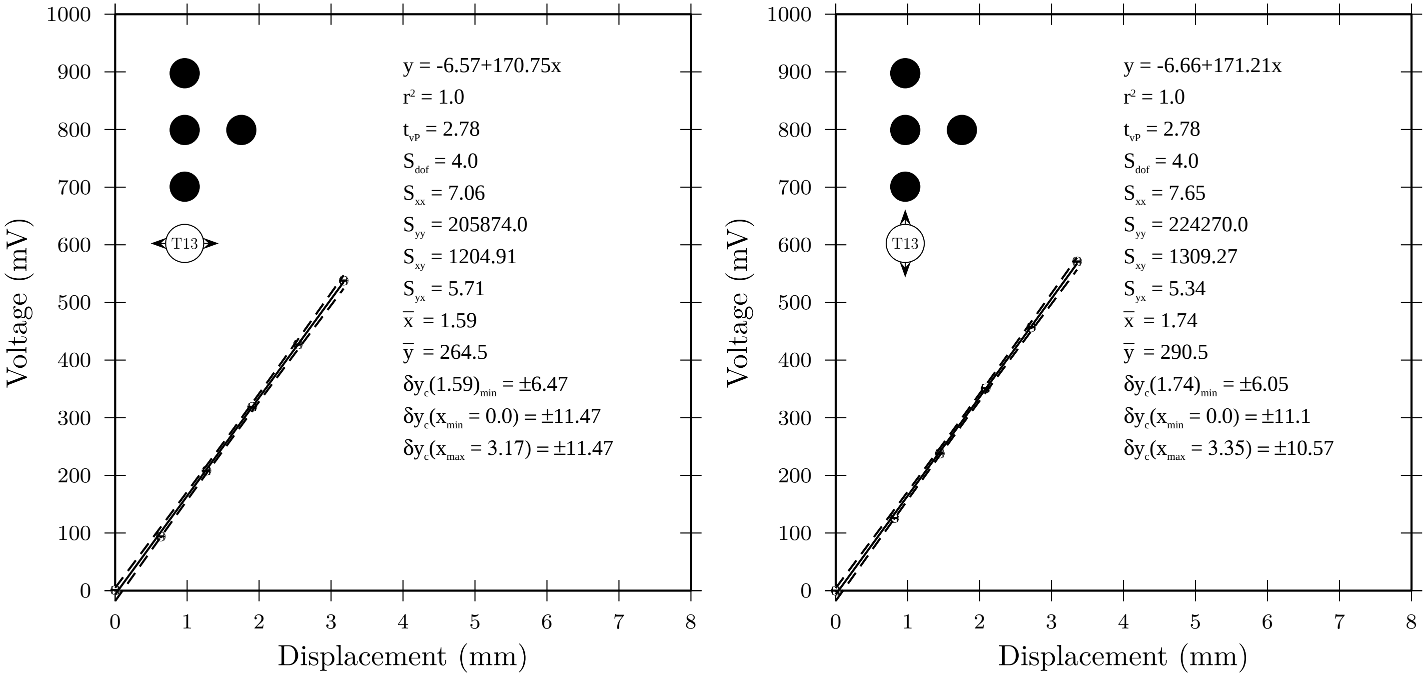

(a) Transverse Direction.

(b) Streamwise Direction.

Figure B.3: Tube T13 Strain Gauge Calibrations.

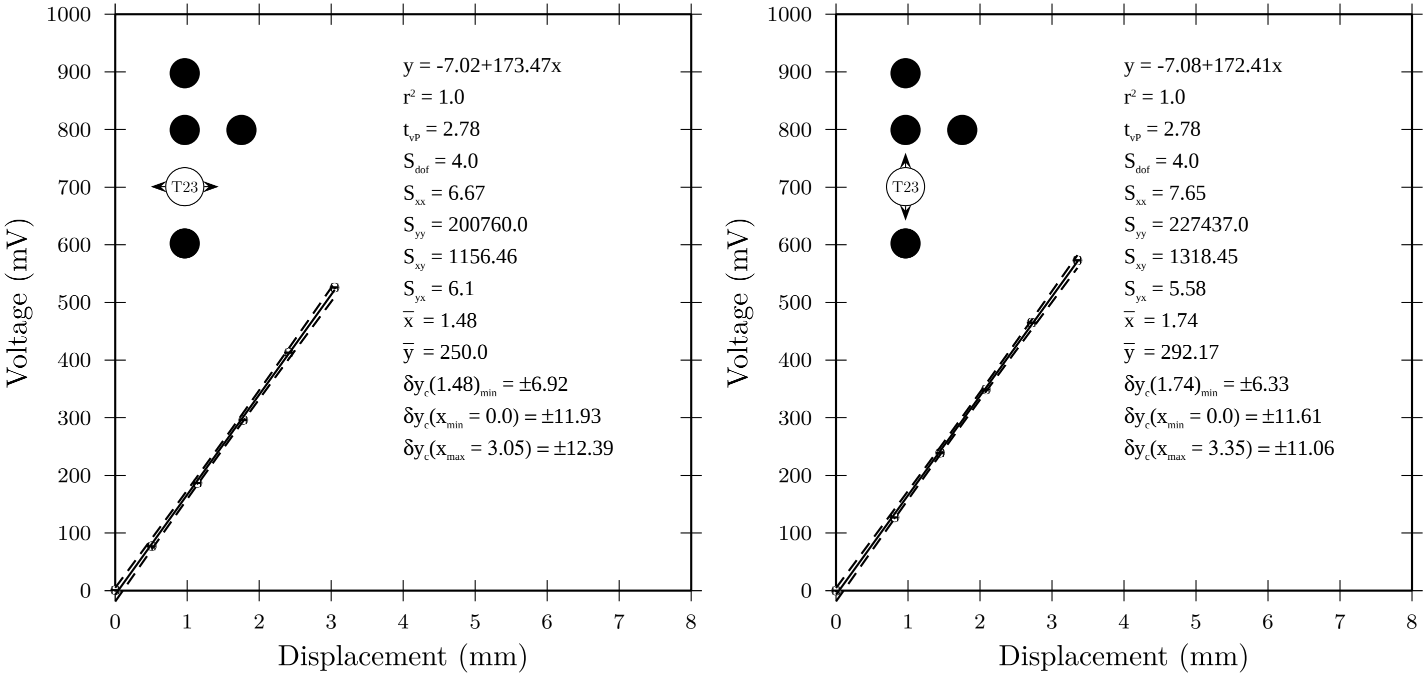

(a) Transverse Direction.

(b) Streamwise Direction.

Figure B.4: Tube T23 Strain Gauge Calibrations.

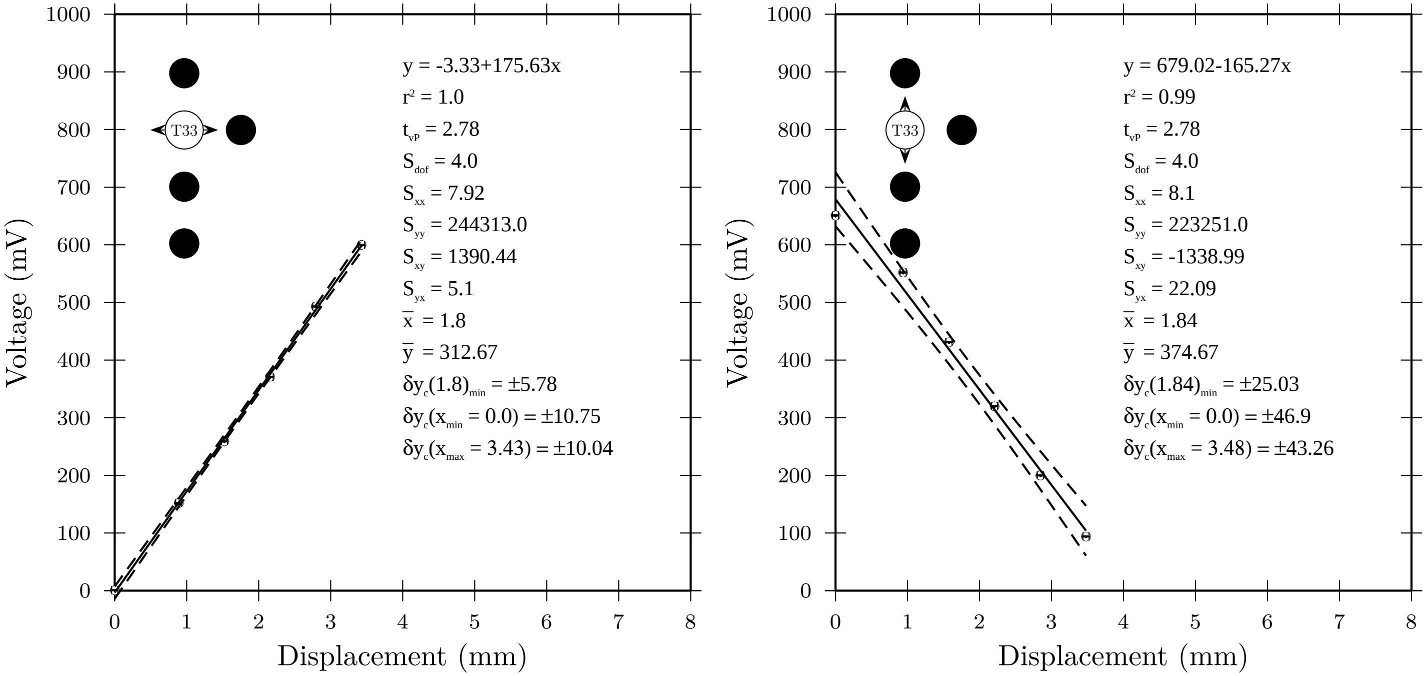

(a) Transverse Direction.

(b) Streamwise Direction.

Figure B.5: Tube T33 Strain Gauge Calibrations.

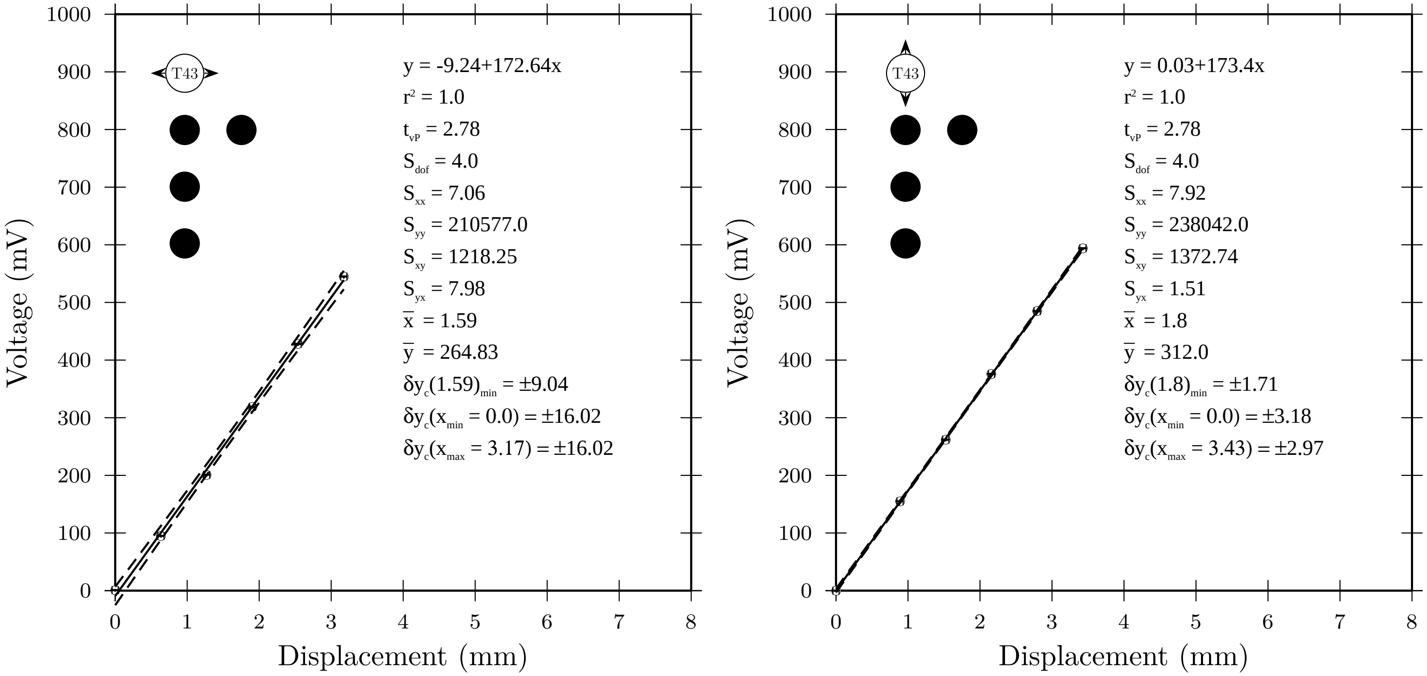

(a) Transverse Direction. **(b)** Streamwise Direction.

Figure B.6: Tube T43 Strain Gauge Calibrations.

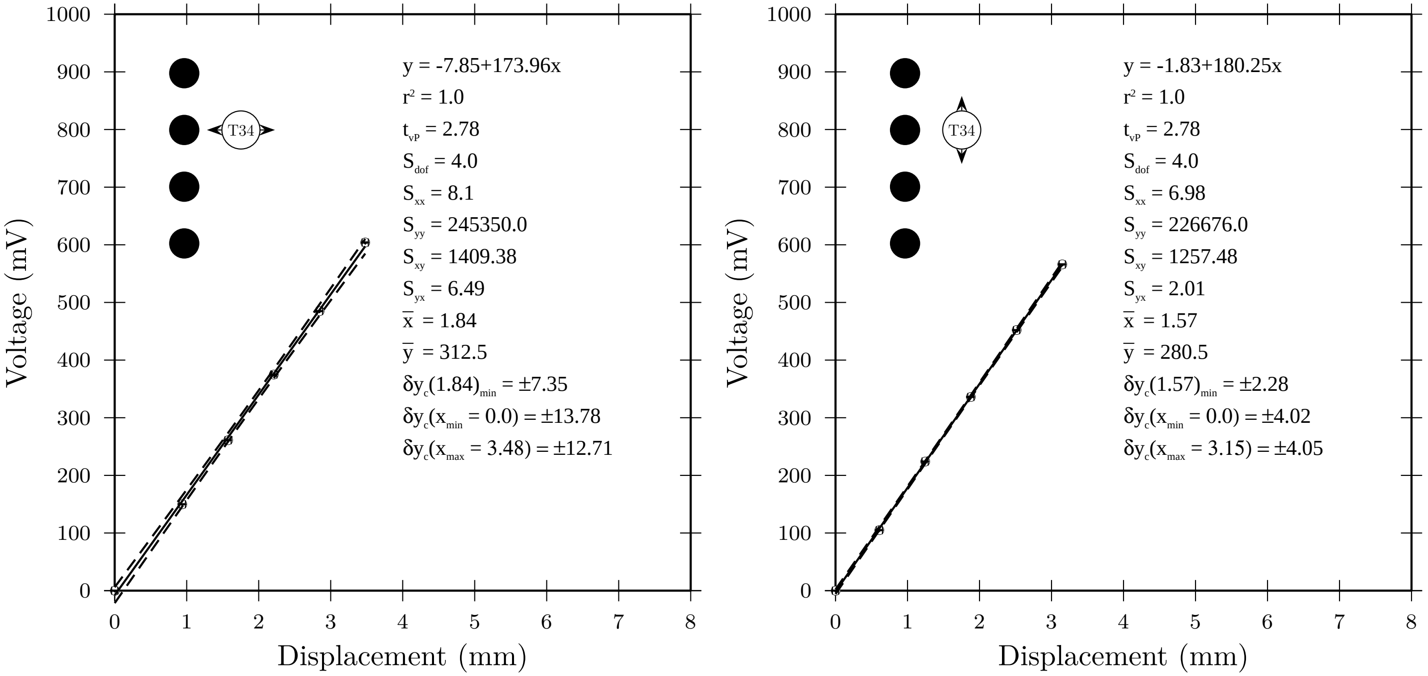

(a) Transverse Direction.

(b) Streamwise Direction.

Figure B.7: Tube T34 Strain Gauge Calibrations.

B.4 Pitot Static Tube Measurements

The wind tunnel mean flow velocity was measured during uniform flow experiments using a pitot-static tube. The induced pressure across the pitot-static tube was measured using an Ashcroft model XL-3-MB8-16-ST-2IW differential pressure transducer. The velocity (V) was determined from the measured differential pressure (ΔP) using Equation (B.32), Fox and McDonald (1998).

$$\begin{aligned} V &= \sqrt{\frac{2\Delta P}{\rho_a}} \\ \Delta P &= \rho_w g h_w \\ V &= \sqrt{\frac{2\rho_w g h_w}{\rho_a}} \end{aligned} \tag{B.32}$$

Figure B.8 shows a two point calibration plot for the Ashcroft transducer. The manufacturer data for this transducer indicates that the transducer voltage output is nominally 1-6 Volts corresponding to a pressure range of 0-2 inches of water column (inWC). For this transducer a rigorous calibration was not necessary since performance specifications are known. However, the full scale output of the transducer is adjustable and thus required measurement to determine. The manufacturer rated accuracy of the Ashcroft transducer is 0.25% of full scale output plus 0.015% per degree Fahrenheit deviation from 70°F/21 °C. The output voltage from the Ashcroft pressure transducer was measured using a Fluke 70 Series II Multimeter. The accuracy ratings for the Fluke meter are provided in Table B.2. The combined maximum uncertainty in the voltage reading was 0.5 % of the reading (RD) plus 0.031 25 % of full scale (FS). From Figure B.8 the maximum measured voltage was 6000 mV which corresponds to the 32 V range for the Fluke 70 Series II. Therefore the maximum combined uncertertainty for the Fluke 70 Series II measurements was approximately 10 mV. The pressure input for the two point calibration shown in Figure B.8 was provided by a Crystal IS33 pressure calibrator with an accuracy rating of 0.05 % of reading plus 1 mm of water column (mmWC). From Figure B.8 the slope of the line connecting the two point calibration is 98.228 mV/mmWC. However, this line is not a regression fit since only two points exist.

The maximum error estimate for the slope can be derived from the errors in the full scale reading:

$$
\begin{aligned}
S &= \frac{y_{fs} - y_0}{x_{fs} - x_0} = \frac{(y_{fs} \pm \delta y_{fs}) - 1000\,\mathrm{mV}}{(x_{fs} \pm \delta x_{fs}) - 0} \\
\delta S &= \left|\frac{\partial S}{\partial y_{fs}}\right| \delta y_{fs} + \left|\frac{\partial S}{\partial x_{fs}}\right| \delta x_{fs} \\
&= \left|\frac{1}{x_{fs}}\right| \delta y_{fs} + \left|\frac{-(y_{fs} - 1000\,\mathrm{mV})}{x_{fs}^2}\right| \delta x_{fs} \\
&= \left|\frac{1}{50.8\,\mathrm{mmWC}}\right| (0.005 \times 5990\,\mathrm{mV} + 0.0003125 \times 32\,000\,\mathrm{mV}) \\
&+ \left|\frac{-(5990\,\mathrm{mV} - 1000\,\mathrm{mV})}{(50.8\,\mathrm{mm} \cdot \mathrm{W} \cdot \mathrm{C} \cdot)^2}\right| (0.0005 \times 50.8\,\mathrm{mmWC} + 1\,\mathrm{mmWC}) \\
&= 2.769\,\mathrm{mV/mmWC} \\
S &= 98.228 \pm 2.769 \mathrm{mV/mmWC}
\end{aligned}
$$

The error in the voltage reading during the calibrations and experiments was dependent on the reading value and the full scale range required for the measurement. During calibration the maximum reading was 5990 mV and this is reflected in the error estimate for S above. However, during the uniform flow measurements the voltage output from the Ashcroft transducer did not exceed the lower 3200 mV range. The maximum error estimate for voltage readings taken during experiments is thus:

$$\delta E = \pm\,|0.005 \times 3200\,\mathrm{mV}| + |0.0003125 \times 3200\,\mathrm{mV}| = \pm 17\,\mathrm{mV}$$

Equation (B.32) and Figure B.8 were used to determine the velocity versus voltage relationship which is represented by Equation (B.33).

$$h_w = \frac{E - 1000\,\mathrm{mV}}{S} \times \frac{1\,\mathrm{m}}{1000\,\mathrm{mm}}$$

$$V = 4.041 \left(\frac{\mathrm{m/s}}{\sqrt{\mathrm{mm}}}\right) \sqrt{\frac{E - 1000\,\mathrm{mV}}{S}} \tag{B.33}$$

The resulting error in the velocity can be estimated using the rss method as shown below. The uniform flow experiment resulted in a critical gap flow velocity of 12 m/s. This value was obtained by measuring the upstream velocity which was 6 m/s and multiplying by the tube array contraction ratio $P/(P - D)$. The minimum upstream flow velocity measured was 5.25 m/s.

The velocity range from 5.25 m/s to 6 m/s corresponds to the approximate voltage range of 1165 mV to 1216 mV.

Below we evaluate the uncertainty estimate in the velocity measurement at 6 m/s corresponding to 1216 mV.

$$\delta V = \pm\sqrt{\left(\frac{\partial V}{\partial E}\delta E\right)^2 + \left(\frac{\partial V}{\partial S}\delta S\right)^2}$$

$$\delta V = \pm\sqrt{\left(\frac{4.041}{2S\sqrt{\frac{E-1000}{S}}}\delta E\right)^2 + \left(\frac{-4.041\sqrt{E-1000}}{2S^{3/2}}\delta S\right)^2}$$

$$\delta V = \pm\sqrt{\left(\frac{4.041}{2\times 98.228\sqrt{\frac{1216-1000}{98.228}}}(17)\right)^2 + \left(\frac{-4.041\sqrt{1216-1000}}{2\times 98.228^{3/2}}(2.769)\right)^2}$$

$$\delta V = \pm 0.25\,\mathrm{m/s}$$

$$\frac{\delta V}{V} = \pm 4.2\%$$

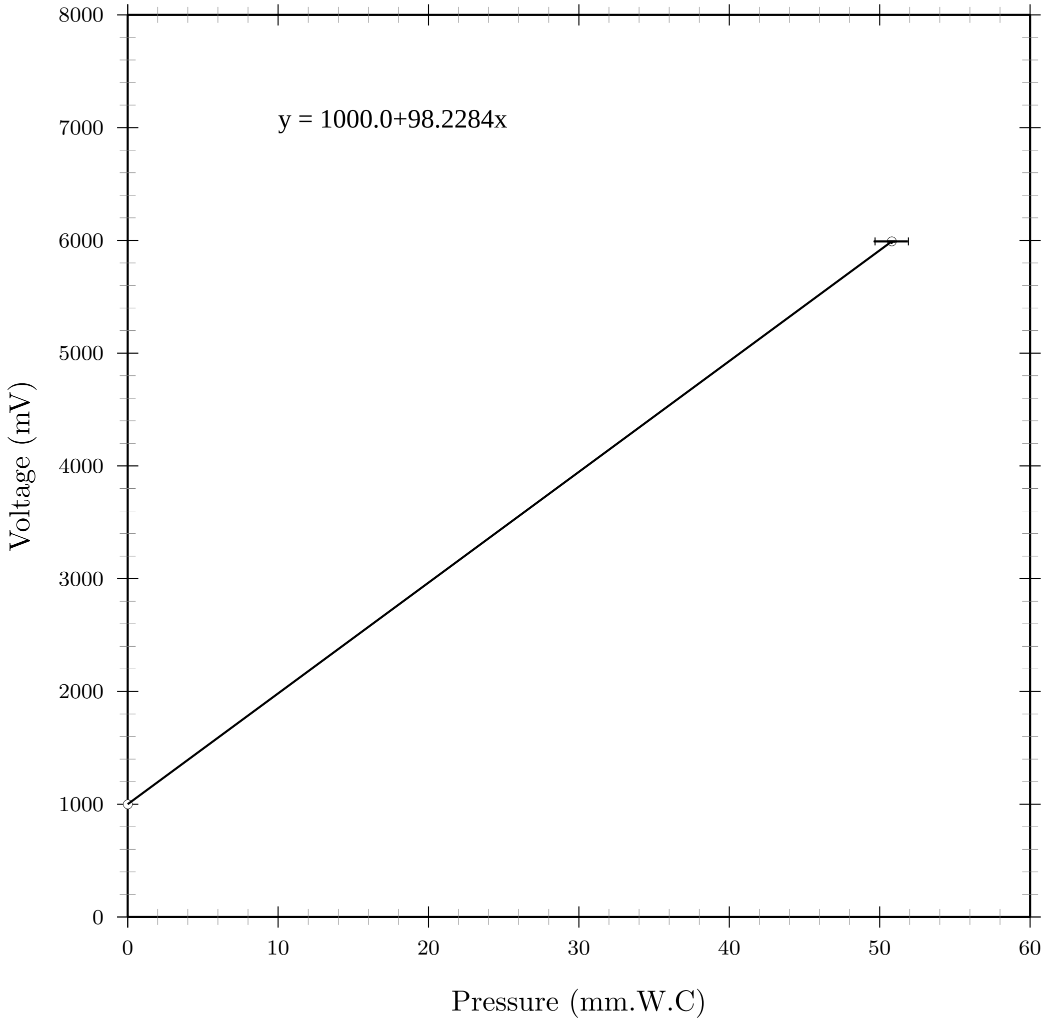

Figure B.8: Ashcroft XL-3-MB8-16-ST-2IW pressure transducer calibration.

B.5 Hot-wire Measurements

The detailed velocity measurements were completed using a Dantec model 55P14 miniature hot-wire probe connected to a Dantec model 55M10 Constant Temperature Anemometry (CTA) bridge (hot-wire system). The hot-wire system was calibrated using a dedicated calibration nozzle which achieved an area contraction ratio of 16:1. Figure B.9 shows a diagram of the calibrator nozzle. For the purpose of calibration the velocity of the fluid exiting the nozzle was determined using a pitot static tube and a Validyne DP45-30 differential pressure transducer. The DP45-30 pressure transducer has an accuracy rating of $\pm 0.5\,\%$ of full scale output which corresponds to $\pm 50\,\mathrm{mV}$. The output voltage from the Validyne pressure transducer was measured using a Fluke 70 Series II Multimeter. The accuracy ratings for the Fluke meter are provided in Table B.2. From the table the combined maximum uncertainty in the Fluke voltage reading was $0.5\,\%$ of the reading plus $0.031\,25\,\%$ of full scale. The pressure input was provided by a Crystal IS33 pressure calibrator with an accuracy rating of $0.05\,\%$ of reading plus $1\,\mathrm{mmWC}$. Figure B.10 shows a calibration plot for the Validyne transducer. Equation (B.32) was used with the calibration information to determine the velocity versus voltage relationship which is represented by Equation (B.34).

$$V = \sqrt{\frac{2\rho_w g h_w}{\rho_a}} \tag{B.32 revisited}$$

From Figure B.10:

$$h_w = \frac{E}{11.4674\,\mathrm{mV/mmWC}}$$

$$V = \sqrt{\frac{2 \times 1000\,\mathrm{kg/m^3} \times 9.8\,\mathrm{m/s^2} \times E}{1.20\,\mathrm{kg/m^3} \times 11.4674\,\mathrm{mV/mmWC}} \times \frac{1\,\mathrm{m}}{1000\,\mathrm{mm}}}$$

$$V = 1.193\left(\frac{\mathrm{m/s}}{\sqrt{\mathrm{mV}}}\right)\sqrt{E} \tag{B.34}$$

The estimated error in the velocity can be calculated by combining the estimated measurement error δE_m and the estimated calibration error δE_c using the rss method. From Figure B.10 the maximum measured voltages were greater than $3.2\,\mathrm{V}$ which corresponds to the $32\,\mathrm{V}$ full scale range for the Fluke 70 Series II. Figure B.10 shows voltage reading up to approximately

7.5 V, therefore we will use 7.5 V as our reading estimate and 32 V as our full scale estimate.

$$\begin{aligned}
\delta E_m(7500\,\mathrm{mV}) &= \pm\left|0.005\times 7500\,\mathrm{mV}\right| + \left|0.0003125\times 32\,000\,\mathrm{mV}\right| = \pm 47.5\,\mathrm{mV}\\
\delta E_c(7500\,\mathrm{mV}) &\approx \pm 73\,\mathrm{mV}(\text{from Figure B.10})\\
\delta E(7500\,\mathrm{mV}) &= \pm\sqrt{(\delta E_m)^2+(\delta E_c)^2} \approx \pm 87\,\mathrm{mV}\\
\delta V(7500\,\mathrm{mV}) &= \pm\left(\frac{\partial V}{\partial E}\delta E\right) = \pm\left(\frac{1.193}{2\sqrt{E}}\delta E\right)\\
&= \pm\left(\frac{1.193}{2\sqrt{7500\,\mathrm{mV}}}(87\,\mathrm{mV})\right)\\
&= \pm 0.599\,\mathrm{m/s}\ (\text{corresponds to } 103.32\,\mathrm{m/s})\\
\frac{\delta V(7500\,\mathrm{mV})}{V(7500\,\mathrm{mV})} &= \pm 0.580\%
\end{aligned}$$

From the calculation above we can see that δV has a non-linear dependence on E. It would appear that the error is reduced for increasing values of E. To assess the error low values of E, we can use Equation (B.34) to calculate E at a low velocity. For a velocity V of 20 m/s the corresponding voltage output E of approx 300 mV, which corresponds to the 320 mV full scale range on the Fluke 70 Series II Multimeter.

$$\begin{aligned}
\delta E_m(300\,\mathrm{mV}) &= \pm\left|0.005\times 300\,\mathrm{mV}\right| + \left|0.0003125\times 320\,\mathrm{mV}\right| = \pm 1.6\,\mathrm{mV}\\
\delta E_c(300\,\mathrm{mV}) &\approx \pm 41\,\mathrm{mV}(\text{from Figure B.10})\\
\delta E(300\,\mathrm{mV}) &= \pm\sqrt{(\delta E_m)^2+(\delta E_c)^2} \approx \pm 41\,\mathrm{mV}\\
\delta V(300\,\mathrm{mV}) &= \pm\left(\frac{\partial V}{\partial E}\delta E\right) = \pm\left(\frac{1.193}{2\sqrt{E}}\delta E\right)\\
&= \pm\left(\frac{1.193}{2\sqrt{300\,\mathrm{mV}}}(41\,\mathrm{mV})\right)\\
&= \pm 1.412\,\mathrm{m/s}\ (\text{corresponds to } 20.66\,\mathrm{m/s})\\
\frac{\delta V(300\,\mathrm{mV})}{V(300\,\mathrm{mV})} &= \pm 6.834\%
\end{aligned}$$

From the result above, the absolute error estimate δV and the relative error increase for decreasing velocity/voltage. This increase in relative uncertainty asymptotically approaches $\pm\infty$ as E, V approach zero. The relative error estimates at 10 m/s (70 mV) and 5 m/s (18 mV) are approximately 53 % and 205 %, respectively. This signifies that the velocity measurements used for calibration (the independent variable) which is supposed to be devoid of error is actually quite error prone for low velocityis (below 20 %). The great majority of this error estimate comes from the uncertainty in the calibration of the pitot ststic tube and the associated Validyne DP45-30 differential pressure transducer. The errors due solely to measurement uncertainty are actually quite low 0.32 % and 0.53 % for 10 m/s (70 mV) and 5 m/s (18 mV), respectively. The fit error could be reduced by adding additional data points. However, most of the significant velocity data collected for this research was above 20 m/s.

Figures B.11 and B.12 show calibration plots for hot-wire probe no.1. Figures B.13 and B.14 show calibration plots for hot-wire probe no.2. hot-wire probe no.1 was operated with an overheat ratio of 1.8 and hot-wire probe no.2 was operated with an overheat ratio of 1.5. The overheat ratio was reduced for probe no.2 as probe no.1 failed due to overheating. The physical relationship between hot-wire bridge output voltage and the flow velocity is represented by Equation (B.35) (King's Law). This equation relates the voltage (E) and the velocity (V) using the constants (A, B) and exponent (n). Equation (B.35) is non-linear with respect to the unknown coefficients and cannot be fitted using linear regression directly. Equation (B.36) represents a linearization of Equation (B.35) which can be fitted using linear regression provided the constant B is known. The constant B can be determined by measuring the voltage output E_0 from the hot-wire bridge when $V = 0$, since $B = E_0^2$. Figures B.11 and B.13 show the linear regression results using Equation (B.36) for probes no.1 and no.2, respectively. These plots also show the relevant linear regression statistics which apply to the transformed coordinates. Figures B.12 and B.14 show the calibration plots in terms of the untransformed coordinates with the untransformed linear regression equations.

$$E^2 = AV^n + B \tag{B.35}$$

$$\log_{10}\left(E^2 - B\right) = n\log_{10}(V) + \log_{10}(A) \tag{B.36}$$

The hot-wire voltage output is sensitive to ambient temperature variations. This is due to the fact that the hot-wire bridge output is proportional to the power required to maintain the hot-wire at a constant temperature. Therefore, hot-wire measurements are typically corrected for the variation from the calibration temperature T_0. Equation (B.37) is used to calculated the corrected voltage E_c using the hot-wire temperature T_w, the calibration ambient temperature T_0, the acquisition ambient temperature T and the acquired voltage E.

$$E_c = E\left(\frac{T_w - T_0}{T_w - T}\right)^{1/2} \tag{B.37}$$

Therefore to calculate the velocity from measured voltage we can rearrange Equation (B.35) and substitute Equation (B.37):

$$V = \left(\frac{E_c^2 - B}{A}\right)^{(1/n)}$$

$$V = \left(\frac{T_w - T_0}{T_w - T}\right)^{(1/n)}\left(\frac{E^2 - B}{A}\right)^{(1/n)} \tag{B.38}$$

The error in the calculated velocity due to calibration error can be estimated by re-arranging Equation (B.36) as shown below. In this form the error can be assessed in terms of the 95 % confidence limits provided in Figure B.11 or Figure B.13. From Figure B.12 the error in V appears to be a maximum at the maximum recorded velocity (97 m/s). Referring back to Figure B.11 the error in the transformed coordinates is ±0.0033 at the corresponding point. Note that although the error structure in the transformed coordinates is additive the error structure in the normal coordinates is multiplicative as described in Section B.1. Therefore we can use the absolute error in the transformed coordinates to estimate the relative error in the normal coordinates, this relative error estimate then applies to the entire velocity range.

$$V = 10^{\left(\frac{\log_{10}(E^2 - B) - \log_{10}(A)}{n}\right)}$$

$$\delta V_c = \pm\frac{\partial V}{\partial(\log_{10}(E^2 - B))}\delta(\log_{10}(E^2 - B))$$

$$\delta V_c = \pm\frac{\log_e(10)10^{\left(\frac{\log_{10}(E^2 - B) - \log_{10}(A)}{n}\right)}}{n}\delta(\log_{10}(E^2 - B))$$

$$\delta V_c = \pm\frac{\log_e(10)10^{\left(\frac{1.36 - \log_{10}(2.93)}{0.45}\right)}}{0.45}(0.0033)$$

$$\delta V_c = \pm 1.63\,\mathrm{m/s}$$

$$\frac{\delta V_c}{V} = \pm\frac{1.63\,\mathrm{m/s}}{97\,\mathrm{m/s}} = \pm 1.68\%$$

To estimate the error in the velocity due to measurement error we use the rss method described by Equation (B.30). The temperatures during calibration and experiment were measured using a mercury thermometer with a resolution of ±1 °C. The estimated uncertainty in the temperature readings is thus ±0.5 °C. However, the temperature was not monitored continuously and was only checked before and after experiment. Therefore the uncertainty should be increased to ±1 °C. The hot-wire bridge voltage was measured during experiments using the National Instruments AT-MIO-16 data acquisition system the rated accuracy was ±4.88 mV. The error estimate was evaluated for probe no.1 using the following values $T_w = 248\,^\circ\mathrm{C}, T_0 = 25.5\,^\circ\mathrm{C}, T = 21.5\,^\circ\mathrm{C}, E = 5.5\,\mathrm{V}$.

$$\delta V_m = \pm\left(\left(\frac{\partial V}{\partial T_w}\delta T_w\right)^2 + \left(\frac{\partial V}{\partial T_0}\delta T_0\right)^2 + \left(\frac{\partial V}{\partial T}\delta T\right)^2 + \left(\frac{\partial V}{\partial E}\delta E\right)^2\right)^{(1/2)}$$

$$\delta V_m \approx \pm 1.347\,\mathrm{m/s}$$

$$\frac{\delta V_m}{V} = \pm\frac{1.347\,\mathrm{m/s}}{97\,\mathrm{m/s}} = \pm 1.39\%$$

The error estimate δV_m represents the maximum absolute error. However, the relative error in the velocity due to the measurement uncertainty increases for decreasing velocity. If we recalculate the error at a small value of E the absolute error will be smaller than above but the relative error will be greater. This increase in relative uncertainty asymptotically approaches $\pm\infty$ as E, V approach zero. A reasonable lower limit on the velocity is 5 m/s, the majority of measurements made for this work were above this value and those measurements below 5 m/s have little significance.

$$E = \sqrt{2.93 \times 5^{0.45} + 7.65} = 3.7\,\mathrm{V}$$

$$\delta V_m \approx \pm 0.0927\,\mathrm{m/s}$$

$$\frac{\delta V_m}{V} = \pm\frac{0.0927\,\mathrm{m/s}}{5\,\mathrm{m/s}} = \pm 1.85\%$$

The combined measurement and calibration uncertainty can then be calculated again using Equation (B.30). The resulting error estimate is ±2.5% which is more than adequate for the purposes of this work.

$$\delta V = \sqrt{\left(\frac{1.85}{100} \times 5\,\mathrm{m/s}\right)^2 + \left(\frac{1.68}{100} \times 5\,\mathrm{m/s}\right)^2} = 0.125\,\mathrm{m/s} \tag{B.39}$$

$$\frac{\delta V}{V} = \pm\frac{0.125}{5} = \pm 2.5\% \tag{B.40}$$

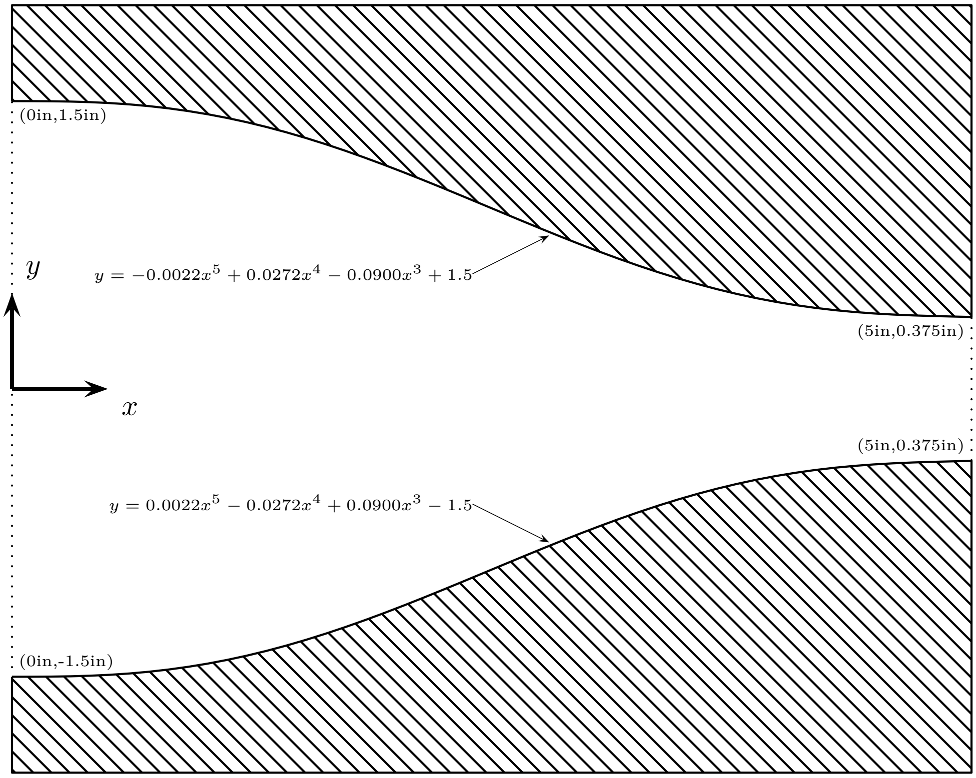

Figure B.9: Hot-wire calibrator nozzle.

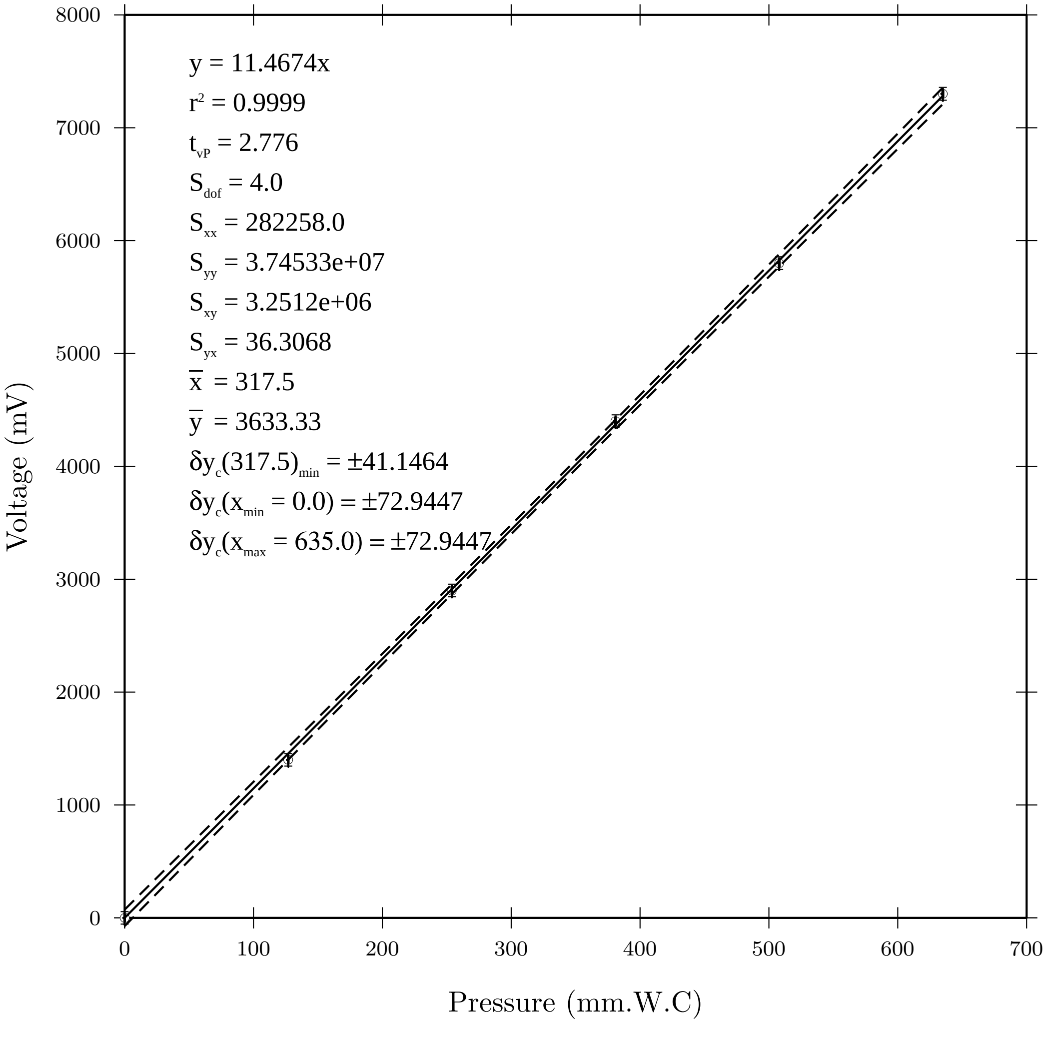

Figure B.10: Validyne DP45-30 pressure transducer calibration.

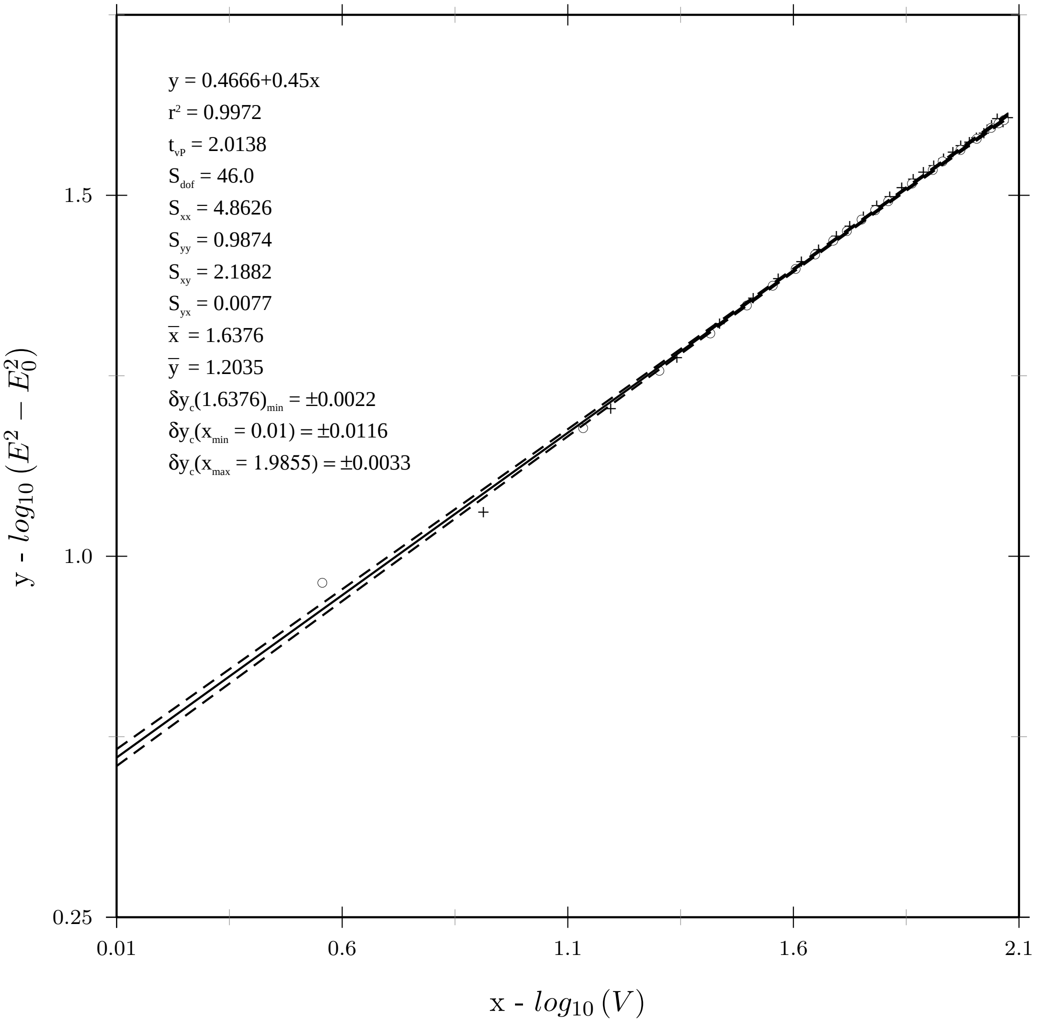

Figure B.11: Hot-wire probe no.1 (Dantec model 55P14) calibration in transformed coordinates. Calibration data was collected before and after experiments. The data points represented by (+) were collected before experiments with ambient temperature T_0 of 26 °C and a barometric pressure of 753 mmHg. The data points represented by (○) were collected before experiments with ambient temperature T_0 of 25 °C and a barometric pressure of 756 mmHg. For temperature correction the average T_0 of 25.5 °C was utilized. The value of E_0 was measured before experiments as 2.806 V and after experiments as 2.726 V, the average value of 2.766 V was used for the linear regression. The dashed lines represent the 95% confidence interval of the fit as described by Equation (B.18).

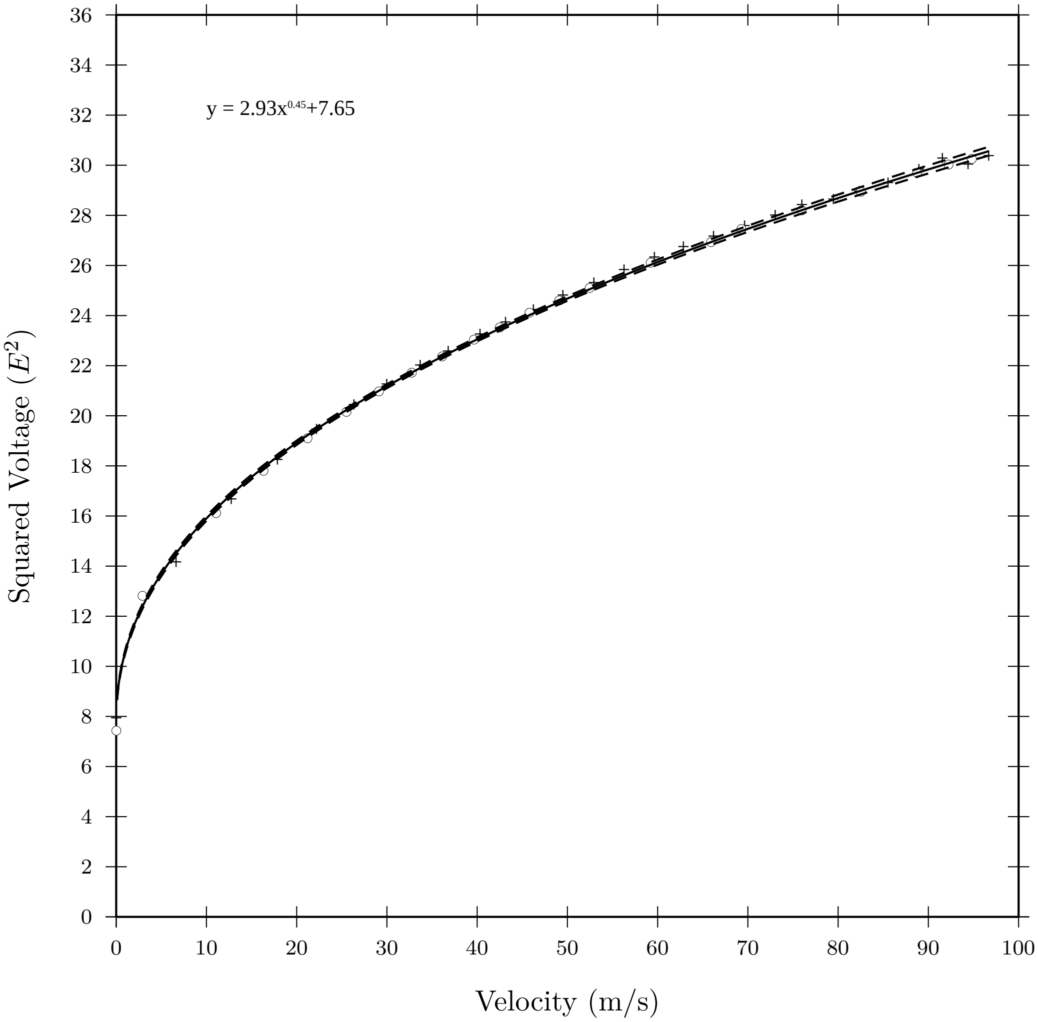

Figure B.12: Hot-wire probe no.1 (Dantec model 55P14) calibration in normal coordinates, same data as shown in Figure B.11. The solid line represents the linear regression fit calculated via linearization of King's law and the dashed lines represent the 95% confidence interval of the fit, both of which are shown in Figure B.11 in the transformed coordinates.

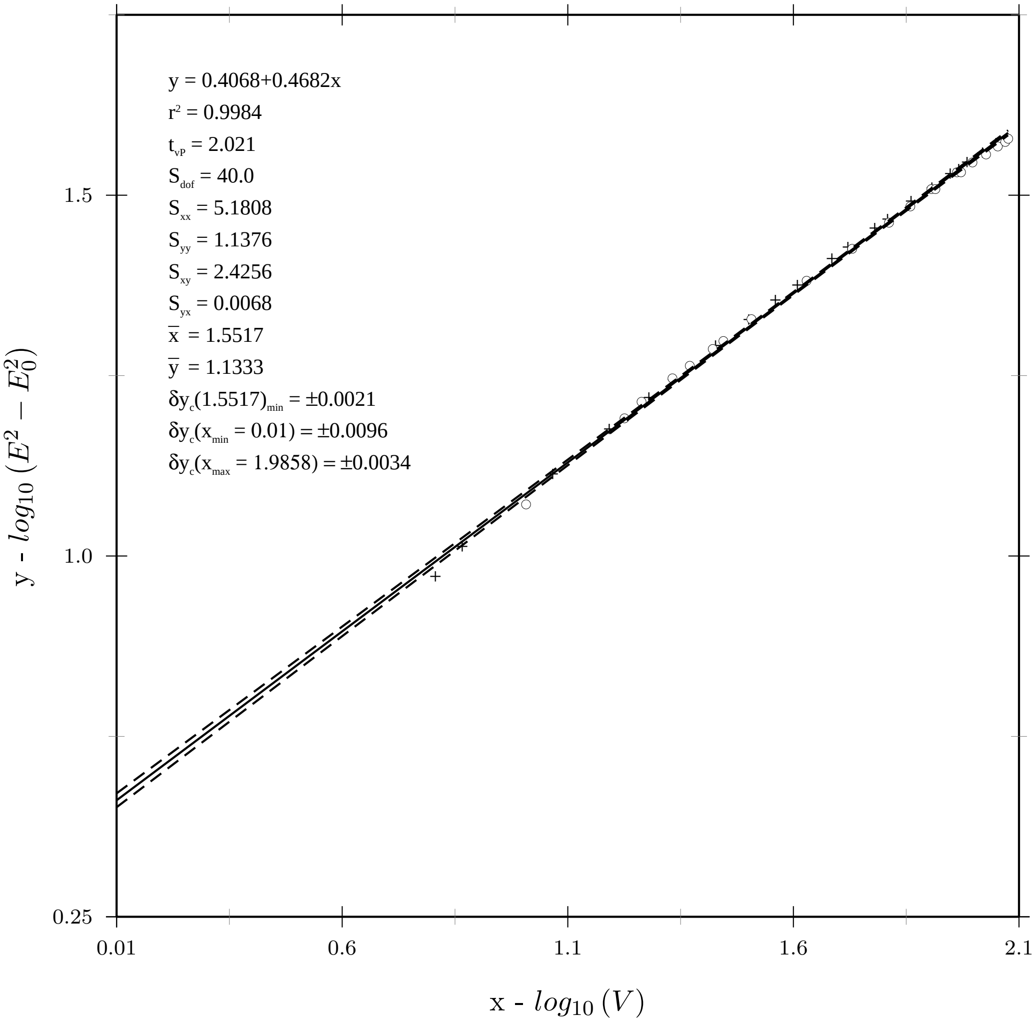

Figure B.13: Hot-wire probe no.2 (Dantec model 55P14) calibration in transformed coordinates. Calibration data was collected before and after experiments. The data points represented by (+) were collected before experiments with ambient temperature T_0 of 25 °C and a barometric pressure of 768 mmHg. The data points represented by (○) were collected after experiments with ambient temperature T_0 of 26 °C and a barometric pressure of 769 mmHg. For temperature correction the average T_0 of 25.5 °C was utilized. The value of E_0 was measured before experiments as 2.344 V and after experiments as 2.385 V, the average value of 2.364 V was used for the linear regression. The dashed lines represent the 95% confidence interval of the fit as described by Equation (B.18).

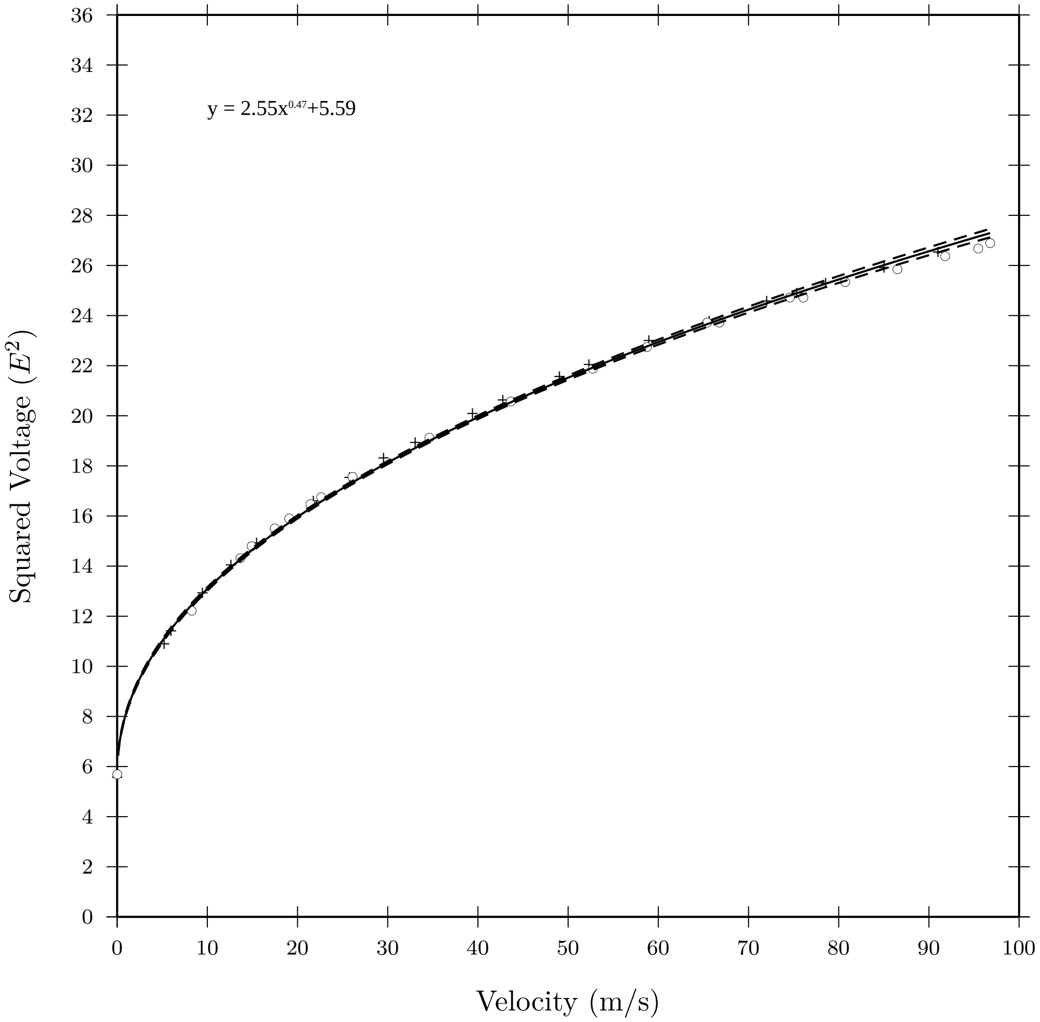

Figure B.14: Hot-wire probe no.2 (Dantec model 55P14) calibration in normal coordinates, same data as shown in Figure B.13. The solid line represents the linear regression fit calculated via linearization of King's law and the dashed lines represent the 95% confidence interval of the fit, both of which are shown in Figure B.11 in the transformed coordinates.

Appendix C.

Experimental Results

This appendix contains the detailed plots of the measured velocity profiles for the jet flow experiments.

C.1 Jet Flow Centered between Tubes

Figures C.1 and C.2 show the non-normalized jet entry velocity profiles. This data is presented in normalized format in Figure 5.1. Figures C.3 to C.19 show the detailed velocity profiles measured in the horizontal plane. Figures C.20 to C.27 show the detailed velocity profiles measured in the vertical plane. Figures 4.10 and 4.11 present all of the data in Figures C.3 to C.27 in a summary format.

C.2 Jet Flow Centered on a Tube Face

Figures C.28 and C.29 show the non-normalized jet entry velocity profiles. This data is presented in normalized format in Figure 5.2. Figures C.30 to C.39 show the detailed velocity profiles measured in the horizontal plane. Figures C.40 to C.43 show the detailed velocity profiles measured in the vertical plane. Figures 4.18 and 4.19 present all of the data in Figures C.30 to C.43 in a summary format.

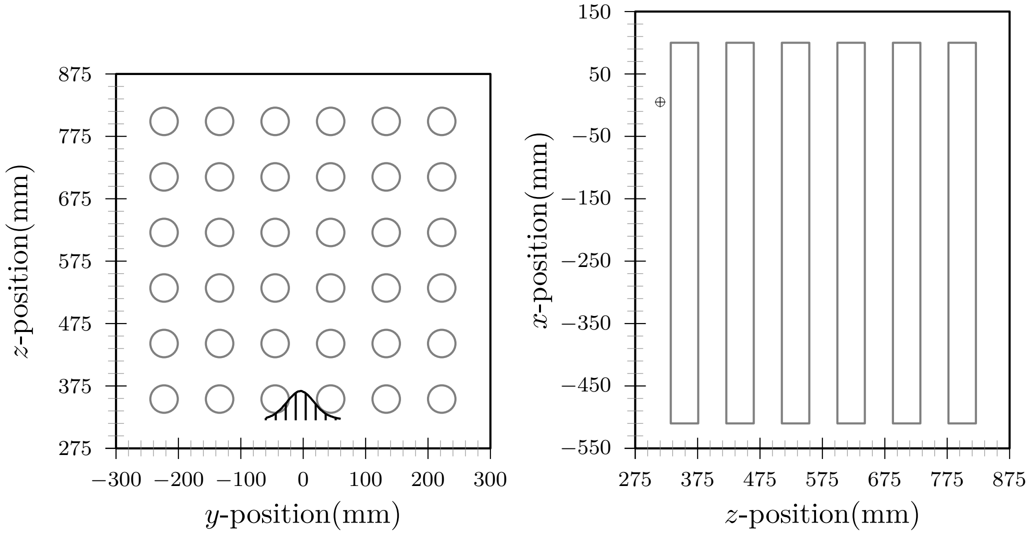

(a) Traverse path, plan view.

(b) Traverse path, side view.

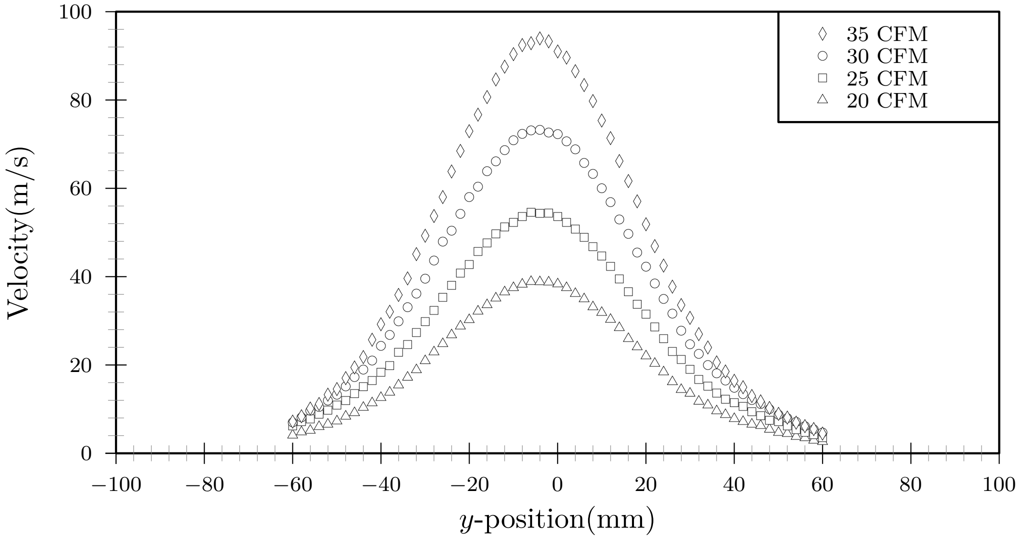

(c) Jet fluid velocity along traverse path.

Figure C.1: Jet entry velocity profiles for various nozzle flow-rates taken across horizontal axis (y-axis) with jet centred between T13 and T14.

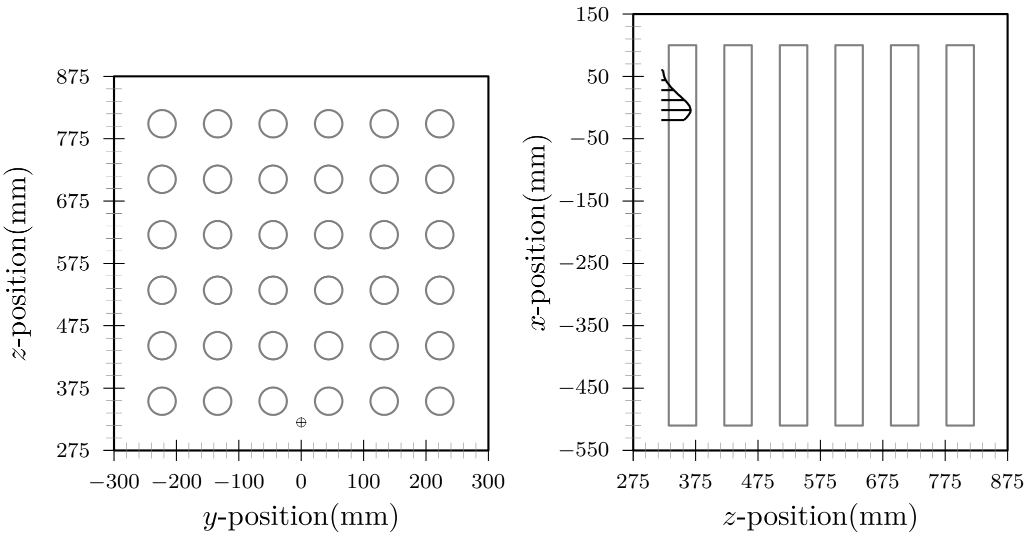

(a) Traverse path, plan view.

(b) Traverse path, side view.

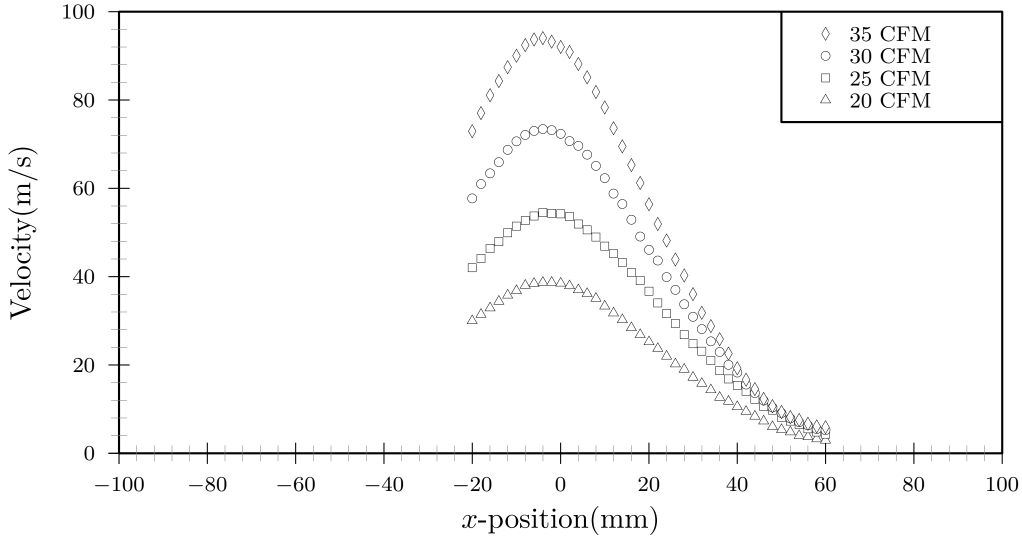

(c) Jet fluid velocity along traverse path.

Figure C.2: Jet entry velocity profiles for various nozzle flow-rates taken across vertical axis (x-axis) with jet centred between T13 and T14.

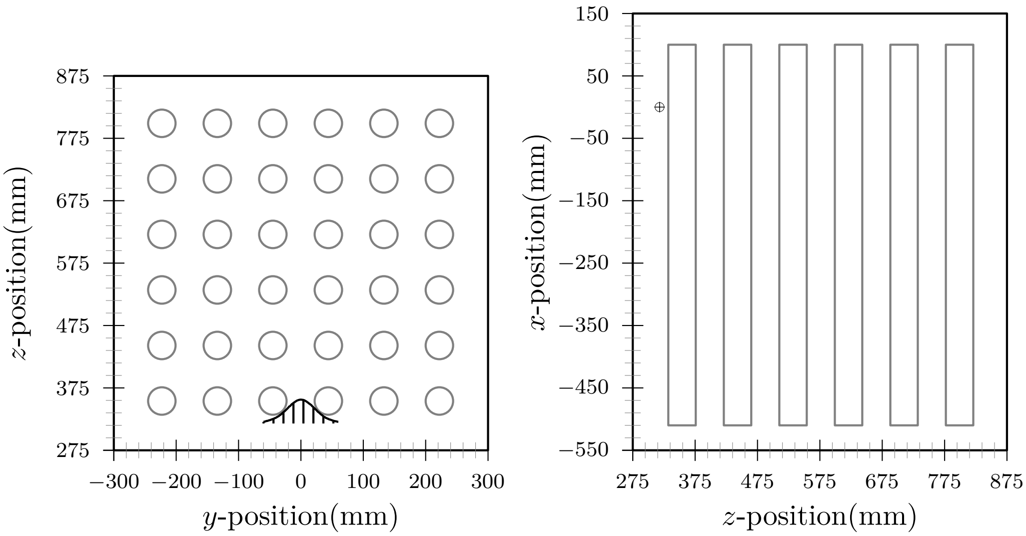

(a) Traverse path, plan view.

(b) Traverse path, side view.

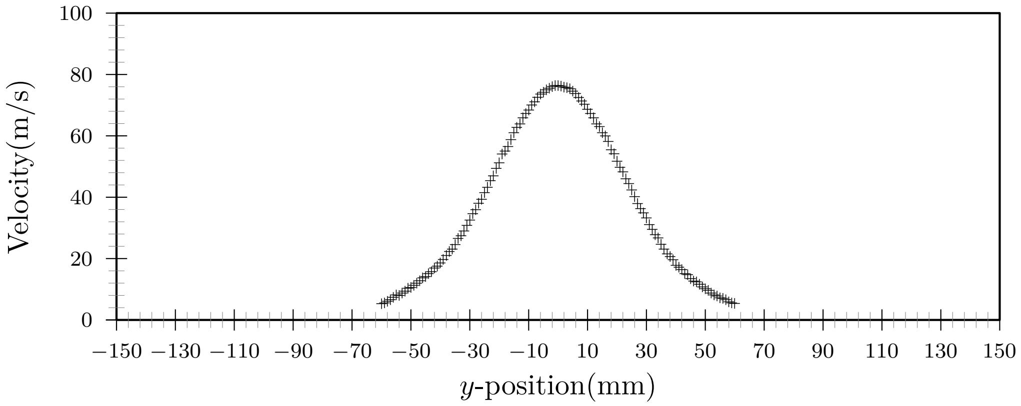

(c) Fluid velocity along traverse path.

Figure C.3: Jet centred between tubes, velocity profile along (0,y,318).

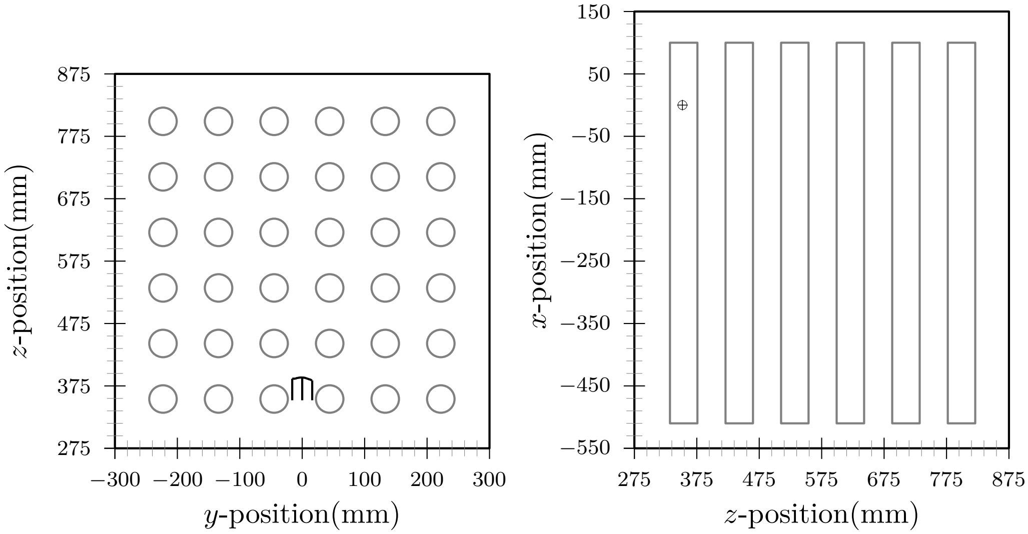

(a) Traverse path, plan view.

(b) Traverse path, side view.

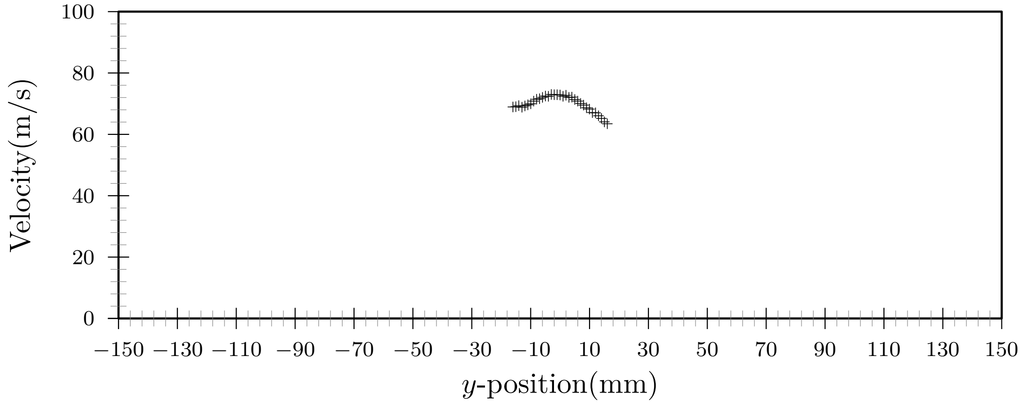

(c) Fluid velocity along traverse path.

Figure C.4: Jet centred between tubes, velocity profile along (0,y,352).

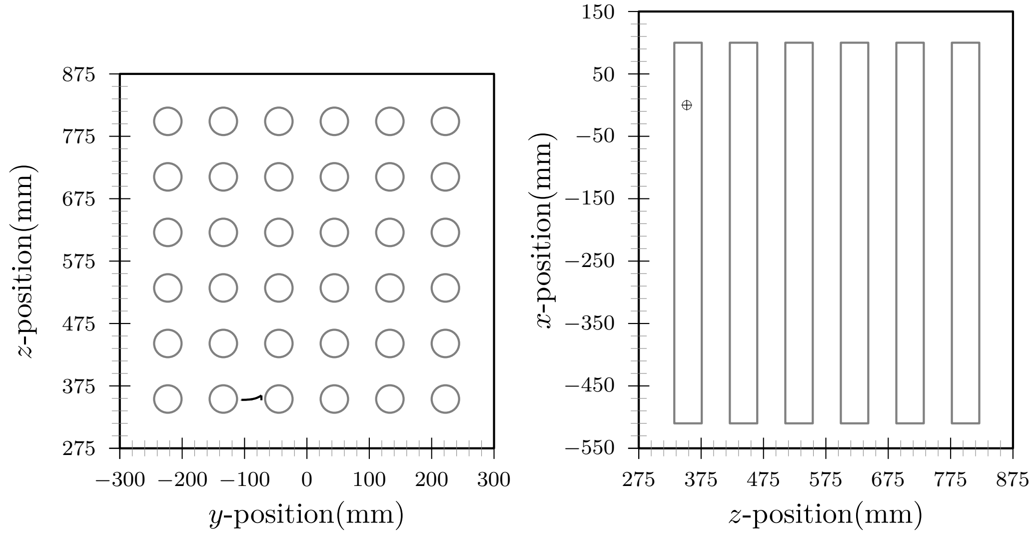

(a) Traverse path, plan view.

(b) Traverse path, side view.

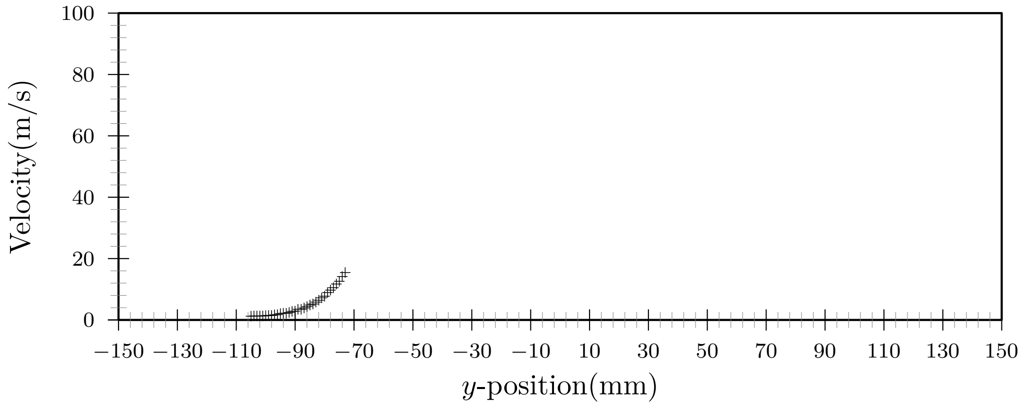

(c) Fluid velocity along traverse path.

Figure C.5: Jet centred between tubes, velocity profile along (0,y,352).

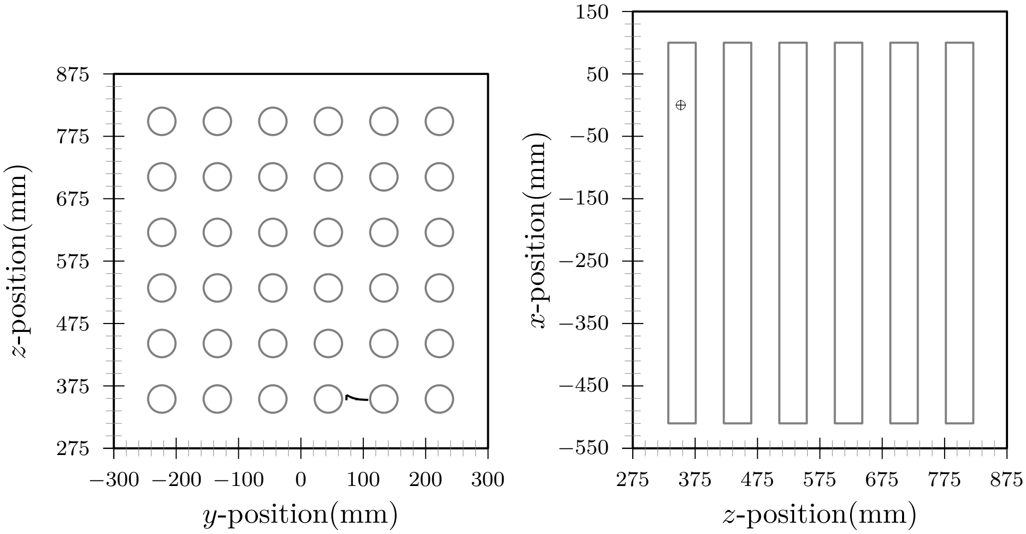

(a) Traverse path, plan view.

(b) Traverse path, side view.

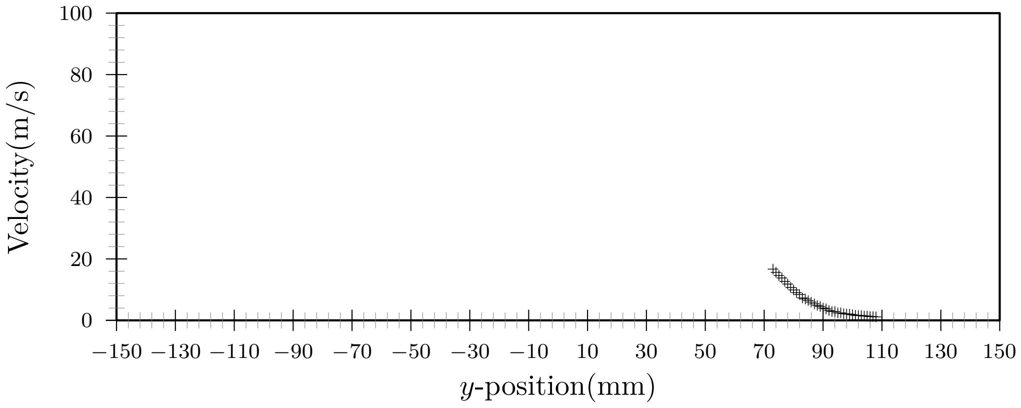

(c) Fluid velocity along traverse path.

Figure C.6: Jet centred between tubes, velocity profile along (0,y,352).

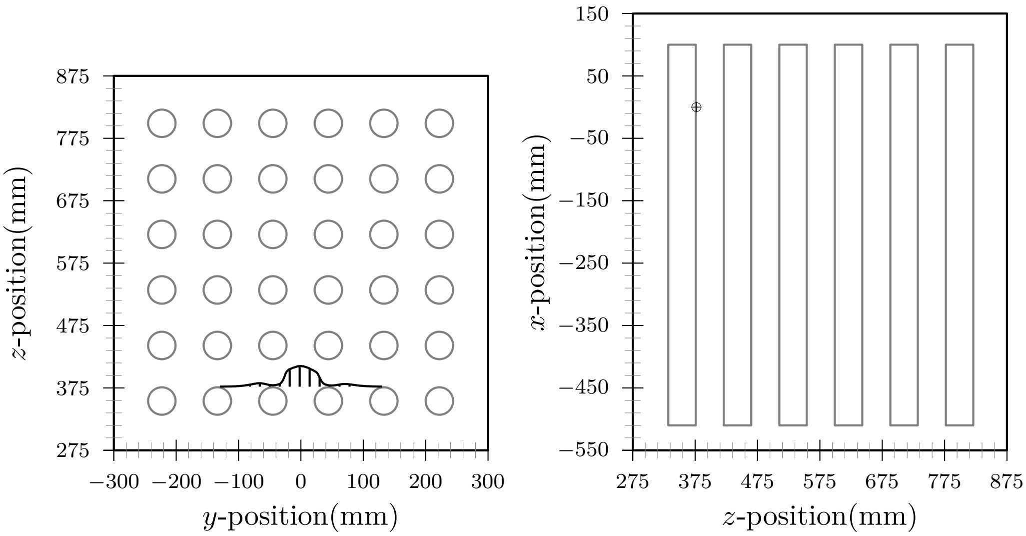

(a) Traverse path, plan view.

(b) Traverse path, side view.

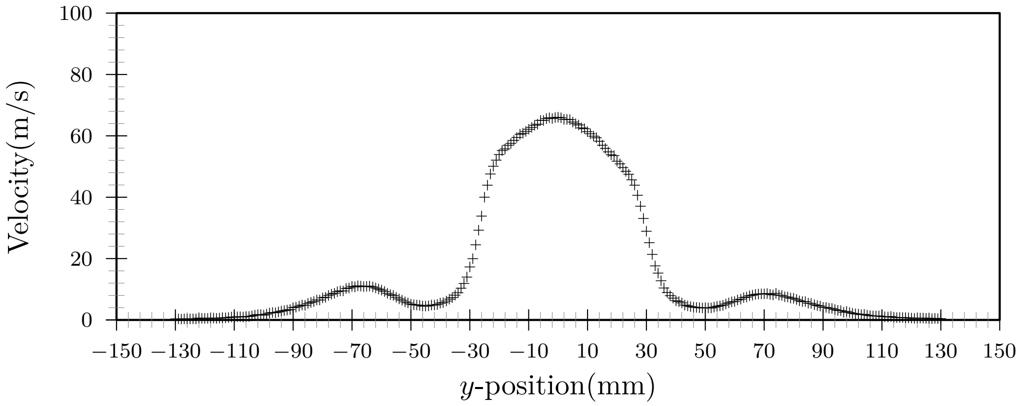

(c) Fluid velocity along traverse path.

Figure C.7: Jet centred between tubes, velocity profile along (0,y,377).

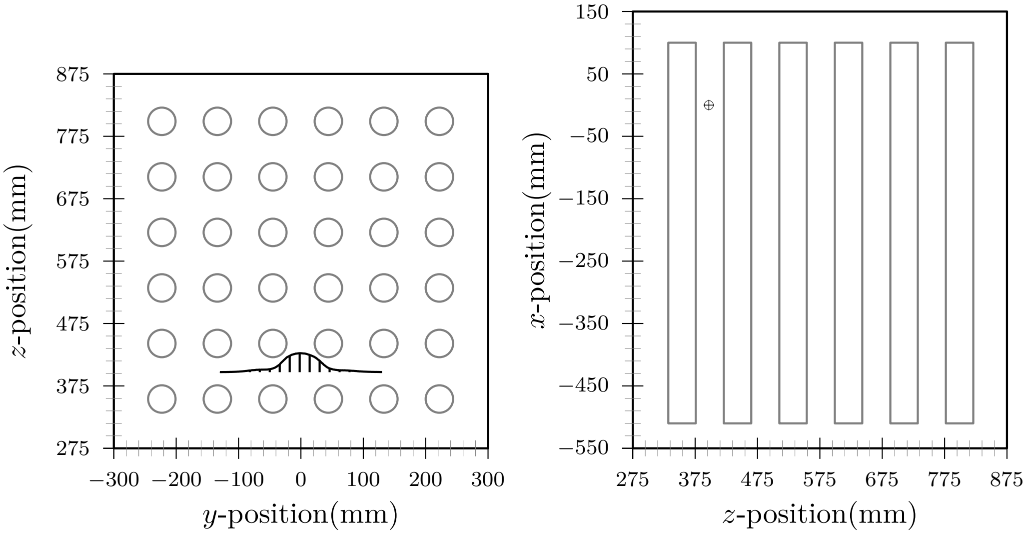

(a) Traverse path, plan view.

(b) Traverse path, side view.

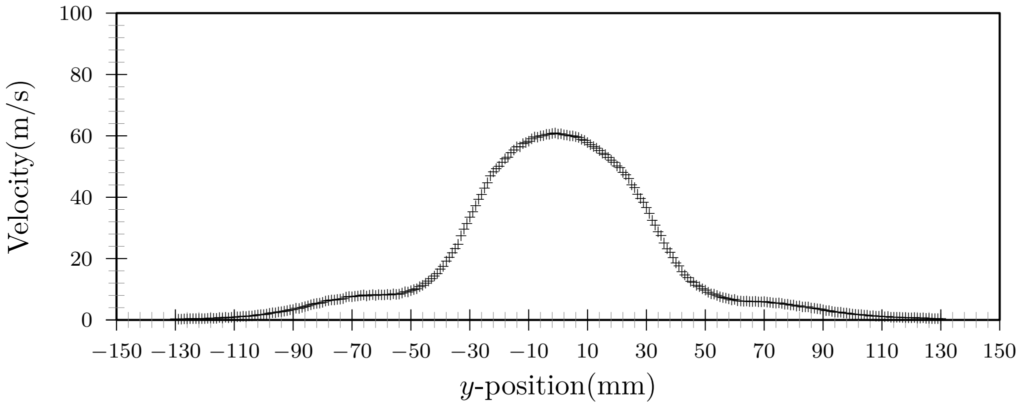

(c) Fluid velocity along traverse path.

Figure C.8: Jet centred between tubes, velocity profile along (0,y,397).

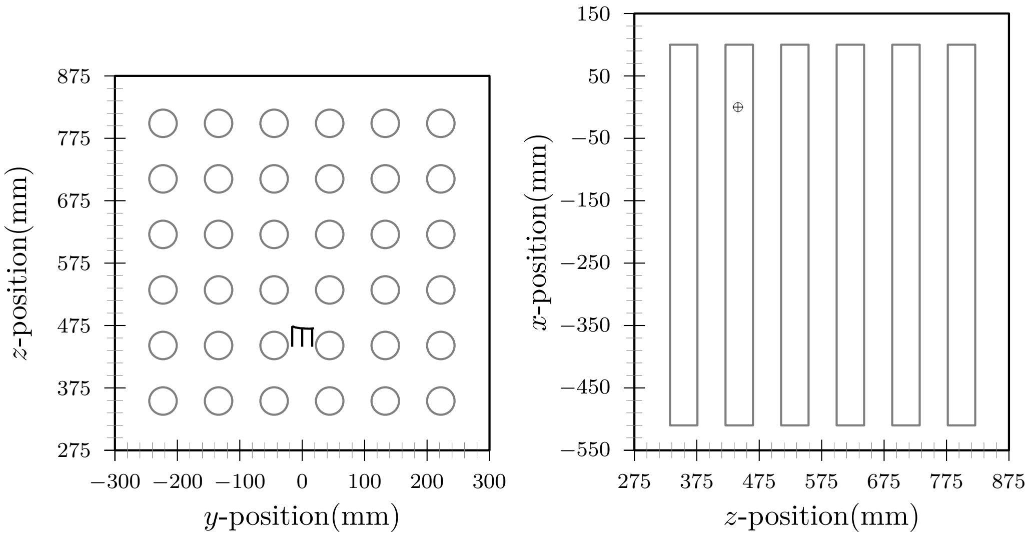

(a) Traverse path, plan view.

(b) Traverse path, side view.

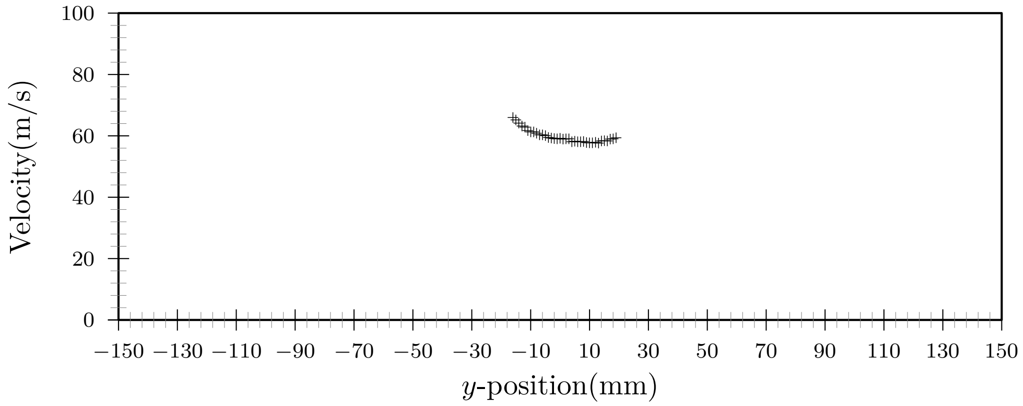

(c) Fluid velocity along traverse path.

Figure C.9: Jet centred between tubes, velocity profile along (0,y,441).

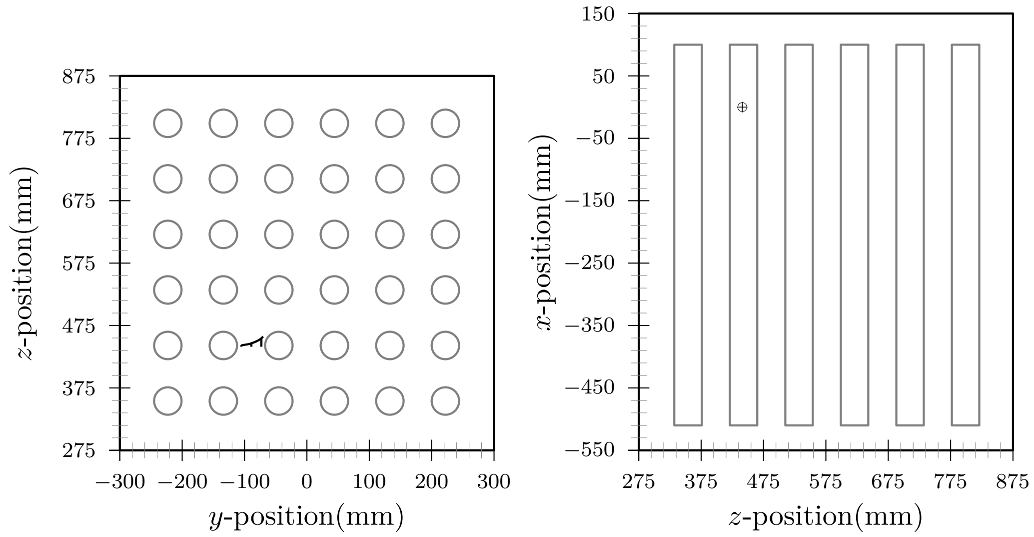

(a) Traverse path, plan view.

(b) Traverse path, side view.

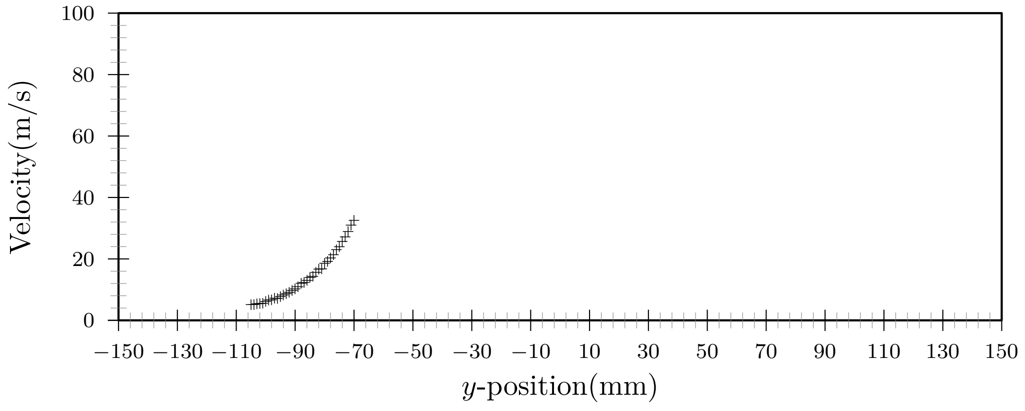

(c) Fluid velocity along traverse path.

Figure C.10: Jet centred between tubes, velocity profile along (0,y,441).

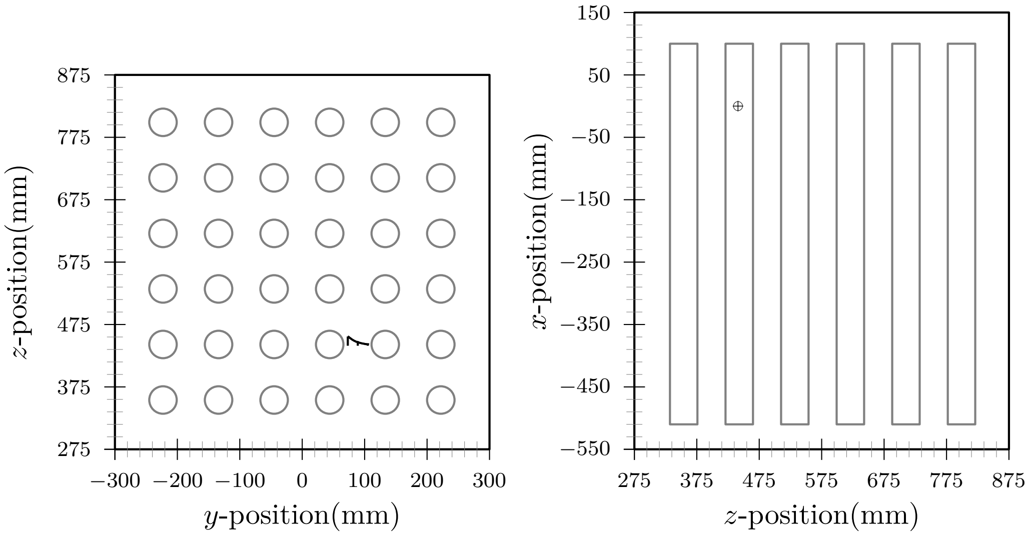

(a) Traverse path, plan view. **(b)** Traverse path, side view.

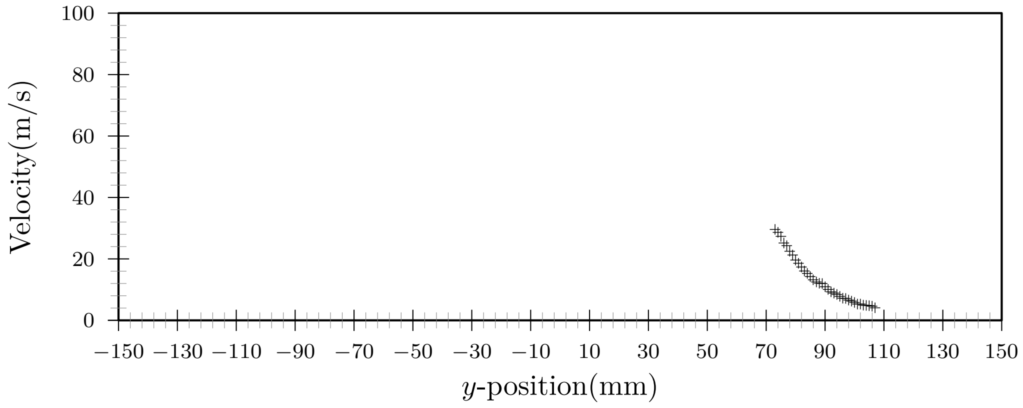

(c) Fluid velocity along traverse path.

Figure C.11: Jet centred between tubes, velocity profile along (0,y,441).

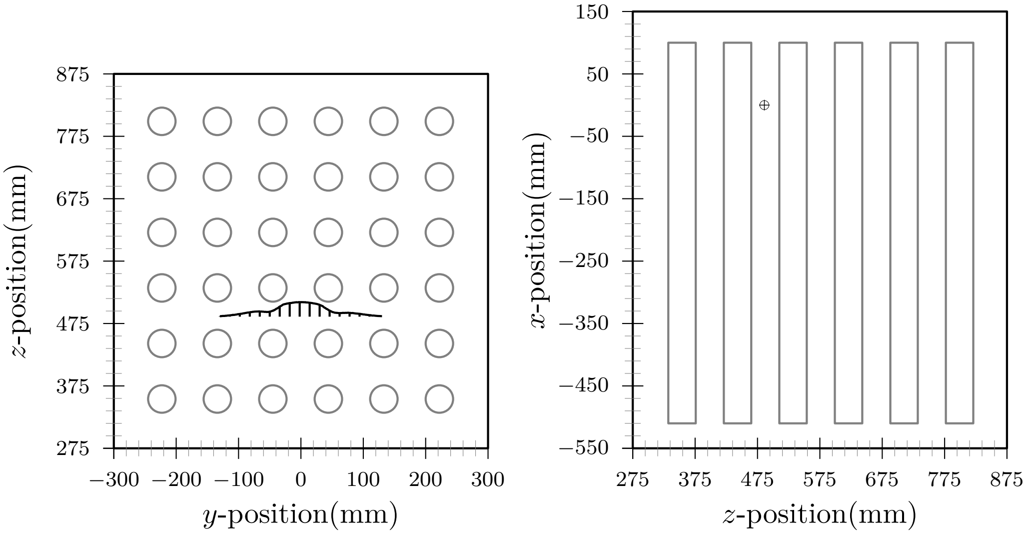

(a) Traverse path, plan view.

(b) Traverse path, side view.

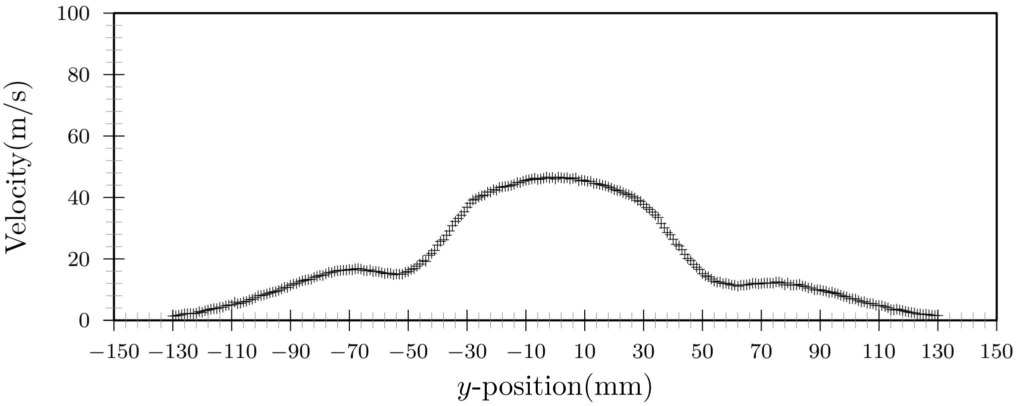

(c) Fluid velocity along traverse path.

Figure C.12: Jet centred between tubes, velocity profile along (0,y,486).

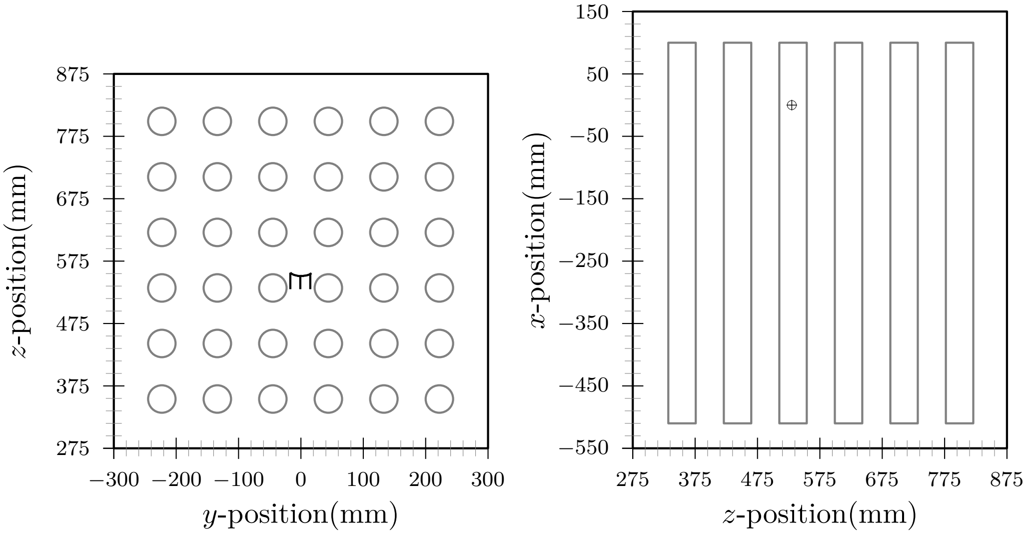

(a) Traverse path, plan view.

(b) Traverse path, side view.

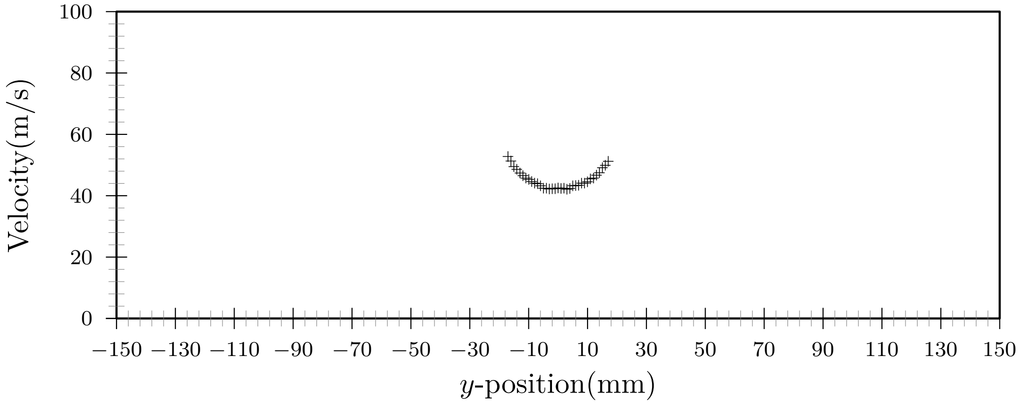

(c) Fluid velocity along traverse path.

Figure C.13: Jet centred between tubes, velocity profile along (0,y,530).

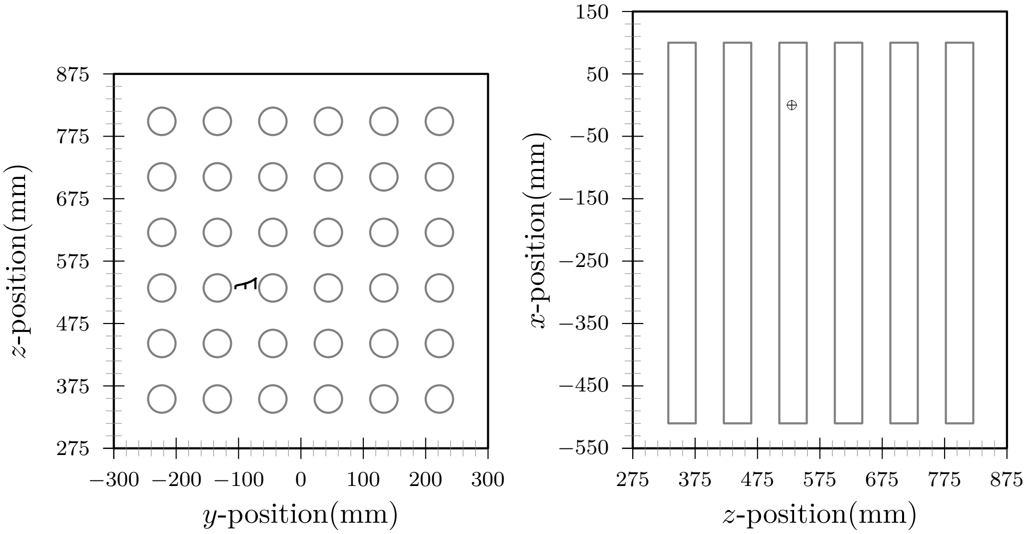

(a) Traverse path, plan view.

(b) Traverse path, side view.

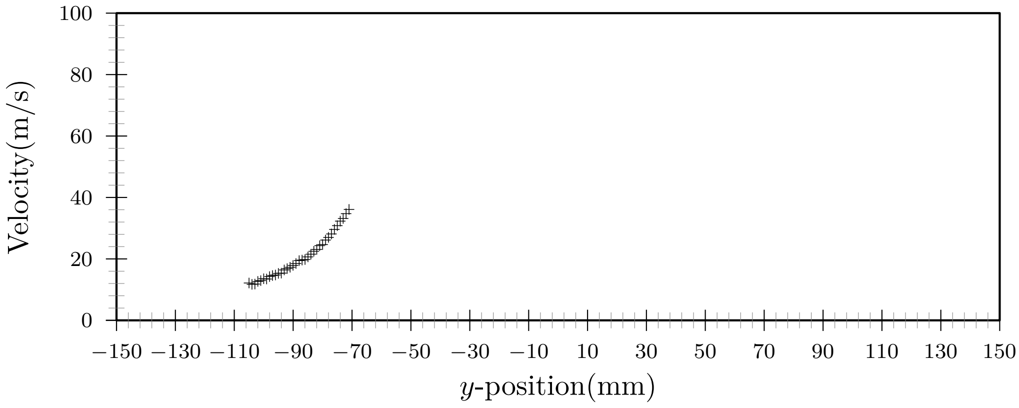

(c) Fluid velocity along traverse path.

Figure C.14: Jet centred between tubes, velocity profile along (0,y,530).

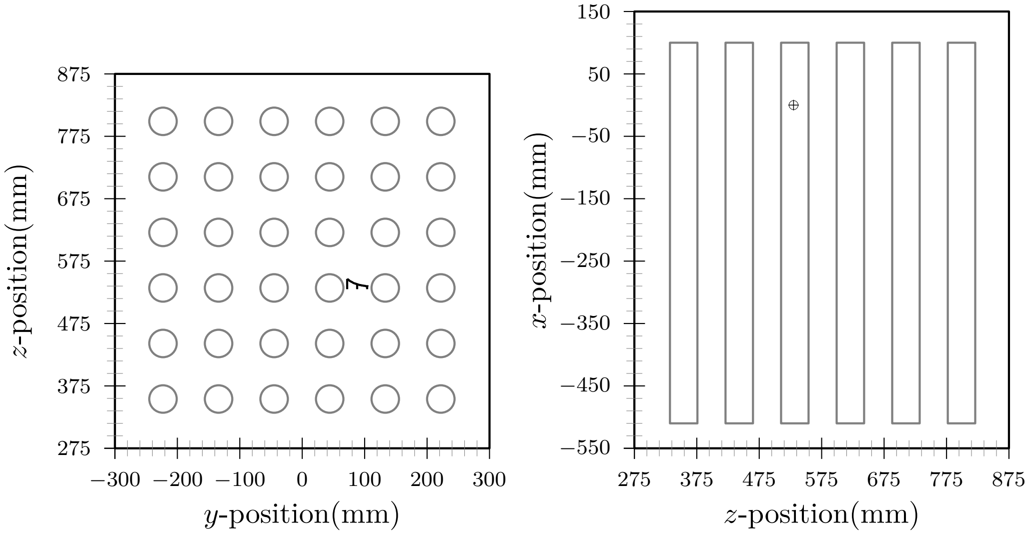

(a) Traverse path, plan view.

(b) Traverse path, side view.

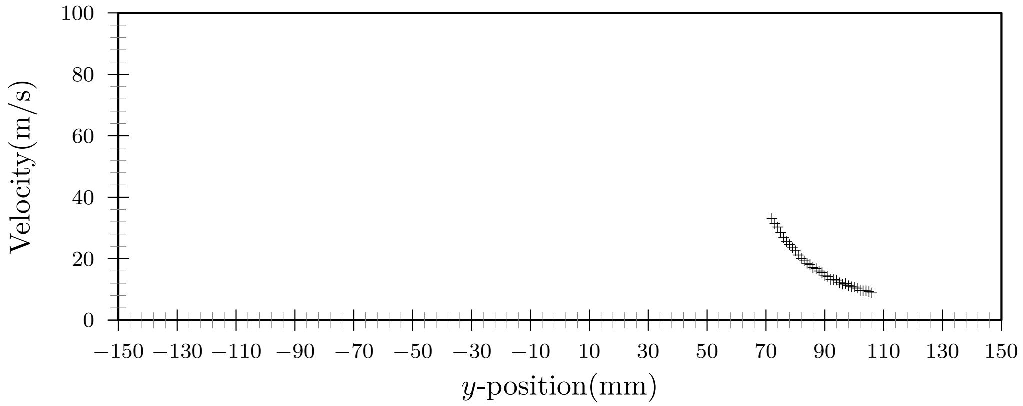

(c) Fluid velocity along traverse path.

Figure C.15: Jet centred between tubes, velocity profile along (0,y,530).

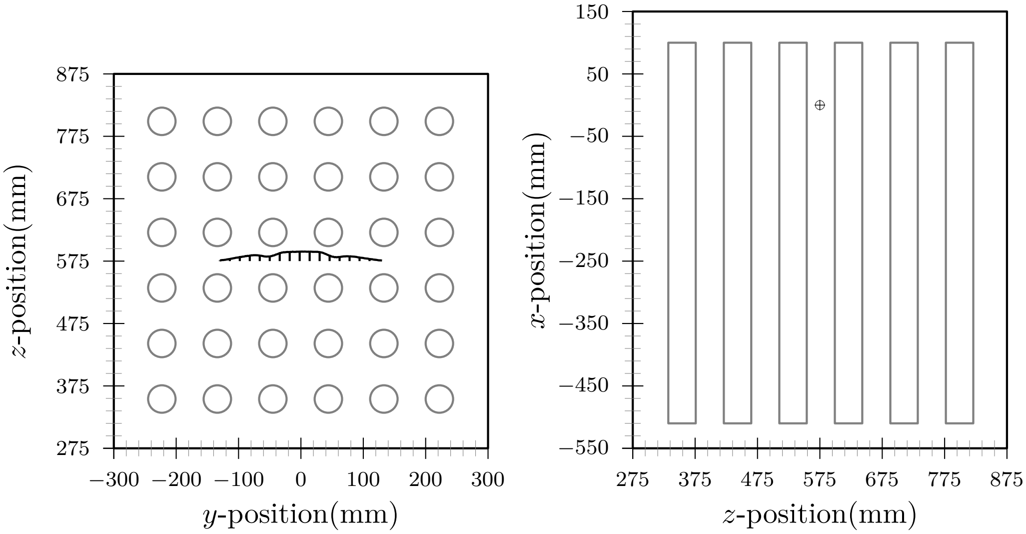

(a) Traverse path, plan view.

(b) Traverse path, side view.

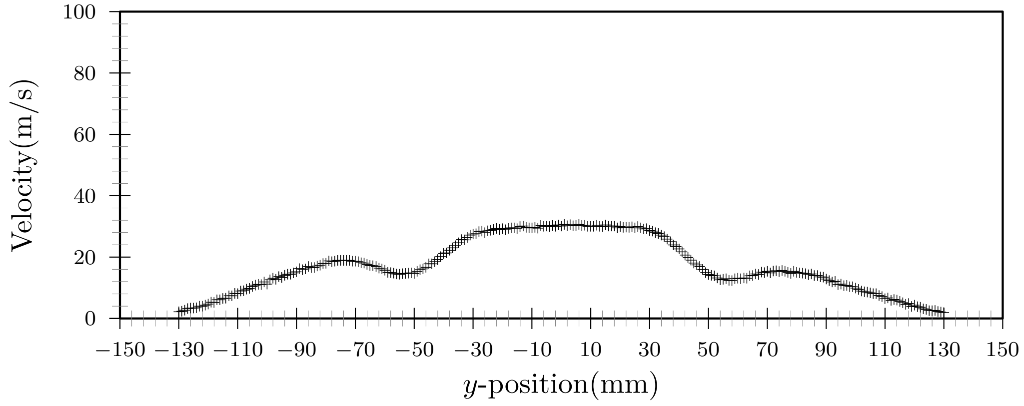

(c) Fluid velocity along traverse path.

Figure C.16: Jet centred between tubes, velocity profile along (0,y,575).

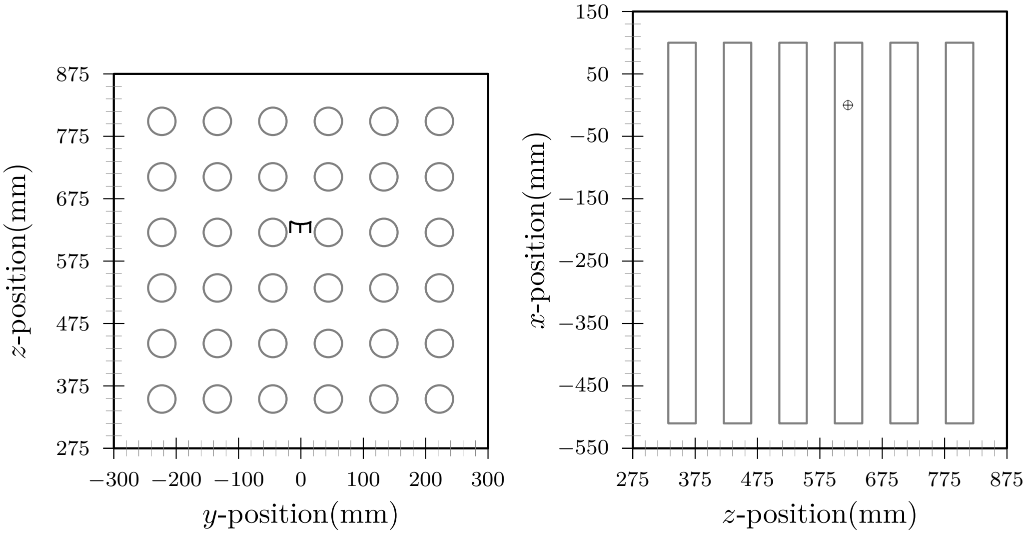

(a) Traverse path, plan view.

(b) Traverse path, side view.

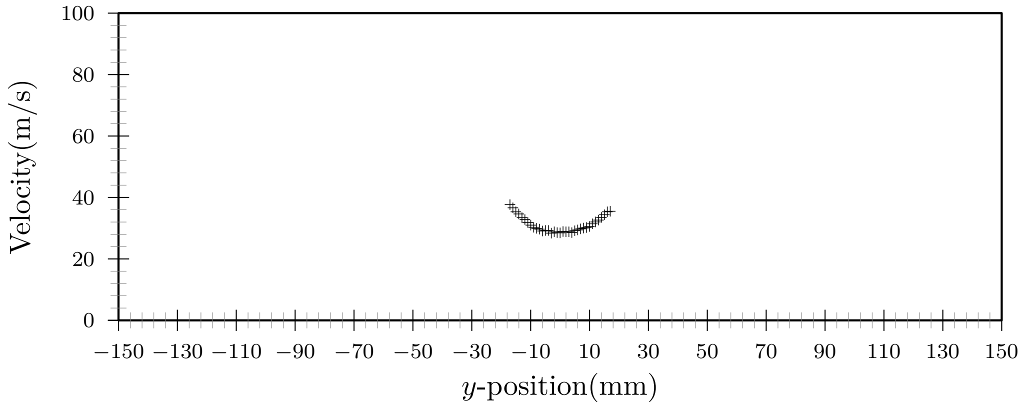

(c) Fluid velocity along traverse path.

Figure C.17: Jet centred between tubes, velocity profile along (0,y,620).

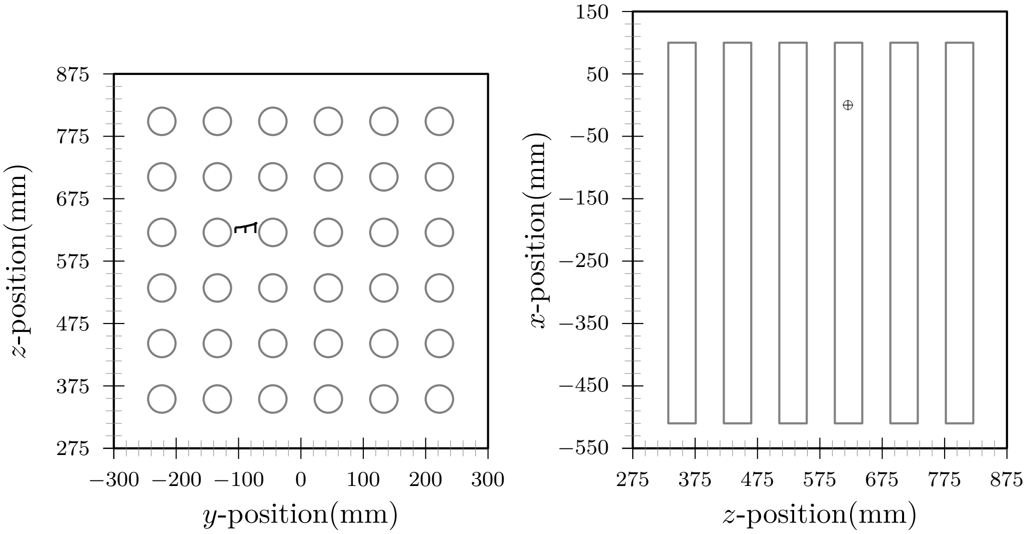

(a) Traverse path, plan view.

(b) Traverse path, side view.

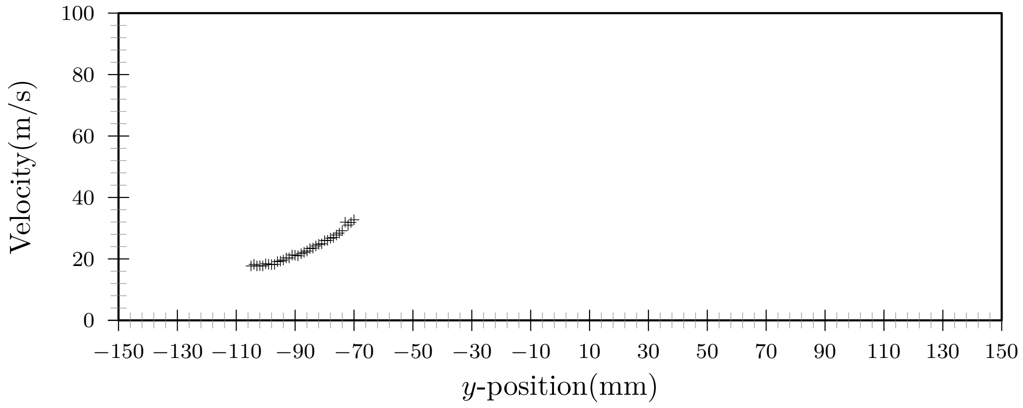

(c) Fluid velocity along traverse path.

Figure C.18: Jet centred between tubes, velocity profile along (0,y,620).

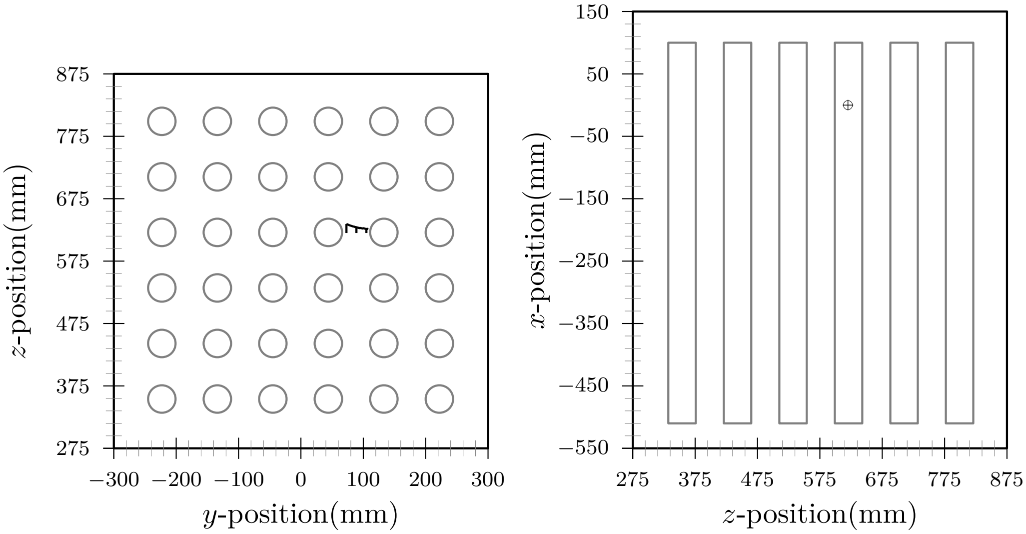

(a) Traverse path, plan view.

(b) Traverse path, side view.

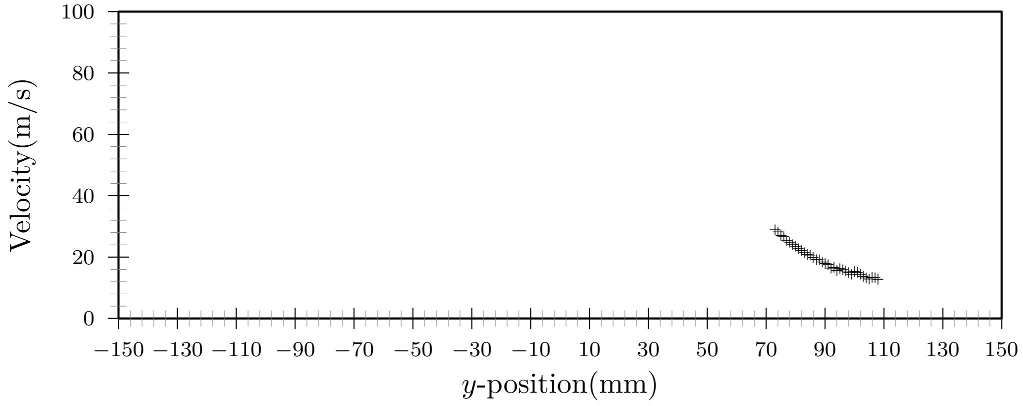

(c) Fluid velocity along traverse path.

Figure C.19: Jet centred between tubes, velocity profile along (0,y,620).

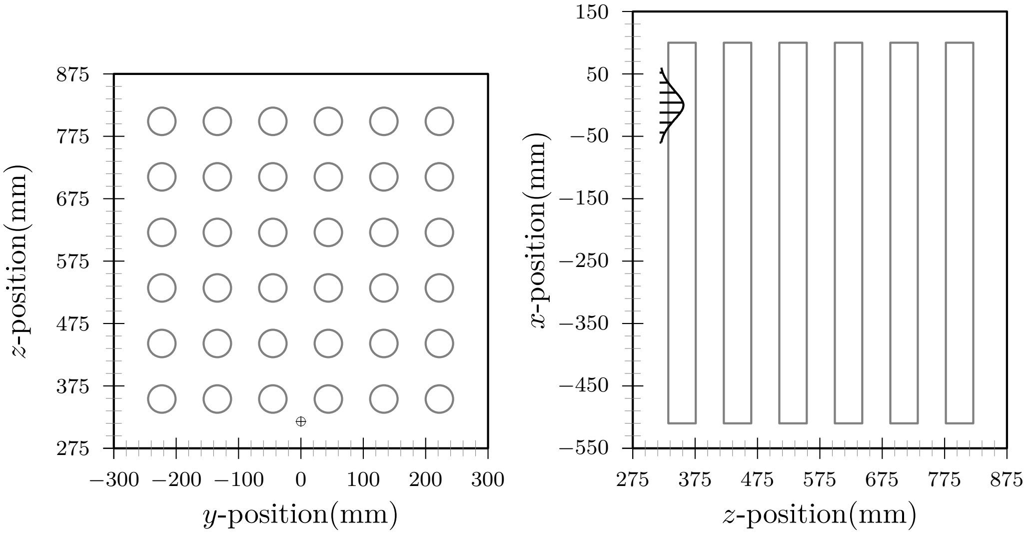

(a) Traverse path, plan view.

(b) Traverse path, side view.

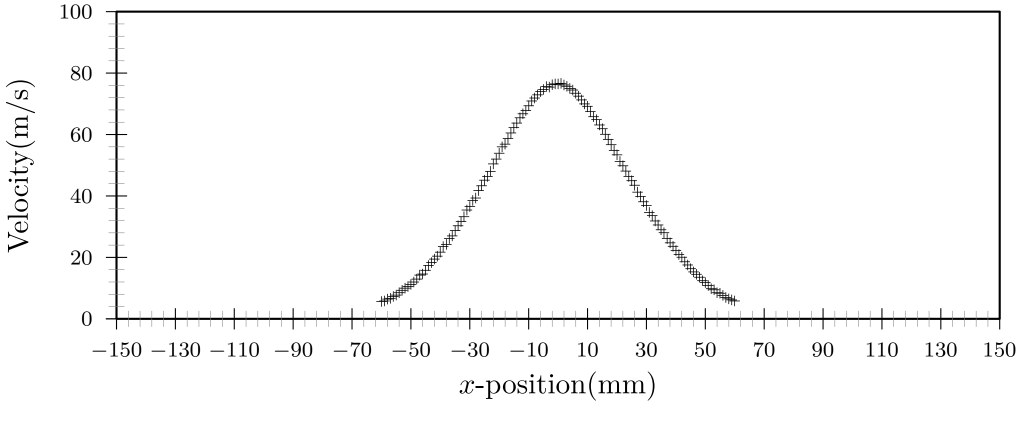

(c) Fluid velocity along traverse path.

Figure C.20: Jet centred between tubes, velocity profile along (x,0,318).

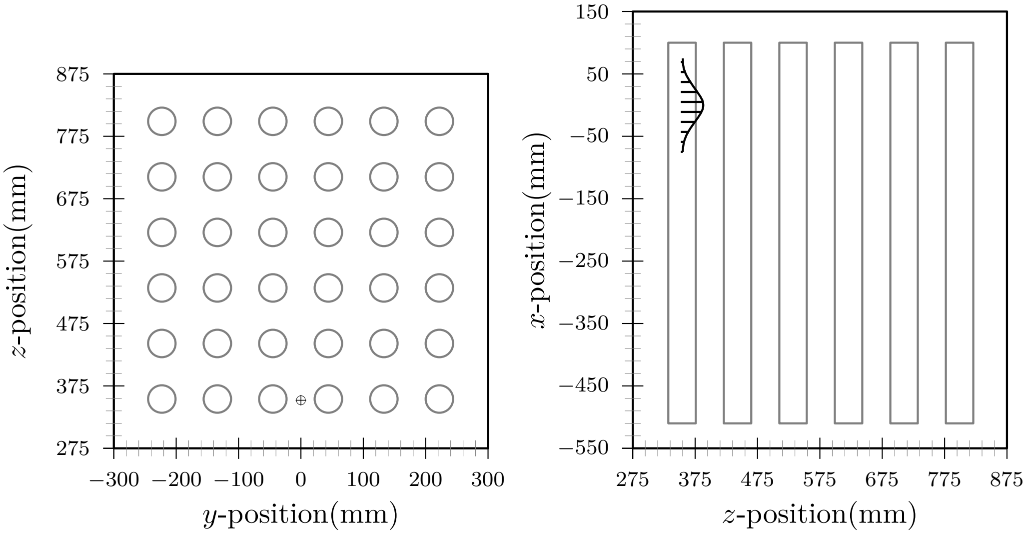

(a) Traverse path, plan view.

(b) Traverse path, side view.

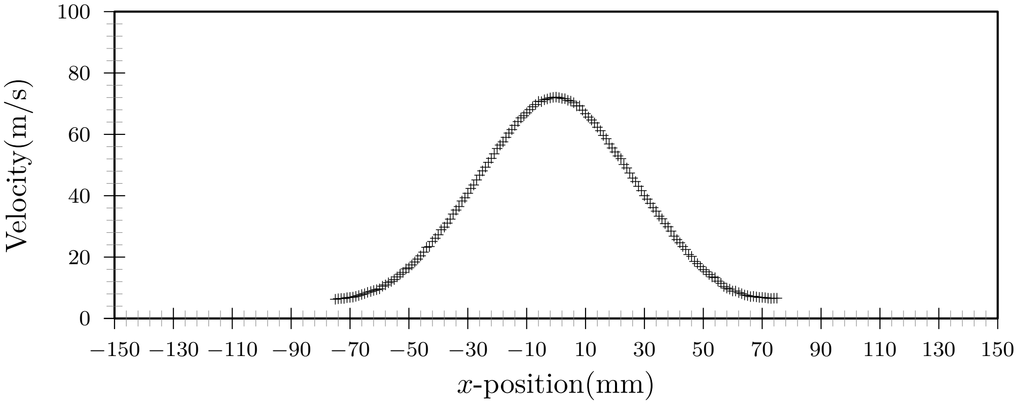

(c) Fluid velocity along traverse path.

Figure C.21: Jet centred between tubes, velocity profile along (x,0,352).

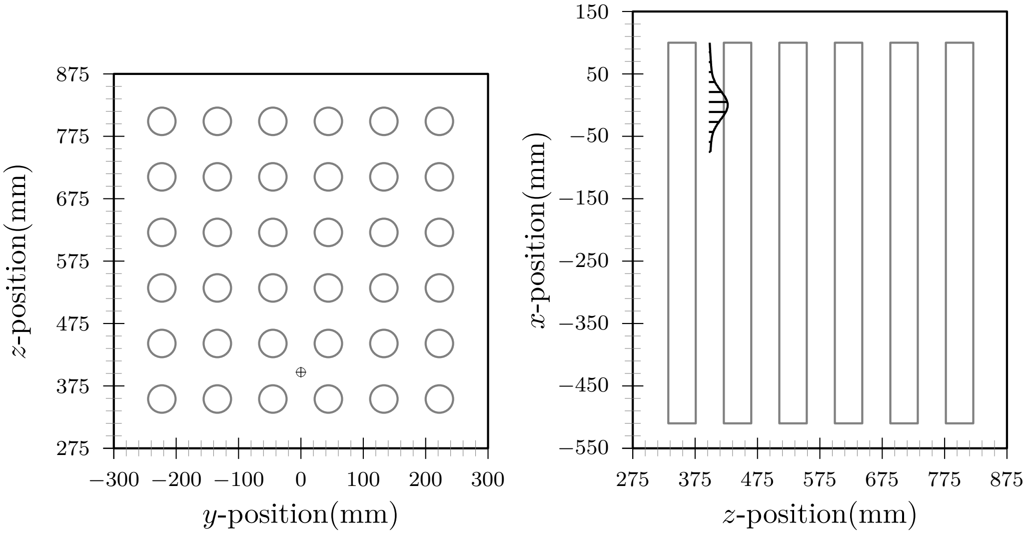

(a) Traverse path, plan view. **(b)** Traverse path, side view.

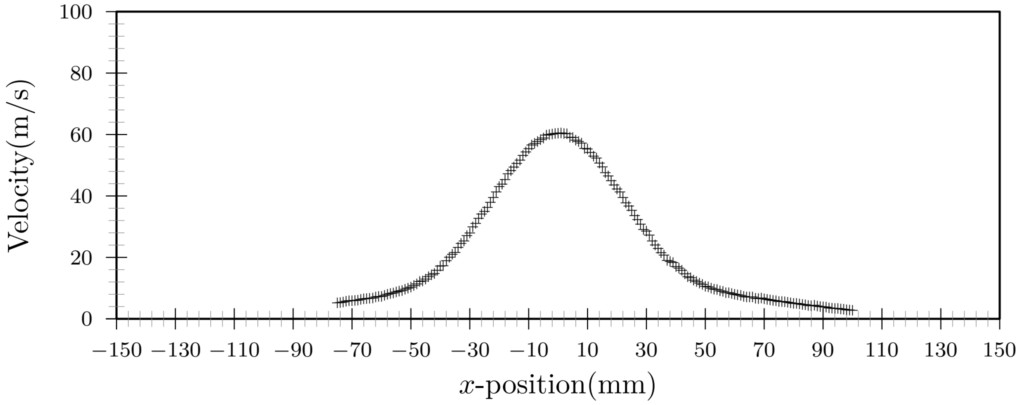

(c) Fluid velocity along traverse path.

Figure C.22: Jet centred between tubes, velocity profile along (x,0,397).

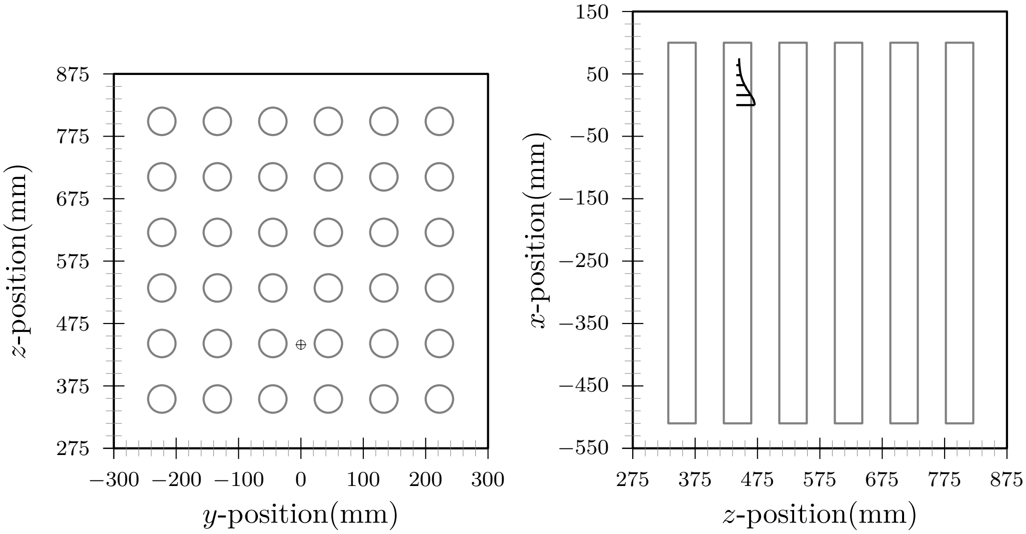

(a) Traverse path, plan view.

(b) Traverse path, side view.

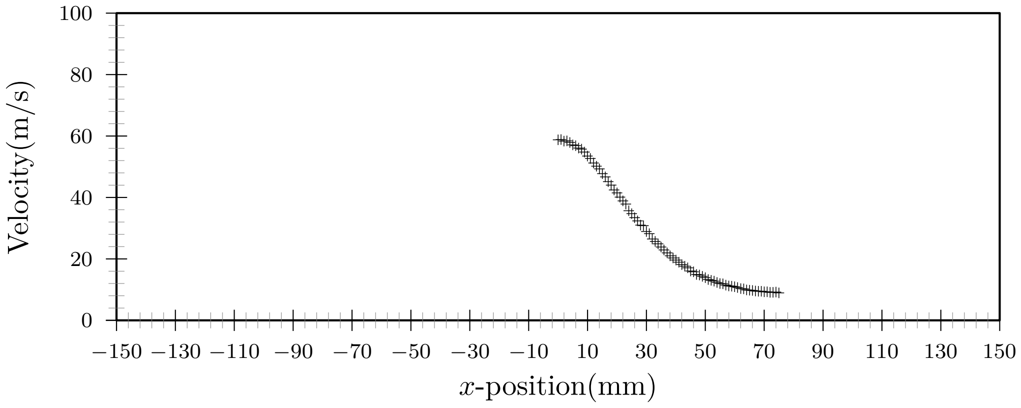

(c) Fluid velocity along traverse path.

Figure C.23: Jet centred between tubes, velocity profile along (x,0,441).

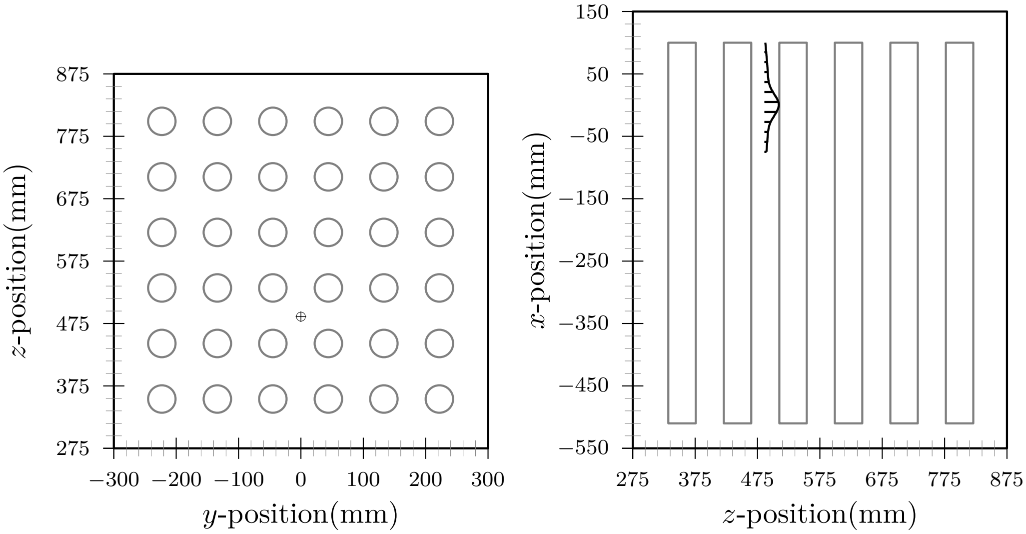

(a) Traverse path, plan view.

(b) Traverse path, side view.

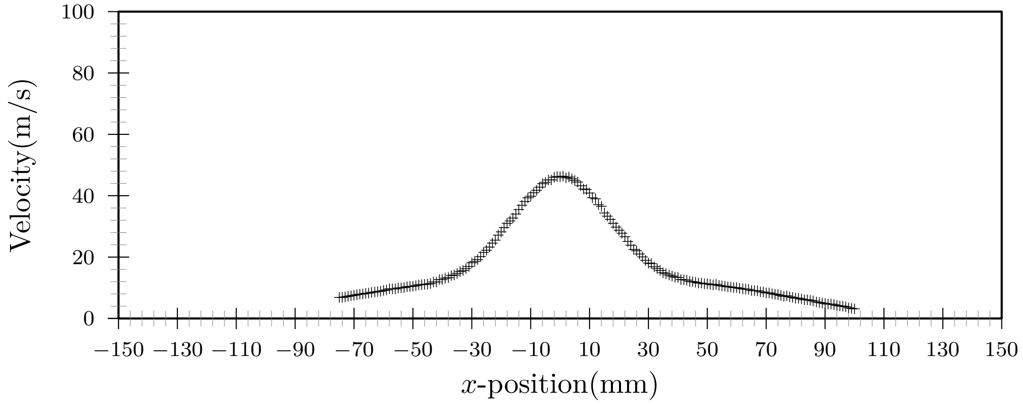

(c) Fluid velocity along traverse path.

Figure C.24: Jet centred between tubes, velocity profile along (x,0,486).

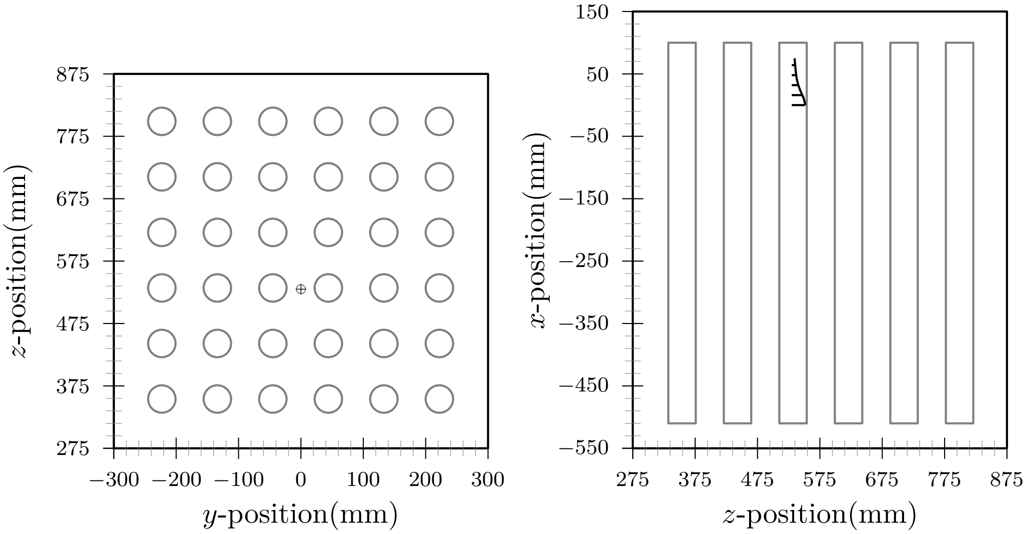

(a) Traverse path, plan view.

(b) Traverse path, side view.

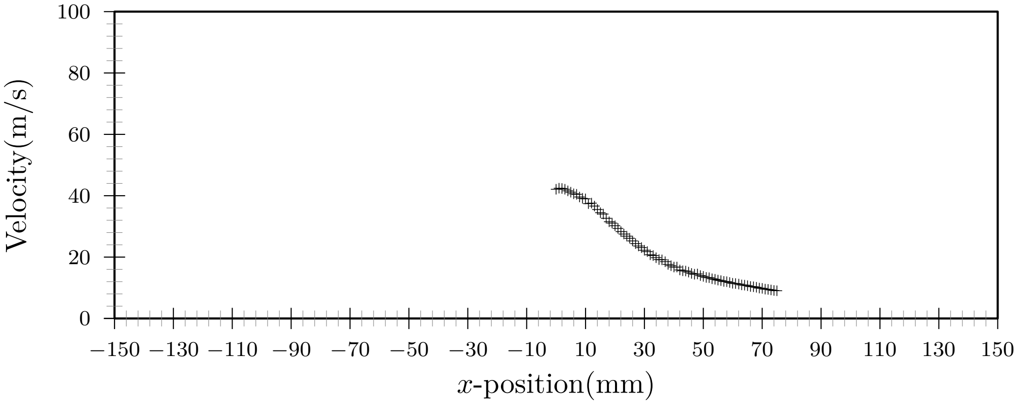

(c) Fluid velocity along traverse path.

Figure C.25: Jet centred between tubes, velocity profile along (x,0,530).

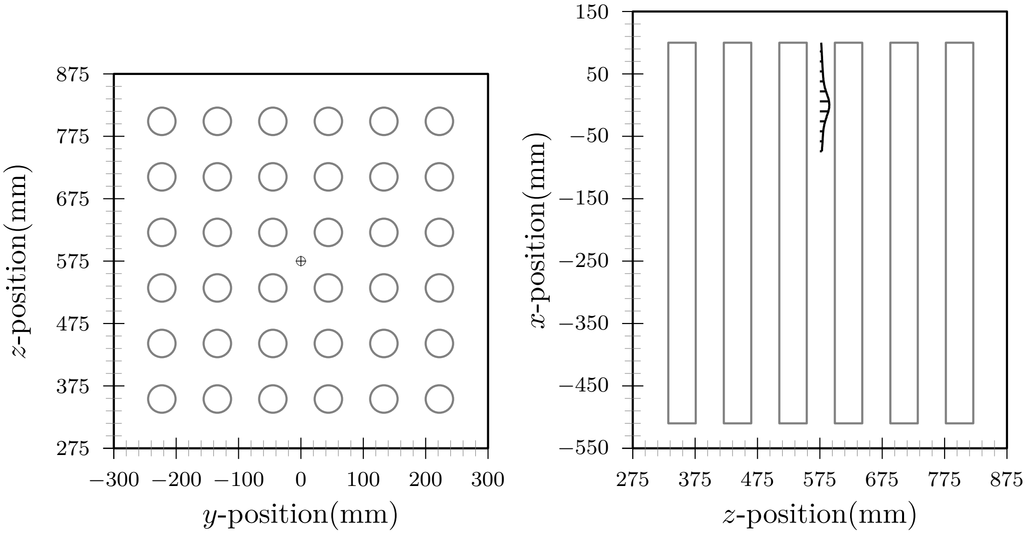

(a) Traverse path, plan view.

(b) Traverse path, side view.

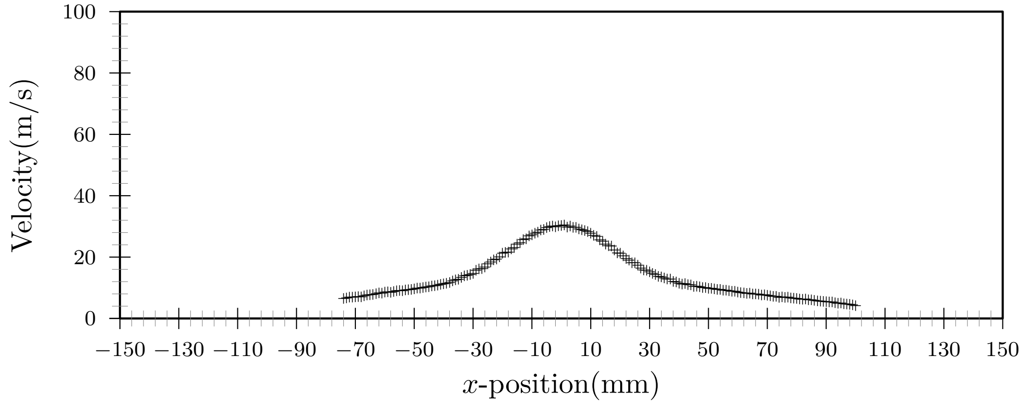

(c) Fluid velocity along traverse path.

Figure C.26: Jet centred between tubes, velocity profile along (x,0,575).

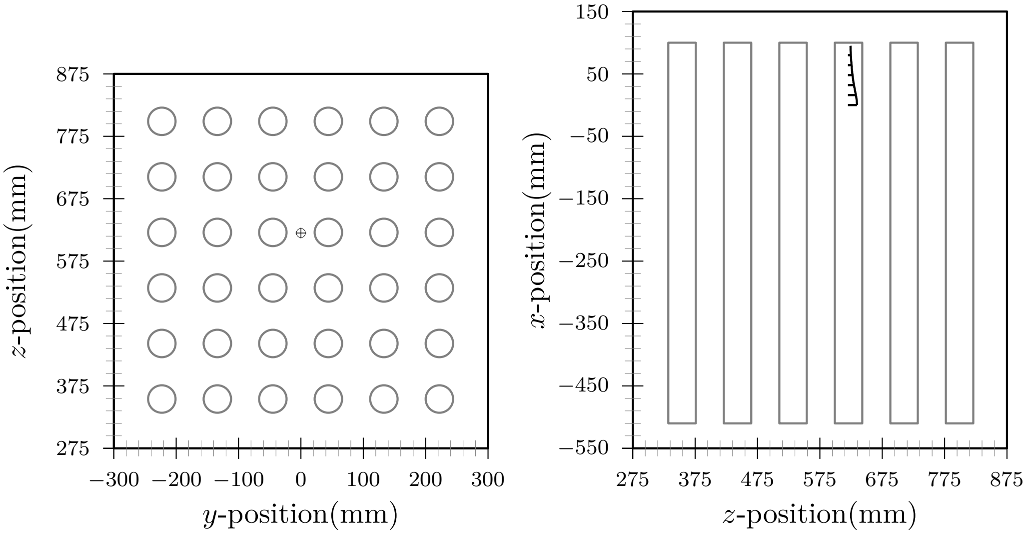

(a) Traverse path, plan view.

(b) Traverse path, side view.

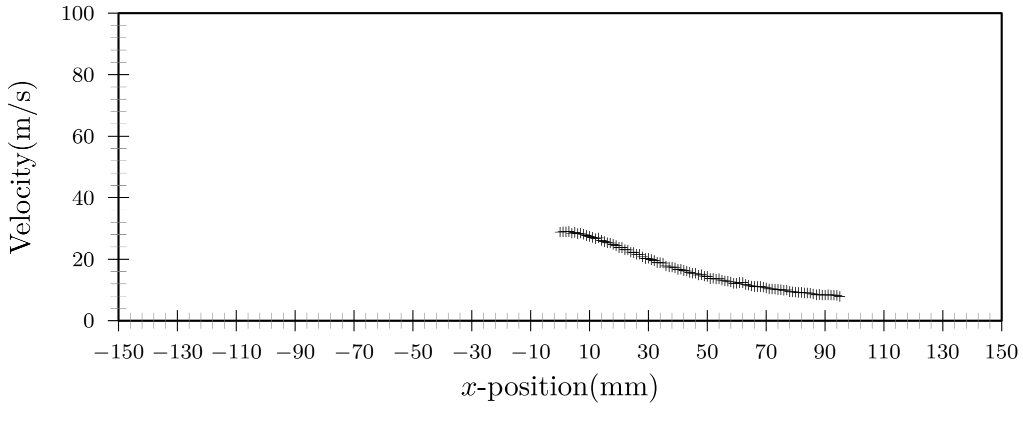

(c) Fluid velocity along traverse path.

Figure C.27: Jet centred between tubes, velocity profile along (x,0,620).

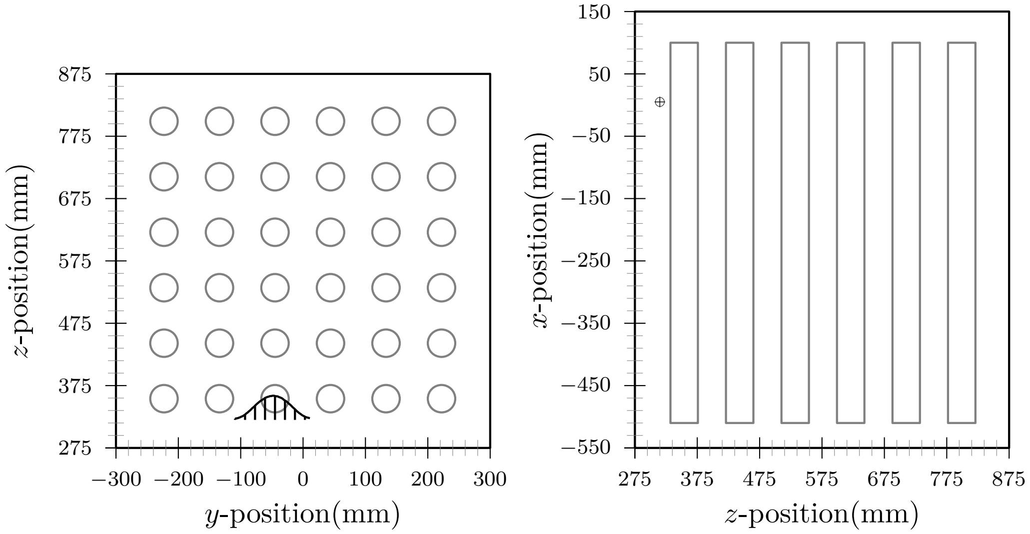

(a) Traverse path, plan view.

(b) Traverse path, side view.

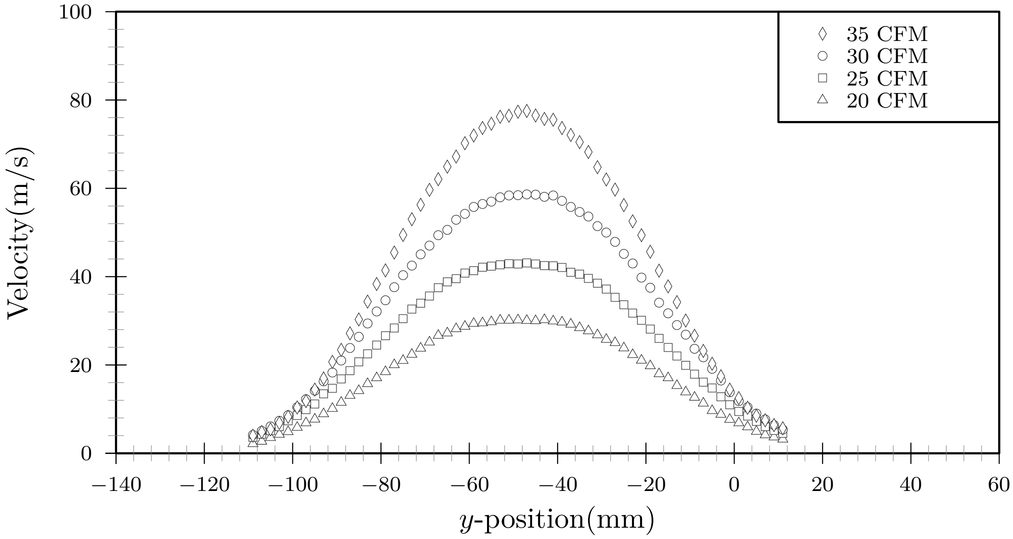

(c) Jet fluid velocity along traverse path.

Figure C.28: Jet entry velocity profiles for various nozzle flow-rates taken across horizontal axis (y-axis) with jet centred on face of tube T13.

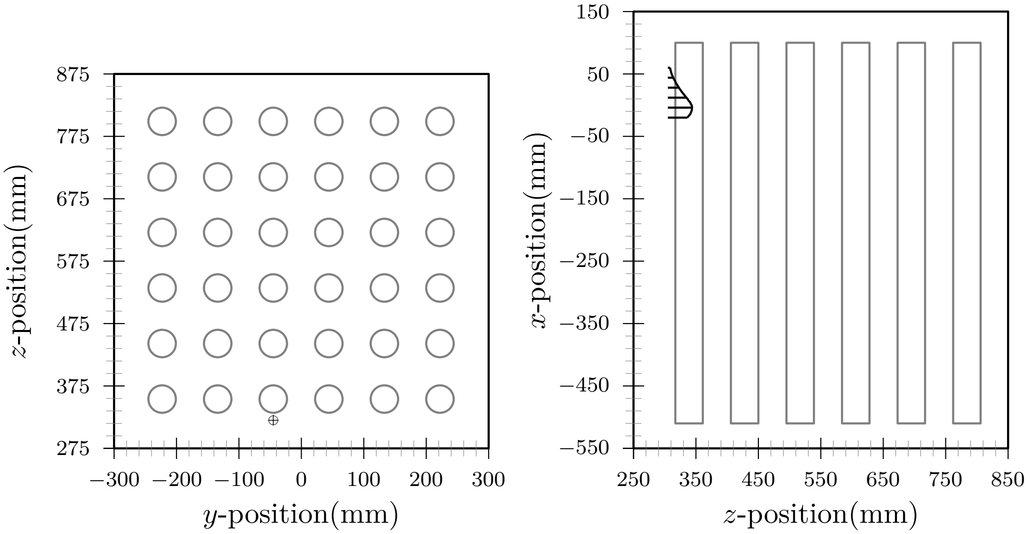

(a) Traverse path, plan view.

(b) Traverse path, side view.

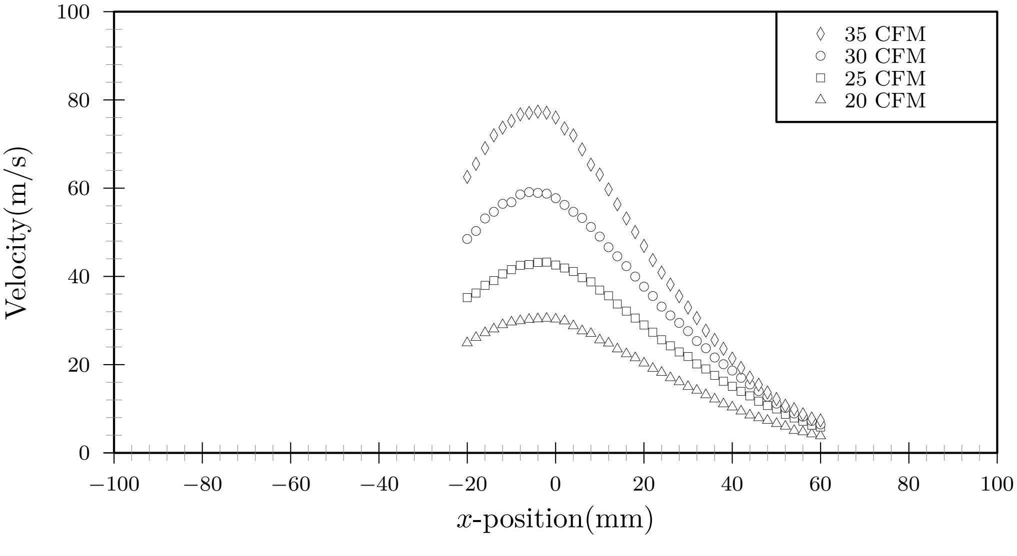

(c) Jet fluid velocity along traverse path.

Figure C.29: Jet entry velocity profiles for various nozzle flow-rates taken across vertical axis (x-axis) with jet centred on face of tube T13.

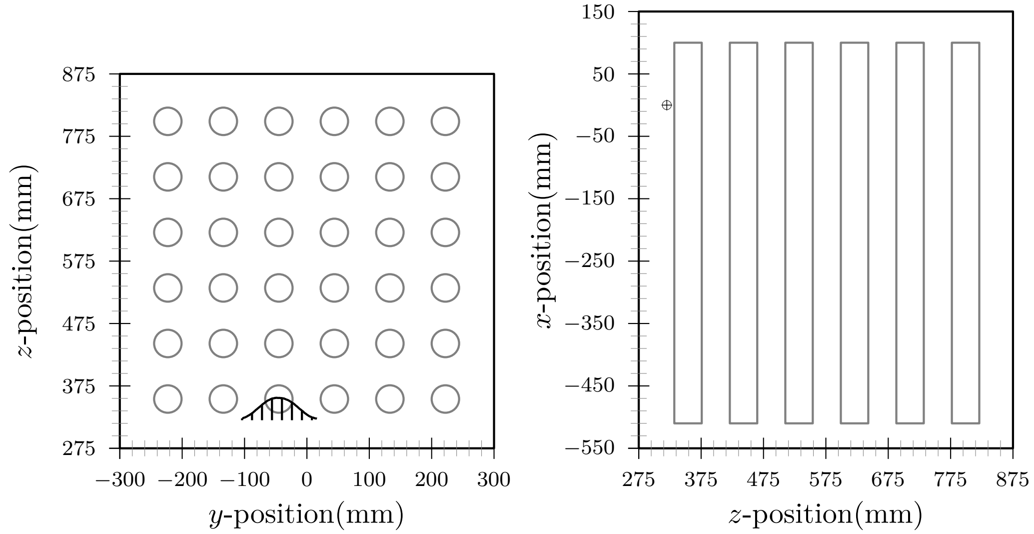

(a) Traverse path, plan view.

(b) Traverse path, side view.

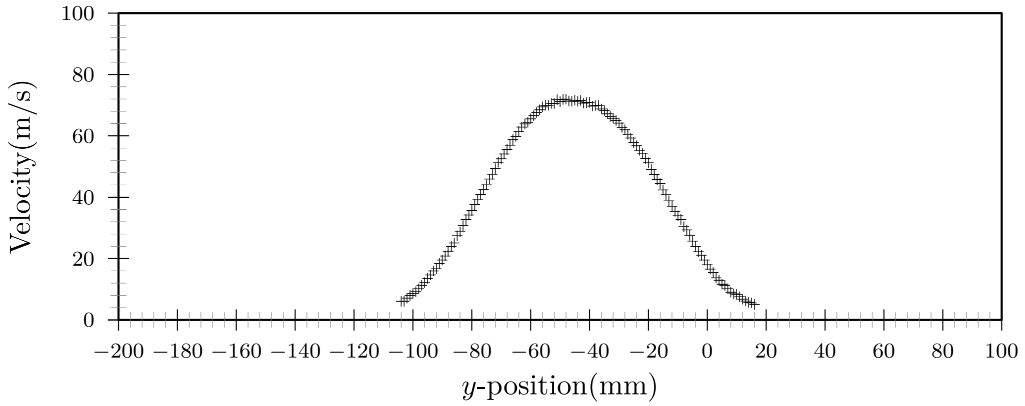

(c) Fluid velocity along traverse path.

Figure C.30: Jet centred on a tube face, velocity profile along (0,y,320).

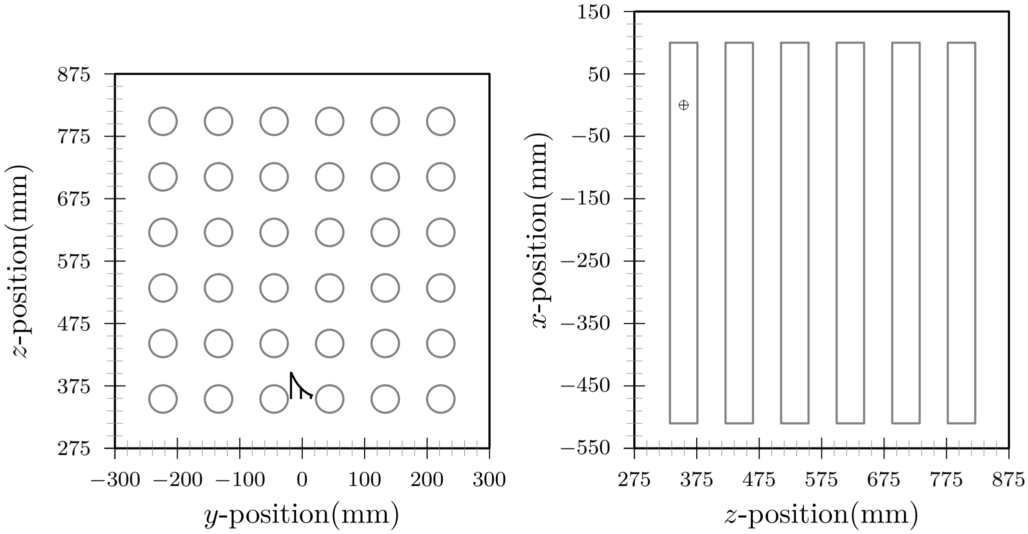

(a) Traverse path, plan view.

(b) Traverse path, side view.

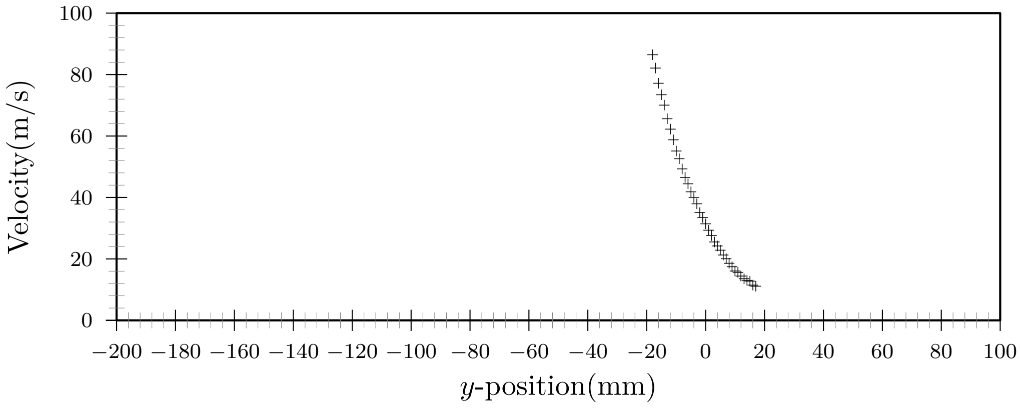

(c) Fluid velocity along traverse path.

Figure C.31: Jet centred on a tube face, velocity profile along (0,y,354).

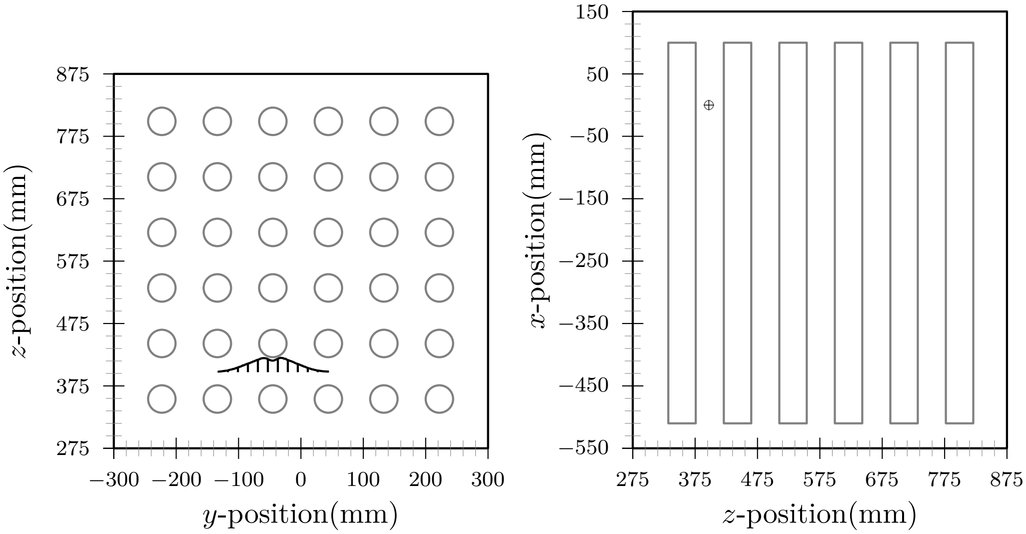

(a) Traverse path, plan view.

(b) Traverse path, side view.

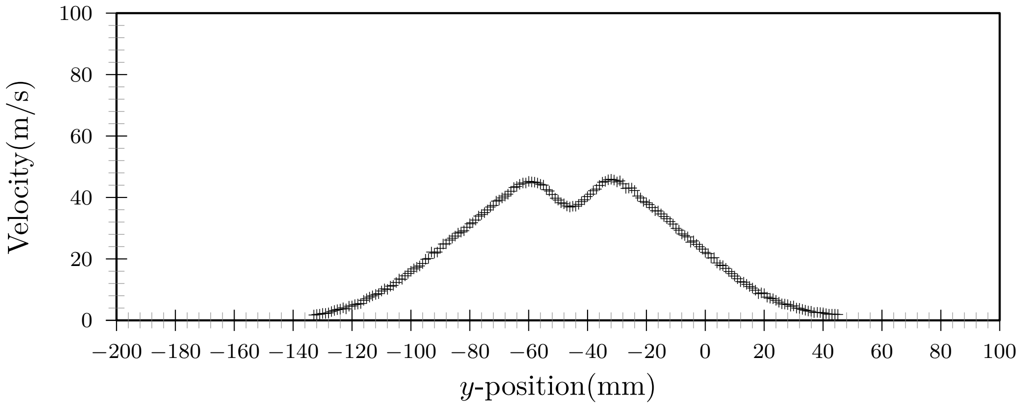

(c) Fluid velocity along traverse path.

Figure C.32: Jet centred on a tube face, velocity profile along (0,y,397).

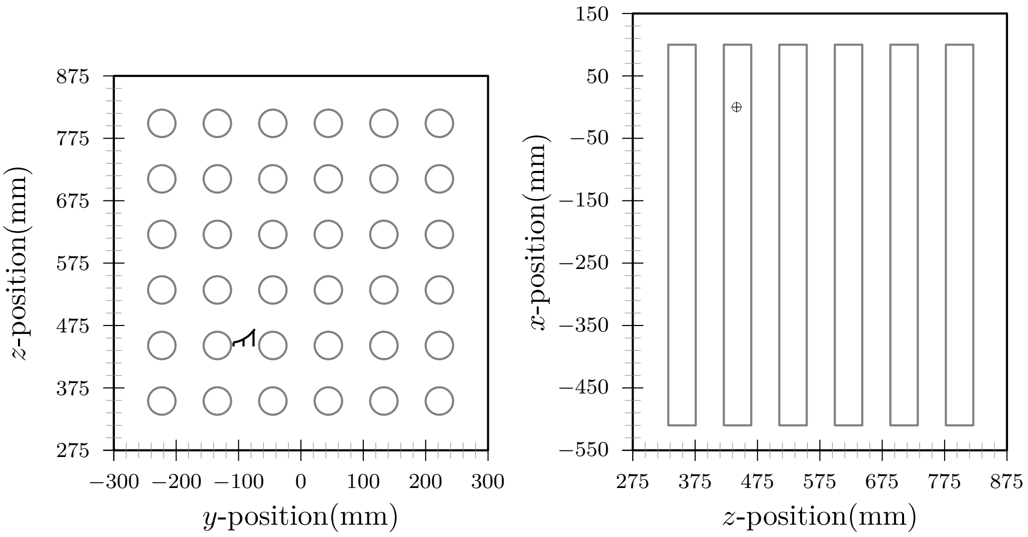

(a) Traverse path, plan view.

(b) Traverse path, side view.

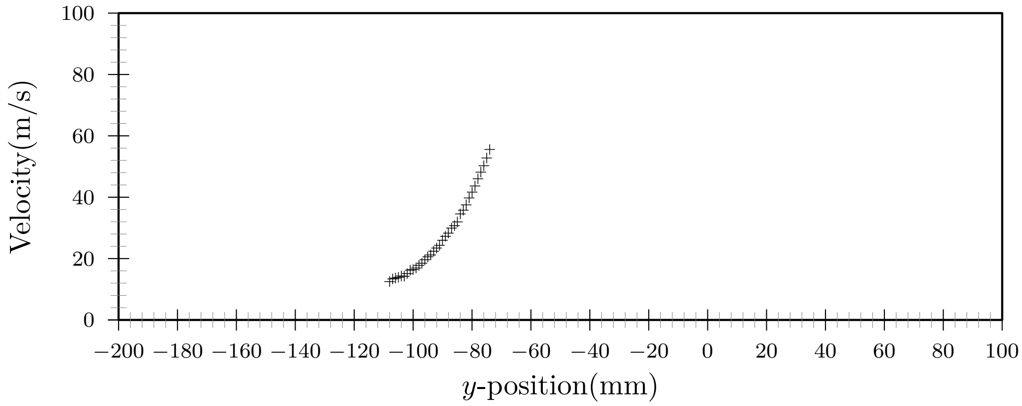

(c) Fluid velocity along traverse path.

Figure C.33: Jet centred on a tube face, velocity profile along (0,y,441).

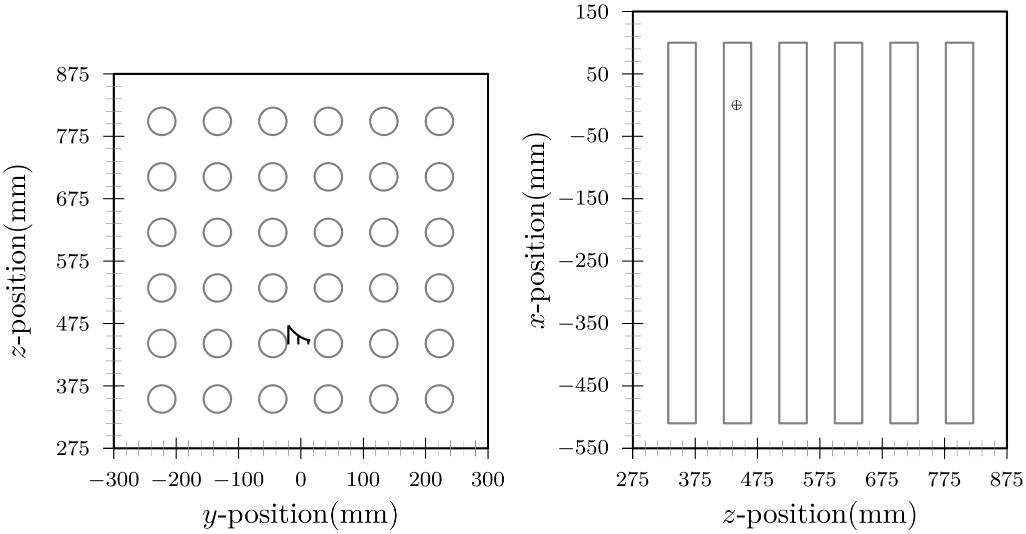

(a) Traverse path, plan view. **(b)** Traverse path, side view.

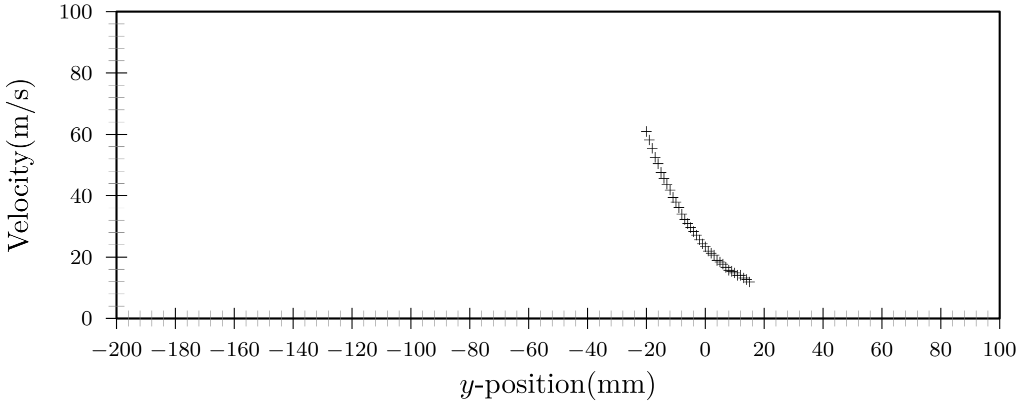

(c) Fluid velocity along traverse path.

Figure C.34: Jet centred on a tube face, velocity profile along (0,y,441).

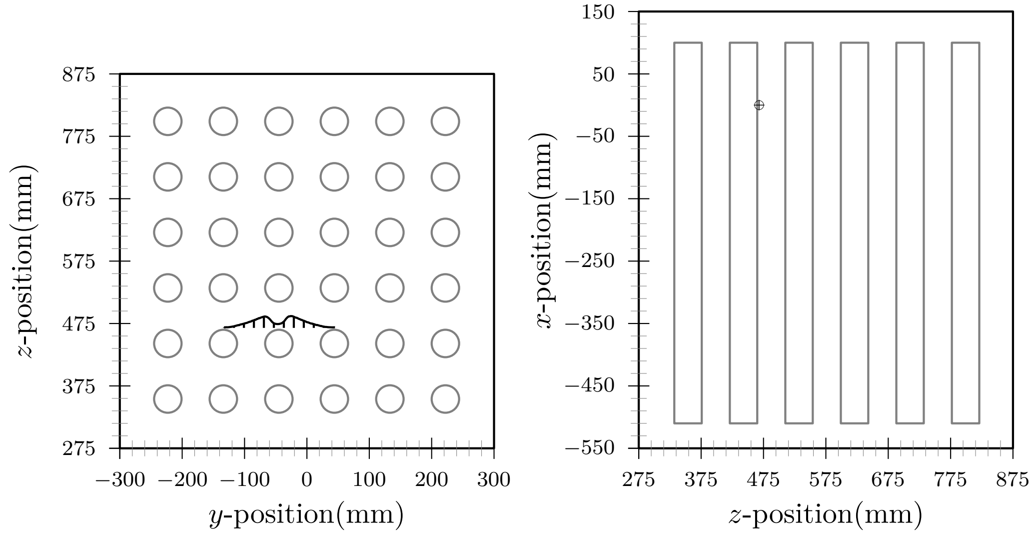

(a) Traverse path, plan view. **(b)** Traverse path, side view.

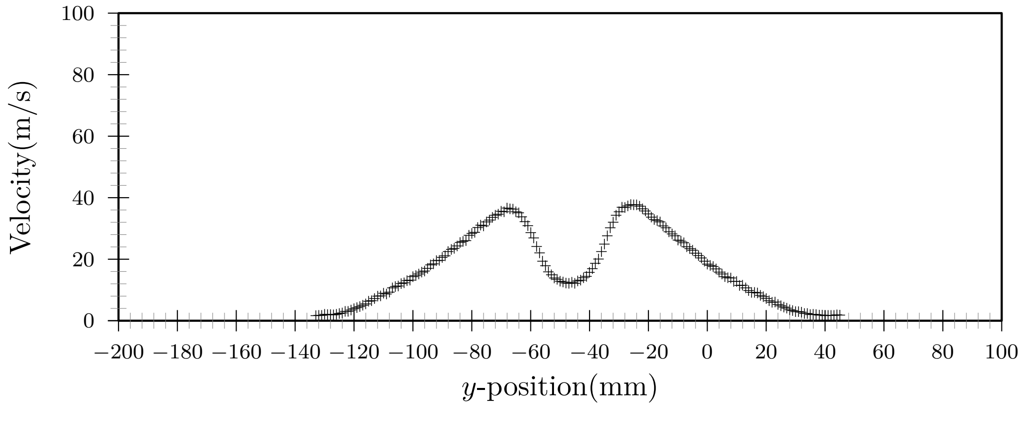

(c) Fluid velocity along traverse path.

Figure C.35: Jet centred on a tube face, velocity profile along (0,y,468).

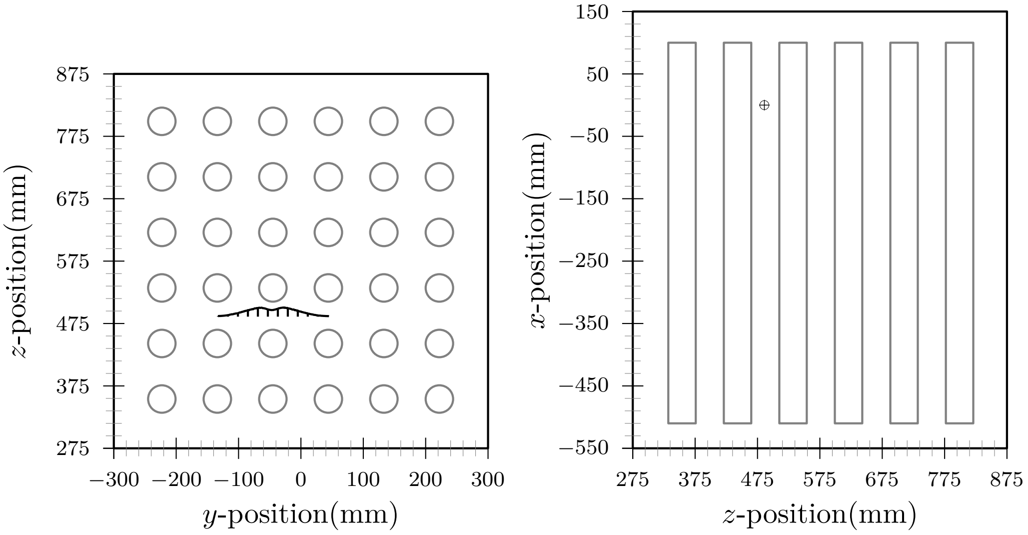

(a) Traverse path, plan view.

(b) Traverse path, side view.

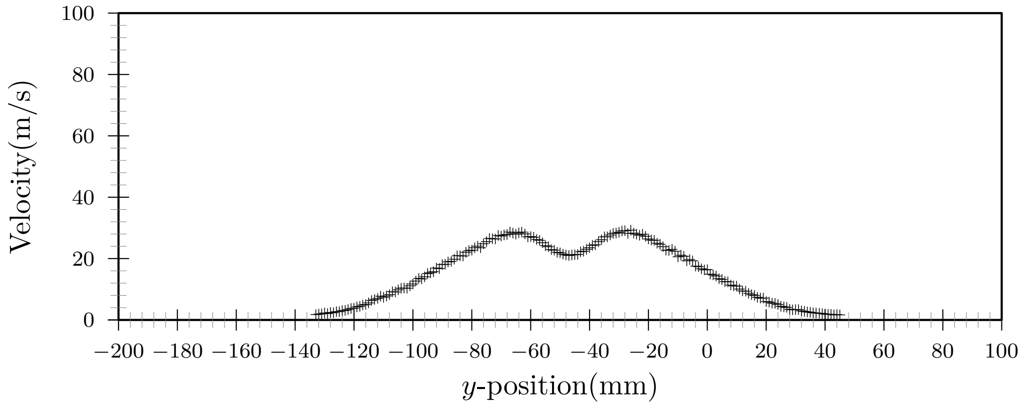

(c) Fluid velocity along traverse path.

Figure C.36: Jet centred on a tube face, velocity profile along (0,y,486).

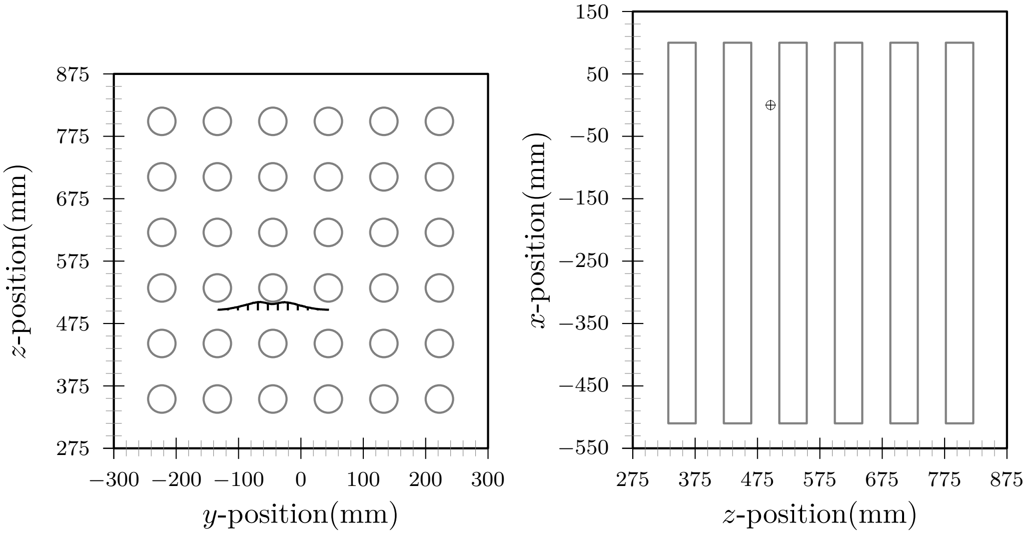

(a) Traverse path, plan view.

(b) Traverse path, side view.

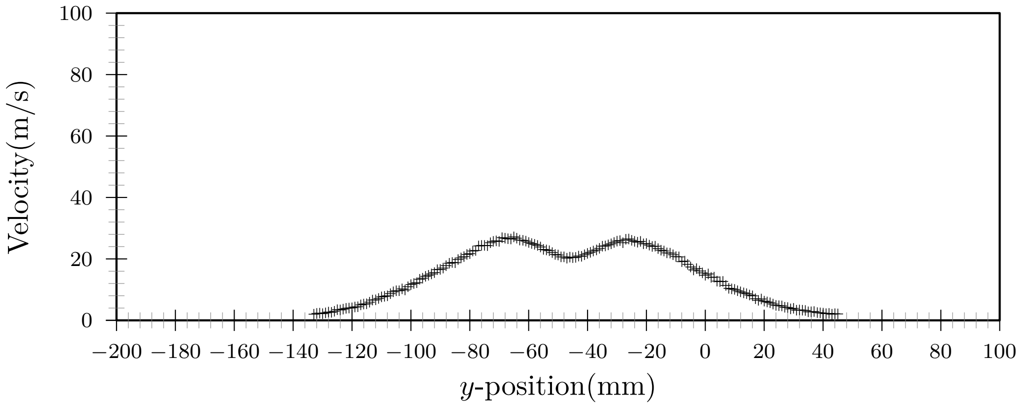

(c) Fluid velocity along traverse path.

Figure C.37: Jet centred on a tube face, velocity profile along (0,y,496).

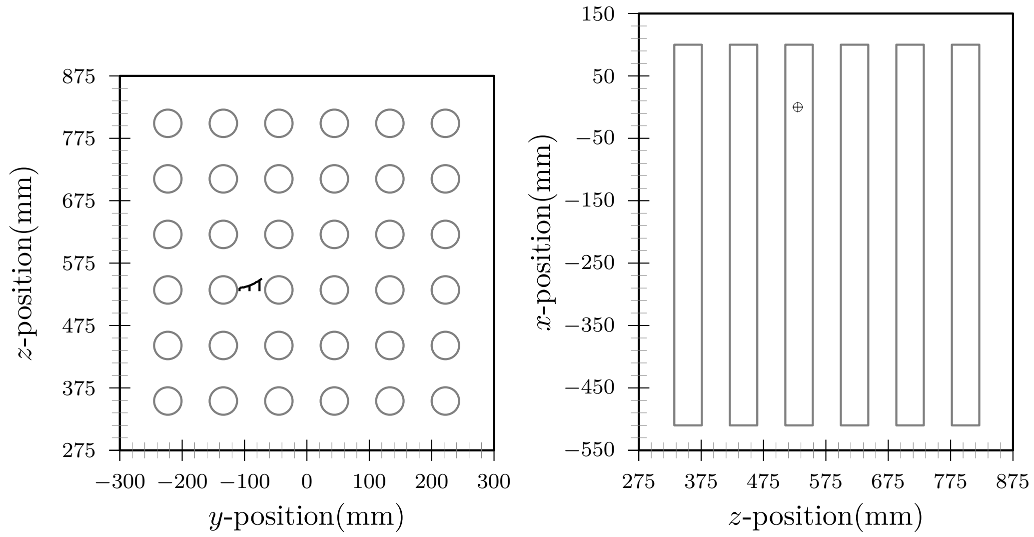

(a) Traverse path, plan view.

(b) Traverse path, side view.

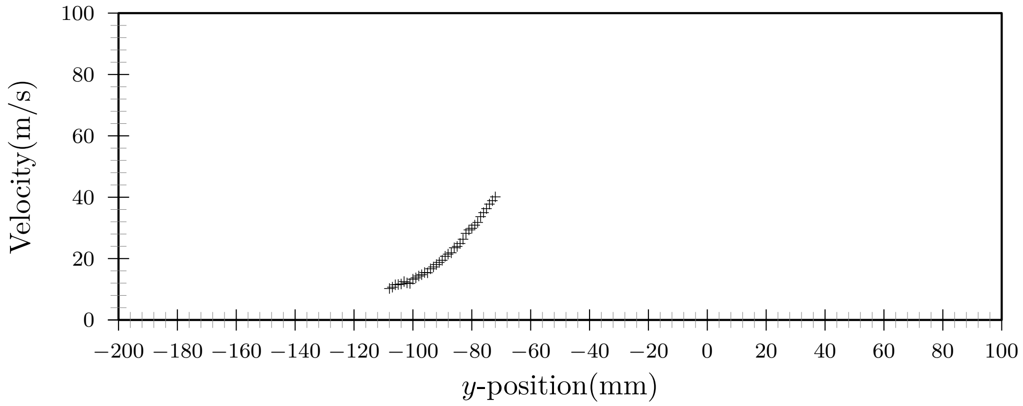

(c) Fluid velocity along traverse path.

Figure C.38: Jet centred on a tube face, velocity profile along (0,y,530).

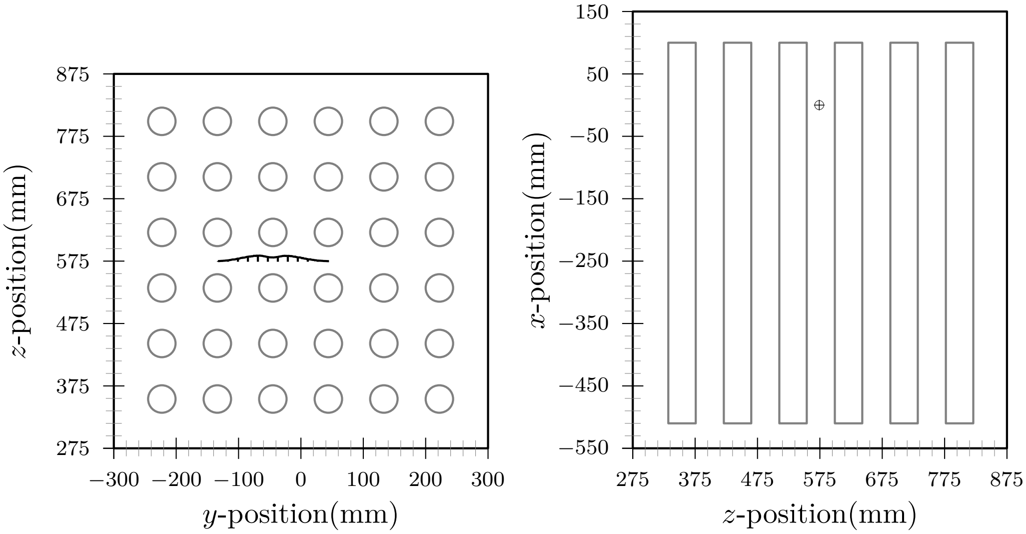

(a) Traverse path, plan view. **(b)** Traverse path, side view.

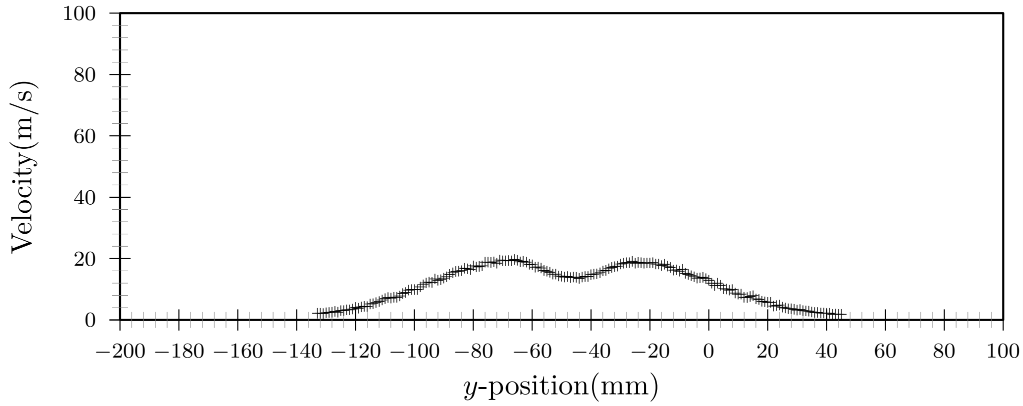

(c) Fluid velocity along traverse path.

Figure C.39: Jet centred on a tube face, velocity profile along (0,y,574).

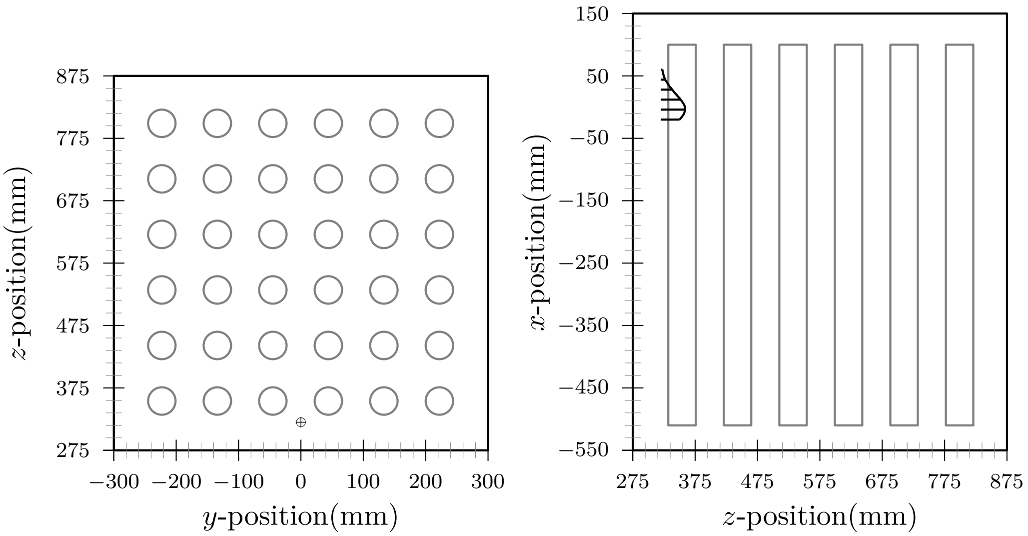

(a) Traverse path, plan view.

(b) Traverse path, side view.

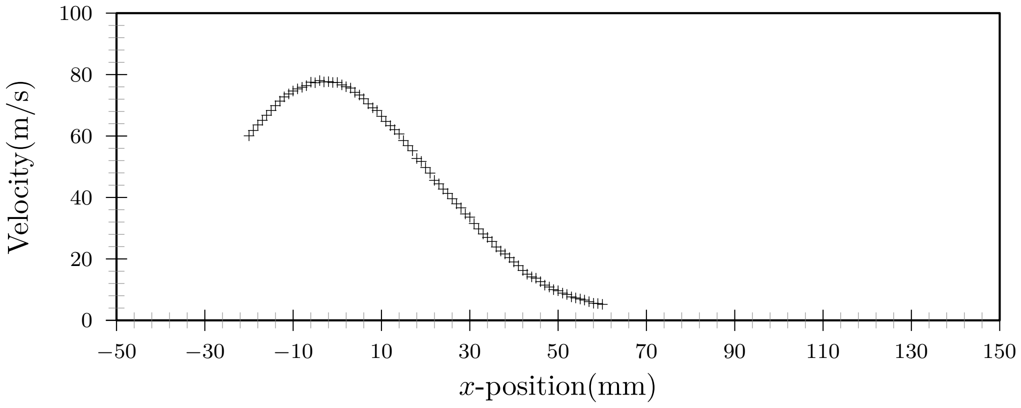

(c) Fluid velocity along traverse path.

Figure C.40: Jet centred on a tube face, velocity profile along (x,0,320).

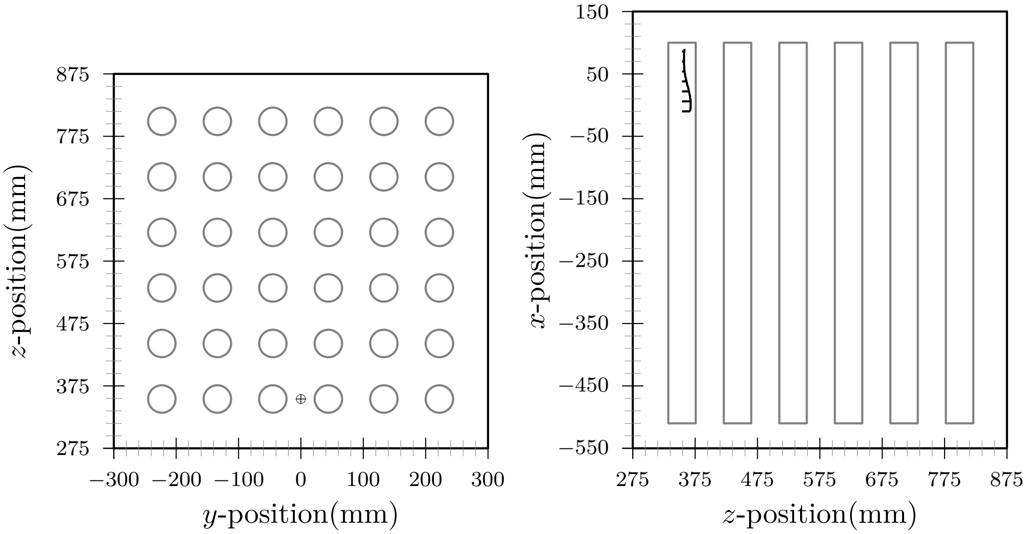

(a) Traverse path, plan view.

(b) Traverse path, side view.

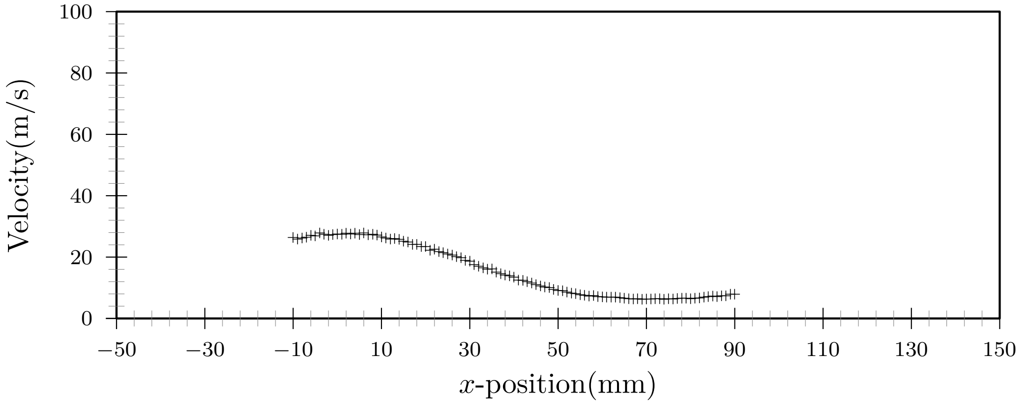

(c) Fluid velocity along traverse path.

Figure C.41: Jet centred on a tube face, velocity profile along (x,0,354).

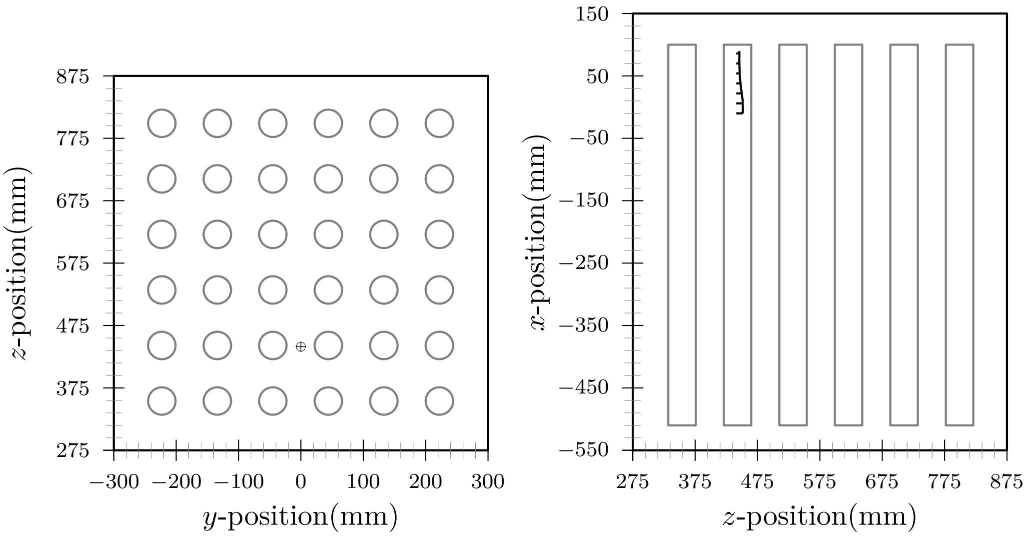

(a) Traverse path, plan view.

(b) Traverse path, side view.

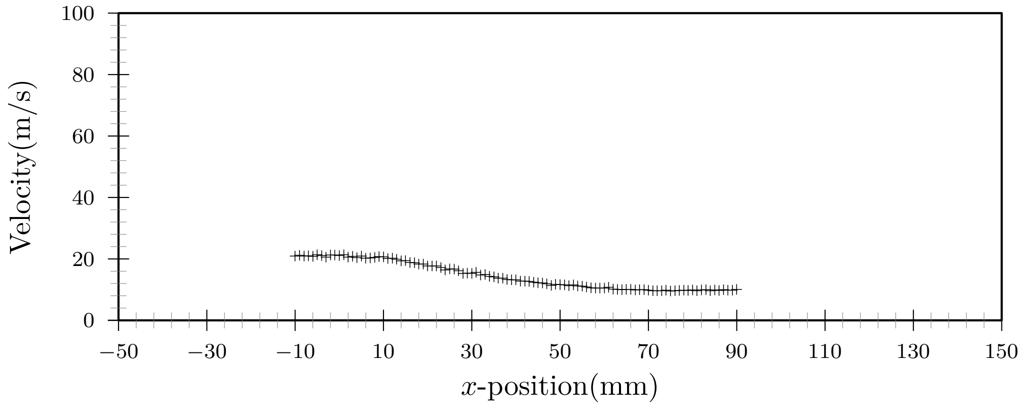

(c) Fluid velocity along traverse path.

Figure C.42: Jet centred on a tube face, velocity profile along (x,0,441).

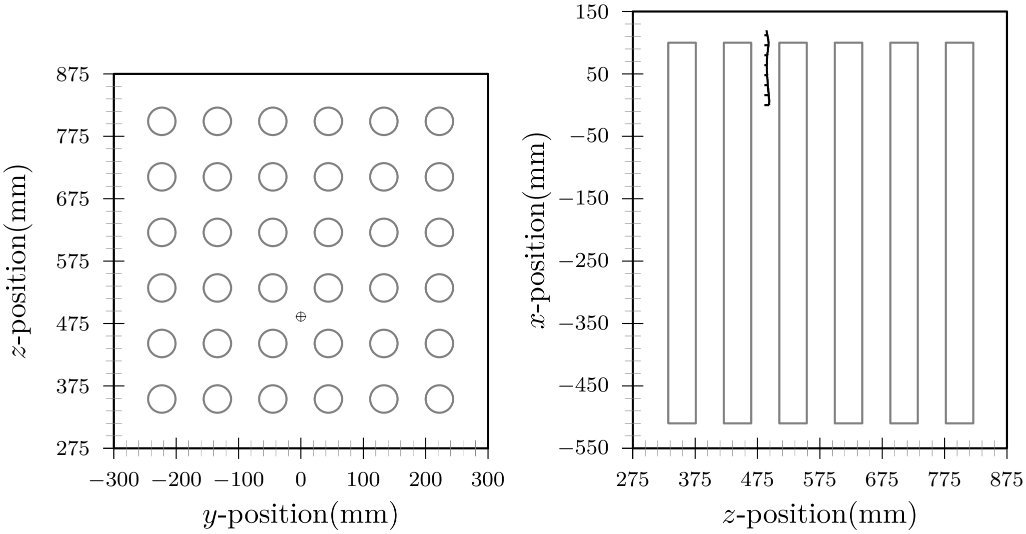

(a) Traverse path, plan view.

(b) Traverse path, side view.

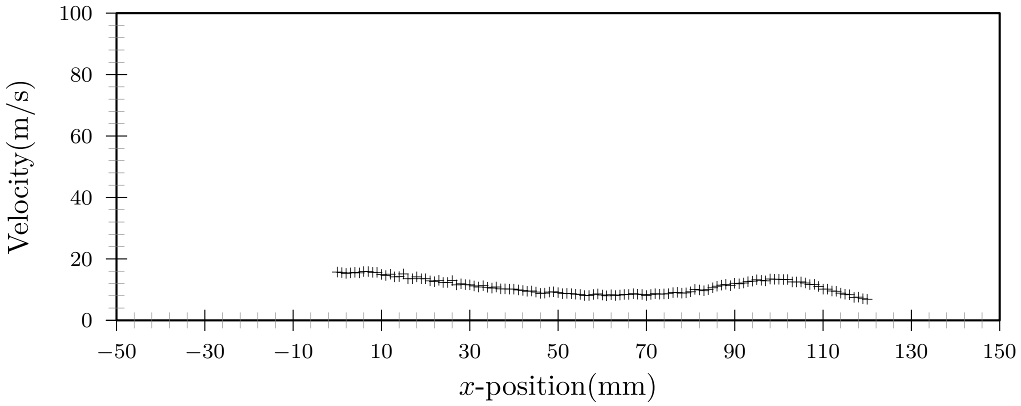

(c) Fluid velocity along traverse path.

Figure C.43: Jet centred on a tube face, velocity profile along (x,0,486).